Università degli Studi di Napoli Federico II
Department of Industrial Engineering - DII

Optimization of Heat Transfer with novel approaches

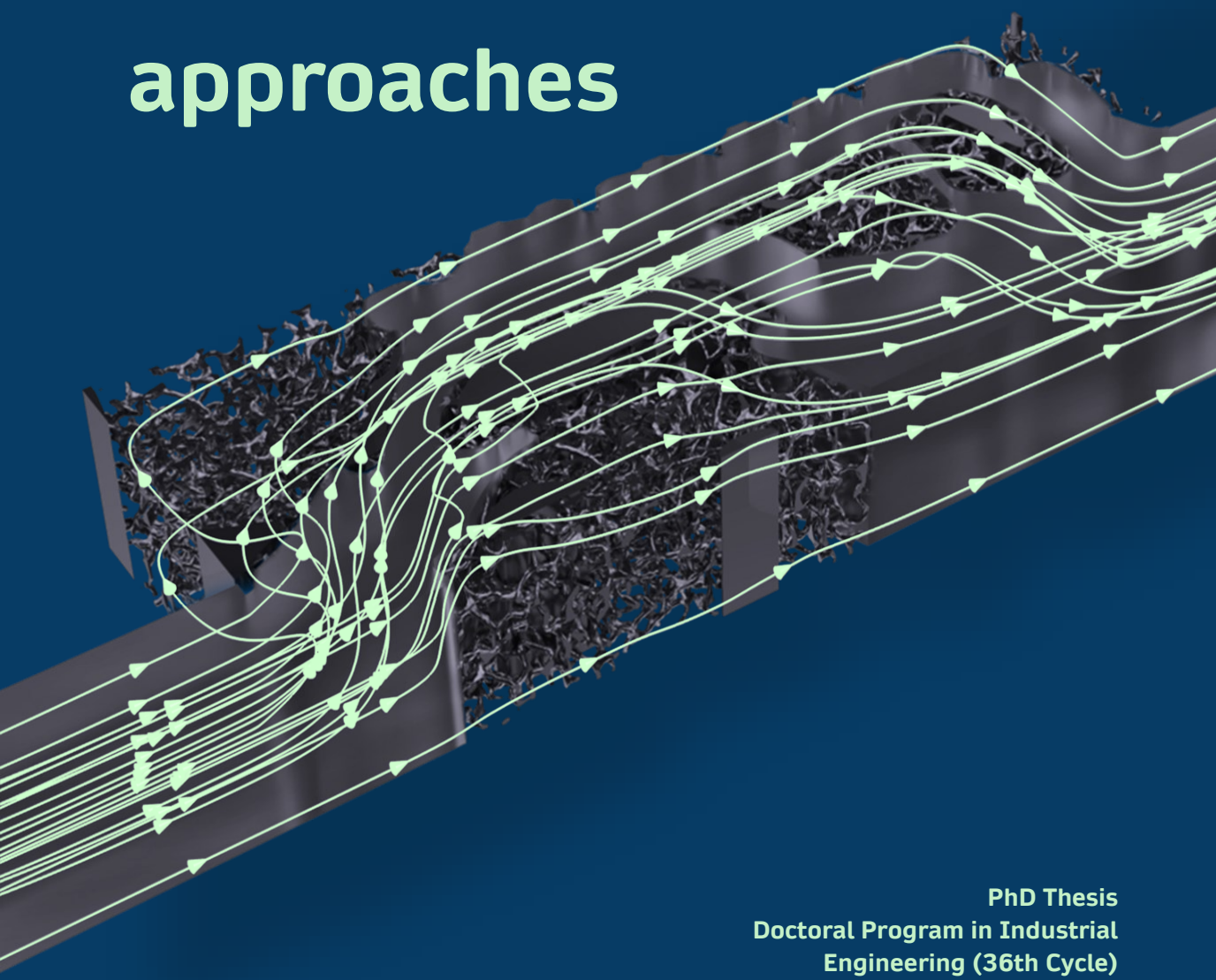

PhD Thesis
Doctoral Program in Industrial Engineering (36th Cycle)

by Andrea Fragnito

Optimization of Heat Transfer with novel approaches

Andrea Fragnito

Ph.D. Thesis

Napoli, 2023
Università degli Studi di Napoli Federico II
Dipartimento di Ingegneria Industriale - DII
Piazzale Tecchio, 80 – 80125 Napoli (Italia)

Optimization of Heat Transfer with novel approaches

Doctoral Dissertation
Doctoral Program in Industrial Engineering (36th Cycle)

Ph. D. Coordinator:
Prof. Michele Grassi
Università degli Studi di Napoli Federico II

Approved as to style and content by:

Prof. Nicola Bianco, *Tutor and Supervisor*
Università degli Studi di Napoli Federico II

Prof. Marcello Iasiello, *Co-supervisor*
Università degli Studi di Napoli Federico II

Prof. Gerardo Maria Mauro, *Co-supervisor*
Università degli Studi del Sannio

Declaration

I hereby declare that the contents and organization of this dissertation constitute my own original work and does not compromise in any way the rights of third parties, including those relating to the security of personal data.
Parts of this dissertation have been published in international journals and/or conference articles (see list of the author's publications of the thesis).

Napoli, October 31, 2023

Andrea Fragnito

* This dissertation is presented in partial fulfilment of the requirements for Ph.D. degree in the Department of Industrial Engineering of University Federico II.

Ai miei genitori

Acknowledgment

Sitting in front of two drinks in a bar at a gas station, on a sultry May afternoon in 2020. It might sound like the beginning of a Clint Eastwood film. Instead, it was the beginning of my PhD.

I would like to express my deepest gratitude to all those who have contributed to the completion of this Ph.D. journey, which began during the challenging background of the COVID-19 pandemic. The path was not without its obstacles, but it was illuminated by the unwavering support and encouragement of many individuals and institutions.

First and foremost, I extend my heartfelt appreciation to my dedicated and inspiring supervisors: Prof. Nicola Bianco, Prof. Marcello Iasiello, and Prof. Gerardo Maria Mauro. Your *guidance, mentorship*, and belief in my abilities have been the cornerstone of my academic growth. Your solid commitment to encourage my potential and providing a supporting working environment have been invaluable. I am grateful for the countless hours of insightful discussions, the encouragement to explore new horizons, and the relentless dedication to excellence that you have instilled in me.

I wish to express my sincere thanks to the DTU TopOpt group for their warm and generous hospitality during my six-month tenure as a guest. This invaluable experience has not only enriched me academically but has also contributed significantly to my personal growth. I am deeply appreciative of the support, guidance, and knowledge of my supervisor there, Prof. Casper Schousboe Andreasen, whose passion for topology optimization have been contagious, igniting my own interest in the field and fuelling its growth day by day.

I would also like to extend my gratitude to my colleagues and fellow researchers who have shared this journey with me (Peppe, Giò, Franco, Ali, Terry, Abi, Gabri *et al.*). Your friendship, your kindness and pure friendship have enriched this journey immeasurably. Together, we have faced the challenges of this travel, and together, we have shared lovely moments inside and outside the university.

To my friends and family, your encouragement, patience, and understanding have sustained me throughout this journey. Your belief in me, at every step, has

been my driving force. your presence has always been my certainty, your love my strength. Thank you for standing by me through thick and thin.

To my brother, a source of experience. To the words spoken and those that do not need to be said. Because that is what brothers are.

To my soul, in another body. To my infinite source of love, which never runs out. To my faith. My Fede.

This thesis stands as a gift to the collective efforts of all those who have been part of my journey. I am forever grateful for your belief in me and for the opportunities you have provided for me to grow.

With sincere gratitude

Andrea Fragnito

The research presented in this dissertation has been partly supported by the Italian Ministry of Economic Development, within the research project "RdS-PAR 2019-2021", in collaboration with the Italian Agency for Energy Efficiency (ENEA).
The author's work has been supported by a PhD scholarship funded by the University of Napoli Federico II.

Abstract

In the field of thermal engineering and science, heat transfer problems are essential for designing and operating various systems. As these problems become more complex, the use of numerical tools becomes increasingly crucial. Different heat transfer mechanisms, including conduction, convection, and radiation, require tailored approaches for analysis and optimization. The choice between gradient-based methods and non-gradient-based techniques like genetic algorithms depends on the system's size and complexity.

Large-scale systems, such as industrial heat exchangers and power plant components, benefit from genetic algorithms, which focus on optimizing parameters directly impacting thermal performance. They are efficient, scalable, and prioritize energy efficiency. Genetic algorithms excel in addressing highly complex heat transfer problems by navigating intricate design spaces effectively.

In contrast, small-scale systems like microfluidic devices or compact electronic components demand precision, making gradient-based techniques, especially topology optimization, more suitable. Topology optimization allows to fine-tune every aspect of the system to achieve maximum heat transfer efficiency, offering flexibility in design and innovative form factors.

The choice of optimization technique should align with the specific goals and constraints of the heat transfer problem, considering scale, complexity, and design requirements. This thesis provides a comprehensive analysis of various optimization choices for heat transfer devices, offering examples and case studies to enrich the understanding of tools and techniques applicable to different systems and heat transfer mechanisms.

Summary

In the landscape of thermal engineering and science, understanding and investigating heat transfer problems is a fundamental pursuit, supporting the design and operation of countless systems in our modern world. As the complexities of these problems continue to grow, the need for numerical tools becomes increasingly apparent. Numerical methods empower us to analyse, and ultimately address the intricate challenges posed by heat transfer phenomena. However, these problems are far from uniform; they span a wide spectrum of scenarios, each governed by distinct heat transfer mechanisms, starting from the generalities of heat transfer problems, recognizing the indispensable role of numerical tools while also acknowledging the diversity inherent in these challenges. As we delve into this topic, we must appreciate that heat transfer is not a one-size-fits-all domain. The approach to analysing and solving these problems must be tailored to the specific heat transfer mechanism at play, whether it be conduction, convection, radiation, or a combination thereof. This is fundamental in laying the groundwork for a comprehensive understanding of the need for different optimization approaches. Whether one opts for gradient-based methods, which rely on mathematical derivatives, or non-gradient-based techniques, *e.g.,* genetic algorithms, which simulate natural selection, the choice is inherently tied to the distinctions introduced by different heat transfer mechanisms, but not only.

Heat transfer problems can vary greatly in size and complexity, ranging from microscale phenomena in electronics to macroscale heat exchangers in industrial processes. The choice of optimization method must be tailored to the specific characteristics and constraints of each problem. Each approach has its strengths and weaknesses, and the selection between them often hinges on the size and complexity of the system under examination and the desired level of design freedom. This thesis delves into considerations surrounding the use of these optimization techniques, emphasizing the preference for genetic algorithms in large-scale systems while highlighting the advantages of gradient-based methods, particularly topology optimization-based one, in small-scale systems that demand a high degree of thermo-fluid-dynamic precision. Large-scale heat transfer systems, such as industrial heat exchangers and power plant components, pose unique challenges. These systems often feature intricate geometries and intricate thermal interactions, making it impractical to delve into the details of fluid dynamics. In such cases, treating

the system as an energy system is a pragmatic approach, and genetic algorithms are the preferred choice. GAs focus on optimizing parameters directly impacting thermal performance, sidestepping the computational burden associated with detailed computational fluid dynamics (CFD) simulations or complex numerical formulations. They excel in large-scale systems where the overarching goal is enhancing heat transfer efficiency. This approach is faster, more scalable, and maintains a sharp focus on energy efficiency, all of which are crucial factors in large-scale heat transfer applications. Furthermore, genetic algorithms shine when the complexity of the heat transfer problem is exceptionally high. Complex geometries and intricate thermal interactions can overwhelm traditional modeling approaches. GAs offers a pragmatic solution by navigating these intricate problem spaces effectively, optimizing performance without an exhaustive exploration of all possible configurations. In contrast, small-scale heat transfer systems, such as microfluidic devices or compact electronic components, requires precision and detail. Here, entering the field of fluid dynamics is imperative to exploit the system's full thermo-fluid-dynamic potential. This is where gradient-based techniques, particularly topology optimization, come to the forefront. Topology optimization enables intricate control over design parameters, allowing to optimize fluid pathways and heat transfer surfaces with precision. The approach ensures that every aspect of the system is fine-tuned to achieve maximum heat trans-fer efficiency.

One of the key advantages of gradient-based techniques, especially topology optimization, is the freedom they afford in design. Engineers can explore innovative configurations and geometric patterns, optimizing not only for energy efficiency but also for innovative form factors and structural considerations. This level of design flexibility is invaluable, particularly in small-scale systems where every element must be meticulously tuned for optimal performance. Ultimately, the selection of the most suitable optimization technique should be a well-considered decision that aligns with the specific goals and constraints of the heat transfer problem at hand. By carefully weighing the scale, complexity, and design requirements, engineers and researchers can leverage these powerful optimization tools to achieve superior heat transfer performance across a wide range of applications.

In this thesis will present a critical analysis of possible choices for heat transfer device optimization, offering a variety of examples, case studies, and numerical details that encompass systems of varying sizes and the intricate heat transfer mechanisms at play. By the conclusion of this thesis, readers will be enriched of a further point of view on diverse tools and techniques available to enhance the performance of heat transfer devices, adaptable to systems both small and large, and accommodating the shades of various heat transfer mechanisms.

Publications

The following publications – J states for journal papers, C states for conference papers and P for patents – are part of this thesis:

[J1] Bianco, N., Fragnito, A., Iasiello, M., & Mauro, G. M. (2021). A comprehensive approach for the multi-objective optimization of Heat Recovery Steam Generators to maximize cost-effectiveness and output power. Sustainable Energy Technologies and Assessments, 45, 101162.

[J2] Bianco, N., Fragnito, A., Iasiello, M., Mauro, G. M., & Mongibello, L. (2022). Multi-objective optimization of a phase change material-based shell-and-tube heat exchanger for cold thermal energy storage: Experiments and numerical modeling. Applied Thermal Engineering, 215, 119047.

[J3] Fragnito, A., Bianco, N., Iasiello, M., Mauro, G. M., & Mongibello, L. (2022). Experimental and numerical analysis of a phase change material-based shell-and-tube heat exchanger for cold thermal energy storage. Journal of Energy Storage, 56, 105975.

[J4] Bianco, N., Fragnito, A., Iasiello, M., Mauro, G. M., & Mongibello, L. (2023). Subcooling Effect on PCM Solidification: A Thermostat-like Approach to Thermal Energy Storage. Energies, 16(12), 4834.

[J5] Bianco, N., Fragnito, A., Iasiello, M., & Mauro, G. M. (2023). A CFD multi-objective optimization framework to design a wall-type heat recovery and ventilation unit with phase change material. Applied Energy, 121368.

[J6] Bianco, N., Cherella, N., Fragnito, A., Iasiello, M., & Mauro, G. M. (2023). Multi-material topology optimization of innovative microchannel heat sinks equipped with metal foams. Under Review on International Journal of Heat and Mass Transfer.

[J7] Fragnito, A., Bianco, N., Iasiello, M., Mauro, G. M., & Schousboe Andreasen, C. (2023). Exploring thermal insulation enhancement in rectangular differentially heated cavities through topology optimization. To be submitted to International Communication in Heat and Mass Transfer.

[C1] Bianco, N., Fragnito, A., Iasiello, M., & Mauro, G. M. (2023, May). Design of PCM-based heat sinks through topology optimization. In Journal of Physics: Conference Series (Vol. 2509, No. 1, p. 012001). IOP Publishing.

[C2] Bianco, N., Fragnito, A., Iasiello, M., & Mauro, G. M. (2023). Topology optimization of a pseudo 3D microchannel heat sink: influence of the initial guess. In Proceedings of the 40$^{\text{th}}$ International Heat Transfer Conference (UIT).

[C3] Fragnito, A., Iasiello, M., Mauro, G. M., Menna, C., & Schousboe Andreasen, C. (2023). Topology optimization to design innovative high thermal resistance 3D printed walls. In Proceedings of the 17$^{\text{th}}$ International Heat Transfer Conference (IHTC-17).

[C4] Abate, L., Bianco, N., Fragnito, A., Iasiello, M., & Mauro, G. M. (2023). Topology optimization for the CFD design of heat sinks coupled with phase change materials. In Proceedings of the 29$^{\text{th}}$ Therminic Workshop.

[C5] Fragnito, A., Iasiello, M., Mauro, G. M., & Menna, C. (2022). Simultaneous Heat and Moisture Transport in 3D Printed Walls. In Proceedings of 8th World Congress on Mechanical, Chemical, and Material Engineering (MCM 2022), ISSN 23698136, ISBN 978-199080010-8.

[P1] Bianco, N., Fragnito, A., Iasiello, M., Mauro, G. M., & Menna, C. (2022). IT. Patent No. 102021000028745, "Elemento autoportante per costruzione di strutture e metodo di realizzazione associato", accepted on 28/11/2023, classification: E04C, deposit date: 11/11/2021.

The following publications are not included in this thesis:

[J8] Bianco, N., Caliano, M., Fragnito, A., Iasiello, M., Mauro, G. M., & Mongibello, L. (2023). Thermal analysis of micro-encapsulated phase change material (MEPCM)-based units integrated into a commercial water tank for cold thermal energy storage. Energy, 266, 126479.

[C6] Bianco, N., Fragnito, A., Iasiello, M., & Mauro, G. M. (2023). CFD optimization of a fan radiator design: a novel hydronic terminal for space conditioning. In Proceedings of the 17$^{\text{th}}$ International Heat Transfer Conference (IHTC-17).

Contents

Part I: Generalities on Heat Transfer Problems

In the field of thermal engineering and science, understanding and investigating heat transfer problems is a fundamental pursuit, supporting the design and operation of countless systems in our modern world. As the complexities of these problems continue to grow, the need for numerical tools becomes increasingly apparent. Numerical methods empower us to dissect, analyse, and ultimately address the intricate challenges posed by heat transfer phenomena. However, these problems are far from uniform; they span a wide spectrum of scenarios, each governed by distinct heat transfer mechanisms.

This section embarks on a journey into the generalities of heat transfer problems, recognizing the indispensable role of numerical tools while also acknowledging the diversity inherent in these challenges. As we delve into this topic, we must appreciate that heat transfer is not a one-size-fits-all domain. The approach to analysing and solving these problems must be tailored to the specific heat transfer mechanism at play, whether it be conduction, convection, radiation, or a combination thereof. From the basic conduction of heat through solid materials to the convective streams that carry warmth through fluids and the recirculating motions that occur with phase change phenomena, each mechanism introduces its own set of equations, intricacies, and restraints. Consequently, the tools and techniques employed to tackle these heat transfer problems must be finely tuned and selected with utmost precision. As we journey through this section, we will explore the general principles that underlie heat transfer analysis, with a keen eye on the nuances introduced by different heat transfer mechanisms. This section is fundamental in laying the groundwork for a comprehensive understanding of the need for different optimization approaches. Whether one opts for gradient-based methods, which rely on mathematical derivatives, or non-gradient-based techniques like genetic algorithms, which simulate natural selection, the choice is inherently tied to the nuances introduced by different heat transfer mechanisms.

Preface

In the pursuit of understanding the complex interplay of heat transfer mechanisms, two fundamental pillars stand as driving lights: the numerical treatment of Partial Differential Equations (PDEs) and the concept of characteristics (dimensionless) numbers. These principles form the bedrock of our exploration in this thesis, offering insight into the intricate world of heat transfer in a manner both comprehensible and applicable. By discretizing the governing equations and employing computational techniques, we transform abstract mathematical models into actionable insights. In this thesis, we embark on a journey through various numerical methods, exploring finite difference, finite element, and finite volume methods, each with its unique strengths and suitability for specific heat transfer scenarios. Heat transfer is governed by a multitude of physical parameters such as temperature gradients, fluid velocities, and material properties. Understanding how these parameters interact and influence heat transfer processes is essential for designing efficient systems and predicting behaviour accurately. To this end, dimensionless numbers encapsulate the ratios of relevant physical quantities and enable us to categorize heat transfer regimes. Since this thesis deals extensively with natural convection, forced convection, and heat conduction, the introduction of dimensionless numbers becomes a pivotal means of capturing the true essence of the problems at hand.

Numerical resolutions of PDEs

The numerical treatment of Computational Fluid Dynamics (CFD) problems is a pivotal aspect of modern engineering and scientific simulations, offering a profound understanding of fluid behaviour within various physical systems. This multidisciplinary field employs a range of numerical methods to discretize and solve the governing partial differential equations (PDEs) that describe fluid flow phenomena. These methods, which include Finite Difference (FDM), Finite Volume (FVM), Finite Element (FEM) among others, are indispensable tools that enable researchers and engineers to tackle complex fluid dynamics problems across diverse applications [1].

Finite difference methods break down the spatial and temporal domains into discrete grids, approximating the derivatives in the governing equations at mesh *points*. These techniques are particularly valuable for problems involving simple geometries and uniform grid structures. Finite volume methods focus on conserving

mass, momentum, and energy within control volumes or *cells*. They excel at handling complex geometries and unstructured grids, making them suitable for a wide range of practical applications, from aerodynamics to combustion modeling. Finite element methods, on the other hand, excel in handling irregular geometries by dividing the domain into finite *elements* with polynomial approximations for the unknown variables. These numerical approaches, along with various hybrid and specialized methods, form the backbone of CFD simulations. This overview will provide a quick but targeted into each method, exploring their principles, advantages, and limitations, offering a comprehensive understanding of their role in the numerical treatment of CFD problems. This section, for instance, serves as a mandatory and propaedeutic step for introducing later phase change materials and topology optimization modeling.

The process of solving a CFD problem follows a structured workflow, described in the following and resumed in Fig. I.1 It begins with problem definition, where the specific physical problem to be simulated is clearly outlined, including details such as geometry, fluid properties, boundary conditions, and analysis objectives. Following problem definition, the next step is the creation of the computational domain's geometry.

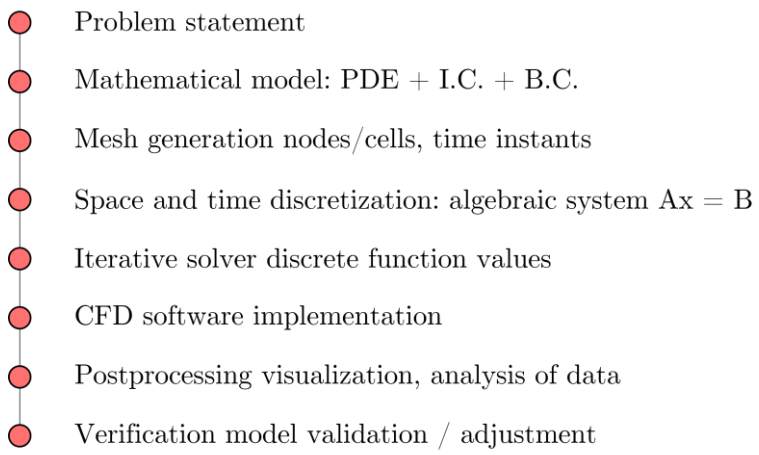

Fig. I. 1 CFD resolution workflow

This involves generating a 3D model representing the physical system under study. Subsequently, mesh generation is carried out, discretizing the geometry into

smaller elements or cells. It's important to ensure that the mesh is appropriately sized to capture significant flow features without introducing excessive computational overhead. The choice of numerical methods and solvers is crucial in the CFD process. These methods are selected to approximate the governing equations of fluid flow, such as the Navier-Stokes equations. Common approaches include the FVM or the FEM. Once the numerical method is chosen, the next phase is the discretization of the governing equations. This step involves breaking down the equations into discrete forms and applying numerical schemes to approximate derivatives. Boundary conditions are then applied to define the behaviour of the fluid at the domain's boundaries. These conditions specify parameters such as inlet velocities, pressure outlets, wall conditions (no-slip, slip), and temperature or heat flux conditions. Initialization is critical, as it involves setting initial values for flow variables (velocity, pressure, temperature) within the domain. These initial conditions are necessary to initiate the numerical simulation. For problems with time-dependent phenomena, time stepping is performed. This entails iterating over time intervals using schemes like implicit or explicit methods to update flow variables at each time step. The numerical solution phase follows, where the discretized equations are solved iteratively using suitable solvers. This may encompass iterative linear equation solvers for pressure-velocity coupling and non-linear solvers for turbulence models. Post-processing involves analysing the simulation results. This includes tasks such as visualizing flow patterns, calculating performance metrics (e.g., lift, drag, heat transfer), and extracting data such as velocity profiles, pressure distributions, and temperature contours. Validation and verification are integral steps in assessing the accuracy of the simulation. Comparison with experimental data or analytical solutions, when available, helps ensure the reliability of the results. Sensitivity analysis may be performed to understand the impact of parameter variations on the simulation outcomes. This aids in identifying influential factors in the analysis. Optimization techniques can be applied if the objective is to enhance designs or operating conditions, especially for performance improvement.

As aforementioned, when approaching to a CFD problem, the resolution methods to solve partial differential equations that govern fluid flow and heat transfer are the following: FDM, FVM and FEM. Each method (see Fig. I.2) has its own approach and characteristics, and here's an introduction to the key differences between them:

FDM

- FDM discretizes the domain using a regular grid, such as a Cartesian grid.
- It approximates derivatives in the governing equations using finite difference approximations.
- FDM is relatively simple to implement and is often used for educational purposes and for problems with simple geometries and boundary conditions. It may not be as accurate as FEM or FVM for complex problems, it can still provide reasonable results for certain applications [2].
- It can suffer from stability issues when applied to certain types of problems, and special care must be taken to ensure stability, especially for time-dependent problems [2].

FVM

- FVM discretizes the domain into a grid of control volumes or cells, typically using structured grids (Cartesian or curvilinear) or unstructured grids (triangular, quadrilateral, or polyhedral).
- It is particularly well-suited for problems involving conservation laws (e.g., mass, momentum, and energy conservation), making it a popular choice for CFD simulations of fluid flow.
- FVM focuses on the conservation of quantities within control volumes, which leads to a natural formulation for the discretization of the governing equations (integral form, see Fig. 1.2)
- It requires the calculation of fluxes at the faces of control volumes, which can be computed using various numerical schemes, such as upwind, central, or hybrid schemes.

FEM

- FEM is a numerical method that discretizes the domain into finite elements, which are typically triangles or quadrilaterals in 2D and tetrahedra or hexahedra in 3D.
- It is widely used for problems involving complex geometries or irregular domains because it allows for flexible meshing.
- FEM can handle both structured and unstructured meshes.

- FEM approximates the solution within each element using piecewise functions (usually polynomials), and the solution is then interpolated across the entire domain.
- It requires solving a system of algebraic equations, often resulting in sparse matrices, which can be computationally demanding for large-scale problems.

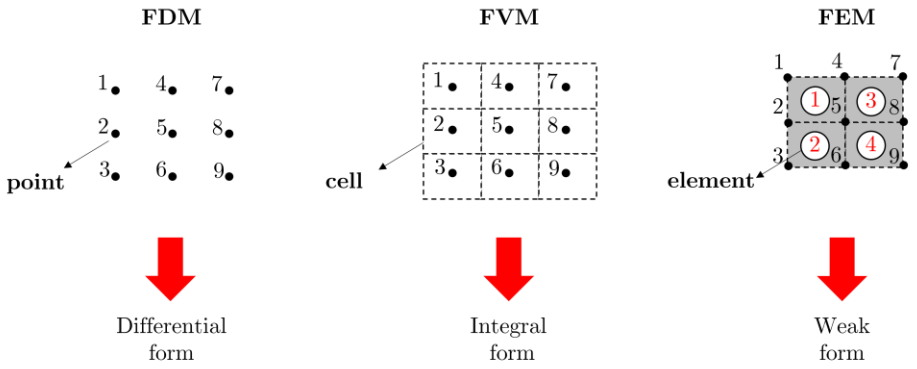

Fig. I. 2. Finite difference (FDM), finite volume (FBM) and finite element (FEM) methods

In this thesis, directly or not, problems formulation and resolutions are computed through a FEM approach. Therefore, the attention is placed only on this approach. Moreover, this thesis primarily focuses on the field of heat transfer, and while FEM plays a significant role in the analysis, a comprehensive exposition of FEM theory is not provided here, as the primary emphasis is on heat transfer phenomena rather than computer science aspects. However, a brief explanation of how to pass from differential equation to weak form is provided in the following [3].

Under the hypothesis of steady-state approach, two-dimensional isotropic medium, the Poisson's equation to solve the temperature field (T) inside a generic domain Ω, with an internal heat generation per unit area Q(x, y), can be written as follows:

$$-\frac{\partial}{\partial x}\left(k\frac{\partial T}{\partial x}\right)-\frac{\partial}{\partial y}\left(k\frac{\partial T}{\partial y}\right)=Q \tag{I.1}$$

In order to solve this equation, we must define specific boundary conditions. In this frame, a first type, *i.e.,* Dirichlet, and a third type, *i.e.,* Robin, boundary condition types are here applied:

$$T = T\ s \quad on\ \Gamma_T \tag{I.2}$$

$$q_n = \left(k_{xx}\frac{\partial T}{\partial x}n_x + k_{yy}\frac{\partial T}{\partial y}n_y\right) + h_c(s,T)(T - T_c) = f\ s \quad on\ \ \Gamma_q \tag{I.3}$$

where q_c is the convective heat flux, h_c is the convective heat transfer coefficient, and (n_x, n_y) is the direction of the unit normal vector on boundary Γ.

The primary characteristic of the finite element method involves the creation of approximation functions necessary for solving differential equations through a variational or weighted-integral approach. In the finite element method, this is achieved by dividing the given domain into a collection of subdomains known as finite elements. The term "finite element" often encompasses both the geometric attributes of the element and the level or order of approximation utilized for the dependent variable within the element. A fundamental feature of this methodology is that the element (Ω_e) may take the form of a triangle or quadrilateral, and the level of interpolation applied to it can vary, such as linear, quadratic, and others. The aggregation of all non-overlapping elements employed to represent the actual domain is referred to as Ω.

By doing this we can reformulate the unknown T(x,y) as the sum of the values of the function T^e(x,y) at the element nodes multiplied by approximation functions ($\psi^e{}_j$) associated with the element itself:

$$T\ x,y\ \approx T^e\ x,y\ \approx \sum\nolimits_{j=1}^{n} T_j^e \psi_j^e\ x,y \tag{I.4}$$

In the majority of cases, approximation functions are represented as polynomials. This choice is influenced by two main factors: firstly, polynomials can be easily derived using interpolation theory, and secondly, numerical integration methods allow for precise evaluation of integral expressions involving polynomials. The utilization of function values as unknown parameters primarily aims to enforce the continuity of the dependent variable across element boundaries.

To find the values T_j^e, we need to ensure that the approximate solution T^e(x, y) meets the requirements of the governing equation and the specified boundary

conditions for the problem. Similar to the approach used in variational and weighted-residual methods, our goal is to precisely satisfy the boundary conditions by selecting appropriate approximation functions. Then, we determine the unknowns of the approximation by satisfying the governing differential equation in a weighted-integral manner.

Because we are dealing with a typical element, we achieve satisfaction of the differential equation by employing a weighted-integral approach over the element Ω_e. This procedure results in a system of n algebraic equations involving the nodal values (T^e_1, T^e_2, ..., T^e_n). This collection of algebraic equations is referred to as a *finite element model* of the original differential equation over the element.

Is it now possible to write the weighted-residual statement, *i.e.,* multiplied to the weight function w, and integrated over the elements:

$$0 = \int_{\Omega_e} \left[-\frac{\partial}{\partial x}\left(k\frac{\partial T^e}{\partial x}\right) - \frac{\partial}{\partial y}\left(k\frac{\partial T^e}{\partial y}\right) - Q\ x, y \right] dxdy \tag{I.5}$$

When selecting any weight function w(x, y), it results in an algebraic equation derived from Eq. (X) involving the nodal values T^e_j. To n different choices of weight functions corresponds a collection of n algebraic equations that are linearly independent. This collection is referred to as a finite element model using the weighted-residual approach.

A second-order differential equation requires that the approximation functions ψ^e_j, have second derivatives on both x and y. As a result, ψ^e_j must be at least a quadratic or higher-order polynomial concerning the x and y coordinates. In the context of the weak form this continuity requirement is relaxed by redistributing on the weight function w the differentiation of T^e. This means that w needs to be differentiable only once. Resorting to integration by parts, we obtain:

$$\begin{aligned} 0 = \int_{\Omega_e} & \left(k_{xx}\frac{\partial w}{\partial x}\frac{\partial T^e}{\partial x} + k_{yy}\frac{\partial w}{\partial y}\frac{\partial T^e}{\partial y} - wQ \right) dxdy \\ & - \oint_{\Gamma_e} w\left(k_{xx}\frac{\partial T^e}{\partial x}\ n_x + k_{yy}\frac{\partial T^e}{\partial y}n_y \right) ds \end{aligned} \tag{I.6}$$

Finally, extending the formulation to a case for which the secondary variable includes both conductive and convective terms, *i.e.,* heat flux to the boundary, we obtain:

$$0 = \int_{\Omega_e} \left(k_{xx} \frac{\partial w}{\partial x} \frac{\partial T^e}{\partial x} + k_{yy} \frac{\partial w}{\partial y} \frac{\partial T^e}{\partial y} - wQ \right) dxdy - \oint_{\Gamma_e} w \left[k_{xx} \frac{\partial T^e}{\partial x} \, n_x + k_{yy} \frac{\partial T^e}{\partial y} n_y - h_c \, T - T_c \, \right] ds \tag{I.7}$$

Dimensionless groups

Before delving into the analysis of different heat transfer mechanism it is useful to present some – those of interest in this thesis – dimensionless group that depending on the problem nature are crucial to capture physical insights of various terms in the system of governing equations. Moreover, by comparing the relative magnitudes of these dimensionless numbers, we can predict how heat is transferred within different fluids, geometries, and environments, guiding us in designing efficient heat exchangers, optimizing cooling systems, and understanding natural convection processes.

They are expressed as function of these thermophysical parameters and variables: α = thermal diffusivity, D = diameter, h = convective heat transfer coefficient, g = gravitational constant, k_f = fluid thermal conductivity, k_s = solid thermal conductivity, L_c = characteristic length, ν = dynamic viscosity, ϱ = density, t = time, T_∞ = bulk temperature, T_s = surface temperature, u = fluid velocity.

Table I. 1. Main dimensionless group for heat transfer

Name	Formulation	Physical meaning
Biot, *Bi*	$Bi = \frac{hL_c}{k}$	Internal thermal resistance/surface resistance.
Fourier, *Fo*	$Fo = \frac{t}{\alpha L_c^2}$	Thermal conduction/thermal inertia. Describe the propagation of heat in solids
Grashof, *Gr*	$Gr = \frac{\rho g \, T_s - T_\infty \, L_c^3}{\nu^2}$	Buoyancy to viscous forces acting on a fluid.
Nusselt, *Nu*	$Nu = \frac{hL_c}{k}$	Convective/conductive heat transfer
Peclet, *Pe*	$Pe = \frac{\rho c_p u L_c}{k}$	Advective/diffusive transfer rate

Prandtl, Pr	$Pr = \frac{c_p \mu}{k}$	Momentum/thermal diffusivity
Rayleigh, Ra	$Ra = \frac{\rho g \beta \ T_s - T_\infty \ L_c^3}{\nu \alpha}$	Buoyancy/thermal diffusivity
Reynolds, Re	$Re = \frac{\rho u L_c}{\mu}$	Inertial/viscous forces

1. Introduction

In the field of heat transfer analysis, it's crucial to employ different optimization approaches based on the scale of the problem being analysed. Heat transfer problems can vary greatly in size and complexity, ranging from microscale phenomena in electronics to macroscale heat exchangers in industrial processes.

Before applying an optimization framework, the problem physical statement is mandatory. Depending on this, a variety of numerical methods can be selected to solve the problem. Therefore, together with the presentation of the different heat transfer mechanism at different scales, this chapter has the objective of introducing the suitable (or suggested) methodology.

1.1. Conduction-based problems

Heat conduction is often considered the simplest and most straightforward heat transfer mechanism, especially in solid materials. It occurs through direct contact between particles within a material or between adjacent materials. In heat conduction, energy is transferred as heat from regions of higher temperature to regions of lower temperature through the vibration and collision of atoms and molecules.

Compared to other heat transfer mechanisms like convection and radiation, heat conduction is relatively easier to understand and analyse mathematically, particularly in simple geometries and materials with uniform properties. It follows Fourier's law, which describes how the heat flux (the rate of heat transfer per unit area) is proportional to the temperature gradient (the rate of change of temperature with distance) and the material's thermal conductivity.

However, the ease of modeling of heat conduction as a heat transfer mechanism depends on the specific context and materials involved. Generally, in most of cases, convection (heat transfer through the movement of fluids) or radiation (heat transfer via electromagnetic waves) might be more relevant or dominant. So, while heat conduction is conceptually straightforward, the choice of the most appropriate heat transfer model can vary depending on the circumstances.

Nevertheless, in this thesis the attention is posed on heat conduction on macroscopic scale (bulk conduction), as we can differentiate with microscale heat conduction (lattice vibrations). At the microscopic scale, heat conduction is explained by the movement of atoms or molecules within a material. In solids, atoms or

molecules vibrate around their equilibrium positions. When one part of the material is heated, these vibrations increase in amplitude, and this energy is transferred to neighbouring particles [4]. This process continues, and heat is conducted through the lattice structure. The rate of heat conduction at the microscopic scale is influenced by factors like the mass of the particles and the strength of their interactions.

1.1.1. Thermal conductivity

Thermal conductivity can vary from the macroscale to the microscale due to changes in the material's structure, composition, and size. Here's how thermal conductivity may vary with scale. At the macroscale, thermal conductivity is often measured and characterized for bulk materials. It is typically a well-defined property for homogeneous materials like metals, ceramics, and most solids. Bulk thermal conductivity values are commonly available in material property databases. As you move to the microscale, especially in materials with complex microstructures or nanostructures, thermal conductivity can vary significantly. Several factors contribute to this variation, *e.g.,* size effects, defects and dislocations, nanostructures, anisotropy, porosity etc. At the microscale, size effects become significant. When the dimensions of a material approach or fall below the mean free path of phonons (the average distance they travel before scattering), thermal conductivity can decrease. This phenomenon is more pronounced in nanomaterials. Crystal defects, dislocations, and imperfections within the material's lattice can scatter phonons (quantized lattice vibrations) responsible for heat conduction. This scattering reduces the material's thermal conductivity. In nanomaterials, the size and arrangement of nanoparticles or nanotubes can significantly affect thermal conductivity. For example, carbon nanotubes can exhibit extraordinarily high thermal conductivity due to their unique structure, whereas some nanocomposite materials may have altered thermal properties. In some materials, especially crystalline ones, thermal conductivity may be anisotropic, meaning it varies with direction. This anisotropy can become more pronounced at the microscale due to the crystal lattice's orientation and symmetry [4].

In pure heat conduction heat transfer the evaluation of thermal conductivity is essential for a good prediction of temperature fields/evolution in time. This thesis, as shown in the following chapters, faces – among the others – problems related to 3D printed structures for building applications, made by innovative materials, cementitious mortar, which is a composite material ready-to-use, developed to meet the needs of the user who tends to realize manufactured goods using 3D extrusion technologies. This material is a premixed product with selected sands and specific

components which guarantee the mortar to be self-sustaining during printing, maintaining the shape required by the starting 3D model, and at the same time ensure excellent workability and a progressive development of mechanical resistances. To run CFD simulation, a list of the main parameters for this material is presented in Tab. I.1.

Table 1. 1. Cementitious mortar main features

Parameters	Values		
Fresh mortar density	2150 kg/m^3		
Hardened mortar density	2000 kg/m^3		
Drying time (UNI EN 1963:2017)	Starting: $\leq$ 150 min Final: $\leq$ 200 min		
Compressive strength (UNI EN 196-1:2016)	1 day $\geq$ 15 MPa	7 day $\geq$ 40 MPa	28 days $\geq$ 60 MPa
Flexural strength (UNI EN 196-1:2016)	$\geq$ 3 MPa	$\geq$ 8 MPa	$\geq$ 9 MPa

Its application fields are for the production of both straights and curvilinear models. Obviously, this kind of material is affected by stringent structural constraints in terms of geometrical design. In fact, as a rule, the angular deviation from the vertical direction should not exceed 15 degrees to avoid – at the printing stage – the material collapse. For the purpose of conducting CFD simulations, the final parameter to be ascertained, and arguably the most influential in assessing the thermal performance of the model, is thermal conductivity. A way to find this value is to perform absolute thermal conductivity measurements.

These tests are carried out at the Insulating Material Thermal Analysis Laboratory (IMATlab) at the University of Naples Federico II, utilizing the NETZSCH Guarded Hot Plate (GHP) 456 Titan® system for conducting absolute thermal conductivity measurements. Employing a well-established and standardized guarded hot plate technique such as ISO 8302, ASTM C177, or DIN EN 12667, this system utilizes an absolute measurement method, eliminating the need for calibration standards. Additionally, it allows for higher operating temperatures ranging from -160°C to 600°C without the risk of thermally induced deformation.

The tests are performed on samples of cementitious mortar, as depicted in Fig. 1.2, which were geometrically defined with a square cross-section measuring 30 cm on each side. The thickness (s) of these samples is 5 cm – determined using a calibre – ensuring precise knowledge of the geometry.

Fig. 1. 1. Samples appearance

As depicted in Fig. 1.3., to ensure the achievement and the control of the right temperature depends on the coupling with an auxiliary nitrogen (N_2) tank, that provides the cold temperature level.

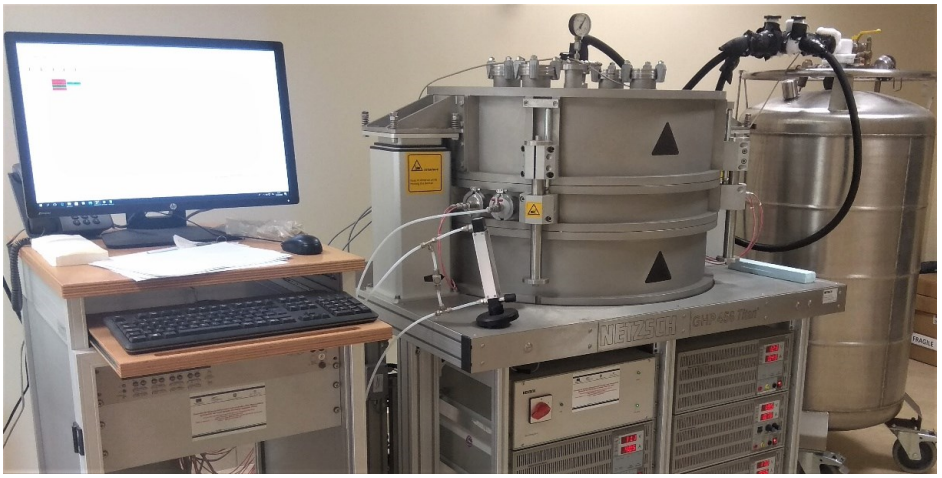

Fig. 1. 2. Configuration of the NETZSCH GHP 456 Titan® system

On the backside and thus not visible are further feedthroughs for temperature sensors, for heaters and for cooling lines for the cold plates as well as a flange for evacuating the instrument. The work principle is illustrated in Fig. 1.4.: the hot plate and the guard ring are sandwiched between two samples of the same material and approximately the same thickness, *s*. Cold plates are placed above and below the samples, kept at temperature by nitrogen. All plate temperatures are controlled such that a well-defined, user-selectable temperature difference, ΔT, is established between the hot and the cold plates – and thus across the sample thickness. The guard ring is maintained exactly at hot plate temperature in order to minimize

lateral heat losses. The great advantage of the GHP method is that it is an absolute method, *i.e.,* no calibration or correction is required at all.

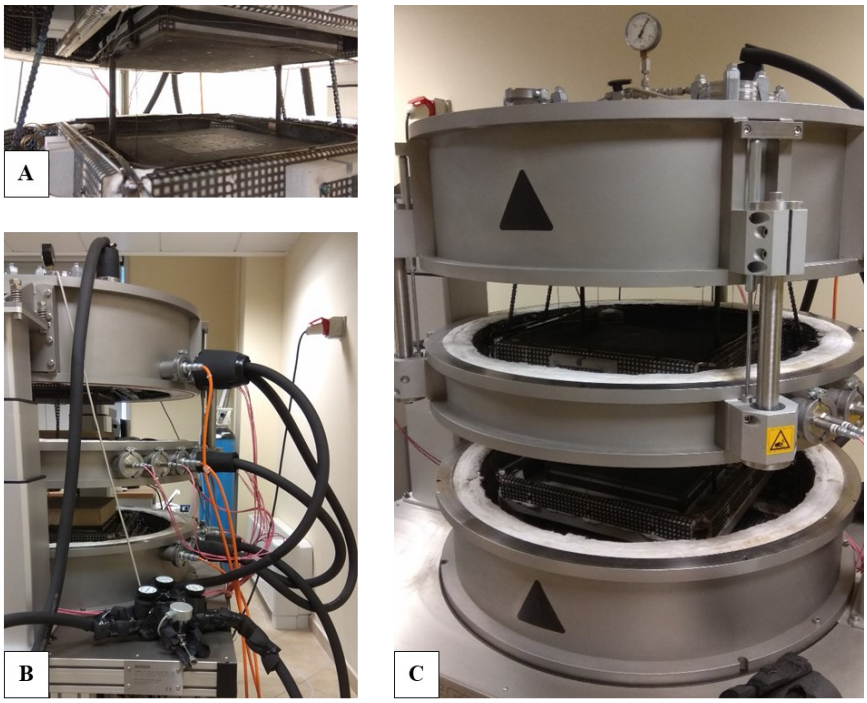

Fig. 1. 3. GHP 456 Titan A) focus on hot plate and guard ring (below), cold plate (above); B) thermocouples and insulated pipes for N2; C) open-system configuration

The thermal conductivity values result in the stationary state simply from the:

- exactly measurement of the total power input into the hot plate, Q which is generated electrically (P = VI);
- average sample thickness, s;
- measurement of the area, A, generally standardized to 0.09 m^2. The factor 2 results for two samples;
- mean temperature difference, ΔT, along the sample or the two samples;

According to the Fourier's law the conductivity is established as follows:

$$k = \frac{Q\ s}{\Delta T\ 2A} \tag{1.1}$$

The experimental analysis – for a set point temperature of 10 °C – returns a conductivity value (k) equal to 1.05 W/(mK).

1.2. Convection-based problems

In this section the focus is mainly on natural convection, which is the predominant heat transfer and fluid flow mechanism in the analysed devices/case studies. Therefore, a brief introduction of this phenomenon is firstly provided. Then, the attention is shifted on phase change problems (solid to liquid and vice-versa), for which natural convection plays a fundamental role.

1.2.1. Natural convection

The aim of this section is to introduce and discuss the role of natural convection and how it can be numerically solved. Natural convection is a fundamental process in fluid dynamics and heat transfer that occurs when a fluid, such as a gas or a liquid, spontaneously moves due to density differences caused by temperature variations. Unlike forced convection, which involves external forces like fans or pumps to induce fluid motion, natural convection relies solely on buoyancy forces generated by the density gradients within the fluid. This phenomenon plays a crucial role in various natural and industrial processes, shaping our everyday lives and influencing the design of numerous systems. In the following, some practical examples of how natural convection is part of our daily lives:

- *Heating a Room:* one of the most common examples of natural convection is the warming of a room through a radiator or a space heater. As the heater warms the air close to it, this air becomes less dense and rises. Meanwhile, cooler air in the room displaces the warm air, creating a continuous cycle of rising warm air and descending cool air, which helps distribute heat throughout the space.

- *Cooking:* when you boil water in a pot or simmer a soup on a stove, natural convection is at play. As the liquid near the bottom of the pot is heated, it becomes less dense and rises, while cooler liquid descends. This circulation helps distribute heat evenly and cook food.
- *Solar Heating Systems:* solar water heaters and passive solar building designs also rely on natural convection. Solar collectors heat a fluid (usually water or a heat-transfer fluid), causing it to rise through pipes or channels. As it cools, it flows back down, creating a natural circulation that transfers heat to a storage tank or the interior of a building.
- *Cooling of Electronics:* in electronic devices such as laptops and desktop computers, natural convection helps dissipate heat generated by components like CPUs and GPUs. As these components heat up, the surrounding air becomes less dense and rises, carrying away heat. Many devices are designed with heat sinks and vents to enhance this cooling process.
- *Geological Phenomena:* natural convection occurs in the Earth's mantle and is responsible for plate tectonics and the movement of continents. Hot molten rock rises at mid-ocean ridges, cools as it approaches the surface, and then sinks back into the mantle, driving the movement of tectonic plates.

In summary, natural convection is a global and essential phenomenon in the natural world and numerous human-made systems. Understanding and harnessing it is crucial for efficient heat transfer, energy conservation, and the functioning of various processes in our daily lives. While in most forced convection scenarios, the flow field is typically well-established or can be addressed independently of the temperature distribution, natural convection arises from the interplay between density variations and gravitational (or another external) force, inevitably intertwining the flow and temperature patterns. In the context of natural convection, it's impossible to separate the solutions for flow and temperature. When natural convection takes place across a vertical plate, the heat transfer characteristics can vary depending on the Prandtl number (Pr) of the fluid involved. Now, let's describe natural convection across a vertical plate for two scenarios: $Pr > 1$ and $Pr < 1$.

Viscous-Dominant Fluids ($Pr > 1$)

When the Prandtl number is greater than 1 ($Pr > 1$), it indicates that momentum diffuses more slowly than heat. This situation is typical for viscous-dominant fluids, like oils and molten metals. When involving natural convection, $Pr > 1$

means that when the plate is heated, the fluid in contact with the hot surface becomes less dense and rises. As it rises, cooler fluid replaces it, setting up a circulation pattern. The temperature boundary layer adjacent to the plate is thinner compared to the velocity boundary layer, reflecting the dominance of heat transfer. This means that the temperature difference across the boundary layer is substantial, leading to efficient heat transfer.

Thermal-Dominant Fluids ($Pr < 1$)

When the Prandtl number is less than 1 ($Pr < 1$), it implies that momentum diffuses more rapidly than heat. This is common for thermal-dominant fluids, such as air and most gases. In natural convection for $Pr < 1$, as the plate is heated, the lighter, warmer fluid rises, and denser, cooler fluid descends to replace it. This circulation is similar to $Pr > 1$ cases but with a different emphasis on the momentum and temperature gradients. The temperature boundary layer adjacent to the plate is thicker compared to the velocity boundary layer, indicating that the temperature difference across the boundary layer is less pronounced than the velocity difference.

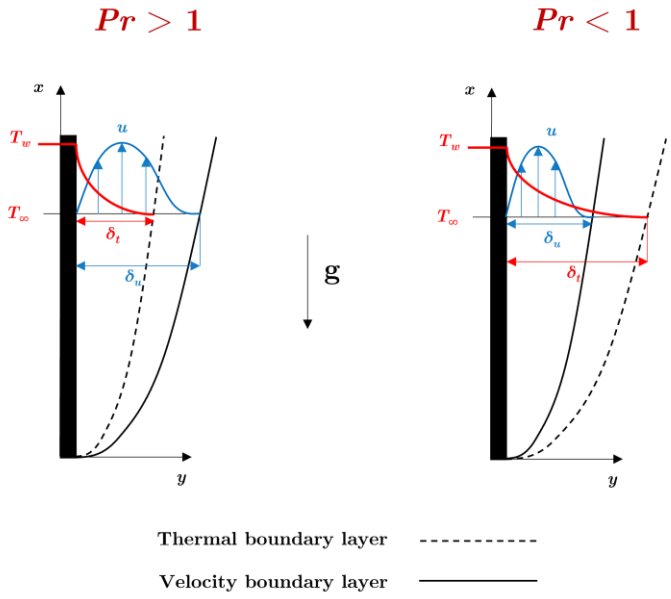

Fig. 1. 4. Difference between thermal and velocity boundary layer thickness depending on the Prandtl number value

In summary, the key distinction in natural convection across a vertical plate between $Pr > 1$ and $Pr < 1$ lies in the dominance of either momentum or thermal diffusion. For $Pr > 1$, the heat transfer is efficient, with a thinner temperature boundary layer. In contrast, for $Pr < 1$, heat transfer is less efficient, with a thicker temperature boundary layer, as the fluid is more effective at conducting heat than transporting momentum.

This thesis is particularly concerned with the case of natural convection within cavity. This phenomenon occurs without the need for any mechanical aids such as fans or pumps, relying solely on the buoyancy-driven flow of the fluid. It is a fundamental mechanism in heat transfer and fluid dynamics and is commonly observed in various everyday situations, including heating a room, enhancing the wall insulating performance or cooling electronic components.

The physical problem consists of the steady incompressible flow of a Newtonian fluid inside a solid structure (cavity). The only driving force for the fluid motion is the buoyancy, due to temperature difference across the enclosure. In the limit of long times, for flows in which neither instabilities nor turbulence appear, we consider the problem to be in steady state conditions.

Fluid flows and heat transfer is described through a steady-state 2D formulation based on Navier-Stokes equation, with the assumption of neglection of density changes of the fluid except for gravitational term, *i.e.,* Boussinesq hypothesis. Under the assumption of constant thermophysical properties and introducing a material distribution γ to indicate the presence of solid, *i.e.,* $\gamma = 0$, or fluid, *i.e.,* $\gamma = 1$ in each point of the domain, governing equations can be written in the following dimensionless form:

$$\nabla \cdot u = 0 \tag{1.2}$$

$$u \cdot \nabla\ u = -\nabla p + \frac{Pr}{\sqrt{Ra}} \nabla^2 u + Pr\, e_i^g \vartheta \tag{1.3}$$

$$\nabla \cdot u\vartheta\ = \nabla \cdot \left(\frac{1}{\sqrt{Ra}} k\ \gamma\ \nabla \vartheta \right) \tag{1.4}$$

This set of equations is defined based on an appropriate scaling for the problem here treated [5], represented by the following reference values: the height of the cavity H is the characteristic length and the temperature difference between the hot and cold wall is the characteristic temperature, $\Delta T = T_H - T_C$. The reference velocity is set to $a/H\, Ra^{0.5}$. Based on these characteristics the dimensionless spatial

coordinates x, y, the velocity field u, v, temperature field ϑ and pressure field p are defined as follows:

$$x = \frac{x^*}{H}; \quad yx = \frac{y^*}{H}; \quad \vartheta = \frac{T - T_C}{\Delta T}; \quad u = \frac{u^*}{u_{ref}} = \frac{u^*}{\frac{\alpha}{H}\sqrt{Ra}};$$
$$p = \frac{p^*}{p\ u_{ref}^2}; \quad s = \frac{Hs^*}{\rho\ u_{ref}^2} \tag{1.5}$$

where the dimensional variables are identified by a star. Thus, the analysis is performed on the rectangular cavity, with aspect ratio A_r = L/H = 0.5. The left wall (at position $x = 0$) is warm and set to a hot temperature, $\vartheta_H = 1$, whereas the right one (at position $x = 1$) is cold and set to a temperature $\vartheta_C = 0$. To express the enclosure attitude to dissipate heat, the Nusselt number, (Nu) is expressed as the relative augmentation effect – with respect to the conductive contribution – of heat transfer due to natural convection.

The model here used – about the natural convection with a dimensionless approach – is tested with reference [6] to the benchmark case of the differentially heated square cavity. The aim is to evaluate the model reliability. Therefore, a comparison in terms of image visualization is firstly proposed in Fig. 1.6.

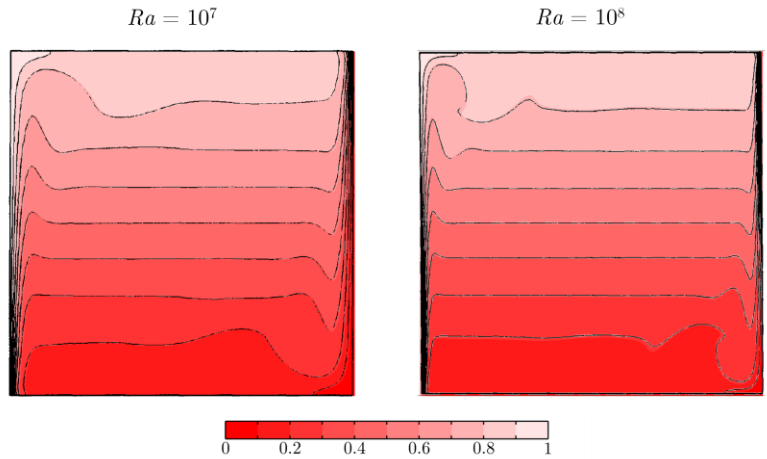

Fig. 1. 6. Verification of temperature filed iso-values, i.e., (0-0.1.1), for Ra = 107 and Ra = 108: black line (reference [6]) and filled contours (present work)

Based on temperature filed iso-values – ranging from 0 to 1 with a step of 0.1 – and for a $Ra = 10^8$, one can see an accurate overlapping between contour levels. Thus, in an eyeball norm the models compare well. On the other hand, referring to the differentially heated rectangular cavity, with an aspect ratio $Ar = 2$, the model is validated with the following correlation [7]:

$$Nu_L = 0.18 \left(\frac{Pr}{0.2 + Pr} Ra_L \right)^{0.29} \tag{1.6}$$

Whose validity is in the following ranges: $1 \leq H/L \leq 2$, $10^{-3} \leq Pr \leq 10^5$, and $10^3 \leq Ra_L Pr/(0.2+Pr)$. Results are presented in Fig. 4, where present work data (dotted) are compared with outcomes from Eq. (1.6).

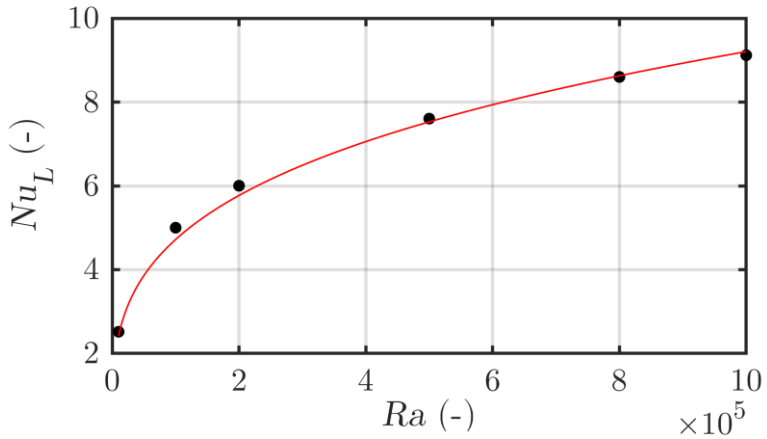

Fig. 1.7. Nusselt number vs Rayleigh number: present work (dotted) – Eq. (1.6) (line)

The Nu value changes by varying the Ra as a consequence of the enhanced convective heat transfer coefficient. Increasing the Rayleigh number leads to enhanced heat transfer rates within the enclosure: convective streams promote better mixing of the fluid, reducing the thermal boundary layer. The more vigorous fluid motion and more complex flow patterns within the enclosure is supported by the rising of convection cells, *e.g.,* plumes, which develop as the fluid experiences thermal gradients. These flow patterns enhance heat mixing and distribution, aiding in the overall heat transfer process (see Fig. 1.8).

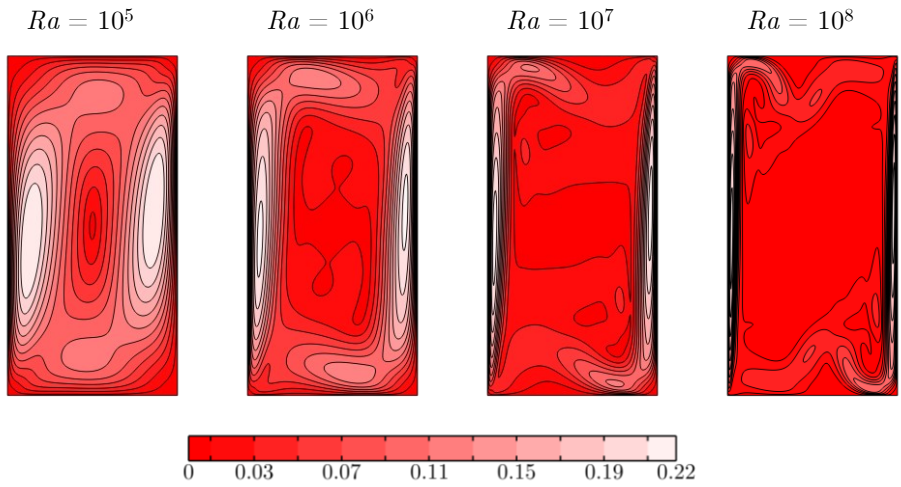

Fig. 1.8. Velocity magnitude field for different Rayleigh numbers, i.e., Ra =10^5, 10^6, 10^7, 10^8

Fig. 1.8 shows how the iso-velocity magnitude contours change for different Rayleigh numbers, *i.e.,* $Ra = 10^5, 10^6, 10^7, 10^8$, to better catch the difference in the fluid flow. If the flow becomes highly supercritical these waves break, resulting in an unsteady disordered interface downstream.

1.3. Phase-change problems

The aim of this section is to introduce the problem of phase transition, with the focus on solid-liquid one. Phase Change Materials (PCMs) represent a remarkable class of materials that play a pivotal role in various scientific, engineering, and industrial applications. These materials possess the ability to store and release thermal energy during phase transitions, making them indispensable in the quest for more efficient and sustainable energy solutions. As the global demand for energy continues to rise, the importance of PCMs in managing and conserving energy resources becomes increasingly evident.

The essence of PCMs lies in their ability to undergo reversible phase transitions, typically between solid and liquid states, while maintaining a nearly constant temperature. This phase change is accompanied by a substantial release or absorption of energy, *i.e.,* latent heat, providing a means to store heat when in the liquid phase and release it when reverting to the solid phase. This inherent property has

broadened the applications of PCMs, ranging from passive temperature regulation in buildings to advanced cooling systems in electronics, and even in sustainable energy storage solutions such as solar thermal systems.

To harness the full potential of PCMs in these diverse applications, the development of numerical models has become an essential tool. These models serve as tools to understand the complex behaviour of PCMs under various conditions and to optimize their integration into systems. Numerical modeling provides insights into the thermal performance, efficiency, and eventually long-term stability of PCM-based systems, which are vital for their successful implementation in real-world scenarios.This thesis explores the critical role of PCMs in modern energy management and conservation, emphasizing the need for numerical models to understand and enhance their performance. In detail, we will focus on application related to energy storage, whose role is crucial for integration of renewable energy systems and energy efficiency enhancement. Therefore, this section introduces a comprehensive overview on numerical modeling, with particular attention on CFD-based approaches. The aim is to present most used and reliable method, emphasizing drawbacks and advantages in applying one or the other. The main difference between solving for analytical and numerical solutions – beyond the resolution method – is the possibility to adapt the problem formulation to complex geometries and applications. On the other hand, using numerical solutions open the doors to front-tracking method [8], or fixed grid methods [9]. The former allows to obtain more accurate results in the solid-liquid interface, as is to solve the governing equations at each time step by first evaluating the position of the moving interface; however, when interfaces are subjected to large deformations, *e.g.,* for 3D cases with large domains, it becomes unsuitable. The second class of methods, *i.e.,* fixed gird ones, while being easier in the implementation, they do not explicitly track the melting front. To this end, a single energy equation is solved for both phases, so that the melting front evolution in time is pursued implicitly. In the following, an overview of the aforementioned methods is proposed.

1.3.1. Material properties

Numerical modelling of these materials is well-established, and various experimental analyses on their usage for thermal management or latent heat storage have been carried out [10]. Most of these approaches are based on 1D or 2D modelling [11], [12], and little effort has already been made for 3D models due to their high non linearities and computational times [13]. As regards 1D and 2D models, the

most used ways to describe the phase transition are i) enthalpy-porosity method; ii) apparent heat capacity method; iii) source-based [14]. These approaches can reveal significant discrepancies from the experimental evidence, and the main reasons can be the temperature dependence of thermophysical properties, or the ideal shape of the step function used to model the phase transition; above all, the neglection of phenomena as subcooling and thermal hysteresis might affect modeling quality too. When using these approaches, rarely subcooling and hysteresis are considered [15] because of the model complexity. To this end, a fundamental point is the distinction between the definitions of subcooling and hysteresis. According to the subcooling, PCM requires cooling to a temperature below the theoretical solidification point before it starts to crystallize; this has an impact on how latent heat is released and used [16]. This translates in PCM not crystallizing at the theoretical solidification point. Therefore, the subcooling degree is the term used to describe the discrepancy between actual and theoretical solidification temperatures. On the other hand, thermal hysteresis causes the phase change material solidification temperature to deviate from its melting temperature [17]. Thus, PCMs have distinct enthalpy values in the same condition and melt and solidify at different temperatures [18]. Whenever a comparison was made between models with and without hysteresis, it was found that the poor accuracy of the non-hysteresis model in representing the melting and solidification processes of the PCM storage represents an important limitation [19], [20]. Thus, it further emphasizes the importance of considering hysteresis effects in simulations involving PCM materials. Since heating and cooling can show different thermal behaviours because of their nucleation mechanisms, we generally refer to distinction as hysteresis. A graphical comparison of the differences between subcooling and hysteresis is provided in Fig. 1.9, showing which temperature ranges are labelled as subcooling or hysteresis.

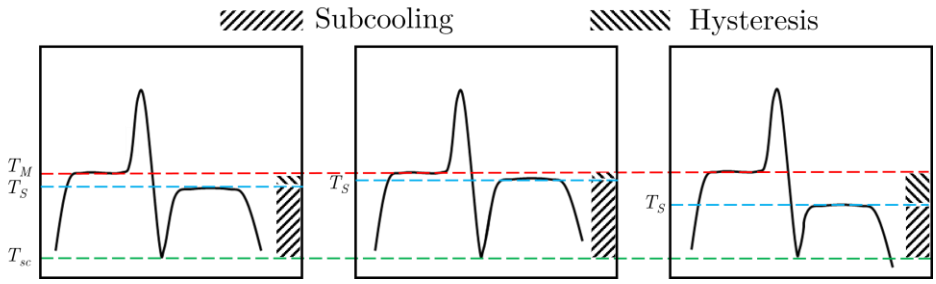

Fig. 1. 9. Variations of subcooling and hysteresis as the solidification temperature (T_S) varies, fixing melting (T_M) and subcooling (T_{SC}) temperatures: a higher T_S implies higher subcooling and lower hysteresis.

The nucleation rate of PCM is proportional to two main factors: the nucleation rate factor, which affects the hysteresis, and the atomic diffusion probability, which influences the subcooling [21]. During the solidification process, the temperature of PCM steadily falls. When the temperature falls below freezing one, two contrasting effects occur: the nucleation power increases while the rate of nucleation drops. When the temperature continues to fall to the lower one reached under the cooling load, atomic diffusion becomes constrained because of the lower temperature, and the nucleation rate reduces rapidly. In this work, we will focus on subcooling, which indicates that, at least within some temperature range, distinct states can exist at the same temperature. This point represents the main issue when adding subcooling in numerical models. There is still no harmony about subcooling inclusion in numerical models. The major point is the unpredictable behaviour of PCM with subcooling level. The occurrence of crystallization is reliant on several factors and thus is case-sensitive. Rate of cooling [22], volume of liquid PCM [23], thermal history of PCM [24], roughness of surfaces [25] and additives [26], are all factors that have a more or less significant influence on the probability of subcooling occurring.

The challenge in modeling supercooling consists in accurately simulating the thermal behaviour of PCMs during the solidification phase while preserving continuity of enthalpy, temperature, and melt fraction [27]. The subcooling is incorporated into models using a variety of methods, as including an instantaneous isenthalpic transformation between the PCM crystallization temperature and its enthalpy curve of melting [28]. However, this model is only partially validated because the numerically modelled recalescence process does not fit well with experimental temperature data. Alternatively, a heat source term to model recalescence can be added into each node of the numerical model when the node temperature falls below the nucleation temperature or when the liquid node is in direct contact with a solid neighbour node [29]. The subcooling can also be considered by dividing the solidification phase into four stages: regular solidification; liquid cooling while the PCM is in a metastable state; kinetic nucleation to model the temperature increase during recalescence; and cooling of the solid phase [30]. Other researchers have proposed alternative methods that utilize temperature functions, solidified-fraction functions, and heat source terms [31]. Finally, a novel formulation that considers the effective heat capacity as negative during the recalescence process has been recently proposed [32], which allows for modeling the temperature increase during recalescence.

The evolution of the temperature during the subcooling can be assumed to be similar to the one that characterizes a thermostat working principle. Fig. 1.10 resumes this analogy between an ideal thermostat and subcooling during the PCM

charging phase. In control theory, an on-off controller is a form of feedback controller that changes between two states.

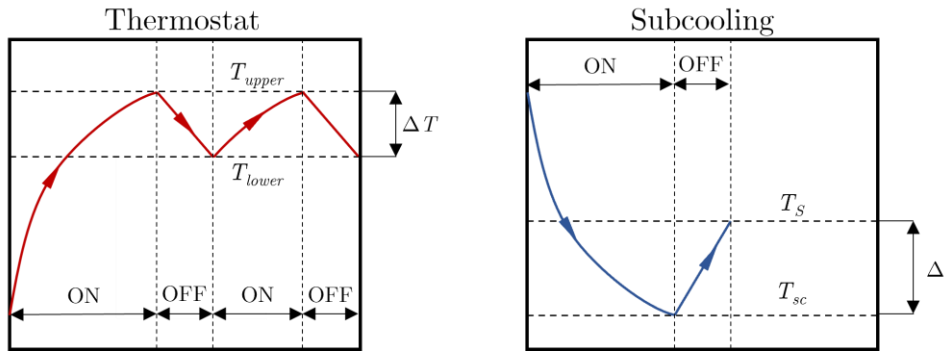

Fig. 1. 10. Comparison between ideal thermostat temperature evolution and temperature of PCM during subcooling.

A classic example is a domestic thermostat, which switched off/on to regulate the home temperature at a designed temperature. Thus, a temperature sensor placed within the system – which can be a room as well as a water tank, makes the thermostat (Fig. 1.10) turning the heater on when the temperature drops below a certain lower limit, and turning it off when it exceeds an upper limit.

Without considering thermal inertia, the reaction of the system is ideally instantaneous, and the temperature is guaranteed to be inside the DT control band. Likewise, the PCM behaviour during subcooling is such that, after it reaches a bottom temperature equal to $T_{sc,}$ the temperature increases because the thermostat-like subcooling effect is switched off; this happens until the phase change is reached. In conclusion, one can argue that a thermostat-like control process can be applied to include the subcooling effect within the PCM modelling behaviour, to include it in a mathematical model.

As discussed in the literature review, an issue of including subcooling in numerical models lies in the enthalpy dependence on temperature. When resorting to a simplified model, from the evaluation of enthalpy vs temperature curve, one can evaluate the derivative $\mathrm{d}h/\mathrm{d}T$ to smear the latent heat of fusion peak, to be included in a c(T) function too [16]. When the subcooling is included, the enthalpy does not depend on T anymore since, at the same temperature, one can found two different enthalpy values (Fig. 1.11). Looking at the cooling phase (blue line), the PCM temperature decreases until it approaches the solidification one. At this point, while normally there is a phase transition with release of the stored latent

heat, when subcooling occurs the temperature continues to drop to T_{sc}. Once this temperature has been reached, the solidification of the PCM – in liquid phase until that point – begins.

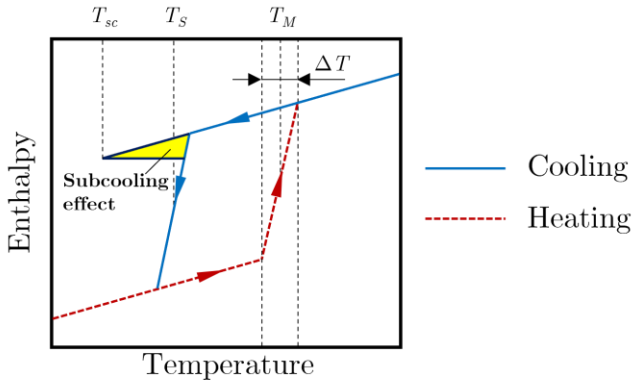

Fig. 1. 11. Subcooling effect on enthalpy: temperature

After that, so-called recalescence occurs, *i.e.,* to the detriment of a portion of the latent heat, PCM temperature increases, and the enthalpy returns to follow the initial path. Thus, in the interval between T_{sc} and T_S, it can be seen that depending on whether the PCM is in the cooling or heating phase, it has two different enthalpy values. To overcome this challenge, this work introduces a new approach that considers subcooling by means of control variables. As for a thermostat, subcooling should be activated/turned off depending on the temperature history of the PCM. In detail, we introduce two Boolean control variables, named φ_{state} and Q_{state}. The first is responsible for the changing in the liquid fraction behaviour, *i.e.,* it activates subcooling if the temperatures drop down; on the other hand, the second controls the recalescence, *i.e.,* how fast is the release of latent heat inside PCM to cause a temperature increase after subcooling occurs. Both variables can vary from 0 (Off) to 1 (On). What allows these variables to change their binary state is a condition (an inequality, in this case defined on temperatures) that can be fulfilled depending on the history of the system temperature. Then, depending on whether the inequality is more or less respected, the state of the variable changes from 0 to 1, or vice-versa. The following scheme (Figure 6) resumes the logical framework applied to the "cold charging" phase.

The function of φ_{state} is to control the phase during subcooling. Thus, as depicted in Fig. 1.12, φ_{state} starts from an initial value of 1, and then it remains equal to 1 until the temperature doesn't reach the subcooling temperature T_{sc}.

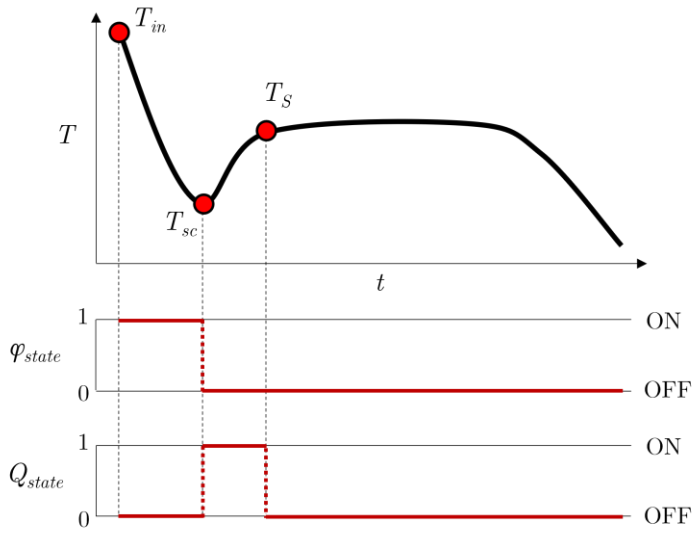

Fig. 1. 13. Scheme of the state variables working principles for subcooling modeling: φ_{state} is responsible for the changing in the liquid fraction behaviour, and Q_{state} controls how fast is the release of latent heat inside PCM to cause a temperature increase after subcooling occurs

From this point, its value becomes 0 and continues to be 0 until the transient finishes, as the effect of subcooling does not occur a second time. Differently, as regards the second control variable Q_{state}, looking at Fig. 1.13 one can observe that it starts from 0 and continue to be off until temperature reaches onset crystallization point (T_{sc}). Then, it is switched on – reaching $Q_{state} = 1$ - until the nearly constant temperature section is reached (T_S). At this point, Q_{state} needs to be deactivated. The reason why we need both j_{state} and Q_{state} is that we must maintain the two phenomena independent: indeed, the role of Q_{state} is just to determine how fast the temperature raises up from T_{sc} to T_s.

Therefore, in order to include the introduced subcooling effect – via control variables – in our mathematical model, we have to introduce the variable φ_{new}, as well as a modified form of both S_h and k_{eff}. To this end, φ_{new} is defined as:

$$\varphi_{new}\ T\ = \varphi_1\ T_{sc}\ \varphi_{state} + \varphi_2\ T_S\ (1 - \varphi_{state}) \tag{1.7}$$

where φ_1 and φ_2 are the liquid fractions computed with respect to the subcooling temperature and the solidification temperature, respectively (see Fig. 1.14). Therefore, during the cooling, φ_1 is equal to 1 until temperature reaches T_{sc}, and becomes 0 for lower temperatures. Likewise, φ_2 stays equal to 1 until $T = T_S$ and then becomes 0. By doing so, in the first stage the PCM will follow the φ_1 curve that imposes a value of the liquid fraction equal to 1 until the subcooling point is reached. As soon as temperature drops below this value, φ_{state} turns into 0 and the original curve (φ_2) becomes the new liquid fraction curve to be followed.

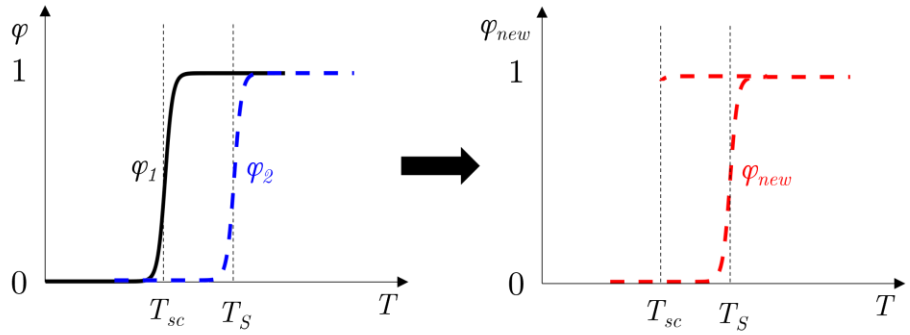

Fig. 1. 14. Subcooling effect on melt fraction, φ_{new}.

On the other hand, the way the variable Q_{state} influences the PCM behaviour is explained in the following equation. This variable defines a new contribution in the energy equation due to recalescence. Specifically, this term reduces the overall "cold energy" that can be stored by the PCM, of a quantity that is the energy required to bring the temperature back from subcooling to solidification temperature. Thus, an energy source term (S_{sc}) needs to be summed to the original one (S_h) that accounts for latent heat. In detail, the integral of the thermal power exchanged between the two time instants T_{sc} and T_S is equal to the stored energy with respect to the corresponding temperatures, T_{sc} and T_S. Summarized:

$$\int_{t_{sc}}^{t_S} S_{sc}\, dt = \int_{t_{sc}}^{t_S} c_{PCM}\rho_{PCM}\, dT \tag{1.8}$$

Referring to the mean value (S_{sc}) and considering the control variable governing its activation (Q_{state}), the contribution is written as:

$$S_{sc} = Q_{state} c_{PCM} \rho_{PCM} (T_S - T_{sc}) / \Delta t_{sc} \tag{1.9}$$

where Δt_{sc} is the time interval that defines how long the subcooling lasts, *i.e.,* how much time is required for the system to go from T_{sc} to T_s. In the presented model, Δt_{sc} needs to be set according to experimental results and therefore involves a calibration process of the model. The source term for the energy equation is formulated as:

$$S_{tot} = S_h + S_{sc} = \rho_{PCM} L_f \frac{\partial \varphi_2}{\partial t} \; 1 - \varphi_{state} \; + Q_{state} c_{PCM} \rho_{PCM} (T_S - T_{sc}) / \Delta t_{sc} \tag{1.10}$$

Lastly, the effect of subcooling on the thermal conductivity is encompassed through the definition of an effective property (k_{eff}), whose definition is strictly linked to the one of φ_{new}:

$$k_{eff} = k_s + \; k_l - k_s \; \varphi_{new} \tag{1.11}$$

Eq. (1.11) makes the effective thermal conductivity equal to k_l until φ_{new} is equal to 1, after which the actual value of k_{eff} depends on the melt fraction value (φ_2). The second predictive model proposed in this study is here shown. From the DSC analysis one can evaluate the main parameters associated with melting/solidification, i.e., melting/crystallization temperature, enthalpy, and latent heat. The melting temperature is the temperature at the onset of the peak, evaluated by the intersection between the baseline and the tangent to the decreasing branch on the inflexion point [33]. The enthalpy of fusion is computed as the integral over the curve and the baseline with respect to the time.

The thermal analysis of PureTemp15 is performed using the differential scanning calorimetry (DSC) 250 from TA Instruments, with a sample weight of 7.19 mg. Data have been sampled every 0.1 s and the following test schedule has been adopted:

- isotherm at 40 °C (2 min);
- ramp from 40°C to 0 °C, at -0.5 °C/min;
- isotherm at 0 °C (2 min);

- ramp from 0 °C to 40 °C at +0.5 °C/min.

Fig. 1.15 shows the normalized heat flow exchanged - by dividing the heat flow signal by the sample weight – with the sample during solidification and melting together with the experimental apparatus used to perform the evaluation. Results from the present biological PCM sample show a latent heat of 181.89 J/g if referred to the solidification and 180.61 J/g if on melting, which is in good agreement with the certified values from the PureTemp15 catalogue. The peak temperature for solidification and melting are 8.98 °C and 13.46 °C, respectively.

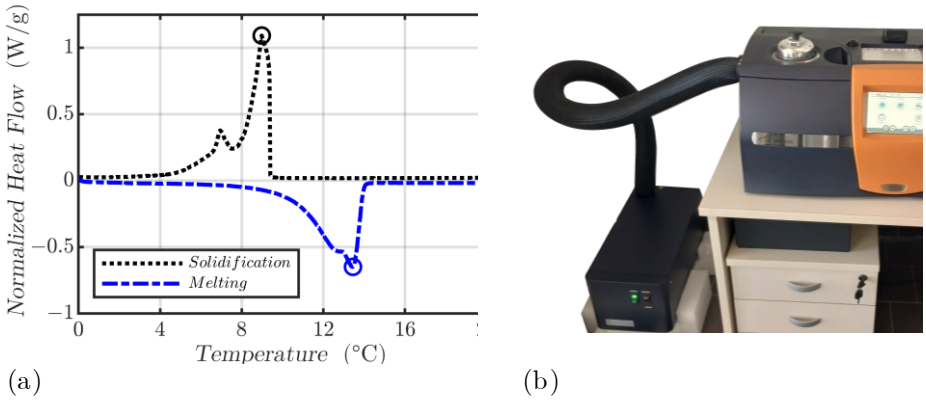

Fig. 1. 55. DSC analysis results: (a) normalized heat flow for solidification and melting; (b) TA Instruments DSC 250 equipment (b).

The DSC analysis is propaedeutic to the evaluation of the specific heat that is used in the DSC-based model to properly define the energy stored by the PCM during the phase change. Thus, considering that when a material is heated at a constant rate, the heat flow into it is related to its specific heat, we can evaluate this property as follows:

$$c = \frac{1}{m}\frac{dH}{dt}\frac{dt}{dT} \tag{1.12}$$

where m is the sample mass, $\mathrm{d}H/\mathrm{d}t$ is the heat flow and $\mathrm{d}t/\mathrm{d}T$ is the reciprocal of the heating rate. The resulting c curves for both solidification and melting are displayed in Fig. 1.16. The solidification curve is fitted into the model so that each temperature value is associated with the actual value of the specific heat of the PCM. This allows the model to be modified without imposing a priori the value of the solidification temperature T_S.

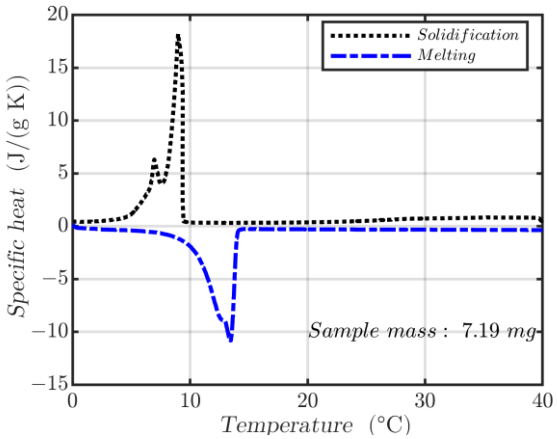

Fig. 1. 16. Specific heat curves for heating and cooling rate of 0.5 °C/min.

1.3.2. Analytical solution: Stefan problem

The classical formulation of the Stefan problem involves establishing relationships among various factors that govern the melting process. These factors encompass the temperature distribution over time, and the precise location of the boundary separating the solid and liquid phases, which is the reason why this is recognized as a moving boundary problem. Further, factors include the thermophysical properties of the material, including thermal conductivities and specific heats for both phases. In its simplest formulation a Stefan problem is a linear 1D problem, where heat conduction is the predominant heat transfer mechanism, and natural convection is not included in the mathematical formulation, which allows to avoid the momentum equations for the fluid flow motion.

These relationships manifest as partial differential equations within the solid and liquid regions, coupled with additional conditions at the moving boundary that reflect local energy conservation and temperature behaviour at the interface

between the solid and liquid materials. Solving this problem presents the challenge of capturing two different evolutions of temperature, which simultaneously varies depending on the region where it is computed that evolves in time. For instance, in the solid region, temperature remains constant, while within the liquid, it necessitates solving an equation within a dynamically changing region, whose determination represents the crucial aspect of the problem.

The main assumptions are here listed [34]:

- zero-thickness of the solid-liquid interface: the phase change does not occur in a fixed temperature range, *i.e.,* there is no mushy zone;
- absence of subcooling;
- diffusion is assumed to be the prevalent heat transfer mode in the liquid phase.

A schematic of the 1D heat transfer process is presented in Fig. 1.17. The PCM medium is semi-infinite, initially solid at its melting temperature T_m, and at $t = 0$ a Dirichlet boundary condition, *i.e.,* fixed wall temperature ($T_w > T_m$) is assumed. As a consequence, the PCM starts melting, with an evolution of the melting front parallel to the boundary. Thus, the front propagates from x = 0, switching from pure conduction in solid to liquid.

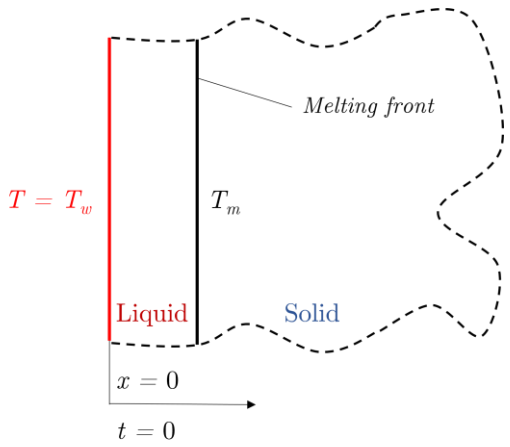

Fig. 1. 17. Sketch of the Stefan problem formulation

The energy equation referred to the liquid, solid, and interface regions is written as:

$$\rho c_{\ l} \frac{\partial T_l}{\partial t} = k_l \frac{\partial^2 T_l}{\partial x^2} \quad x < s\ t\ , t > 0 \tag{1.13}$$

$$\rho c_{\ s} \frac{\partial T_s}{\partial t} = k_s \frac{\partial^2 T_s}{\partial x^2} \quad x > s\ t\ , t > 0 \tag{1.14}$$

$$\rho L \frac{ds}{dt} = k_s \frac{\partial T_s}{\partial x} - k_l \frac{\partial T_l}{\partial x} \quad x = s\ t\ , t > 0 \tag{1.15}$$

Where ϱ is the density, c is the specific heat, k is the thermal conductivity, L is the latent heat of fusion, x and t are special and temporal coordinates, $s(t)$ is the position of the melting front that evolves in time, and the subscripts s and l stands for solid and liquid. With the following boundary conditions:

$$T(x = 0, t > 0) = T_w \tag{1.16}$$

$$T(x = s(t), t > 0) = T_m \tag{1.17}$$

The Stefan problem in its generality can be solved both numerically and analytically. However, based on its strong simplifications, an analytical resolution is favourable, leaving to more detailed and complex models the burden to be solved numerically.

For all details about the analytical solution one can refer to [34]. In this context, we present the relationship to evaluate the transient temperature distribution in the liquid:

$$\frac{T_l\ x, t\ - T_w}{T_m - T_w} = \frac{\text{erf}\ (\frac{x}{2\quad \overline{\alpha_l t}})}{\text{erf}\ (\beta)} = \frac{\text{erf}\ (\eta)}{\text{erf}\ (\beta)} \tag{1.18}$$

where:

$$\beta e^{\beta^2} \text{erf}\ (\beta) = \frac{Ste}{\sqrt{\pi}} \tag{1.19}$$

When dealing with a finite domain, the problem becomes significantly more intricate, and finding an exact solution is not possible. Therefore, an approximate approach is employed, resulting in the formulation of a non-linear system comprising two equations and two unknowns.

1.3.3. Numerical approaches

As aforementioned, when resorting to numerical methods, for tackling phase-change material (PCM) problems and solving them, we can use two main methods: the front-tracking method and fixed grid methods. The front-tracking method revolves around explicitly tracking the moving interface that separates different phases within the PCM system. This approach adopts a Lagrangian framework, as a set of markers or particles closely follows the interface as it advances or recedes. This allows for highly accurate representations of complex interface dynamics and sharp phase transitions. However, it is important to note that implementing front-tracking methods can be computationally demanding and intricate, as it necessitates maintaining the shape of the interface and ensuring element quality.

Fixed grid methods, in contrast, rely on a stationary grid that discretizes the computational domain. In PCM problems, this grid remains fixed in space, while the properties of individual cells or grid points are updated over time to simulate phase-change phenomena. Unlike the Lagrangian approach of front-tracking, fixed grid methods employ a Eulerian framework, where equations governing heat transfer and phase change are solved at discrete grid points.

One advantage of fixed grid methods is their relative ease of implementation compared to front-tracking techniques, as they do not require the explicit tracking of the interface. However, handling phase-change processes efficiently on a fixed grid may involve additional strategies, *e.g.,* methods like the enthalpy-porosity technique. In this thesis we will not focus on front-tracking methods, whose details can be found in [35], but rather on fixed grid methods.

1.3.4. Fixed grid methods

This subsection briefly presents fixed grid methods to solve the Stefan problem, *i.e.,* enthalpy [36] and enthalpy-porosity approach [37], apparent heat capacity [38], and volume of fluid (VOF) [39].

Enthalpy method

The enthalpy method defines an implicit way of tracking the melting front by properly define the material enthalpy. Hence, a challenge emerges when attempting to account for the evolution of heat transfer and fluid motion near the interface. The governing energy equation for this method is written as:

$$\frac{\partial H}{\partial t} + \nabla(\rho u H) = \nabla(k \cdot \nabla T) \tag{1.20}$$

Where H is the total enthalpy, which includes both sensible and latent heat, as follows:

$$H = h_0 + \int_{T_0}^{T} \rho c dT + \varphi L \tag{1.21}$$

Where φ is the liquid fraction that can be defined as a piecewise function. For the flow field, continuity and momentum equations are written as:

$$\nabla \cdot u = 0 \tag{1.22}$$

$$\rho \left(\frac{\partial u}{\partial t} + u \nabla \cdot u \right) = -\nabla p + \mu \nabla^2 u + \rho g \tag{1.23}$$

Enthalpy porosity method

This method considers the PCM phase transition considering the latent heat evolution by defining a source term. This technique is used to ensure a zero-velocity field in the solid phase by means of a penalization source term, which is introduced in the momentum equation to allow the switch from the full Navier–Stokes equations in the liquid phase to a Darcy equation for porous media. The mushy region is thus regarded as a very dense porous medium that sharply brings the velocity to zero in the solid region. The expression of the penalization source term generally follows the Carman-Kozeny model for the permeability of a porous medium [40].

The following assumption are fixed for the thermal model definition:

- PCM is isotropic but not homogeneous;
- phase change during solidification/melting occurs in a temperature range that can be established from differential scanning calorimetry (DSC);
- the volume reduction/expansion during the phase change is ignored, together with air gaps caused by this;
- laminar flow model for PCM liquid phase, which is treated as a Newtonian fluid;
- Boussinesq terms to include the buoyancy effects.

The phase change modeling is based on three distinct regions, *i.e.,* a totally liquid region, a solid one and a mushy zone, where both phases coexist. In order to model the above-mentioned phase change, the three basic conservation equations have to be solved throughout the computational domain, *i.e.,* mass (1.24), momentum (1.25) and energy conservation (1.26). Therefore, the model equations are written as follows:

$$\nabla \cdot u = 0 \tag{1.24}$$

$$\rho \left(\frac{\partial u}{\partial t} + u \nabla \cdot u \right) = -\nabla p + \mu \nabla^2 u + F_g + F_v \tag{1.25}$$

$$\rho c \left(\frac{\partial T}{\partial t} + u \cdot \nabla T \right) = \nabla (k \cdot \nabla T) + S_h \tag{1.26}$$

Where ϱc is the product between the density and the specific heat at constant pressure of the PCM, that represents the volumetric heat capacity, k is the thermal conductivity, t the time, T the temperature, p the pressure and μ the dynamic viscosity. Natural convection phenomena can play a key role in the PCM motion. Therefore, the Boussinesq hypothesis is adopted to consider these buoyancy effects, and at the same time to reduce the complexity of the Navier-Stokes equations. In this regard, the Boussinesq term (1.27) has been added for the evaluation of the volume force in the momentum conservation equation (1.25), as follows:

$$F_g = \rho g \beta (T - T_{ref}) \varphi(T) \tag{1.27}$$

where, g is the gravitational acceleration, β is the volumetric thermal expansion coefficient, T_{ref} is the reference temperature, fixed equal to the melting point temperature, T_m and φ is the melt fraction, *i.e.,* the non-dimensional parameter that

quantifies the percentage of liquid phase contained in the mushy zone, evaluated as follows:

$$\varphi\ T\ = \frac{T - T_s}{T_l - T_s} = \frac{T - T_m + \Delta T_m}{2\Delta T_m} = \begin{cases} 0 & for\ T < T_s \\ 0 < \varphi < 1 & for\ T_s \leq T \leq T_l \\ 1 & for\ T > T_l \end{cases} \tag{1.28}$$

The function from Eq. (1.28) is included in Eq. (1.27) also to consider buoyancy effects in the mushy zone [41]. In Eq. (1.28) the definition of the melt fraction is based on: the phase change temperature interval, ΔT_m– assumed symmetrical with respect to the T_m –; the maximum temperature at which the PCM is completely solid, T_s; and the minimum temperature at which the PCM is completely liquid, T_l. These temperatures have been evaluated as a function of the PCM melting point T_m and the phase change interval ΔT_m as follows:

$$\begin{aligned} T_s &= T_m - \Delta T_m \\ T_l &= T_m + \Delta T_m \end{aligned} \tag{1.29}$$

The evolution of the melt fraction can be visualized in the following (see Fig. 1.18). It can be seen how the liquid phase (red one) evolves from right to left under the strong influence of natural convection motions. The recirculation, in the case without fins is evident, and strongly affect the melting. The solid region of PCM (blue one) is confined in the bottom left corner, as the region with lower temperature.

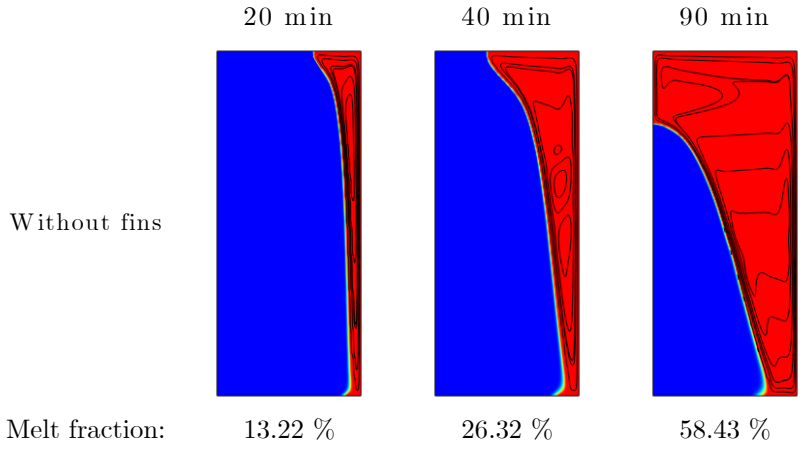

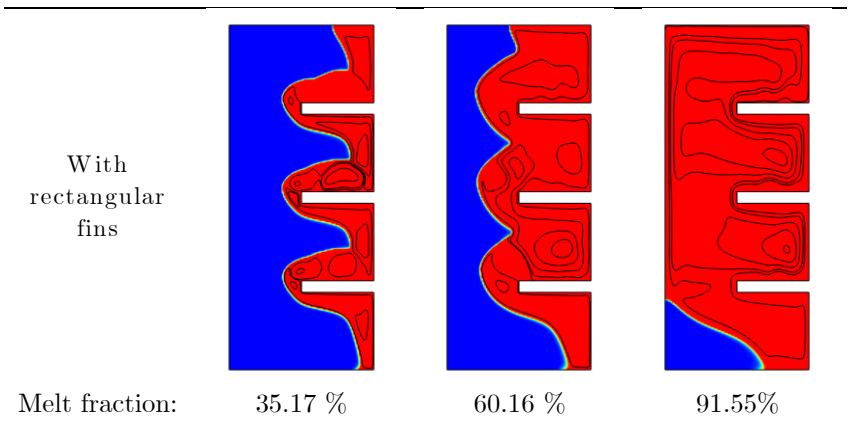

Fig. 1.18. Evolution of melt fraction for rectangular enclosure with and without rectangular fins.

Fig. 1.18 also shows what happens if the surface on which the boundary condition is applied becomes finned. In detail, adding rectangular fins strongly enhance the melting process because of the increased heat transfer area and then the possibility to spread heat with a faster rate. Since the computational resolution is performed by means of a fixed mesh, the condition that all velocities in solid regions are zero is accounted for in the enthalpy-porosity approach by appropriately defining the volume force source term S (Eq. (1.30)), based on the Carman-Kozeny equation [37]. The basic principle is to gradually reduce the velocities from a finite value in the liquid, to zero in the full solid, over the parts of the domain that are changing phase. This can be achieved by assuming that such cells behave as porous media [37].

$$S(T) = A_{mush} \frac{[1 - \varphi\ T\ ]^2}{\varphi\ T\ + \delta} \tag{1.30}$$

In the Carman-Kozeny term, A_{mush} is an arbitrary constant that influences the effective viscosity into the mushy zone. Its value – set within the range of 10^3-10^7 – is generally determined based on experimental study and varies with the geometrical and operational parameters. Based on our similar previous study [42], in this thesis we will assume $10^{3.7}$. This value is a compromise between computational time/effort, that is always challenging in PCMs modelling [43], and solution accuracy. This value has showed to be valid in our previous similar study [42], and also Kheirabadi and Groulx [44] showed that for rectangular PCMs a value of 10^4, close

to our $10^{3.7}$, is reasonable to obtain good predictions. Moreover, δ is an arbitrary constant, usually set equal to 10^{-3}, introduced to avoid a null denominator. Therefore, the source term defined in the momentum equation is computed as the product of S and the fluid velocity:

$$F_v = S(T)u \tag{1.31}$$

Thus, since *S(T)* is zero in full liquid elements, it has no influence in the momentum equation. Conversely, during the phase change, the value of S dominates over the other momentum equations terms. Finally, in totally solid elements, the final large value of S overcomes all terms. Furthermore, in using a fixed grid approach for the analysis of solidification and melting phenomena – to overcome the issues of the evaluation of heat and mass transfer near the phase change layer – the basic approach consists of defining an appropriate generation term. In detail, for the enthalpy-porosity approach the latent heat influence is accounted by the definition of the energy equation generation term (S_h), as follows:

$$S_h = -\rho L \frac{\partial \varphi}{\partial t} \tag{1.32}$$

In order to prove the affordability of the enthalpy porosity formulation, a benchmark case is here presented and discussed [45]. The configuration is represented by a cavity measuring 0.05 m in width and 0.12 m in length, which is filled with lauric acid. This cavity is surrounded by plexiglass panels, each 0.025 m thick, on the bottom, left, and top sides. The external surfaces of these plexiglass panels are insulated. In the experimental arrangement, the entire right side of the apparatus is sealed off by a 35 mm thick aluminium plate, which is at a constant temperature. Therefore, for modeling purposes, the assumption – also made in [46] – is to consider on the entire right side of the system a constant temperature of $T_w = 70$ °C. Initially, the entire system is at a uniform temperature of $T_0 = 26$°C. Regarding material properties, the phase change material (PCM) employed in this research is lauric acid, and its thermophysical characteristics can be found in [46]. The temperature at which melting begins, as indicated (43.55 °C), concurs with widely accepted values and experimentally observed results [46].

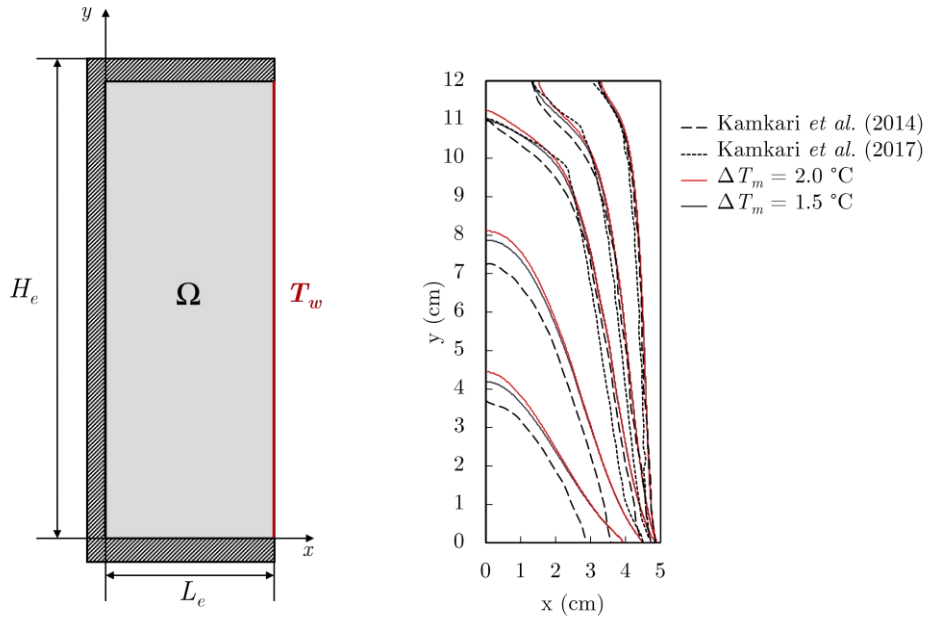

Fig. 1. 69. Validation of melt fraction evolution in time, with difference temperature ranges.

Apparent heat capacity

The AHCM assumes that the heat transfer and thermal storage in a PCM can be represented by an equivalent heat capacity, known as the apparent heat capacity (C_{app}). The energy equation then can be written as:

$$\rho C_{app} \frac{\partial T}{\partial t} = \nabla(k \nabla T) \tag{1.33}$$

Where the apparent heat capacity is defined as:

$$C_{app} = \frac{\partial H}{\partial t} = C\ T\ + L\delta_d(T - T_m) \tag{1.34}$$

In this equation L is the latent heat, while δ_d is the Dirac-delta. It's meaning is to define the temperature derivative of the melting fraction. However, using the

Dirac-delta introduces numerical complexities, which can be overwhelmed resorting to an approximated heat capacity:

$$C_{app}(T) = \begin{cases} C_s\ T & for\ T < T_m - \Delta T \\ L + \int_{T_m-\Delta T}^{T_m} C_s\ T\ dT + \int_{T_m}^{T_m+\Delta T} C_l\ T\ dT & for\ T_m - \Delta T \leq T \leq T_m + \Delta T \\ C_l\ T & for\ T > T_m + \Delta T \end{cases} \tag{1.35}$$

This formulation can be simplified if considering the heat capacity of the solid and liquid independent from temperature – which means that the melting fraction varies linearly in the mushy zone.

$$C_{app}(T) = \begin{cases} C_s & for\ T < T_m - \Delta T \\ \frac{L}{2\Delta T} + \frac{C_s + C_l}{2} & for\ T_m - \Delta T \leq T \leq T_m + \Delta T \\ C_l & for\ T > T_m + \Delta T \end{cases} \tag{1.36}$$

This approach offers several notable advantages: temperature takes center stage as the primary dependent variable, and when employing this method, it generally eliminates the fluctuations commonly encountered with the latent heat source approach [47]. However, it's worth noting that this formulation does provide approximate solutions and faces challenges related to the singularity problem associated with physical properties, namely C and k.

Volume of fluid

In the Volume of Fluid (VOF) method, we represent the interface using a scalar function, typically the melting fraction φ, within a computational cell. The VOF method operates within a Eulerian framework on a fixed grid, making it well-suited for scenarios with significant interface distortions and changes in geometry. However, it is important to note that the VOF function is not continuous at the interface. To use the VOF function accurately, a geometric technique is necessary to reconstruct the interface [X]. Thus, it may lack precision in directly calculating parameters like normal and curvature due to the discontinuous spatial derivative of the VOF function near the interface.

Part II: Numerical modeling of CFD-based optimizations

The success of the transition from a World of uncontrolled urbanization, energy poverty, and global warming to a World of sustainability nowadays depends on whether the optimization of energy systems is performed. Luckily, in the last decades the global awareness for climate change provided a quick development of sustainable technologies to manage such problems. Nevertheless, there is much progress still to be made, representing a breeding ground for scientific progress. In this context, the optimization – seen as a process to improve a system from its initial state – is a significant tool in engineering for determining the best, or optimal, value for the decision variables of a system. For various reasons, it is important to optimize processes/systems so that a desired quantity, known as the objective function, is maximized, or minimized, *e.g.,* the output, profit, productivity, product quality, and so on, to be maximized, or the cost per item, investment, energy input, and so on, to be minimized. Therefore, for improved performance, such engineering devices must be optimized for designs that are more compact, lighter, with fewer frictional losses, and increased in thermal efficiency. The most crucial and difficult stage in this process is typically formulating a suitable optimization problem, for which there are numerous elements that need to be defined, i.e., system boundaries, optimization criteria, decision variables, and objective functions. Depending on the application, all these elements may notably differ. Therefore, the overall aim of the activity of the second year was to define, depending on the application, the behaviour of a certain system – by focusing on the Heat Transfer – and then to optimize its performance.

The choice of optimization techniques is a pivotal decision, with profound implications for the success of a project. Two prominent methodologies, genetic algorithms (GAs) and gradient-based techniques like topology optimization, have emerged as key players in this domain. Each has its strengths and weaknesses, and the selection between them often hinges on the size and complexity of the system under examination and the desired level of design freedom. This thesis delves into the intricate considerations surrounding the use of these optimization techniques, emphasizing the preference for genetic algorithms in large-scale systems while

highlighting the advantages of gradient-based methods, particularly topology optimization, in small-scale systems that demand a high degree of thermo-fluid-dynamic precision.

Large-scale heat transfer systems, such as industrial heat exchangers and power plant components, pose unique challenges. These systems often feature intricate geometries and intricate thermal interactions, making it impractical to delve into the minutiae of fluid dynamics. In such cases, treating the system as an energy system is a pragmatic approach, and genetic algorithms are the preferred choice.

GAs focus on optimizing parameters directly impacting thermal performance, sidestepping the computational burden associated with detailed computational fluid dynamics (CFD) simulations or complex numerical formulations. They excel in large-scale systems where the overarching goal is enhancing heat transfer efficiency. This approach is speedier, more scalable, and maintains a sharp focus on energy efficiency, all of which are crucial factors in large-scale heat transfer applications. Furthermore, genetic algorithms shine when the complexity of the heat transfer problem is exceptionally high. Complex geometries and intricate thermal interactions can overwhelm traditional modeling approaches. GAs offers a pragmatic solution by navigating these intricate problem spaces effectively, optimizing performance without an exhaustive exploration of all possible configurations.

In contrast, small-scale heat transfer systems, such as microfluidic devices or compact electronic components, requires precision and detail. Here, entering the field of fluid dynamics is imperative to harness the system's full thermo-fluid-dynamic potential. This is where gradient-based techniques, particularly topology optimization, come to the forefront. Topology optimization enables intricate control over design parameters, allowing to optimize fluid pathways and heat transfer surfaces with precision. The approach ensures that every aspect of the system is fine-tuned to achieve maximum heat transfer efficiency.

One of the key advantages of gradient-based techniques, especially topology optimization, is the freedom they afford in design. Engineers can explore innovative configurations and geometric patterns, optimizing not only for energy efficiency but also for innovative form factors and structural considerations. This level of design flexibility is invaluable, particularly in small-scale systems where every element must be meticulously tuned for optimal performance.

The choice between genetic algorithms and gradient-based techniques in heat transfer analysis is far from arbitrary. It hinges on the size and complexity of the system under investigation, as well as the desired level of detail in modeling and design freedom. Genetic algorithms, with their energy-centric approach, are the preferred choice for large-scale systems, where the emphasis is on enhancing heat

transfer efficiency without delving deeply into fluid dynamics. On the other hand, gradient-based techniques, particularly topology optimization, excel in small-scale systems, allowing engineers to exploit the system's full thermo-fluid-dynamic potential while maintaining design flexibility.

Ultimately, the selection of the most suitable optimization technique should be a well-considered decision that aligns with the specific goals and constraints of the heat transfer problem at hand. By carefully weighing the scale, complexity, and design requirements, engineers and researchers can leverage these powerful optimization tools to achieve superior heat transfer performance across a wide range of applications.

Preface: What moves innovation?

Scientific innovation is a dynamic process, similar to a circular domino effect, where the evolution of materials, designs, applications, mathematical models, and challenges continuously influence and propel one another. This interconnected cycle serves as the driving force behind progress in various fields, from technology and engineering to healthcare and beyond.

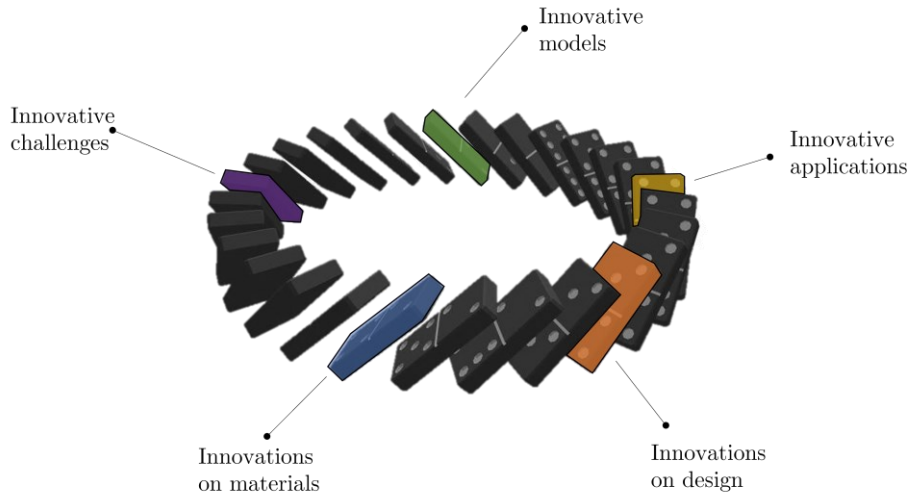

Fig. II. 1. Innovation domino's effect

To explain the evolution of this loop, one can start from each point. For instance, at the heart of this circular cascade can be placed the evolving materials. Researchers persistently explore and refine novel substances, seeking to enhance their properties, durability, and versatility. These materials serve as the initial domino,

setting the stage for the entire innovation process. They become the starting point from which groundbreaking solutions are predicted. In the field of thermal science several materials fall in this group, *e.g.,* advanced thermoelectric materials, metamaterials, and phase change materials (PCM). The former materials like organic thermoelectric, and nanocomposite thermoelectric are enabling efficient conversion of heat into electricity for applications in energy harvesting. Metamaterials for passive radiative cooling have been developed to cool surfaces below ambient temperatures passively, making them useful in building cooling and refrigeration without active energy consumption. Phase Change Materials (PCMs) for thermal energy storage are being used for efficient thermal energy storage in applications such as solar energy storage, building temperature control, and portable thermal management.

As materials advance, they ignite a transformative phase in design. Researchers try to explore the potential of these materials to envision solutions that challenge conventional thinking. This design domino pushes the boundaries of what is possible, spanning across diverse domains such as thermal management, cooling, power systems. The fall of the design domino leads to the expansion of applications. These innovative solutions permeate various sectors, including healthcare, transportation, energy, and information and communication technologies (ICT). They become integral to daily life and industry operations, driving demand for further advancements. The applications domino represents the real-world impact of scientific innovation. Simultaneously, mathematical models evolve as another domino in the circular cascade. There is a continuous refinement and development of models that better describe complex real-world phenomena. These models enable a deeper understanding of phenomena and inform the design and optimization process. However, models do not always correctly predict what happens in reality and therefore raise new challenges and obstacles. They serve as pivotal catalysts within this circular cascade. They act as triggers, prompting researchers and innovators to respond creatively to real-world problems. These challenges often lead to breakthroughs in materials, designs, applications, mathematical models, and beyond. The beauty of this circular domino effect lies in its interconnectedness and feedback loop. Each element continuously influences and inspires the others. Emerging materials spark the creativity of designers, compelling them to think differently and create innovative solutions previously considered out of reach. Ambitious designs necessitate materials with specific properties, stimulating researchers to develop or adapt materials and mathematical models to meet these unique requirements. Real-world applications dictate the choice of materials and inform enhancements to mathematical models. Their performance in practical scenarios provides valuable

feedback, driving ongoing improvement. Challenges and real-world problems serve as pivotal triggers within this circular domino effect, compelling inventive responses, and motivating advancements in various aspects of scientific innovation.

Classification

The choice of optimization method must be tailored to the specific characteristics and constraints of each problem. Here, we will discuss the need for different optimization approaches based on the scale of the problem analysed:

1. Large Scale Heat Transfer (Centimeters to Meters):

The macroscale heat transfer scenarios include heat exchangers inside boilers, or HVAC systems, for which convection and radiation become more prominent. These systems often involve complex geometries and multiple heat transfer modes. Optimization techniques for macroscale heat transfer problems encompass:

- Geometric optimization: adjusting the geometry of heat exchangers or surfaces characteristics.
- Operating parameters optimization: changing working conditions, like mass flow rate, velocities, pressure drop.

2. Medium Scale Heat Transfer (Millimeters to Centimeters):

The mesoscale represents an intermediate range where both conduction and convection are significant. This scale is relevant in applications like heat sinks, heat exchangers, electronic components on circuit boards or microreactors. Optimization strategies for mesoscale heat transfer problems may involve:

- Geometry and shape optimization: altering geometry to achieve local thermal enhancement, *e.g.,* designing efficient fluid channels to remove heat from electronic components.
- Flow control: managing flow to maximize convective heat transfer.

3. Small Scale Heat Transfer (Nanoscale to Millimeters):

At the microscale, such as in microelectronics or microfluidic devices, heat transfer phenomena are often dominated by conduction and diffusion processes. The primary challenges include maximizing heat dissipation while minimizing the thermal resistance. Optimization methods for microscale heat transfer problems typically involve:

- Topology Optimization: determining the optimal placement of conductive materials or microstructures to enhance heat conduction/convection.
- Material selection: choosing materials with high thermal conductivity to improve heat transfer efficiency.
- Microscale fluid flow control: enhancing microchannels and microfluidics characteristics, e.g., tubes surface, to enhance convective heat transfer.

4. Multiscale Heat Transfer (Combining Multiple Scales):

In some scenarios, heat transfer problems span multiple scales, requiring a multiscale optimization approach. For instance, cooling a data center involves macroscale considerations for the facility's layout, mesoscale optimizations for server racks, and microscale strategies for individual chips. At this point, having provided a classification of heat transfer mechanisms at different scales, it is possible to provide a framework for real situations*, i.e.,* practical cases, in which this classification can be found and applied. The next figure, in fact, shows how one can go from very complex systems such as heat recovery steam generators (HRSG) to microchannel heat sinks (MCHS)s and consequently shifting on different scales that therefore involve different modelling approaches. This in fact also influences the next optimization step.

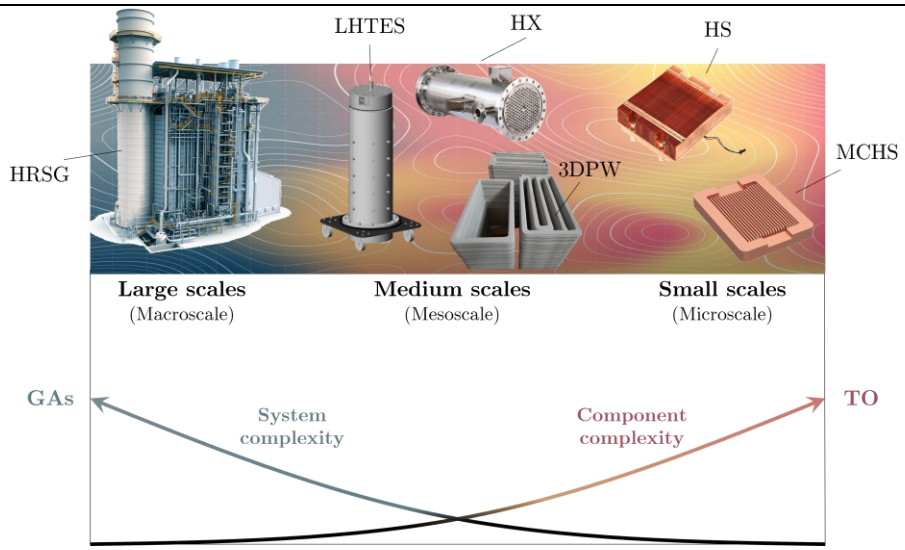

HRSG	Heat Recovery Steam Generator
LHTES	Latent Heat Thermal Energy Storage
HX	Heat Exchanger
3DPW	3D Printed Wall
HS	Heat Sink
MCHS	Micro-Channel Heat Sink
GA	Genetic Algorithm
TO	Topology Optimization

Fig. II. 2. From large scale to small scale heat transfer systems

What optimizing means

The optimization process is a dynamic and iterative journey that unfolds from the initial problem formulation to the attainment of optimality or the fulfilment of termination criteria. It encompasses various essential stages, each of which contributes to refining the solutions in pursuit of the best outcome.

At the outset, the optimization begins with a comprehensive problem formulation. This phase entails the explicit delineation of the objective function that necessitates minimization or maximization, coupled with the assessment of

constraints that must be satisfied. If the optimization does not include constraints, it is called *unconstrained optimization*. Decision variables, along with their permissible ranges, are also explicitly defined during this critical stage. Following the problem formulation – which is described in Fig. X – the optimization loop proceeds with an initialization step. Here, a set of candidate solutions is introduced to the process. These initial solutions can be generated randomly or based on prior domain knowledge, setting the stage for subsequent iterations. In the heart of the optimization loop lies the evaluation of the objective function and the associated constraints. In each iteration, the objective function is scrutinized for each candidate solution, along with any pertinent constraint functions. The objective function serves as the benchmark for assessing the performance of each solution in its quest to achieve the desired goal, while constraint functions ascertain whether the solution meets the problem's constraints.

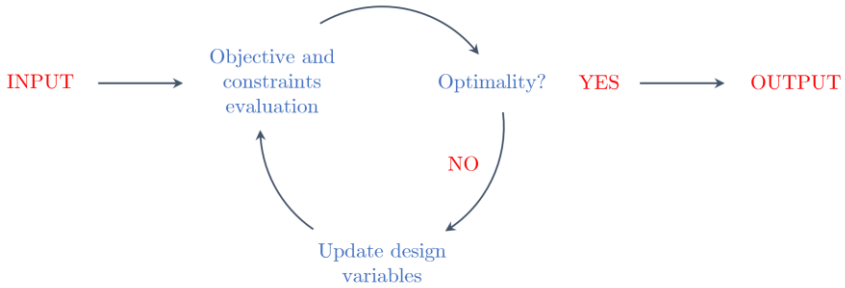

Fig. II. 3. General scheme of an optimization

Once the objective and constraint evaluations are completed, the optimality of each candidate solution is considered. At this point, the objective function values, and the degree of constraint violations, if any, are considered. Two possible scenarios emerge: the feasible solution, wherein all constraints are met, and the desired objective is reached; or the infeasible or suboptimal solution, which fails to fulfil either or both of these criteria. In the latter case, the optimization process persists in pursuit of better solutions. The optimization algorithm employs various strategies and methodologies to recalibrate candidate solutions that fall short in terms of feasibility or optimality. These optimization techniques, ranging from gradient-based methods to genetic algorithms or simulated annealing, guide the search towards improving the objective function while adhering to the constraints.

Following each iteration, a convergence check arises, aimed at determining whether the optimization algorithm is progressing towards an optimal solution.

The assessment depends on factors such as changes in objective function values, constraint violation reductions, or the attainment of predefined tolerance levels. The optimization process culminates when convergence is achieved or when predefined termination criteria are met. These termination criteria encompass parameters such as reaching a maximum number of iterations, adhering to a time constraint, or securing a satisfactory solution within an established tolerance range. Once the criteria are met, the optimization loop concludes, and the best-found solution is unveiled.

Optimization challenges: navigating local minima/maxima

One of the foremost challenges encountered in the field of optimization is the presence of local minima and maxima. This issue adds a layer of complexity to the optimization process and underscores the importance of a systematic and thoughtful approach to problem-solving.

A local minimum refers to a point within the search space of an optimization problem where the objective function reaches its lowest value within a small neighbourhood (see Fig. II. 4).

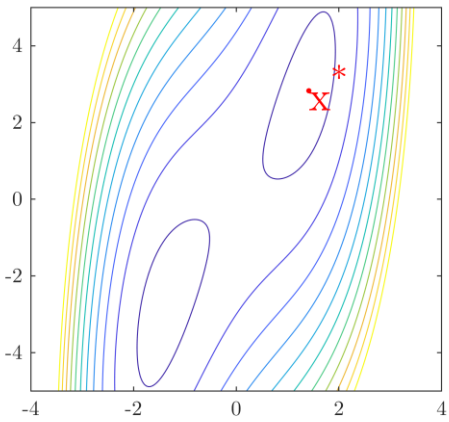

Fig. II. 4. Example of local minimum for a 2D variables function

It indicates a solution that outperforms nearby solutions but may not necessarily be the best solution in the entire search space, akin to a dip or valley in the

function's landscape. Gradients, which are vectors indicating the direction of steepest ascent or descent of a function at a specific point, play a crucial role in locating local optima in optimization. Gradient descent, a commonly used optimization algorithm, leverages gradients to minimize the objective function iteratively. Starting with an initial guess for the parameters, the algorithm calculates the gradient of the objective function with respect to these parameters at the current point (see Fig. X). The negative gradient points in the direction of steepest decrease, enabling parameter adjustments to minimize the function. This process continues until convergence to a local minimum. While gradients are fundamental for finding local minima, a potential drawback is that if the optimization starts with an initial guess too close to a local minimum, it may get trapped without exploring the broader parameter space (see Fig. II. 5). Consequently, a better global minimum or alternate local minima may remain undiscovered.

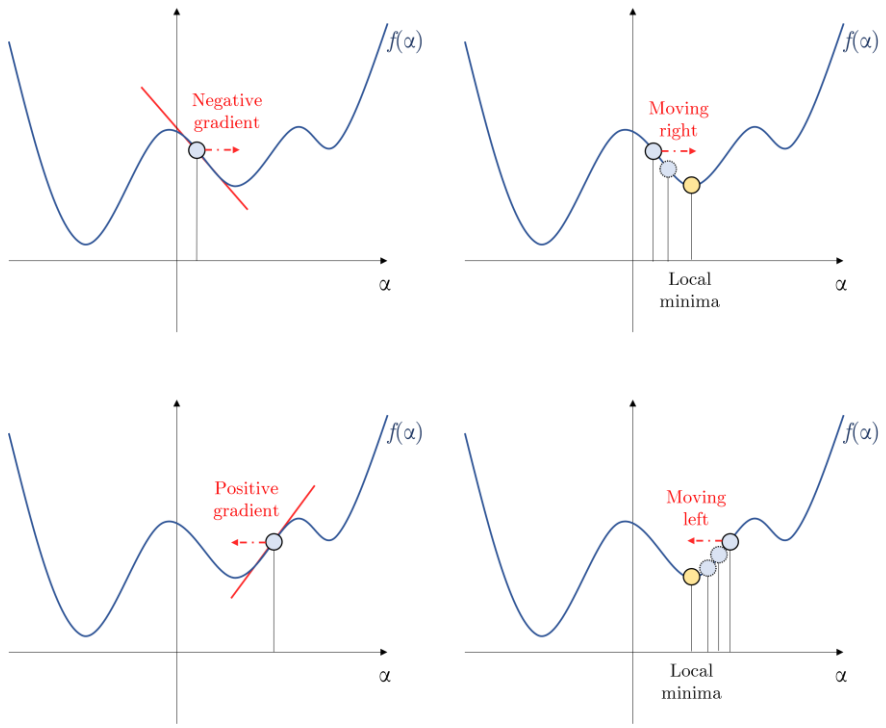

Fig. II. 5. Gradient descendent search: local minima

To counteract this issue and enhance the likelihood of discovering the global minimum or superior local minima, employing multiple starting points is a recommended strategy. Randomly initializing the optimization algorithm with various initial guesses promotes the exploration of different regions within the parameter space. Each of these starting points may lead to distinct local minima or the global minimum. After optimizing the objective function from each starting point, ensemble methods can be employed to aggregate the results. This may involve selecting the best solution from all runs or creating an ensemble of models trained on the solutions obtained from different starting points. This approach enhances the robustness of the optimization process, diminishing the risk of converging to suboptimal local minima.

The Rosenbrock function, often referred to as the Rosenbrock's valley or Rosenbrock's banana function, is a mathematical function commonly used in optimization and numerical analysis. It is named after Howard H. Rosenbrock, who introduced it in the early 1960s as a benchmark problem for optimization algorithms [48]. The general form of the Rosenbrock function for a two-variable case is:

$$f\ x,y\ =\ a-x\ ^{2}+b\ y-x^{2}\ ^{2} \tag{II.1}$$

Here, a and b are constants that can be adjusted to vary the shape of the function. The most commonly used values are $a = 1$ and $b = 100$, which create a distinctive narrow, curved valley with a single global minimum (see Fig. II. 6).

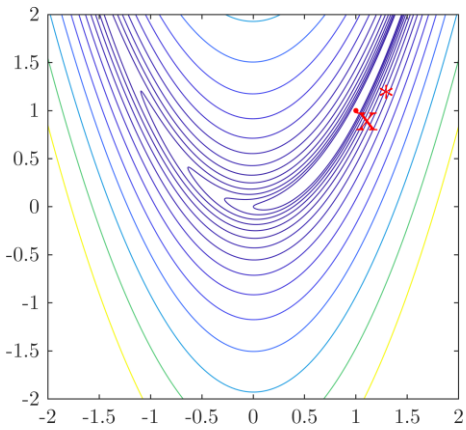

Fig. II. 6. Example of global minimum for a 2D variables function: Rosenbrock function

The Rosenbrock function has several noteworthy characteristics. It exhibits a narrow valley with a corridor-like structure, making it challenging for optimization algorithms to navigate. The primary goal when dealing with the Rosenbrock function is to find its global minimum, which is typically located at the point (1, 1) when specific constants are used. However, the presence of numerous local minima along the valley can lead optimization algorithms astray if not carefully handled.

2. Gradient-free algorithms

Gradient-free optimization, also known as derivative-free optimization (DFO), is a class of optimization techniques used to find the minimum or maximum of a function without relying on its gradient information. Traditional optimization methods often require knowledge of the function's gradient (a vector of partial derivatives with respect to each input variable) to guide the search for the optimal solution. However, gradient-free optimization methods do not make this assumption and are designed to work with functions that may be non-smooth, noisy, or computationally expensive to evaluate.

In gradient-free optimization, the primary goal is to find the optimal input values that minimize or maximize the objective function, typically by iteratively exploring the input space and adjusting the input values. These methods rely on various strategies, such as sampling points, approximating the function locally, or using heuristics to make informed decisions about where to search for the optimum. Among the several types of DFO algorithms, some are:

- *Random Search*: a straightforward method that randomly samples input values from the search space and evaluates the objective function. Over time, it accumulates information about the function's behaviour and refines the search [49].
- *Nelder-Mead Algorithm:* also known as the downhill simplex method, is an iterative optimization method that builds a simplex (a geometrical shape) in the input space. It then contracts, expands, or reflects the simplex to explore the space and converge towards an optimal solution [50]
- *Simulated Annealing:* a probabilistic optimization technique inspired by the annealing process in metallurgy. It explores the input space by accepting moves that reduce the objective function value, even if they occasionally increase it. Over time, it gradually decreases the acceptance probability, allowing it to escape local optima [51].
- *Genetic Algorithms:* optimization methods inspired by the process of natural selection. They keep a population of candidate solutions and iteratively evolve them through selection, crossover (recombination), and mutation operations. Genetic algorithms can handle both continuous and discrete search spaces [52].

- *Particle Swarm Optimization:* a population-based optimization algorithm inspired by the social behaviour of birds or fish. Particles in the population explore the search space, adjusting their positions based on their own experience and the experiences of their neighbours [53].
- *Bayesian Optimization:* a probabilistic optimization approach that builds a surrogate model (typically a Gaussian process) to approximate the objective function. It iteratively selects points in the input space based on the surrogate model's uncertainty to balance exploration and exploitation [54].

These gradient-free optimization methods are valuable in scenarios where the gradient of the objective function is unknown, expensive to compute, or noisy. They have applications in various fields, including machine learning hyperparameter tuning, engineering design, finance, and simulations. The choice of method depends on the problem's characteristics and computational resources available. However, the overall cost of gradient-free optimization is sensitive to the cost of the function evaluations because they require many iterations for convergence, and the number of iterations scales poorly with the number of design variables.

In the following the primary focus or emphasis is placed on the Genetic Algorithm (GA) among the various discussed.

2.1. Genetic algorithms

The classic Genetic Algorithm operates with a collection of candidate solutions that serve as representations for potential solutions to the optimization problem at hand. Each solution represents a possible candidate for achieving an optimum in the optimization problem. The chosen representation of these solutions plays a pivotal role because it dictates the selection of genetic operators. These representations typically take the form of lists of values and are generally founded on sets of symbols. When these representations involve continuous values, they are referred to as vectors, and when composed of binary digits, they are termed bit strings. In the case of combinatorial problems, solutions often consist of symbols that are present within a list. For instance, consider the representation of a tour for solving the traveling salesman problem.

Genetic operators come into play by generating fresh solutions within the selected representation and facilitating exploration within the solution space. The

encoding of a solution as a representation, which undergoes the evolutionary process, is commonly known as the genotype or chromosome.

2.1.1. GA working principles

The idea is to create the next generation (and the successive ones) in this way:

- Best individuals from the previous generation.
- Individuals resulting from the crossover of individuals with average performance.
- Individuals resulting from the mutation of individuals with mediocre performance.

The idea of the genetic algorithm was initially conceived by Turing in 1950 [X], who recognized the potential of possible optimization based on bio-evolutionary algorithms. The first successful implementation of a genetic algorithm was carried out by Holland in 1969 [X], and in the following years, efforts began to be made towards the integration of enhanced mechanics into the typical genetic algorithm.

Each individual is characterized by a specific set of parameters (finite values of variables).

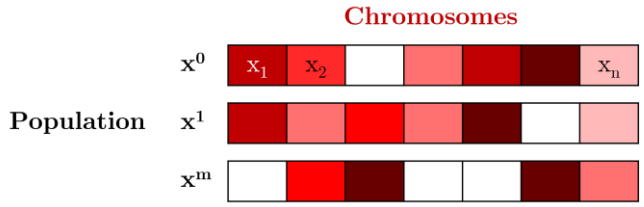

Fig. 2. 1. Individual encoding

For instance, if one were to optimize a heat exchanger, the relevant variables could be the material of the tubes, the diameter of the tubes, the number of tubes, etc. Each individual needs encoding in order to be evaluated and to enable the crossover and mutation functions to occur. One possible encoding is *direct vector* encoding [X], where the individual is identified through a vector containing the values of the variables as they are. An example of direct vector encoding is shown below:

Fig. 2. 2. Example of direct encoding

This method has the advantage of being direct and intuitive, but canonical operations such as crossover and mutation may be challenging to implement in the algorithm using this type of encoding. Therefore, *binary vector* encoding [X] is preferred, where each variable is converted into binary format based on the number of values the variable can take. For instance, if the tube diameter can assume four values (0.05, 0.08, 0.01, 0.02), two bits will be needed to represent the individual. If there are eight values, three bits will be required. In general, the number of bits required is equal to $log_2\ n$, where n is the number of values a single variable can assume.

The individual binary value associated with the individual real value will be assigned based on cardinality. In other words, considering this set of values (0.05, 0.08, 0.01, 0.02), the 0.05 value will be associated with the binary value 00, the value 0.08 with the value 01, and so on. This method, even though it is less intuitive and direct in implementation, offers significant advantages in facilitating crossover and mutation operations. Furthermore, it allows for the encoding of "non-numerical" values. For instance, using direct vector encoding does not allow to directly insert the material of the heat exchanger tubes (what numerical value would it take?), but one would need to insert all of its properties instead. However, through binary encoding, one can assign a binary number to each tube material, providing greater flexibility in optimization.

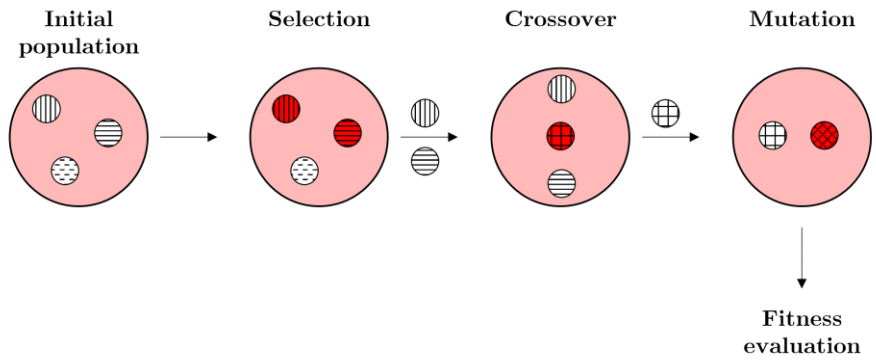

Fig. 2. 3. GA framework

2.1.2. Initial population

In a genetic algorithm (GA), the initial population is a crucial starting point for the evolutionary process. It comprises individual solutions, represented as chromosomes, which hold potential answers to the optimization problem being addressed. Here's an overview of how the initial population is typically established and selected in a GA. First, you need to decide on the size of the initial population, which is a user-defined parameter. This size can vary depending on the problem's complexity. A larger population size can enhance diversity but might also increase computational requirements. The order of magnitude of the population size have to be one order of magnitude higher than the number of design variables.

Next, you must choose how to represent potential solutions as chromosomes. Common representations include binary strings, integer arrays, real-valued vectors, or custom structures tailored to the specific problem domain. To create the initial population, individuals (chromosomes) can be generated *randomly*. Within each chromosome, values are chosen randomly from the problem's search space. This randomization helps ensure a diverse starting population.

Depending on the nature of the problem and optimization goals, various strategies can be employed to create the initial population. These strategies may include completely random selections (uniform random), leveraging domain-specific knowledge or heuristics (heuristic initialization), or starting with promising individuals from previous runs or expert guidance (seed population). In this frame, a suitable option to create initial population for GA is using latin hypercube sampling (LHS). It was initially developed to create a diverse distribution of parameter values from a multidimensional distribution and achieves this goal by ensuring that the sample points are arranged in a Latin square, meaning that each row and column contain only one sample.

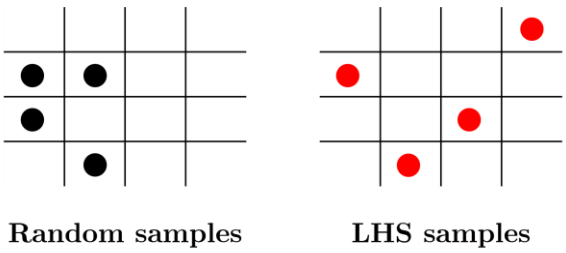

Fig. 2. 4. LHS principle

LHS's versatility becomes evident when it's applied to problems involving a multitude of dimensions. It generalizes the Latin square concept to handle an arbitrary number of dimensions effectively. When LHS is used to sample a function with k variables, it divides the range of each variable into n equally probable intervals. Subsequently, it selects n sample points in such a way that a Latin Hypercube is constructed. One of the key advantages of Latin Hypercube sampling is its ability to provide more efficient estimates of desired parameters compared to simple Monte Carlo sampling methods. This efficiency derives from the careful arrangement of sample points, which ensures that the exploration of the parameter space is systematic, diverse, and representative.

2.1.3. Selection

Among the various techniques used to establish the selection process, one of the most widespread is the *tournament selection*. It is designed to emulate the competitive dynamics of a tournament setting. Here's an outline of its operation. Initially, the tournament size is set as a user-defined parameter. This value dictates how many individuals participate in each tournament round, offering flexibility to adapt to the problem's nature and desired selection intensity. In each round of selection, a random subset of the population, comprising the specified tournament size, is assembled. This grouping, termed a "tournament," ensures that each individual is involved once and only once. Within each tournament, individuals compete based on their fitness scores. The individual with the highest fitness score (in the context of maximizing fitness) or the lowest fitness score (in minimizing fitness) is declared the tournament winner. The selected tournament champion assumes the role of a parent for the subsequent generation. This preference leans toward individuals with higher fitness scores, aligning with the fundamental principle of "survival of the fittest."

This iterative process repeats to choose multiple parents for reproduction, with the key point that each tournament operates independently. Consequently, the same individual may participate in multiple tournaments, offering numerous opportunities for selection. Tournament selection's appeal lies in its capacity to strike a balance between diversity and selection pressure while introducing an element of randomness into the selection process. This stochastic nature helps prevent premature convergence and promotes exploration of a broader solution space within genetic algorithms.

2.1.4. Crossover

The crossover operation involves the interaction between two individuals (parents) to generate a new individual (kid) with characteristics belonging to both parents. An example of crossover using binary vector encoding is as follows:

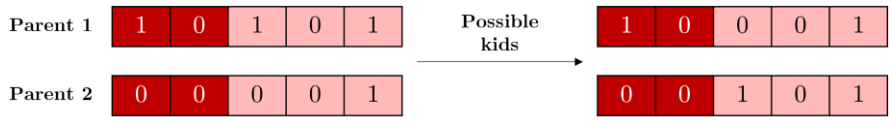

Fig. 2. 5. Example of crossover

The two parents can combine to generate a kid characterized by the first variable being the same as that of parent 1 and the second variable being the same as that of parent 2, and vice versa. Additionally, there are also combinations where crossover doesn't actually occur, so the kid will be identical to one of the two parents.

2.1.5. Exploring design space: mutation

In genetic algorithms (GAs), the mutation process is a fundamental genetic operator that introduces small, random changes into the genetic information of individuals (chromosomes) within the population. These changes help diversify the population and explore new regions of the solution space.

During mutation, a random subset of genes within an individual's chromosome is selected. Then, these selected genes undergo random alterations.

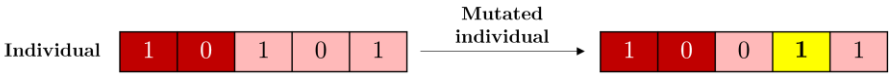

Fig. 2. 6. Example of mutation

The nature and extent of these alterations, such as flipping a bit in a binary representation or adding a small random value in a real-valued representation, are determined by the mutation rate, which is a user-defined parameter. Mutation serves as a vital source of genetic diversity in GAs, complementing other genetic operators like crossover. It helps prevent premature convergence by occasionally introducing novel genetic material into the population, enabling the algorithm to discover potentially better solutions. The mutation rate can be adjusted to control

the intensity of this diversification, striking a balance between exploration and exploitation.

2.1.6. Elitism

Elitism in a Genetic Algorithm (GA) is a strategy that ensures that the best-performing individuals from one generation are preserved and carried over to the next generation without undergoing any genetic operations like crossover or mutation. These top-performing individuals are often referred to as "elites." By preserving elites, GA aims to maintain the best solutions found so far and prevent them from being lost due to genetic operations that may introduce randomness or errors. Elitism helps improve the convergence and overall performance of a genetic algorithm by consistently keeping the best individuals in the population.

2.1.7. Convergence

The idea of the algorithm is to let the best individuals, those with a higher or lower objective function value depending on whether the problem is about maximization or minimization, "survive". These individuals will either be taken as they are or recombined with other individuals through crossover to form the next generation. However, this logic could present a drawback, which is the convergence towards local optima. Within the context of heat exchangers, if the best individuals all shared a common characteristic, *i.e.,* tubes material, for instance, aluminium, only that characteristic would continue. If there were combinations of variables that could make steel or copper heat exchangers efficient as well, they wouldn't be explored. Consequently, the inclusion of mutation within the algorithm is of fundamental importance to increase its variability and make the optimization as global as possible.

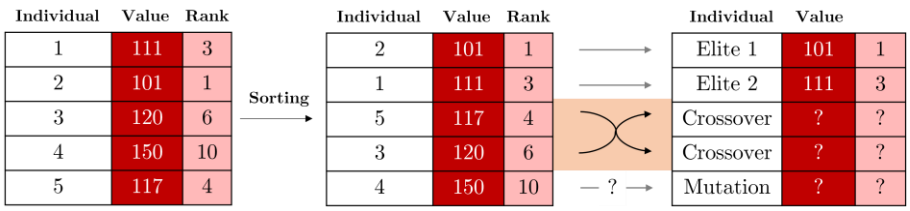

Fig. 2. 7. Sketch of GA evolution

As an example, the steps leading to the creation of a new generation from the previous one will be shown. In this case, the chosen population consists of 5 individuals, the problem requires the minimization of the objective function value, and the new generation will be composed of 40% elite individuals, 40% individuals derived from crossover, and 20% mutated individuals. The evaluation of the objective function is carried out using a fitness function, which is responsible for taking the parameters that make up the individual and evaluating it. After calculating the value of the objective function, a ranking operation must be performed to order the population. The next generation will then consist of the best individuals from the previous generation as they are, the intermediate individuals will undergo crossover, and the last individuals will undergo mutation. This is just one of many approaches. It is also possible to have only one individual undergoing mutation and three elite individuals, for example.

2.2. Multi-Objective Optimization

Multi-objective optimization (MOO) is a powerful mathematical and computational technique that addresses problems involving multiple, often conflicting, objectives. In the context of engineering and heat transfer, MOO is indispensable for finding optimal solutions that balance various competing goals. This chapter explores the concept of multi-objective optimization, with a focus on its relevance to heat transfer problems. Additionally, it introduces the concept of the Pareto front, which is a fundamental concept in MOO, and highlights the significance of MOO in addressing multi-physics problems in heat transfer.

In heat transfer applications, engineers often encounter problems where multiple objectives need to be considered simultaneously. Consider a heat sink design as an example. A generic task may want to simultaneously optimize the base temperature of the heat sink (to ensure efficient cooling) and minimize its weight (to reduce material costs and improve portability). These objectives are typically conflicting; decreasing the base temperature may require adding more material, which increases weight. Therefore, traditional single-objective optimization approaches are inadequate, as they prioritize one goal at the expense of others. Another common scenario is the trade-off between pressure drop and thermal resistance in a heat exchanger/microchannels design. Reducing pressure drop may require using larger flow channels, which in turn can increase thermal resistance. These competing objectives must be considered together to find an optimal design that suits the specific requirements of the application. In a general view, multi-objective optimization is particularly crucial in scenarios involving multi-physics problems, which regards

the interplay of multiple physical phenomena, such as fluid flow, heat conduction, and radiation, among others. By employing MOO techniques, it becomes possible to explore a vast solution space.

2.2.1. Pareto front/surface

Central to multi-objective optimization is the concept of the Pareto front/surface. The Pareto front represents the set of optimal solutions, where no single solution is superior to another in all objectives. Instead, each solution on the Pareto front represents a trade-off between the conflicting objectives. The term front is used when referring to a bi-objective analysis. Conversely, the term surface is used when three objective functions are involved (Fig. 2.8). Once a Pareto front has been defined, the solution space can be divided in two groups:

- *Dominated Solutions*: in a multi-objective optimization problem, a solution is said to be dominated if there exists another solution that is at least as good in all objectives and strictly better in at least one objective. Dominated solutions are not on the Pareto front and can be "virtually" eliminated. Dominated solutions are evidenced in red in Fig. 2.8.
- *Non-Dominated Solutions:* solutions that are not dominated by any other solutions are considered non-dominated and lie on the Pareto front. These are the optimal solutions that provide the best trade-offs between the competing objectives. Highlighted in blue in Fig. 2.8.

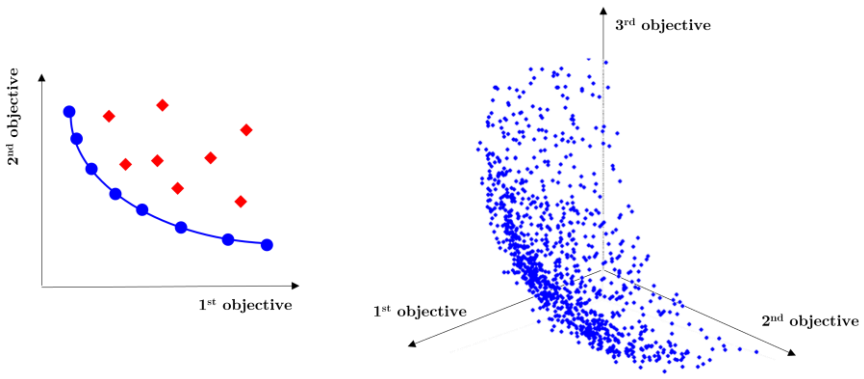

Fig. 2. 8. Pareto front for a two-objectives optimization (left); Pareto surface for a three-objective optimization.

3. Gradient-based algorithms

In the convergence of mathematics, computer science, and engineering, gradient-based optimization algorithms have emerged as indispensable tools that have redefined the landscape of complex system design and optimization. They serve as foundational components in contemporary computational methods, finding application across a wide spectrum of domains, including machine learning, neural networks, structural engineering, and finally – of our interest – heat transfer.

The focus on this kind of algorithms is motivated by the interest of converge on a specific allocation of such tools: topology optimization.

Indeed, these algorithms are characterized by their ability to unleash the potential of topology optimization – an avant-garde approach that changes the fundamentals of design. This chapter elucidates the fundamental principles of gradient-based optimization while elucidating their seamless integration into the world of topology optimization.

It is worth noting that topology optimization must not be seen as a sub-category of gradient-based optimization methods. Basically, among the various ways of solving the formulation of a topological problem, one of the most effective is to resort to the density-based method, which allows for the use of efficient gradient-based. Many mathematically rigorous and heuristic methods are available to address discrete combinatorial problems. Nonetheless, none of these methods are particularly suitable for dealing with problems involving thousands or even millions of variables, such as those commonly encountered in topology optimization. Criticisms of employing non-gradient discrete approaches in topology optimization can be found in [55].

3.1. Introduction

The primary concept behind gradient-based optimization methods involves the iterative refinement of a solution to a problem with the objective of minimizing or maximizing a given function. These techniques find applications in various domains, such as mathematical optimization, machine learning, and engineering. The central idea is to employ the gradient of the objective function, which is a vector of partial derivatives concerning the problem's variables, to guide the search for an optimal solution [56].

These methods start with an initial estimate of the optimal solution and update it iteratively. The update direction is determined by the negative gradient, which

points towards the steepest decrease (for minimization) or increase (for maximization) of the objective function. A parameter known as the learning rate controls the step size for each iteration. The optimization process continues until a predefined stopping criterion is met, such as reaching a specified number of iterations or achieving a minimal change in the objective function value. The goal is to obtain a solution at which the gradient becomes nearly zero, suggesting the algorithm has likely reached a local minimum (for minimization) or a local maximum (for maximization).

In essence, the core principle of gradient-based methods is to follow the direction indicated by the negative gradient in order to approach a local minimum or maximum of the objective function. This technique relies on the gradient as a guide, highlighting the direction in which the objective function changes most rapidly. Through a sequence of adjustments, the algorithm refines the solution iteratively, moving closer to an optimal point. It's important to acknowledge that gradient-based methods may not guarantee the discovery of the global optimum because they can become trapped in local minima or maxima based on the initial guess and the characteristics of the objective function. Nevertheless, they are favoured for their efficiency, particularly in cases of high-dimensional optimization problems where alternative methods like exhaustive search are impractical.

3.2. Topology optimization

Topology optimization is a computational design method that seeks to determine the best material distribution within a predefined design space, subject to certain constraints and objectives. The goal is to identify the optimal layout of materials to achieve the best performance of a structure or system while minimizing material usage [57]. This approach contrasts with traditional methods that focus on detailed geometric design and then analyse the resulting structure. In topology optimization, the design itself is part of the optimization process, and the outcome often leads to structures that exhibit complex and unconventional geometries.

3.2.1. A brief survey

Four decades ago, Bendsøe and Kikuchi introduced the topology optimization method, originally aimed at designing mechanical structures [58]. Over time, this

method has matured and found widespread use across various industrial and academic domains, including smart and passive material design, mechanism design, heat transfer devices, fluid flow systems and many other applications (see Fig. 3.1).

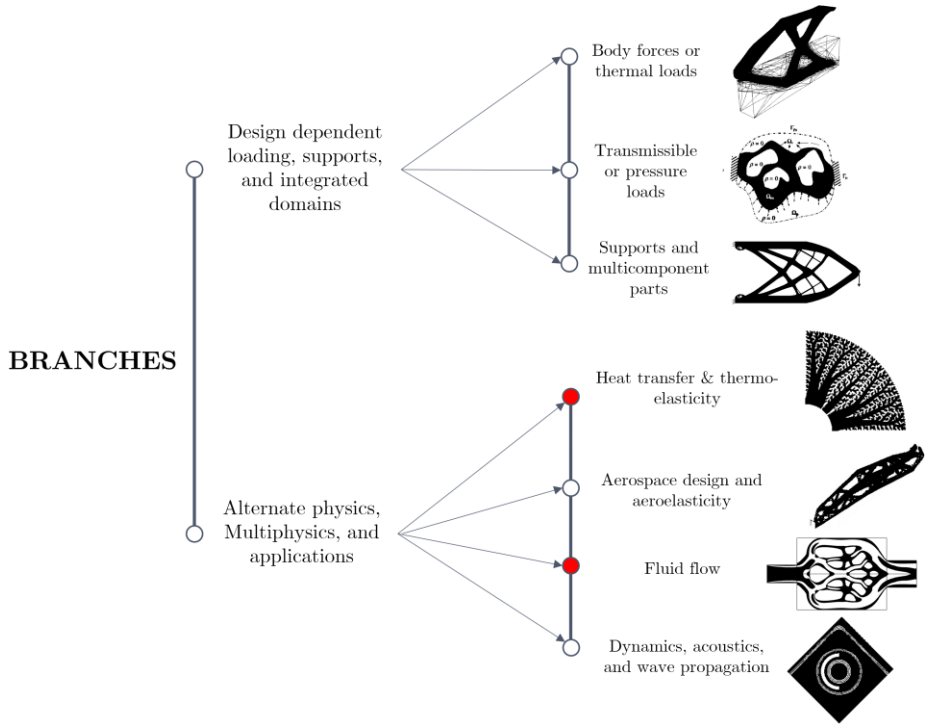

Fig. 3. 1. Some of topology optimization applications

In this discussion, we will delve deeper into topology optimization, explore its applications, and assess its suitability for smart materials design. At its core, a topology optimization problem can be defined as follows: distribute a specified amount of material within a design domain to maximize or minimize an objective function. For example, it may involve designing a load-bearing structure for maximum stiffness or minimum compliance, while keeping the weight within certain limits. The search for the optimal topology involves determining the most effective connectivity, shape, and number of voids or holes in the structure to extremize the objective function.

To initiate the topology optimization process, the design domain is divided into numerous elements. Each element can be either solid or void, effectively creating a pixels-based representation of the structure. However, this presents an ill-posed problem since finer mesh refinements yield more intricate solutions. Optimal structures, particularly in compliance optimization, consist of regions with infinitely fine microstructures [59]. To address this issue and accommodate composites with fine microstructures, the homogenization approach to topology optimization was introduced [60]. Notably, the technique has extended to three-dimensional problems and multiple material scenarios. A drawback of the homogenization approach is its tendency to produce structures with large "grey" regions, comprising perforated materials. This challenge can be mitigated by introducing penalties for intermediate densities.

An alternative to the homogenization approach is the Simple Isotropic Material with Penalization (SIMP) method [61]. Despite its ill-posed nature, the SIMP formulation is favoured for its ease of implementation in commercial finite element software and its flexibility in addressing advanced problems beyond compliance optimization. Well-posedness can be achieved by imposing constraints on density variations in the microstructure, such as perimeter constraints, local gradient constraints, or filtering approaches. Recent work has seen the SIMP approach applied to three-dimensional problems, nonlinear elasticity, plasticity, stress constraints, heat transfer, acoustics, among other applications. It's important to note that the references provided here are not an exhaustive list of the various intriguing applications of the topology optimization method that have emerged in recent years.

In the fields of heat transfer and fluid flow problems the main innovations have been presented in the last 20 years [62]. Some relevant contributions have been resumed in Tab. 3.1 (from 2010 to 2023).

Table. 3.1. Recent works on heat transfer and fluid flow problems

Title	Authors	Year
Topology optimization of heat sink in turbulent natural convection using k-ω turbulent model	Zhang *et al.*	2023
Design complexity tradeoffs in topology optimization of forced convection laminar flow heat sinks	Rogié *et al.*	2023
The influence of temperature dependent fluid properties on topology optimization of conjugate heat transfer	Qian *et al.*	2022
A review of topology optimisation for fluid-based problems	Alexandersen *et al.*	2020
Multi-objective and multi-load topology optimization and experimental validation of homogenized coupled fluid flow and heat transfer and structural stiffness	Francisco *et al.*	2020
Topology optimization of conjugate heat transfer systems: A competition between heat transfer enhancement and pressure drop reduction	Subramaniam *et al.*	2019

A "poor man's" approach for high-resolution three-dimensional topology optimization of natural convection problems	Pollini *et al.*	2019
Topology optimization of heat and mass transfer problems in two fluids-one solid domains	Tawk *et al.*	2019
Topology optimization of microchannel heat sinks using a two-layer model	Yan *et al.*	2019
Design of passive coolers for light-emitting diode lamps using topology optimisation	Alexandersen *et al.*	2018
A “poor man’s” approach to topology optimization of natural convection problems	Asmussen *et al.*	2018
A new interpolation technique to deal with fluid-porous media interfaces for topology optimization of heat transfer	Ramalingom *et al.*	2018
Topology optimization of a pseudo 3D thermofluid heat sink model	Haertel *et al.*	2018
Density based topology optimization of turbulent flow heat transfer systems	Dilgen *et al.*	2018
Investment casting and experimental testing of heat sinks designed by topology optimization	Lei *et al.*	2018
Design of Thermal Systems Using Topology Optimization	Haertel *et al.*	2018
A “poor man's approach” to topology optimization of cooling channels based on a Darcy flow model	Zhao *et al.*	2018
Topology optimization of heat and mass transfer in bi-fluid laminar flow : application to heat exchangers	Tawk	2018
Topology Optimization of Turbulent Flows	Dilgen *et al.*	2018
A review about the engineering design of optimal heat transfer systems using topology optimization	Dbouk	2017
Heat Exchanger Design with Topology Optimization	Manuel *et al.*	2017
A fully developed flow thermofluid model for topology optimization of 3D-printed air-cooled heat exchangers	Haertel *et al.*	2017
Topology optimization for heat conduction using generative design algorithms	Lohan *et al.*	2017
Topology optimization of a coupled thermal-fluid system under a tangential thermal gradient constraint	Qian *et al.*	2016
A level-set method for steady-state and transient natural convection problems	Coffin *et al.*	2016
Industrial application of topology optimization for combined conductive and convective heat transfer problems	Zhou *et al.*	2016
Level set topology optimization of cooling and heating devices using a simplified convection model	Coffin *et al.*	2016
Topology optimization for turbulent flow with Spalart-Allmaras model	Yoon	2016
Topology optimization in thermal-fluid flow using the lattice Boltzmann method	Yaji *et al.*	2016
Efficient topology optimisation of multiscale and multiphysics problems	Alexandersen	2016
Large scale three-dimensional topology optimisation of heat sinks cooled by natural convection	Alexandersen *et al.*	2015
A topology optimization method for a coupled thermal–fluid problem using level set boundary expressions	Yaji *et al.*	2015
Topology Optimization, Additive Layer Manufacturing, and Experimental Testing of an Air-Cooled Heat Sink	Dede *et al.*	2015
Levelset-XFEM Topology Optimization with Applications to Convective Heat Transfer	Coffin	2015
Topology optimisation for natural convection problems	Alexandersen *et al.*	2014

Topology Optimization of Heat and Mass Transfer Problems: Laminar Flow	Marck *et al.*	2013
Development of heat sink device by using topology optimization	Koga *et al.*	2013
Topology Optimisation for Coupled Convection Problems	Alexandersen *et al.*	2013
Topology optimization for fluid–thermal interaction problems under constant input power	Matsumori *et al.*	2013
Adjoint-based constrained topology optimization for viscous flows, including heat transfer	Kontoleontos *et al.*	2013
Topological design of heat dissipating structure with forced convective heat transfer	Yoon	2010

3.2.2. Density-based formulation

In the context of the density approach, the typical solution for the topology optimization problem described above involves subdividing the domain into a substantial number of finite elements. The density distribution is then represented using N element or nodal design variables, and the problem can be formulated as:

$$\begin{cases} min: F\ u\ \gamma\ ,\gamma\ =\ \sum_i\ \int_{\Omega_i} f\ u\ \gamma_i\ ,\gamma_i\ dV \\ s.t.: \begin{matrix} G_0\ \gamma = \sum_i\ v_i\gamma_i - V_0 \le 0 \\ G_j\ u(\gamma\ ,\gamma) \le 0, \quad j{=}1,\ldots,M \\ 0 \le \gamma_i \le 1, \quad i{=}1,\ldots,N \end{matrix} \end{cases} \tag{3.1}$$

where γ is the design variable vector, whose length is N.

The key idea behind the topology optimization method is to turn the challenge of topological design into a material distribution problem. As aforementioned, the density approach [57] is performed discretizing the domain and introducing a design variable (γ). With reference to a conjugate problem that involves heat transfer and fluid flow, the fundamental goal is to figure out how solid and fluid domains are distributed with respect to trivial solutions, *i.e.,* vertical dividers. The value of the design variable in each cell changes independently according to the governing equations and constraint conditions during the iterative process of topology optimization. This can cause a significant variance in the value of design variables in adjacent cells, *i.e.,* checkerboard effect [63]. Meanwhile, oscillatory, and non-convergent solutions in the calculation process of conjugate heat transfer may result from the correlation between design factors and material properties generated by interpolation. A density filter [57] is implemented to filter the design in order to overcome

the problems outlined above. This process is realized by including a Helmholtz-type partial differential equation, which can be expressed as:

$$\gamma = r^2 \nabla^2 \gamma + \gamma \tag{3.2}$$

where, γ is the mathematical design variable, $\tilde{\gamma}$ is the smoothed scalar function, and r is the filter radius. In the filtered design variable, there may be large zones with intermediate values. This makes the optimization problem easier to solve, but the design may rely on areas with nonphysical qualities due to intermediate values. These areas can then be reduced using a projection operation based on the hyperbolic tangent function [64]:

$$\gamma = \frac{\tanh[\beta\ \gamma - \eta\ ] + \tanh(\zeta\eta)}{\tanh[\beta\ 1 - \eta\ ] + \tanh(\zeta\eta)} \tag{3.3}$$

where, γ is the output material volume factor while, η is the projection point, and β the projection steepness. An example of how projection works is provided in Fig. 3.2 and Fig. 3.3. In detail, Fig. 3.2 describes both effects of varying the steepness and the projection point.

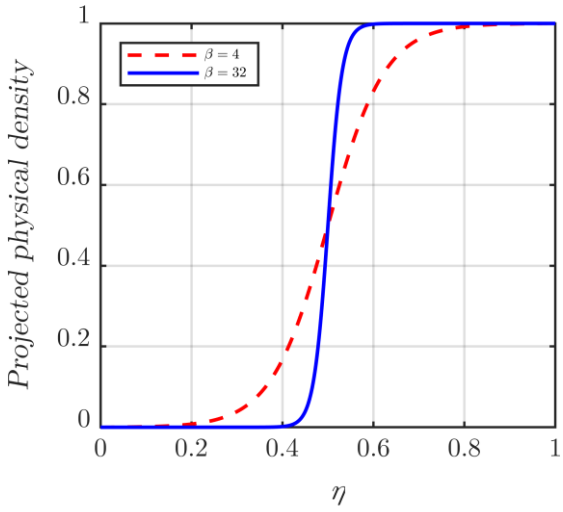

Fig. 3. 2. Heaviside projection: effect of varying the projection steepness

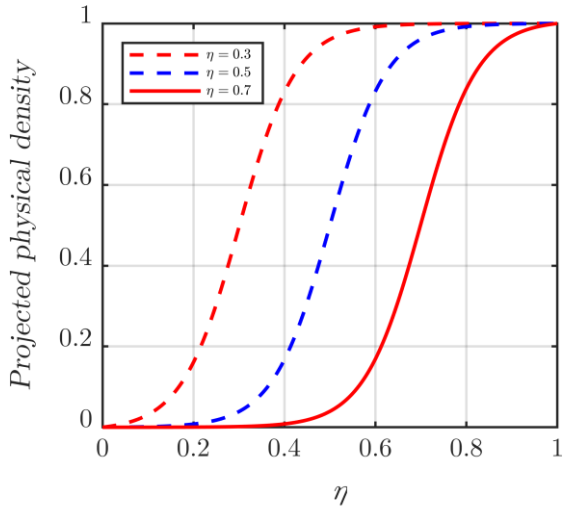

Fig. 3. 3. Heaviside projection: effect of varying projection point

The first parameter strongly penalizes intermediate values since it forces the design variable to be 0 or 1. As β increases, the regions of fully solid/liquid increase. Conversely, Fig. 3.3 shows the effect of varying the projection point η from 0.3 to 0.7. When referring to governing equations for coupled fluid flow and heat transfer problems, thermal conductivity and fluid impermeability are dependent on the design variable γ. The way these variables are linked to the design is expressed through interpolation schemes. In this frame, the RAMP one, *i.e.,* Rational Approximation of Material Properties, is the more reliable one [65]. The aim is to regulate the distribution of the fluid and solid domains by manipulating local impermeability of the medium – referring to $s(\gamma)$ – and the conductivity – referring to $k(\gamma)$. In detail, the following functions are set as thermal conductivity ratio and spatially variable Brinkman permeability, respectively [66]:

$$k(\gamma) = 1 + (C_k - 1)\frac{1-\gamma}{1+q_k\gamma} \tag{3.4}$$

$$s(\gamma) = s_{max}\frac{1-\gamma}{1+q_s\gamma} \tag{3.5}$$

in which q_k and q_s are parameters specifying the steepness of interpolation functions, and s_{max} is the maximum inverse permeability. The value of the impermeability within the solid region should theoretically approach infinity. However, the greater this value is, the more unstable the simulation becomes.

Depending on the approach used in varying the values of the penalizing factors, the final design consequently changes as convective or diffusive transport is facilitated or not. Referring to a problem that involves natural convection, *e.g.,* recirculation due to buoyancy forces in a rectangular cavity, varying the Ra implies changing the velocity magnitude. Both factors that affect the impermeability play a fundamental role on penalizing the fluid flow in the solid regions and avoid altering the velocity magnitude in the fluid ones. While varying the Rayleigh number, values that affect the inverse permeability, *i.e.,* s_{max} and q_s have to be properly changed in order to adapt to different Ra. Higher Ra needs stronger penalization. The way s_{max} and q_s influence the final inverse permeability value is described in Fig. 3.4.

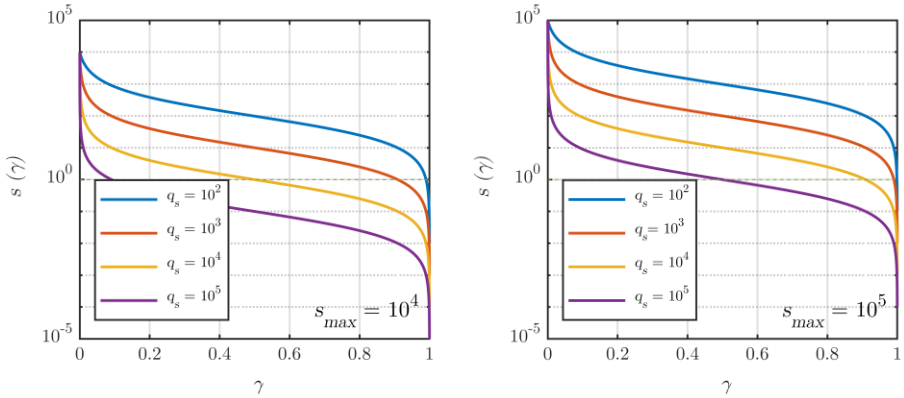

Fig. 3. 4. Effect of varying impermeability parameters

This figure shows what happens by changing the s_{max} from 10^4 to 10^5, while varying q_s in the same range. In detail, as the q_s increases, so the overall value of $s(\gamma)$ decreases, while increasing the value of s_{max} by one order of magnitude leads to a corresponding overall shift of all curves. A further relation between the design variable γ and the properties of the material and more diffuse way to interpolate material properties for heat conduction problems, is usually given by a SIMP (Simplified Isotropic Material with Penalization), as follows:

$$k(\gamma) = k_{min} + (k_0 - k_{min})\gamma^p \tag{3.6}$$

where p is the penalty factor and k_0 describes the material thermal conductivity of the solid, and k_{min} of the void/air/fluid.

3.2.3. Controlling length scale

Controlling length scale is a fundamental aspect of topology optimization that significantly impacts its efficiency, feasibility, and effectiveness. The ability to manipulate the size and distribution of structural features within a design space enables engineers to strike a balance between theoretical optimality and practicality. This control ensures that the optimized designs are not only superior in terms of performance but also manufacturable, adaptable, sustainable, and reliable.

Robust formulation

Resorting the robust formulation, the coefficient η determines the threshold level. For $\eta = 0$, the projection corresponds to the original Heaviside projection concept, for $\eta = 1$ we have the modified Heaviside projection concept and for $\eta = 1/2$ we have the volume preserving projection concept [67]. The robust formulation makes use of three separate projections in each design step; hence η is replaced with the three values 1 - η, 0.5, η with η [0; 0:5] denoting the eroded, the blue-print and the dilated design, respectively. The coefficient b affects the degree of discreteness of the smoothed Heaviside function. Defining as b the minimal design scale, r the Helmholtz filter radius, R the original filter radius, and h the maximum mesh element size, the minimal width ratio (b/r) for different value of the projected threshold η can be derived analytically [68] and represented as follows:

$$\eta_e = \begin{cases} \frac{1}{4}\left(\frac{b}{R}\right)^2 + \frac{1}{2} & \frac{b}{R} \in [0,1] \\ -\frac{1}{4}\left(\frac{b}{R}\right)^2 + \frac{b}{R} & \frac{b}{R} \in [1,2] \\ 1 & \frac{b}{R} \in [2, +\infty] \end{cases} \tag{3.7}$$

Eq. (3.7) is useful for design where, for a desired minimal width b and a given filter radius r, one wants to find the corresponding η. The corresponding plot is presented in Fig. 3.5.

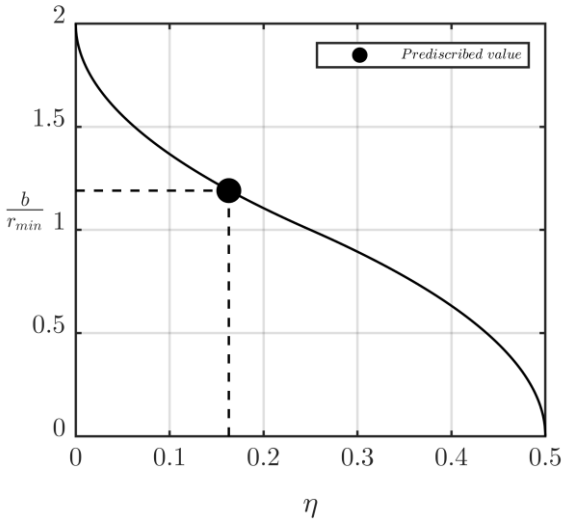

Fig. 3. 5. The η versus b/R curve, useful for design

This approach combined with the filtering implies that for high values of b, the density of the central element is set to 1 if there is at least one element in the neighbourhood which has a density greater than 0.

If this approach is applied to a basic heat transfer problem, i.e., heat conduction, it can prove to be very effective and even computationally acceptable. For instance, referring to conduction in a rectangular domain, subjected to a uniform heat rate, *i.e.,* Q_0, a Dirichlet boundary condition on a portion of the bottom surface, and thermally insulated on remaining surfaces. This implies that only half of the original design space is optimized. A sketch of the design domain is presented in Fig. 3.6.

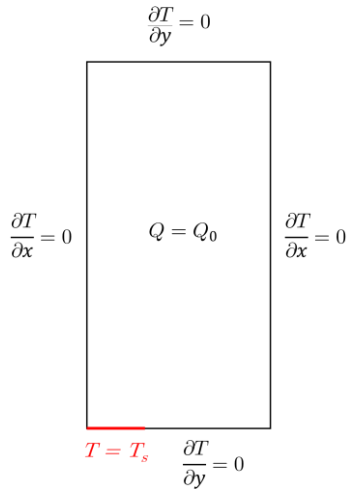

Fig. 3. 6. Heat conduction problem

Parameters used for the resolution of the optimization problem are the following: the height of the domain is equal to 10 cm, the thickness of the boundary with the Dirichlet condition is 1.5 cm. The number of elements on the x direction is 20. The mesh size is then computed as the height divided by the number of elements. The volume fraction is set to 0.5. The steepness parameter for the projection is varied through a continuation scheme. The projection point is set to 0.5. As regard the interpolation scheme for thermal conductivity, the solid one is set to 100, while the void one is set to 10^{-2}. The exponent for the SIMP function is set to 3. Finally, the wall temperature is set to 20 °C and the heat source to 50 W. For the resolution of the robust formulation, three relaxations have been considered, *i.e.,* $\eta = 0.3$, $\eta = 0.3$, and $\eta = 0.3$. This means that we expect for three length scale, and the amount of solid material decreases as η increases.

The optimization problem can be expressed as follows:

$$
\begin{cases}
\underset{\rho}{min} \quad \max\left(f\left(\gamma^e\ \gamma\ \right), f\left(\gamma^e\ \gamma\ \right), \left(\gamma^e\ \gamma\ \right)\right), \\
f = \frac{1}{A}\int_\Omega\ T\ \mathrm{d}\Omega \\
s.t.: \begin{cases}
\boldsymbol{R}(\boldsymbol{u}^e(\gamma^e\ \gamma\ ), (\gamma^e\ \gamma\ )) = 0 \\
\boldsymbol{R}(\boldsymbol{u}^i(\gamma^i\ \gamma\ ), (\gamma^i\ \gamma\ )) = 0 \\
\boldsymbol{R}(\boldsymbol{u}^d(\gamma^d\ \gamma\ ), (\gamma^d\ \gamma\ )) = 0 \\
V(\gamma^d\ \gamma\ ) \leq V_f \\
0 \leq \gamma \leq 1
\end{cases}
\end{cases}
\tag{3.8}
$$

The physical material densities are found from a Heaviside projection of the filtered variable field with the different threshold values corresponding to the three different design realizations, *i.e.,* eroded, intermediate and dilated. It has been pointed out that, due to the unique physics of the problem, the "eroded design" is known to result in the highest heat sink temperature, primarily because it has less surface area than other designs. This prior knowledge allows to avoid the entire "min-max formulation" and simplifies the process by solving the state problem once, using the eroded design's density for thermal conductivity calculations [68]. In order to show the effect of varying the projection steepness, simulations are performed by ramping this value from 1 to 32, and results are presented in Fig. 3.7, for all relaxations. In detail, presented design are the final one at each continuation step.

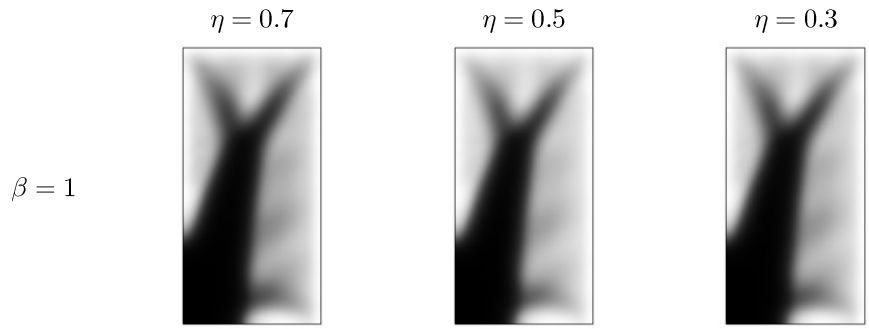

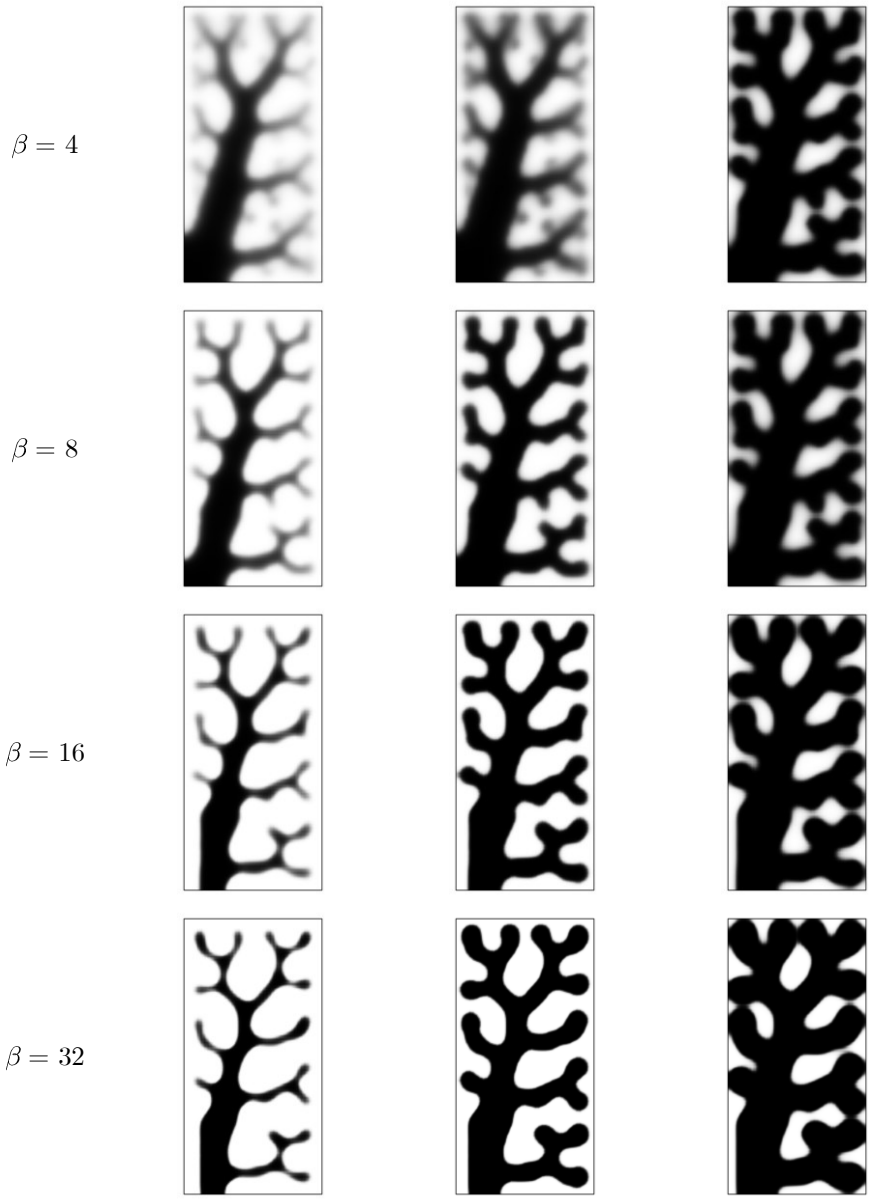

Fig. 3. 7. Robust design of heat conduction problem

The effect of using robust formulation, the evolution with iterations of the objective and volume fraction is presented.

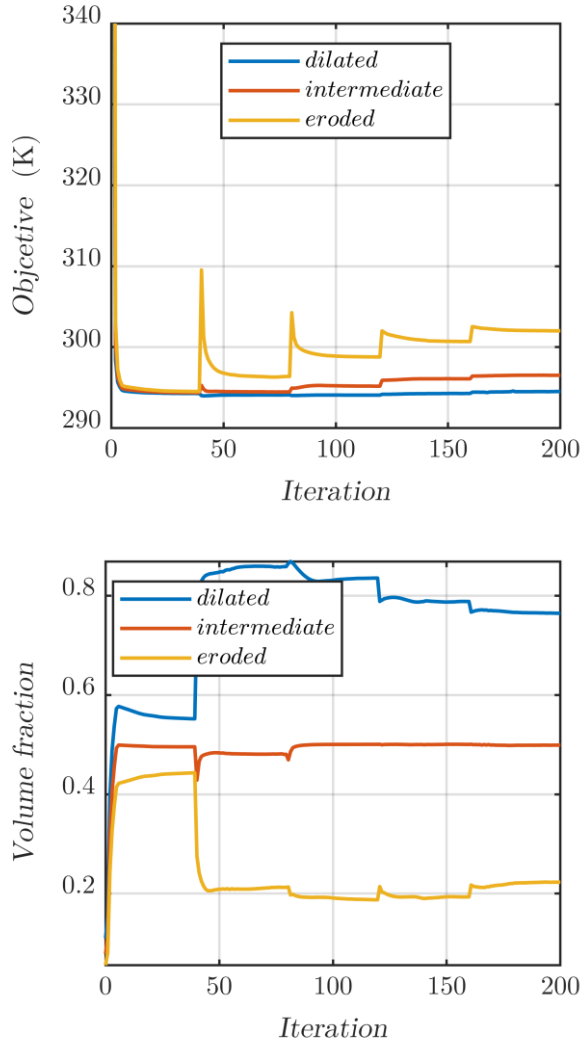

Fig. 3. 8. Evolution of the objective function (above), and volume fraction (below)

One can see how the performance of the dilated one outperforms the others because of the higher amount of material. Furthermore, looking at the history of

the volume fraction is clear that this method allows to perfectly control the amount of material for the intermediate design, ensuring the minimum length scale.

Geometrical constraints

Robust formulation is a powerful tool to control length scale. However, when the state problem become more intricate than the simple heat conduction one, it becomes difficult and sometimes unfeasible to solve three times that problem. Therefore, it may be useful to pursue different paths, *e.g.,* to impose the prescribed length scale using geometrical constraints [69]. These constraints are g_s and g_v, defined for the solid and void fractions, respectively, are dependent on the definition of two indicators, I_s and I_v.

$$\begin{aligned} g_s &= \frac{1}{n}\sum_{i\in\mathbb{N}} \gamma\ e^{-c\cdot|\nabla\gamma|^2}\cdot[\min\{\ \gamma_i-\eta_e\ ,0\}]^2=0 \\ g_v &= \frac{1}{n}\sum_{i\in\mathbb{N}} (1-\gamma)\ e^{-c\cdot|\nabla\gamma|^2}\cdot[\min\{\ \eta_d-\gamma_i\ ,0\}]^2=0 \end{aligned} \tag{3.9}$$

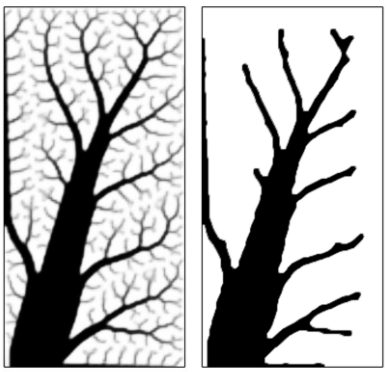

Fig. 3. 9. Imposing length scale control on heat sink branches

It is worth noting that this approach is effective when the geometry constraint is activated at the end of the continuation scheme. The reason is linked to the effect of the constraint magnitude on the algorithm convergence. Indeed, if the constraint is working while parameters like β are still ramping, the method does not work well.

Therefore, while robust formulation requires for solving 3 times the problem – causing a noticeable increase of computational burdens – controlling length scale can be seen as a post-process operation.

3.2.4. Controlling overhang

Overhangs refer to regions of a design where material extends horizontally or at angles that are unsupported from below. These features can pose significant challenges during manufacturing and assembly processes. Overhang control in topology optimization is highly significant for several compelling reasons. First and foremost, overhangs can create manufacturing challenges, as they often necessitate additional support structures and can be difficult to produce using traditional methods. Moreover, the rise of additive manufacturing technologies, such as 3D printing, has accentuated the importance of managing overhangs, as many 3D printers struggle with printing materials in unsupported positions.

Another critical aspect is the impact on material usage. Overhanging regions often require excess support material, leading to inefficient material consumption. Reducing overhangs can result in both cost and time savings, as it minimizes the need for support structure design and implementation.

Gradient based integral approach

As regards the overhang formulation, in this section we investigate the control of the directional gradient of the density field, avoiding the requirement for a priori knowledge of the boundary location and slope [70]. The density gradient is then converted into a single constraint using a Heaviside projection-based integral formulation to effectively limit it over every location in the design domain. In detail, this requires the definition of a normalized build direction (b), *i.e.,* vertical one, and the filtered density field (ρ). The projected perimeter then results from the integration over the domain of the product of the directional gradient and the Heavisided directional gradient. The directional gradient $\mathbf{b} \cdot \nabla \rho$ assumes positive and negative values on the resulting design boundaries and zero values where the design field is 0 (solid) and 1 (air). The Heavisided directional gradient ($H\ \mathbf{b} \cdot \nabla \rho$ changes from 0 to 1 depending on whether directional gradient is lower or larger than 0. This means that the product between these latter results in a field where only regions with positive $\mathbf{b} \cdot \nabla \rho$ are higher than 0, while the remaining zones, for which the directional gradient is greater or less than 0 will be characterized by a null value. Therefore, zones with positive $H\ \mathbf{b} \cdot \nabla \rho\ \mathbf{b} \cdot \nabla \rho\ \mathrm{d}\Omega$ are

accounted in the integration over the domain and effectively affect the undercut perimeter evaluation. To use this approach to control the slope with respect to an overhang angle (α), the Heaviside function is manipulated forcing the transition of the density filed occur at cos(α). Moreover, the directional gradient is normalized, such that the final projected perimeter can be evaluated as:

$$P = \iint H\left(\mathbf{b}\cdot\frac{\nabla\rho}{||\nabla\rho||_2} - \cos(\alpha)\right)\mathbf{b}\cdot\nabla\rho\ \mathrm{d}\Omega \tag{3.10}$$

By doing this, angles – resulting from the directional gradient – lower than α are accounted in the summation (have a cosine higher than the threshold value), otherwise are ignored.

An example of using this methodology, applied to heat conduction, is provided in Fig. 3.10. The angle is varied such that the cosine assumes values of 0.15 and 0.30.

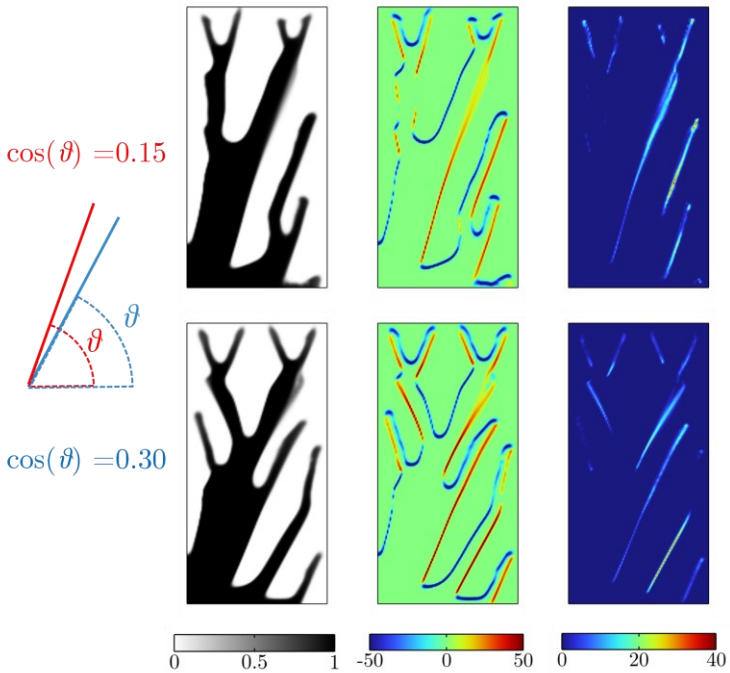

Fig. 3. 10. From left to right: design field, directional gradient, projected undercut, for different cosine of overhang alngles

Design fields clearly show how the soldi material branches develop without violating the imposed constraint.

Overhang and length scale

At this point, one can decide to combine the formulation used to control the overhang and the one used to impose a minimum length scale. The two approaches are not conflicting. The reason has already been mentioned: using geometric constraints act like a post process operation, while the overhang control is involved in the optimization process. The final result of combining these two approaches is shown in Fig. 3. 11.

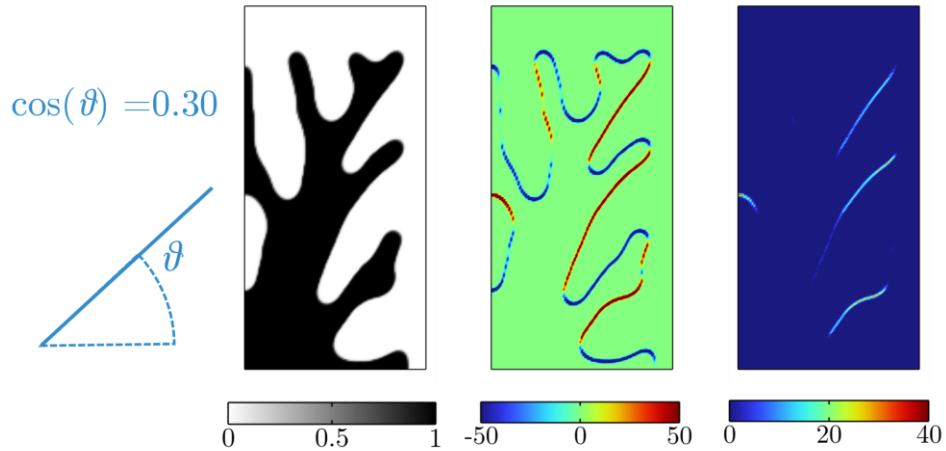

Fig. 3. 11. Combining geometric constraints for minimum length scale and overhang control

Despite these techniques work well together, it is worth noting that the problem solved is relatively simple. Therefore, this approach is not always feasible: satisfying multiple constraints simultaneously with complex physics become challenging. New approaches can be explored.

Nonlinear virtual thermal method

The nonlinear thermal problem introduces a new temperature (T_{NVTM}) – different from the one that solves the convection-diffusion process – which allows to define a temperature distribution that is uniform in the area covered by enclosed

voids [71]. By doing this, after a series of manipulations, a new constraint (C_1) is introduced:

$$C_1 = \log_{10}\left(\sum_{e=1}^{N_e} \frac{\gamma_e}{N_e}\right) + f \leq 0 \tag{3.11}$$

where the sum is made with respect to all elements number (N_e) and such that the logarithm summed to a relaxation parameter (f) is lower or at least equal to zero. Despite the robust formulation would require for the solution of three finite element problems, evaluating the governing equations for the eroded design while imposing the volume constraint on the dilated one allows for solving the current state problem only once [67]. Finally, a volume constraint on the allowed solid fraction is introduced as follows:

$$C_2 = \frac{\int_\Omega \varphi_d \, \mathrm{d}\Omega}{\int_\Omega \mathrm{d}\Omega} - V_{max} \leq 0 \tag{3.12}$$

As previously done, a practical example to show the effectiveness of this method is proposed. In detail, the problem is always about heat conduction, and the angle is varied as shown in Fig. 3.12. The volume fraction is set to 0.5 and boundary conditions are set as shown in Fig. 3.12., The aim is to show how the slope of the solid material path changes depending on the imposed constraints.

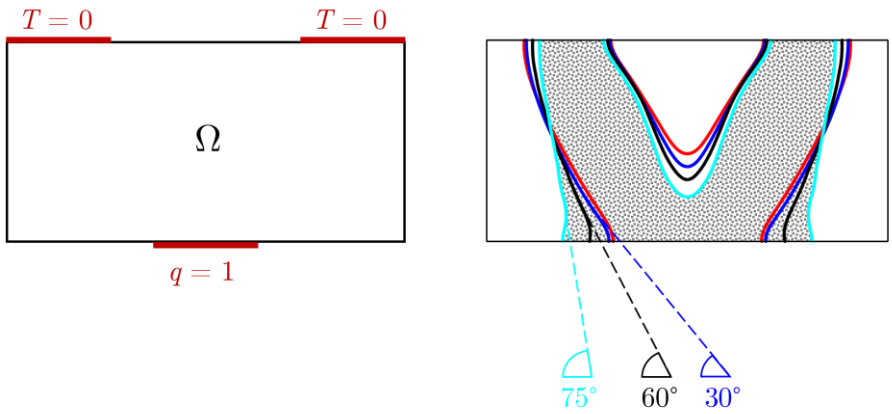

Fig. 3. 12. NVTM example: heat conduction with different overhang angles

The introduction of the aforementioned constraints defines a challenge for the algorithm convergence, as visible in Fig. 3.13. In order to satisfy all constraints the objective value drastically changes, and then once they have been fulfilled, the objective returns to values similar to those obtained without constraint.

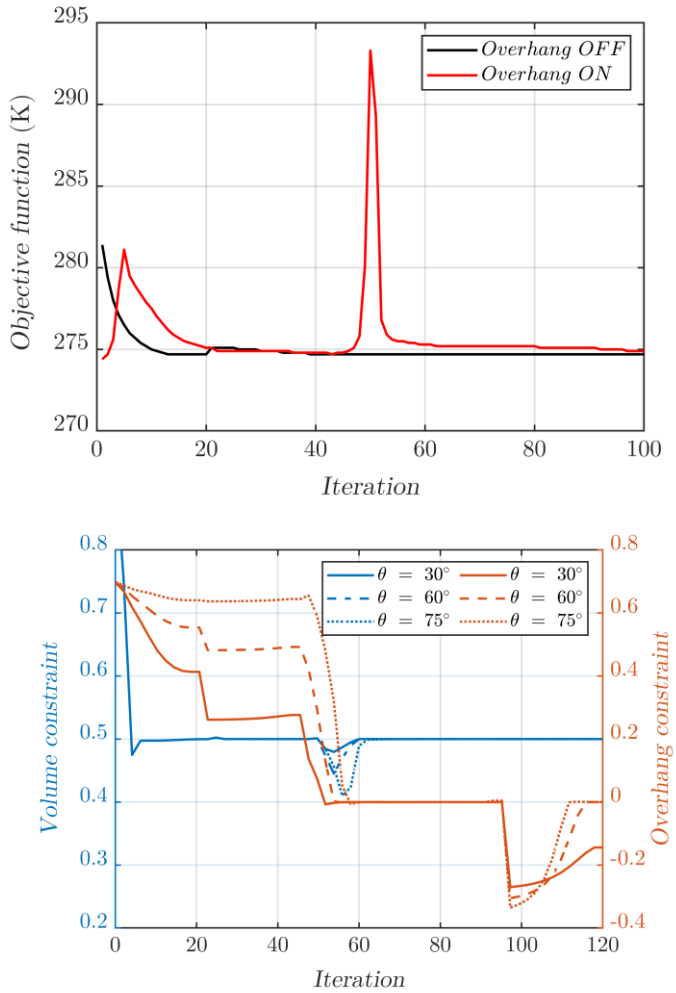

Fig. 3. 13. NVTM: evolution of objective function and constraints with iterations

As previously done, the so-called robust formulation can be used to face the design challenge while avoiding minor features and guaranteeing fixed length scales. Numerical experiments show that the robust filtering concept, which involves optimizing for three different design realizations, *i.e.,* the intermediate (φ_i) design as well as the

eroded (φ_e) and dilated (φ_d) realizations, yields an intrinsic penalization of grey areas, *i.e.,* intermediate design values, to ensure strict control of both solid and void length scales. Robust formulation can be coupled with the overhang restrictions to achieve self-supported enclosed voids, exploiting the overall concept of restricting the length of the overhang interface in enclosed voids and forcing it to be zero is here used. Thus, the nonlinear virtual temperature method (NVTM) is applied to discriminate between enclosed and open voids [71]. Two design variables (ϑ and φ), two filtering and three projection processes are used to satisfy length scale and overhang constraints (Fig. 3.14). See [71] for more details on the methodology.

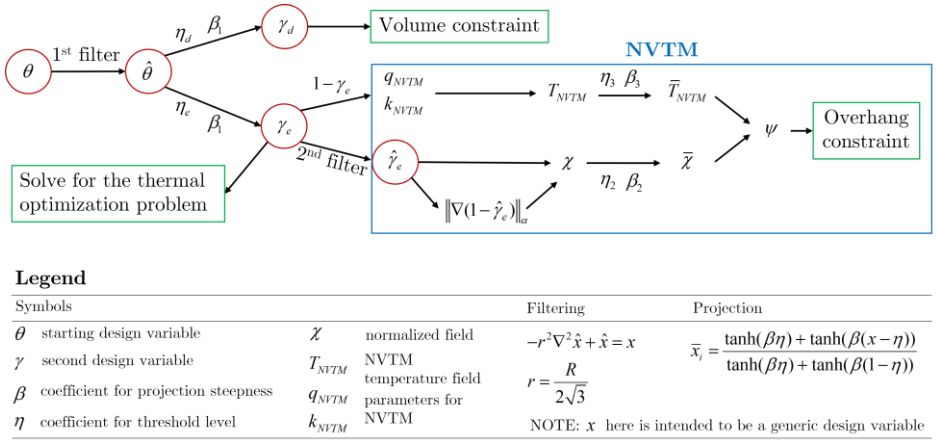

Fig. 3. 14. Summary outline of the methodology to couple TO with NVTM

Therefore, for instance, in the view of an optimization problem that aims at reducing heat transfer across a finite temperature difference, the statement can be formulated as follows:

$$\begin{cases} \min\limits_{\varphi \in \mathfrak{R}^n} & Q/\,\Delta T \\ s.t. & \begin{cases} C_1 \le 0 \\ C_2 \le 0 \end{cases} \end{cases} \tag{3.13}$$

Notably, for stability reasons, the objective function should be computed as the magnitude of the heat flux over the design domain, scaled by the applied different temperature, and it is proportional to the wall thermal conductance K. If

performing TO using COMSOL Multiphysics and optimizing using the Method of Moving Asymptotes (MMA) [72], a continuation approach is applied on projection sharpness coefficients β_1, β_2, and β_3 referred to the design projection and NVTM, respectively. In detail, β_1 is updated six times from 1 to 12 each 20 steps, while β_2 and β_3 from 16 to 32. Conversely, the parameters of the interpolation functions are fixed to $n = 4$, $q_a = 1000$ and $a_{max} = 10^6$. The domain is discretized with a total amount of 22500 cells. The effective filer radius (R) is 10 times the mesh size. Parameters involved in the NVTM are the same implemented in [71]. The eroded design is obtained for $\eta_e = \eta - \Delta\eta$ while the dilated one for $\eta_d = \eta + \Delta\eta$, where $\Delta\eta$ in this work is chosen to be 0.2. The overhang angle is selected to be equal to 15° [73], which implies that the cosine of the overhang angle must not exceed the value of 0.966. Finally, the relaxation parameter f is fixed equal to 1.

The optimization starts with a 0.6 volume fraction of solid in the design domain. Fig. 3.15 shows the evolution of the design along the optimization process and highlights the detail on the effectiveness of the robust formulation in controlling the length scale. From the first iterations, two main branches take place from the lower part of the wall, proceeding approximately parallel to the outer panels. Thus, natural convection is readily impeded. At the 20th iteration, it can also be seen that, due to the limitation imposed on the overhang, there is a detachment between the two branches at the bottom, which then causes a further central branch appearing in the following steps.

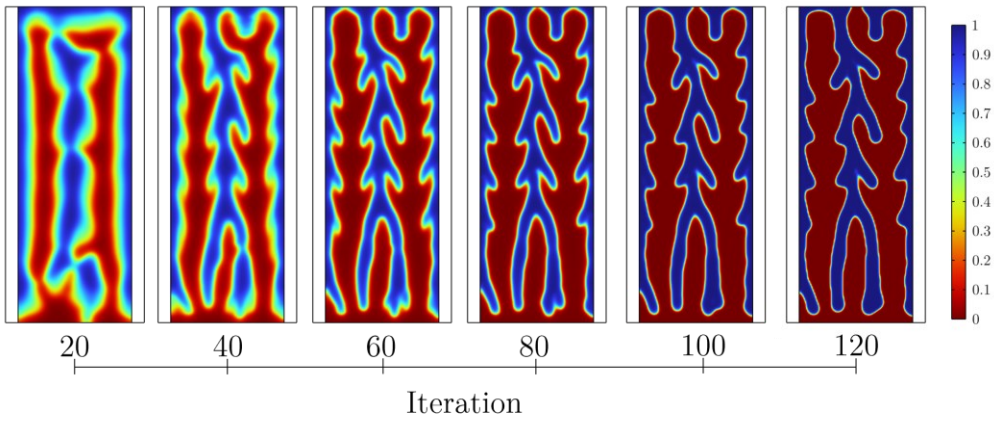

Fig. 3. 15. Design field history (intermediate relaxation) of the 3DPW (0 is solid)

The increase in the coefficients of projection steepness leads to a gradual elimination of the intermediate densities, with a gradual reduction in the thickness of the various branches. Of particular interest is the behavior at the base and top of the wall: in fact, although the objective function seeks a reduction in total heat transport, which includes conductive heat transfer, a layer of cementitious material forms at the base of the wall itself, acting as a bridge for heat transmission. At the top, on the other hand, there is a gradual interruption of the recirculation motion due to an extension of the right branch. This results in a restriction of air circulation and consequently better insulation. Generally, the TO design tends to create vertical barriers – as in the second baseline design – but with the possibility of deflecting the air path and thus reducing its speed.

The history of constraints is examined in Fig. 3.16 so that the design evolution presented in Fig. 3.15 may be completely understood. The history plot effectively illustrates that the problem is affected by an infeasible starting configuration, which results in the first 20 cycles being used to achieve the desired volume. Then the objective slowly decreases until the 80^{th} iteration. At this point the effort of matching constraints translates in jumps in the objective.

As can be seen from Fig. 3.16 the overhang constraint is not fully satisfied, *i.e.,* decreases too slowly to become less than 0. This confirms the outcomes of Fig. 3.15, where in the lower parts all designs satisfy the limit of 15° angle, while the upper right part violates the overhang.

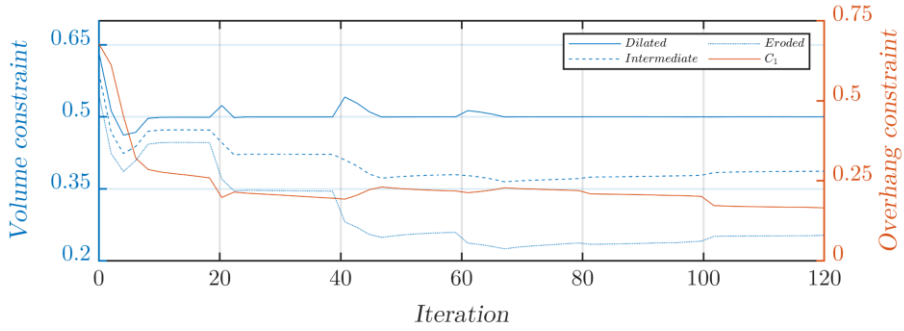

Fig. 3. 16. Constraints evolution: jumps occurs each update of continuation steps

Part III: Specific applications to Heat Transfer problems

Efficient heat transfer devices are at the heart of numerous engineering applications, from small-scale electronics to large-scale industrial processes. Optimizing these devices is a complex task that demands a sophisticated approach, one that is sensitive to the size of the system being analysed and the specific heat transfer mechanisms in play. In this section, we embark on a comprehensive exploration of some examples about optimizing heat transfer devices, acknowledging the need for customized strategies that account for the scale of the system and the intricacies of heat transfer mechanisms.

Within the following pages, we take a deep dive into the intricate realm of heat transfer optimization techniques, shedding light on how these strategies evolve and adapt to meet the unique requirements of various systems. Whether dealing with miniature heat sinks in electronic parts or massive heat exchangers in power plants, and whether addressing conduction-driven or convection-dominated heat transfer mechanisms, we explore the full spectrum of possibilities. As we navigate this landscape, we will present some strategies and innovative methodologies to fine-tune heat transfer processes. The significance of optimizing heat transfer devices cannot be overstated, as they play a pivotal role in determining the efficiency, reliability, and performance of numerous systems in our modern world. From enhancing the thermal management of electronic devices to improving the energy efficiency of power plants, the effectiveness of heat transfer directly impacts energy consumption, cost savings, and environmental sustainability.

In the upcoming sections, we will delve deep into the world of heat transfer device optimization, offering a rich variety of examples, case studies, and theoretical foundations that encompass systems of varying sizes and the intricate heat transfer mechanisms at play. By the conclusion of this exploration, readers will possess a comprehensive understanding of the diverse tools and techniques available to enhance the performance of heat transfer devices, adaptable to systems both small and large, and accommodating the nuances of various heat transfer mechanisms.

4. Numerical optimization of HRSG

The content here presented were published in Sustainable Energy technologies and Assessments [J1].

Environmental problems have offered new challenges to the energy production sector, starting from the need of increasing the efficiency of thermodynamic systems to preserve fuel consumption. Accordingly, multi-energy generation systems are among the most efficient generation systems, and Heat Recovery Steam Generators (HRSGs) represent key components of such systems. In this regard it is useful to define a comprehensive approach to optimize a HRSG by using a multi-objective Genetic Algorithm (GA). The aim is to highlight how to determine the optimal values of geometrical and thermodynamic design variables according to two objective functions: the global costs to be minimized and the steam turbine output power to be maximized. Starting from a reference HRSG design, thermodynamic modeling and simulations as well as the optimization procedure are performed in MATLAB®. A validation is carried out to show the accuracy of the modeling approach. Latin Hypercube Sampling is applied to create a uniform sample to select the design variables based on a global sensitivity analysis, producing a significant reduction of computational efforts. Then, the GA optimization is performed to achieve the Pareto front, collecting the best trade-off design solutions. Economic savings up to 20% are achieved limiting the HRSG size.

4.1. Introduction

Energy systems are nowadays gradually evolving to adapt the energy supply to the increasing society challenges. The uncontrolled urbanization, the social structure change and the new energy market competitive conditions have altered key success factors for electricity generation. Moreover, the interest in cleaner, flexible and cheaper energy sources is affecting both supply and demand-side activities, requiring new technologies and decision-making processes to face these challenges. The environmental impact of energy uses has led the attention on sustainable solutions to crucial issues of our generation such as energy poverty and global

warming. Luckily, in the last decades the global awareness for climate change provided a quick development of renewable technologies to manage such problems. Although the application of renewable sources matches the sustainability aim, the main limits are the non-programmability and the lower power density compared to the non-renewable ones, varying by three orders of magnitude. In fact, despite the share of modern "alternative energies" in the energy supply brought Europe in 2017 to cover the 30% of gross electricity production, the remaining part is still committed to traditional power plants. However, the negative effects of fossil fuel requirement started to arise at global levels, generating the premise for a transition towards low-carbon energies through the maximization of generation systems' efficiency. The key to the success of this conversion is the economical accessibility, varying in relation to the type of power plants. The requirement is to provide simultaneously a good flexibility to the energy demand with the lowest electricity production costs. In this scenario, the Combined Cycle Power Plants (CCPPs), and the multi-generation systems in general, feature lower global costs and reduced construction times – compared to traditional plants – meeting the strict environmental regulations, with their higher efficiency and lower emissions. These aspects perfectly deal with the increasing requirement of sustainability, which identifies its meaning on three pillars: economic, social and environmental. Access to reliable, low-priced and sustainable energy is essential for improving life quality standards, development and economic growth [74]. From an economic viewpoint, nowadays, the prerequisite consists of adapting the power production to the energy market needs. The energy – bought or sold as in an enhanced flow of information – requires intelligent and automated decisions to be made. In this regard, renewable sources are facing the issue of matching the extremely variable energy demands of consumers, while simultaneously managing transient and intermittent energy supply [75]. Quite the opposite happens for CCPPs, which can supply energy continuously. These aspects are strictly linked to sustainability in its economical and management meaning, ensuring robust and efficient energy distribution. In this frame, the design of Heat Recovery Steam Generators (HRSGs) is being incessantly improved to meet the challenges of higher power plants efficiency, which may reach up to 65% due to enhancement in the gas turbine technology and optimization in HRSG. Among different kinds of power plants, CCPPs have gained increasing attentions because of higher thermal efficiency than individual steam or gas turbine power plants, and due to the lower environmental impact [76]. The severe emission regulations connected to the sustainability concept – beyond having low operating costs – have limited the present-day HRSGs' emissions of CO_2, CO, NO_x, SO_x, and particulates. Thus, a significant reduction of polluting gases emission is a clear advantage of CCPPs. Several research proved that performing optimization

algorithm the exergy efficiency increases, while the CO_2 emissions reduce [76]. The fuel consumption of CCPPs can decrease to less than 200 g per 1 kWh and the fuel saving around 150 g/kWh, corresponding to the annual reduction in harmful hundred tons of NO_x and hundred tons of CO_2 emissions [77]. According to these assumptions, crucial challenges concern the design and the optimization of such power plants. In this background, the paper aims at defining precious guidelines for the formulation of a comprehensive approach for the design optimization of HRSGs, which are a fundamental component of any CCPP.

4.2. Methodology

The proposed methodology performs a multi-objective Pareto optimization to seek cost-optimal energy design solutions for a dual pressure Heat Recovery Steam Generator (HRSG). This strategy can be applied to new or existing power plants to ensure the optimal design of this component. In addition, it can be applied to other plant components as well. As aforementioned, the originality of this study consists in the introduction of a comprehensive approach to such an optimization problem, combining different tools, i.e., a Latin Hypercube Sampling (LHS), a global Sensitivity Analysis (SA) and a Genetic Algorithm (GA). In detail, a smart sampling technique as LHS is implemented to create a representative sample of the design domain to perform SA, which enables a proper choice of the design variables, thereby reducing the computational burden required by the GA running for the HRSG optimization. All these steps are conducted under MATLAB® R2018b environment [78].

4.2.1. Problem formulation

Heat exchangers are usually analysed employing either the Logarithmic Mean Temperature Difference (LMTD) or the Effectiveness – Number of Transfer Units (ε-NTU) methods. The first one is suitable to calculate the overall heat transfer coefficient (U) based on the measured inlet and outlet fluid temperatures. Conversely, the ε-NTU method is more suitable to establish outlet fluid temperatures if the heat transfer coefficient and the inlet temperatures are known. For these reasons, in the present work, the second one is used. The ε-NTU method is based on the evaluation of heat exchanger effectiveness, which is dimensionless and

ranging from 0 to 1. It is defined as the ratio of the effective heat transfer rate to the maximum thermodynamically permitted (ideal exchanger):

$$\varepsilon = \frac{Q}{Q_{max}} = \frac{Q}{C_{min}(T_{h,in} - T_{c,in})} \tag{4.1}$$

where the effective thermal power is:

$$Q = C_h \ (T_{h,in} - T_{h,out}) = C_c \ (T_{c,out} - T_{c,in}) \tag{4.2}$$

The heat capacity rate is divided into minimum and maximum terms:

$$C_{min} = min \ \ (C_h, C_c) \qquad ; \quad C_{max} = max \ \ (C_h, C_c) \tag{4.3}$$

and its ratio is expressed as:

$$C^* = \frac{C_{min}}{C_{max}} = \frac{(mc_p)_{min}}{(mc_p)_{max}} \tag{4.4}$$

with $\mathbf{0} \leq C^* \leq \mathbf{1}$ specifying that for the evaporator and the condenser $C^* = 0$, because of the phase changing. The thermal effectiveness, in general, is dependent on the number of transfer units (NTU), the heat capacity rate ratio C^*, and the flow arrangement:

$$\varepsilon = f \ NTU, C^*, flow \ arrangement \tag{4.5}$$

where the number of transfer units is a dimensionless parameter under designer's control, defined as:

$$NTU = \frac{UA}{C_{min}} \tag{4.6}$$

In particular, for a crossflow arrangement:

$$\begin{gathered} NTU = \ -ln\left[1 + \frac{1}{C^*} ln \ 1 - C^* \varepsilon \ \right] \\ for: \quad C_{max} \ \ mixed \ , \quad C_{min} \ \ unmixed \end{gathered} \tag{4.7}$$

Which can be used under appropriate constraints: the maximum heat capacity rate is referred to the mixed fluid and the minimum one to the unmixed fluid. Otherwise:

$$NTU = -\frac{1}{C^{\cdot}} ln[1 + C^{\cdot}\ ln\ 1 - \varepsilon\ ] \qquad (4.8)$$

$$for: \quad C_{min}\ \ mixed\ , \quad C_{max}\ \ unmixed$$

By applying energy balances in each HRSG section – for both fluid sides – gas temperature and water properties are calculated. Here, the energy balance equations for each section of a double pressure HRSG without re-heater are presented (see Fig. 4.1):

Low pressure economizer (condensate pre-heater):

$$m_{w,tot}\ \ h_2 - h_1\ = m_g c_p\ \ T_{17} - T_{18} \qquad (4.9)$$

Deaerator evaporator:

$$m_{w,tot}\ \ h_3 - h_2\ = m_g c_p\ \ T_{16} - T_{17} \qquad (4.10)$$

Low pressure evaporator:

$$m_{w,LP}\ \ h_5 - h_4\ = m_g c_p\ \ T_{15} - T_{16} \qquad (4.11)$$

Low pressure superheater:

$$m_{w,LP}\ \ h_6 - h_5\ = m_g c_p\ \ T_{14} - T_{15} \qquad (4.12)$$

High pressure economizer:

$$m_{w,HP}\ \ h_8 - h_7\ = m_g c_p\ \ T_{13} - T_{14} \qquad (4.13)$$

High pressure evaporator:

$$m_{w,HP}\ \ h_9 - h_8\ = m_g c_p\ \ T_{12} - T_{13} \qquad (4.14)$$

High pressure superheater:

$$m_{w,HP}\ \ h_{10} - h_9\ = m_g c_p\ \ T_{11} - T_{12} \qquad (4.15)$$

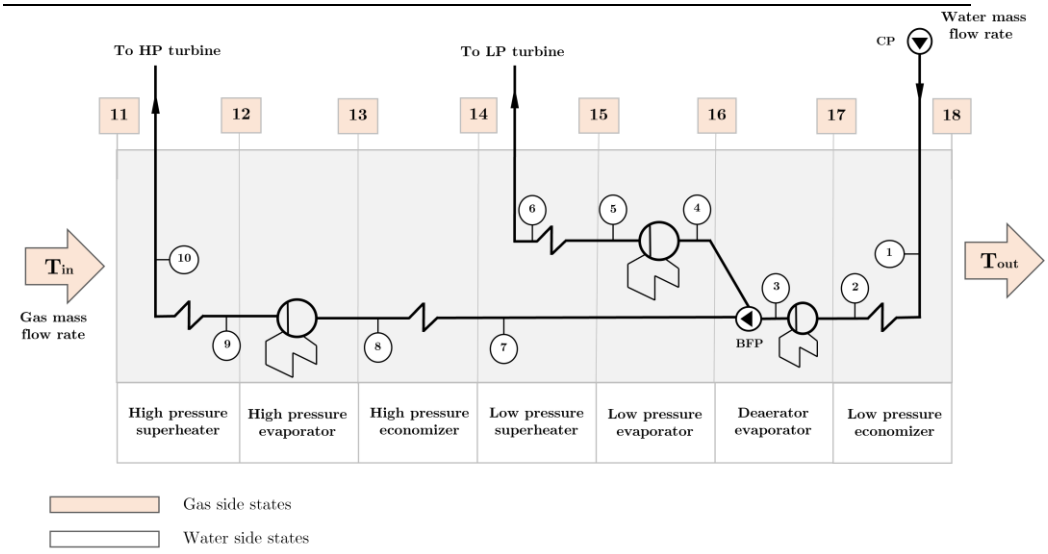

Fig. 4. 1. Schematic diagram of the HRSG sections

As shown in Fig. 1, the water flow rate enters the system in the economizer low pressure section, where preheating occurs. Before partitioning into two different streams – for each pressure level – the deaerator removes dissolved oxygen and carbon dioxide from the condensate water stream. Water flows through the economizer to the steam drum due to the pressure developed in the boiler feed-water pumps. From this section, the two flow rates evolve in different heat exchangers. Each water stream is heated in the evaporator tubes to form a water/steam mixture which flows to the steam drum – designed for separating water and steam – and the last one enters the superheater. This results in two superheated streams at different pressure, which expand through a steam turbine linked to an electrical generator.

4.2.2. Heat exchanger modeling

The HRSG produces water steam by using the heat recovered from exhaust gases. From a constructive point of view – as in traditional steam generators – the three main sections for each pressure level are the economizer, the evaporator, and the superheater, respectively. These sections are characterized by different architectures. Generally, tubes have a vertical arrangement and the gas flow rate flows across them, leaving the system by flowing up to the stack. Generally, the amount of emitted energy from a surface depends on several factors *e.g.,* material, geometry,

orientation, and temperature of the body. Thus, the radiative heat transfer mechanism can be more or less significant. In this study an unfired HRSG is modelled and optimized. Therefore, the absence of a direct flame on the tubes allows to neglect direct radiation. In addition, the gas temperatures – lower than in traditional steam generator configurations – cause a predominant convective heat transfer mechanism. The non-luminous heat transfer coefficient – evaluated by considering the superheater gas inlet temperature of 784 K, and for the water side the mean value between T_9 and T_{10}, equal to 618 K – is negligible with respect to the convective one. In this frame, the nonluminous heat transfer coefficient can be written as [79]:

$$h_n = \sigma_r \varepsilon_g \frac{(T_g^4 - T_s^4)}{(T_g - T_s)} \tag{4.16}$$

The evaluation of this coefficient is linked to the total gas emissivity ε_g, which may be expressed in relation to the water vapor and carbon dioxide emissivity. Thus, ε_g can be estimated from Hottel's charts [80] or by formula if gas temperature, partial pressure of carbon dioxide and water vapor, and beam length are known. Once the emissivity is established, the nonluminous heat transfer coefficient results in 7.36 W/m^{2}K. This quantity is negligible if compared with the convective heat transfer coefficient, which is one order of magnitude greater, h_c = 94 W/m^{2}K. Therefore, even nonluminous radiation for the examined unfired HRSG configuration is irrelevant. The most used method to contrast the interfacial resistance between tubes and gases is the finned tubes' adoption. Various dimensions and arrangements can be used in the main sections of HRSGs. Clearly, each configuration has its own benefit from a thermal and a mechanical point of view. In this regard, there is a large number of geometry variables for each section that significantly affect the operation and performance of the system. Therefore, the design variables should be restricted owing to several factors, *i.e.,* manufacturing, and operative reasons, commercial availability, temperature limitation, thermal efficiency limitation, material temperature limitation, second law of thermodynamic limitation. The limit values for some of these parameters are achievable in literature, e.g., fins per length unit, fin diameter, number of tubes [79]. For instance, gas side convective heat transfer coefficient strongly depends on the gas flow velocity and thus on the HRSG width. A high value of this coefficient could lead to a narrow HRSG and – as a consequence – to an increase in the gas side pressure losses. Therefore, the convective heat transfer coefficient has to be kept between 30 and 100 W/m^2 K

[79]. Gas side pressure drop depends on the cross section of the HRSG for a given gas flow, *e.g.,* a reasonable value is about 5 and 15 mbar. Steam side pressure drop affects the energy spent to pump the water, so this value must be kept low, e.g., less than 10% of the drum pressure [79]. Thus, all the design variables have a strong influence on the system performance. In this work, for each section, different tubes sizes are considered in an inline arrangement. As mentioned before, finned tubes are preferred to balance the low heat transfer coefficient on the gas side. A sketch of a circular finned tube heat exchanger is shown in Fig. 4.2.

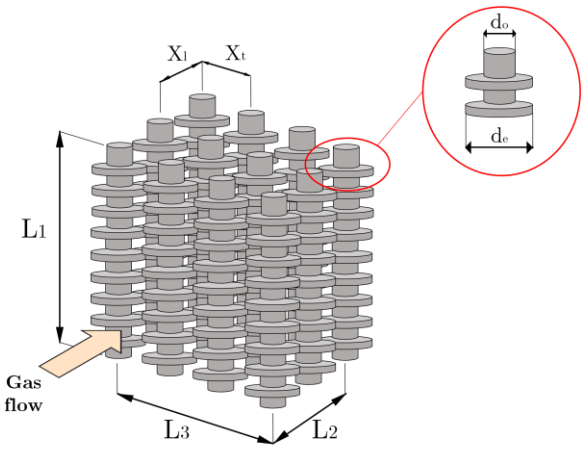

Fig. 4. 2. Circular finned tube heat exchanger

The next lines detail the high pressure economizer modeling as an example. The same modeling technique is used for the other heat exchangers. In this regard, the type of exchanger considered, *i.e.,* a Tube Fin Heat Exchanger, affects the correlations used for the assessment of heat transfer coefficients and pressure drops. To ensure a HRSG configuration with a constant cross-flow section, we consider that the tubes length (L_1) and the width of each section (L_3) are the same for all sections. The total volume can vary by changing the remaining size (L_2). The following correlations are used to define the geometrical parameters, that are the free-flow area A_0, the fin surface area A_f and the primary surface area A_p [80]:

$$A_0 = [\ X_t - d_o\ L_1 - \ d_e - d_o\ \delta N_f L_1]\frac{L_3}{X_t} \tag{5.17}$$

$$A_f = \left[\frac{2\pi\ d_e^2 - d_o^2}{4} + \pi d_e \delta\right] N_f L_1 N_t \tag{5.18}$$

$$A_p = \pi d_o(L_1 - \delta N_f L_1)N_t + 2\left(L_2 L_3 - \tfrac{\pi d_o^2}{4} N_t\right) \tag{5.19}$$

Where the total heat transfer area is:

$$A = A_f + A_p \tag{5.20}$$

The gas-side convective heat transfer mechanism occurs via forced convection because of the non-zero velocity of the hot gas. To calculate the Nusselt number, the correlation of the Hagen number per tube row from Martin [81] for inline tube bundles is here used:

$$Hg = \ Hg_{lam} + Hg_{turb,i}\left[1 - exp\left(1 - \frac{Re_d + 1000}{2000}\right)\right] \tag{5.21}$$

where:

$$Hg_{lam} = 140 Re_d \ \frac{X_l^{*0.5} - 0.6\ ^2 + 0.75}{X_t^{*1.6}(4X_t^* X_l^*/\pi \ \ - 1)} \tag{5.22}$$

$$Hg_{turb,i} = \left\{ \left[0.11 + \frac{0.6\left(1 - \frac{0.94}{X_l^*}\right)^{0.6}}{X_t^* - 0.85\ ^{1.3}} \right] \ 10^{0.47\left(\frac{X_l^*}{X_t^*} - 1.5\right)} + 0.015(X_t^* - 1)(X_l^* - 1) \right\} Re_d^{2-0.1\left(\frac{X_l^*}{X_t^*}\right)} + \Phi_{t,n} Re_d^2 \tag{5.23}$$

considering $\boldsymbol{\Phi_{t,n}} = 0$ since $N_r > 10$ (number of rows) always.
In the previous correlation Re_d is Reynolds number, that is expressed as:

$$Re_d = \frac{\rho u_m d_o}{\mu} \tag{5.24}$$

where:

$$u_m = u_\infty \frac{X_t^*}{X_t^* - 1} \tag{5.25}$$

$$Nu = 0.404\ Lq^{1/3}\ \left(\frac{Re_d + 1}{Re_d + 1000}\right)^{0.1} \tag{5.26}$$

$$Lq = 1.18\ Hg\, Pr \left(\frac{4X_t^*/\pi\ - 1}{X_l^*}\right) \tag{5.27}$$

For the water side, the Fanning factor is used to evaluate the heat transfer coefficient:

$$f_w = 0.00128 + 0.1143\ \ Re_w^{-0.311} \tag{5.28}$$

$$Nu_w = \frac{f_w Re_w Pr_w}{2\ \left[cost + 12.7\ \frac{f_w}{2}^{0.5} \left(Pr_w^{\frac{2}{3}} - 1\right)\right]} \tag{5.29}$$

Clearly, the convective heat transfer coefficients (a) are calculated from the Nusselt number in (5.26) and (5.29). To evaluate the overall heat transfer coefficient, the following correlation is employed [82]:

$$\begin{aligned} \frac{1}{UA} &= R_h + R_{h,f} + R_w + R_{c,f} + R_c \\ &= \frac{1}{(\eta_0 \alpha A)_h} + \frac{1}{(\eta_0 \alpha_{ff} A)_h} + R_w + \frac{1}{(\eta_0 \alpha_{ff} A)_c} + \frac{1}{(\eta_0 \alpha A)_c} \end{aligned} \tag{5.30}$$

Where the fouling coefficients α_{ff} are evaluated as the inverse of the fouling factors *ff*. The extended surface efficiency is defined as:

$$\eta_0 = 1 - (1 - \eta_f)\frac{A_f}{A} \tag{5.31}$$

with the correlation for circular fin efficiency derived from [83]:

$$\eta_{\mathrm{f}} = \begin{cases} \mathrm{a\ ml_e}^{\ -\mathrm{b}} & \text{for } \Phi > 0.6 + 2.257\ \mathrm{r}^{*\ -0.445} \\ \dfrac{\tanh\Phi}{\Phi} & \text{for } \Phi < 0.6 + 2.257\ \mathrm{r}^{*\ -0.445} \end{cases} \tag{5.32}$$

where:

$$r^* = \frac{d_e}{d_o} \tag{5.33}$$

$$a = \ r^{*\ 0.246} \tag{5.34}$$

$$\Phi = ml_e \ r^{*\ n} \tag{5.35}$$

The gas-side pressure drop depends on the crossflow section of the HRSG. This term can be split into 4 terms that refers to entrance, momentum, core and exit effects, considering that the core is the prevalent one [83]:

$$\frac{\Delta p}{p_i} = \frac{G_g^2}{2g_c\rho_i p_i}\left[\ 1-\sigma^2+K_c\ \ +2\left(\frac{\rho_i}{\rho_o}-1\right)+f\frac{L}{r_h}\rho_i\left(\frac{1}{\rho}\right)_m \right. \\ \left. -\ \ 1-\sigma^2-K_e\ \ \frac{\rho_i}{\rho_o}\right] \tag{5.36}$$

Finally, the water side pressure drops are determined in the same manner as that for the gas side, considering the core frictional pressure drop – being the major contribution in the total core pressure drop – here presented [83]:

$$\Delta p_w = \frac{4G_w^2 f_w L}{2g_c D_h \rho_w} \tag{5.37}$$

4.2.3. Optimization

The optimization procedure is implemented by means of a multi-objective Genetic Algorithm (GA) *i.e.*, a non-dominated sorting genetic algorithm NSGA-II [84]. GAs are a family of evolutionary based search methods used to obtain a set of optimal solutions for a given problem. The adopted technique depends on processes existing in evolutionary biology, including learning, selection, mutation and crossover. The process starts with a population of candidate solutions, the so-called individuals, generated by a creation function, the first step randomly performed. To assure the correct implementation of the algorithm, a fitness function is defined in relation to the objective functions. So, each individual is evaluated referring to this function. Then, multiple individuals are selected from the current generation and denoted as parents. Evolutions processes occur, *i.e.,* mutation and crossover, generating a new generation of individuals from the mentioned parents. From

generation to generation, the population improves due to the rank developed on the fitness function. If the objective function has to be minimized, the lower the value obtained from the fitness function, the higher is the rank. Another factor that affects the rank is the crowding distance: individuals that tend to increase this distance to explore the whole domain are rewarded and marked with a higher rank. The reason is to avoid local optimum zones, which inhibits other inspections of the domain and tend to arrest the algorithm. New chromosomes are generated from other ones by passing their own genetic heritage so that the new solutions are similar to the parents. This is a key aspect for the algorithm convergence: every new population comes from the better individuals of the previous one in order to advance the genetic heritage. The crossover or crossing-over deals precisely with this aspect. The iterative procedure goes on until a convergence criterion is satisfied and optimal (or suboptimal) solutions are reached, *e.g.,* the achievement of a maximum number of generations, or the change between two successive Pareto fronts lower than a certain tolerance. Finally, the Pareto front, collecting the non-dominated (thus trade-off) solutions, is achieved. Based on previous similar studies [85] and authors' expertise, the used setting of GA parameters is reported in Tab. 4.1.

Table 4. 1. Genetic algorithm parameters

Parameters	Value
Population size	400
Maximum n° of generation	600
Crossover fraction	60%
Probability of mutation	1%
Minimum tolerance function	1e-1
Selection process	Tournament
Tournament size	4

To improve the algorithm convergence – providing a reduction of running times – a global Sensitivity Analysis (SA) is performed after a Latin Hypercube Sampling (LHS) of the solution domain. The goal is a proper selection of the optimization problem design variables. In particular, many parameters are investigated, especially as for the heat exchangers' geometry modeling, so that performing an intelligent sampling, with the aim of covering uniformly the design domain [86], [87] is highly effective. LHS efficient stratification properties enable the extraction of a large amount of sensitivity information with a relatively small sample size. It is a typology of stratified Monte Carlo sampling that divides the range of each of the K variables included in the analysis (Y_1 , Y_2 ,..., Y_k) into N intervals. In such a way the probability of the variable falling in any of the intervals is equal to $1/N$. The

value selection from each interval is randomly performed and the N values assigned to the first variable Y_1 are paired randomly with the N values of the second one Y_2, and then furthermore combined with the sampled values of the third variable Y_3, and so on. Finally, the domain results in N combinations of K variables, which is the latin hypercube sample that is used to perform the SA. With reference to multi-objective optimization approaches, the employment of Monte Carlo simulation is widely spread [88]. Various methods can be embraced to understand how design parameters affect the objective functions. In this study, to analyse monotonic non-linear correlations, the Standardized Rank Regression Coefficient (SRRC) is operated. SRRCs are selected as sensitivity indices because, varying from -1 to 1, exhibit how influential are the input parameters on the output functions. In particular, negative values are referred to the opposite variation between input and output, conversely a positive one indicates a concordant variation. The magnitude of the influence – growing from 0 to 1 – is estimated by considering the absolute value to assess how the variation of the treated parameters affects the objective functions [89]. The use of such tools allows a substantial reduction of the computational burden compared to exhaustive research by ensuring, at the same time, the rigorous exploration of a huge domain. This becomes increasingly important for cases of advanced energy systems that normally require a large number of design variables for the problem resolution. Hence, the optimization is performed by using a machine with a 1.60 GHz 6-core processor Intel® Core™ i5-8250U with 12 GB of RAM, and the related benefits are deeply analysed in section 4.3.

4.2.4. Objective functions

The objective functions considered in this work are the global costs and the output power of the steam turbine. To define the first one, investment and operative costs are assessed:

$$C_{inv} = (K_{eco}A_{eco} + K_{eva}A_{eva} + K_{sup}A_{sup})_{LP} + (K_{eco}A_{eco} + K_{eva}A_{eva} + K_{sup}A_{sup})_{HP} + K_{deg}A_{deg} \tag{4.38}$$

where heat exchanger costs are listed in Tab. 4.2, taken from [90]. About operative costs, the following relation is used:

$$C_{op} = W_{pump}K_{el}\ H\ CRF \tag{4.39}$$

where K_{el} (electricity cost) and H (annual operation time) are specified in Tab. 4.2, while the capital recovery factor – dependent on the equipment lifetime (n) of 10 years and on the interest rate (i) of 0.05 – is determined using (4.40) [91]:

$$CRF = \frac{i\ 1+i\ ^{n}}{1+i\ ^{n}-1} \tag{4.40}$$

Thus, the global costs – *i.e.,* the first objective function (OF_1) to be minimized – are defined as:

$$OF_1\text{: } C_{tot} = C_{inv} + C_{op} \tag{4.41}$$

The second objective function (OF_2) is defined as:

$$OF_2\text{: } \ W_{st} = m_{w,HP}\,[h\ 10\ - h_{CO}] + \ m_{w,LP}\,[h\ 6\ - h_{CO}] \tag{4.42}$$

Where h_{co} is the water enthalpy referred to the condensate conditions.

Table 4. 2. Parameters used for numerical optimization.

Properties	Unit	Value
T_0	K	298
K_{eco}	\$/m^2	45.7
K_{eva}	\$/m^2	34.9
K_{sup}	\$/m^2	96.2
K_{deg}	\$/m^2	41.1
K_{el}	\$/kWh	0.15
ff_i	m^2 K /W	2e-4
ff_o	m^2 K /W	5e-4
H	h/year	6000

4.2.5. Design variables

The final step for the complete formulation of the optimization problem is the selection of the independent design (or decision) variables. Pursuing the logical sequence of the approach used in this study, 14 parameters (potential variables) are investigated as follows:

- low pressure stream (p_{LP}); high pressure stream (p_{HP}); condensate pump pressure (p_{cp});
- temperature difference between condensate pump temperature and low pressure saturation temperature (ΔT_{cp}); temperature difference between inlet high pressure economizer temperature and high pressure saturation temperature ($\Delta T_{eco,HP}$); temperature difference between gas flow rate and low pressure superheater ($\Delta T_{sup,LP}$); high pressure pinch point temperature difference ($\Delta T_{pp,HP}$); temperature difference between inlet gas temperature and high pressure superheater temperature ($\Delta T_{sup,HP}$);
- gas/water flow rate (r_m);
- outer economizer's tube diameter (d_o);
- length of the tubes (L_1);
- width of each section (L_3);
- longitudinal and transversal tube's pitches (X_l, X_t).

Temperature differences are key design variables for each pressure level of the HRSG. Large temperature differences correspond to lower heat transfer surfaces and a relatively low investment cost for the recovery system. Thus, the importance of supervise the temperature levels for each section assumes great relevance, especially while solving multi-objective optimization problems. In particular – as regards temperature fluctuation ranges – they are dependent on the thermodynamic role of each section, for which energy and mass balance equations are numerically solved to calculate the temperature profiles for the gas and water/steam sides of the HRSG. For instance, the temperature difference between the heat economizers output and the saturation point fluctuates between 5-20 °C in order to avoid the presence of steam that causes the film boiling. The stack temperature has to be kept above the sulphur dew point temperature to avoid corrosion on metal surfaces in the boiler/HRSG and stack. Generally, natural gas contains so little sulphur that the dew point is far below any exhaust gas temperatures. For oil and solid fuels, depending on the sulphur content, the dew point is typically in the range 100-165 °C. Previously, the need to sample the entire domain using the LHS has been highlighted. The LHS analyses a limited number of combinations – compared to the GA – ensuring a reduction of computational costs and time. Then, the sensitivity indices SRRCs for each variable are evaluated. While evolutionary algorithms are known among the best methods for solving optimization problems, constraint handling is still one of the major concerns [92]. To apply the LHS, a list of constraints for the potential design variables is shown in Tab. 4.3.

Table 4. 3. List of the constrains for the potential design variables.

Parameter	Unit	Lower value	Upper value
p_{LP}	kPa	300	1000
p_{HP}	kPa	5000	8000
pcp	kPa	200	400
ΔT_{cp}	K	5	25
$\Delta T_{eco,HP}$	K	30	40
$\Delta T_{sup,LP}$	K	15	25
$\Delta T_{pp,HP}$	K	5	15
$\Delta T_{sup,HP}$	K	30	45
r_m		7	7.8
d_o	mm	33.4	60.3
L_3	m	2	7
L_1	m	2	7
X_t	mm	2	4.5
X_l	mm	2	4.5

Some suitable ranges are taken from [93]. The problem is solved by using a discrete approach, assuming a proper step for each variable that characterizes the variation range. The benefits linked to discrete variables are several, *i.e.,* matching performed values with commercially available ones and reduction of the solution domain, which implies a lower computational burden. The SA is performed to select the GA design variables from the 14 parameters presented, as shown in section 5.4. Accordingly, a variables' screening is carried out thereby reducing the computational burden required by the optimization and speeding up the GA convergence.

4.3. Case study

This study responds to the task of modeling and optimizing a dual pressure level HRSG. These kinds of systems are mainly designed on the mass flow rate and temperature turbine exhaust gases. In particular, an unfired HRSG configuration is considered, and thus the inputs for this component correspond to the outputs of the gas turbine. Input parameters, on which the model is based, are presented in Tab. 4.4, and are taken from the reference model in [85].

The following assumptions are used in the HRSG modeling:

- Steady state conditions;
- Variation in kinetic and potential energies neglected;

- Gas side temperatures not affected by pressure drops;
- Turbine and pump adiabatic;
- Gas side thermo-physical properties evaluated at fluid mean temperature;
- Exhaust gases treated using the ideal gas model;
- No cooling between sections considered.

Table 4. 4. Input parameters.

Item	Unit	Value
Gas mass flow rate	kg/s	500
Inlet gas temperature	K	784
Condensate pump pressure	kPa	10
Boiler feed pump efficiency		0.80
Condensate pump efficiency		0.80
Gas specific heat	kJ/kg K	1.10

4.3.1. Model validation

The model validation process establishes how accurate is the system model here proposed compared to the outputs – of an independent data set – processed in the reference work [85]. Definitely, the modeling and simulation of advanced energy systems, such as HRSGs, require this kind of process to ensure the outcomes' reliability. This purpose can be achieved by setting the same inputs of the selected reference and then comparing the outputs. Such comparison unveils that the results are quite consistent, as shown in Tab. 4.5.
The slight difference between the calculated values is acceptable – showing discrepancies lower than 5% and often close to zero – excepting for the gas outlet temperature from the high pressure economizer (T_{14}). This behaviour can be explained with reference to the simulation results from the mathematical model developed by Duran *et al.* [94]. In particular – according to the reported steam cycle calculation results – the temperature difference across the low pressure superheater is smaller than the one across the high pressure economizer. This leads to a reduced surface area of the low pressure superheater – which exhibits the higher average investment costs – with a consequential reduction of the total cost. To confirm what aforementioned, Tab. 5.6 summarizes the surface areas values for the present study, the reference one and the model developed by Duran *et al.* [94]. These values draw the attention on the lower heat transfer areas resulting from the proposed modeling

approach – except for the low pressure economizer – outlining the economic saving due to the lower investment costs.

Table 4. 5. Model validation on temperatures.

Data	Unit	Reference [85]	Present study	Discrepancy
Input				
Gas inlet temperature	K	784	784	
Drum low pressure	bar	7	7	
Drum high pressure	bar	72	72	
Gas mass flow rate	kg/s	178.5	178.5	
Output				
T_{12}	K	732	726	-0.82%
T_{13}	K	579	576	-0.52%
T_{14}	K	554	515	-7.04%
T_{15}	K	506	509	0.60%
T_{17}	K	433	440	1.62%
T_{18}	K	414	434	4.83%

Table 4. 6. Model validation on surface areas.

Data	Unit	Reference [94]	Reference [85]	Present study
Output				
$A_{sup,hp}$	m^2	4998	5281	4431
$A_{eva,hp}$	m^2	12527	10842.25	9482
$A_{eco,hp}$	m^2	9207	10180	9164
$A_{sup,lp}$	m^2	1049	544.11	483
$A_{eva,lp}$	m^2	7824	7669.09	7497
$A_{eco,lp}$	m^2	2115	1925.62	2684
A_{tot}	m^2	37720	36442.07	33741

4.4. Results and Discussions

This section provides and discusses the results achieved by applying the proposed methodology – which follows the steps described in section 5.2 – to the considered energy system. These results are organized in three subsections to provide a clear and systematic discussion.

4.4.1. Sensitivity analysis

As mentioned in section 4.2.3, Latin Hypercube Sampling (LHS) is an advantageous tool for high computational demanding models to create representative samples for performing global Sensitivity Analysis (SA). This latter is carried out to screen the optimization design variables. For the application of the LHS procedure, each of the 14 potential design variables listed in Tab. 5.3 is provided with maximum and minimum limits of the parameter range. In order to ensure that the sample significantly represents the entire domain, the sample size has to be carefully established. For the present study – considering the number of sampled variables – the sample size is set to 5600, equal to 200 times the product of variables' number and objective functions' number. The values assumed by the objective functions (OF) in correspondence of the 5600 simulations are depicted in the histograms of Fig. 5.3, where the non-uniform distribution of the global costs (Fig. 4.3a) – with a positively skewness, *i.e.*, the peak of the histogram veers to the left – shows a high density in the range around 4 M$ and 5 M$. Conversely, as concerns the turbine output power (Fig. 4.3b) the trend is relatively uniform in the outline range.

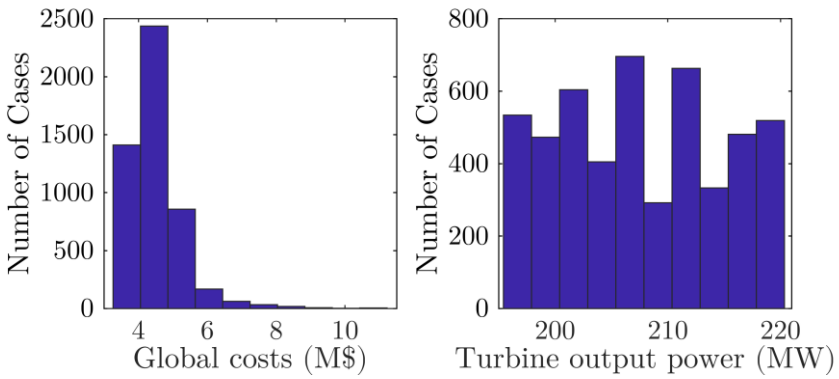

Fig. 4. 3. LHS output distributions of the values assumed by the OFs, global costs (C_{tot}) and turbine output power (W_t).

The efficient stratification properties associated with LHS make its use very effective to define the sample space to be investigated. This is a propaedeutic step to the SA, which aims at underlining how each variable affects the objective functions. To assess this influence, the SRRC (Standardized Rank Regression Coefficient) values are calculated for the 14 potential design variables, including

geometry variables referred to the heat exchangers, and other variables related to the temperature and pressure levels of the bottoming cycle. Fig. 5.4 reports the different SRRCs showing which variables most affect the *OFs*, either with a positive or a negative trend. For instance, the variable r_m is the one that exhibits the highest influence. As the r_m value increases, both global costs (C_{tot}) and turbine output power (W_t) decrease, which results in an advantageous effect and a disadvantageous effect, respectively. In other words, this variable exerts significant contrasting effects on the *OFs*, and therefore it deserves to be one of the decision variables of the multi-objective optimization problem. The temperature differences and condensate pump pressure have the same effects, but with a lower magnitude. Notably, the SRRCs related to the four temperature differences are all negative, unlike the behaviour of p_{cp}. Quite the opposite happens for tube's pitches (transversal and longitudinal) and other geometry variables, which have a considerable influence on C_{tot} whereas the lowest one on W_t. The SRRCs related to X_l and X_t are positive for C_{tot} and negative for W_t. In particular, the higher is the longitudinal pitch, the higher are global costs. Therefore, they are excluded from the successive optimization stage and are set to the minimum value. With reference to the tubes' length (L_1), its value is fixed to the minimum one as a benefit for C_{tot}. Conversely, the width of the heat exchanger (L_3) has a significant negative effect on C_{tot}. Thus, the suggested L_3 value is the maximum of the variation range considered. As concerns the outer tubes' diameter (d_0), likewise the previous variable, this has to be set to the range upper value. Finally, the SRRCs related to the pressure levels are discussed. The sensitivity indices are weak and discordant for both low and high pressure levels. Notably, p_{LP} needs to be minimized to contrast global costs increase, whereas for p_{HP} the suggested value is the lowest because of the negative effect on W_t.

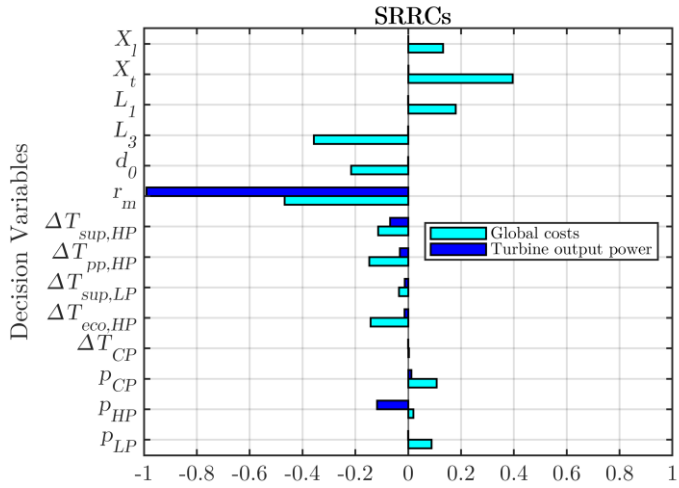

Fig. 4. 4. Standardized rank regression coefficients (SRRCs) for the design variables related to global costs (C_{tot}) and output power (W_t).

Thus, only 6 of the starting 14 variables are considered for the following optimization stage, which are resumed in Fig. 4.5.

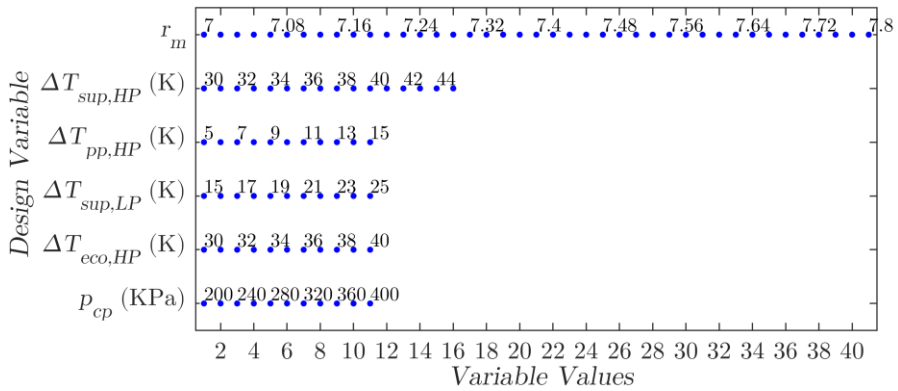

Fig. 4. 5. Design variables selected for the GA optimization.

The variation ranges have been carefully chosen based on similar applications. In particular r_m values are taken with reference to Ganapathy [79], temperature differences values from [22, 23, 46] and p_{cp} values selected based on authors' expertise. Most notably – as stated by the achieved SRRCs of Fig. 4.4 – the r_m

variable is the most influential on both objective functions, thereby requiring a reduction of the range step in order to perform a careful investigation of the optimal value.

4.4.2. Optimization outcomes

The mentioned optimization approach is applied to achieve the Pareto front for the objective functions indicated in Eqs. (4.41, 4.42). This front is obtained starting from the first generation, which generates a primary set of candidate solutions. Moving on to the next generations, new points are added – gradually improving the objective functions – and move closer to the final configuration of the front, shown in Fig. 4.6, where the sub-optimal point evaluated applying the utopia criterion is highlighted and denoted as utopia optimum.

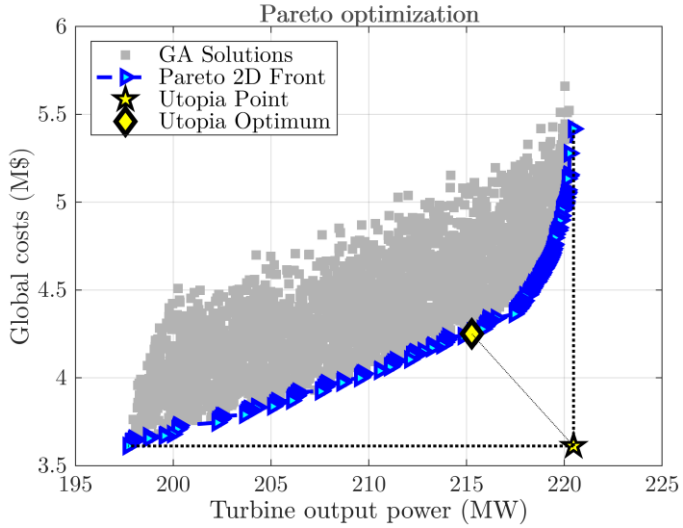

Fig. 4. 6. Pareto front for the multi-objective optimization problem.

Generally, the implementation of multi-objective optimization is required when the case study exhibits conflicting objective functions. In this case, we seek a general criterion to balance the goal of a high turbine output power with limited global costs. The described problem is faced via a Multi-Criteria Decision-Making process, which can be carried out according to different methods. For instance, the utopia criterion picks the non-dominated solution with a minimum distance from

the utopia point (after min-max normalization of the objective functions), which is the one that ideally satisfies the maximization of the output power and the minimization of the global costs. The optimal point detection normally depends on the presence of design constraints considered by the decision maker. In this study, the aforementioned utopia criterion is used without any constraints. The aim is to address the trade-off between lower costs and higher power, since the efforts to minimize the costs cause a consequential reduction in the output power of the steam turbine. This effect is partially explained by the under-sizing of the heat exchangers and therefore by a limited heat recovery. In addition, the TOPSIS technique [95] is employed as a comparison with the results assessed by the utopia criterion. In this regard, the OFs weights are the subjective inputs required by this method, which selects the alternative closest to the ideal solution and farthest from the negative ideal alternative. Therefore, the outcome reveals that – to have the same couple of optimal OFs – the 20:80 weights distribution is required for global costs and turbine output power, respectively. The optimal objective functions values – according with the utopia criterion – are summarized in Table 4.7.

Table 4. 7. Utopia optimum values.

Objective functions	Unit	Value
Global costs	M$	4.252
Turbine output power	MW	215.4

The utopia optimum presents around 215 MW of the output power of the turbine with global costs referred to a 10 years-lifetime around 4.25 M$. Notably, moving away from this optimum point on the Pareto front, the global costs show higher volatility especially in the right part of the front, which is instable, whereas the left part features higher stability. Indeed, a substantial increase in global costs, of the order of 1 M$, leads to an increase in useful steam turbine power around 5 MW, which is just about 2% of utopia optimum power. This means that the non-dominated solutions at the right of the utopia optimum are not recommended, while solutions at the left can be chosen when the economic availability is limited. The results from the multi-objective Genetic Algorithm can be compared with the single objective optimization in order to highlights the compromise of fulfil at the same time the requirements of both objective functions. Thus, all solutions explored by the GA are revealed in Fig. 4.7, which shows respectively the minimum and the maximum value resulting from the optimization of the global costs and the turbine output power.

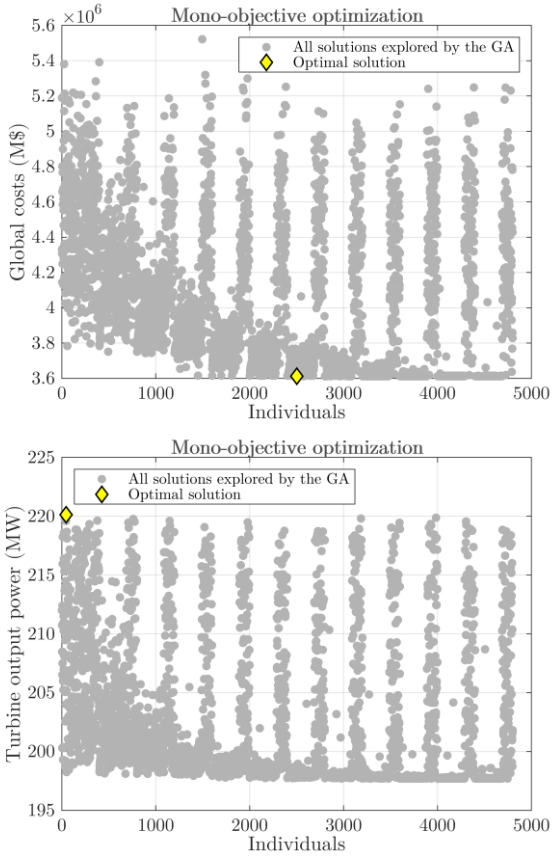

Fig. 4. 7. Mono-objective optimization solutions related to global costs (C_{tot}) and turbine output power (W_t)

The global costs, for instance, when minimized without considering the reduction of the output power, are equal to 3.61 M$. Conversely, the maximum output reachable from the present model is around 221 MW. These outcomes confirm the need of a compromise between the selected OFs illustrated by the Pareto front. Moreover – in order to guarantee stable results – several optimization processes are performed varying different parameters, *i.e.,* the maximum number of generations, the population size, the crossover fraction and the minimum tolerance. The aforementioned parameters are listed in Tab. 4.8.

Table 4. 8. Genetic algorithm parameters for five optimization processes.

Parameters	Values				
	1st	2nd	3rd	4th	5th
Population size	400	400	400	300	500
Maximum n° of generation	600	700	500	600	600
Crossover fraction	60%	60%	80%	80%	70%
Probability of mutation	1%	1%	1%	1%	1%
Minimum tolerance function	1e-1	1e-2	1e-1	1e-2	1e-3
Selection process	Tournament	Tournament	Tournament	Tournament	Tournament
Tournament size	4	4	4	4	4

By comparing the OFs values' resulting from these five optimization processes, the outcomes provide light discrepancies (lower than 2.3%) between the OFs values from the first optimization and the other ones, as summarized in Tab. 4.9.

Table 4. 9. Discrepancies between the five optimization processes OFs.

Processes	OF_1 [M$]	OF_2 [MW]	OF_1 discrepancy	OF_2 discrepancy
1st optimization	4.25	215.3	//	//
2nd optimization	4.31	216.3	1.4%	0.46%
3rd optimization	4.35	217.1	2.3%	0.8%
4th optimization	4.29	215.6	0.94%	0.14%
5th optimization	4.30	216.4	1.2%	0.51%

The design variables' values of the Pareto solutions are depicted in Fig. 4.8, which shows how some values are recurrent and thus optimal. The variable gas/water (r_m) flow, for instance, tends to assume the minimum as more repeated value (Fig. 4.8a). Notably, this figure outlines a higher number of points near the lower bound of the detected range. This can be explained by considering that – fixing the turbine gas flow rate – a reduction of r_m implies an increase in the water availability for the bottoming cycle, which is proportional to the steam turbine output power.

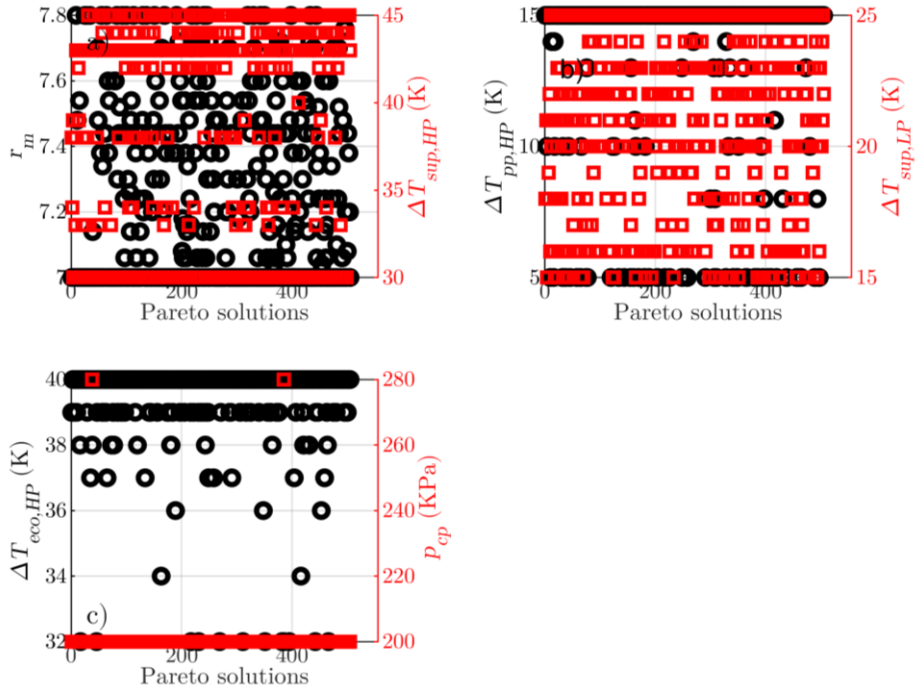

Fig. 4. 8. Scattered distribution of Pareto solutions: design variables' values.

As concerns the $\Delta T_{sup,HP}$ values, the distribution highlights a points' thickening on the limit values, and therefore the optimal value would be a compromise between the considered options. This occurs because – fixing the exhausted gases inlet temperature to high pressure superheater – an increase in the temperature difference leads to a reduction of the water-vapour temperature provided to the steam turbine. This behaviour is in contrast with the maximization of the turbine output power, but at the same time allows a higher thermal level of waste gases for the following sections of the HRSG. Conversely, a limited temperature difference is preferred in terms of heat recovery at the expense of a lower T_{10} and a higher heat exchanger cost due to a higher surface area. With reference to Fig. 4.8b, $\Delta T_{pp,HP}$ is repeatedly equal to 7 K and 15 K, while $\Delta T_{sup,LP}$ exhibits a scattered distribution throughout its allowable domain, with a preference to 15 K, 23 K and 25 K. In both cases the optimal values are a trade-off between heat recovery and costs. A smaller pinch temperature difference corresponds to a larger heat transfer surface area and a more costly system, as well as a higher heat recovery

efficiency. For $\Delta T_{sup,LP}$ similar considerations to the high pressure variable ($\Delta T_{sup,HP}$) can be drawn. Finally, the optimal $\Delta T_{eco,LP}$ value (Fig. 4.8c) is often equal to 40 K and the condensate pump pressure p_{cp} to 200 kPa, the lowest value here investigated (see Fig. 4.5). Table 4.10 summarizes the design variables' values related to the utopia optimum.

Table 4. 10. Utopia optimum design variables' values.

Decision variable	Unit	Value
r_m	-	7.08
$\Delta T_{sup,HP}$	K	45
$\Delta T_{pp,HP}$	K	15
$\Delta T_{sup,LP}$	K	23
$\Delta T_{eco,HP}$	K	40
p_{cp}	kPa	200

4.4.3. Significance of the outcomes

As previously discussed, the model is validated against the reference model in [85], which investigated different configurations of heat exchangers fixing the total volume of the HRSG. This valuable work proposed the constructal design of a dual pressure HRSG by using genetic algorithm optimization method constrained to the constant volume, considering the minimum total entropy generation as objective function. Conversely, this study seeks the trade-off between global costs (C_{tot}) minimization and steam turbine power (W_{st}) maximization, considering the input parameters of Tab. 5.4, with the total volume free to change. Assuming that the length of the economizer tubes (L_1) and the width of this section (L_3) are both equal to 7.5 m, the optimal volume value of the high pressure economizer achieved by [85] is about 127 m^3 by performing the genetic algorithm. According to [85], the length of such component characterizes around 17% of the total one. Thus, fixing the base and the height of the heat exchangers, the total volume results in 750 m^3. Implementing this configuration, applying the utopia criterion defined in the present study, the optimal values of the objective functions are the following: $OF1_{\text{ref}}$) $C_{tot} = 5.45$ M\$; $OF2_{\text{ref}}$) $W_{st} = 217$ MW. The L_2 value obtained is about 2.25 m, so that, following the 17 % proportional coefficient, the total length of the HRSG is about 13 m, similar to the reference one [85], for which the total length of the HRSG as function of the inlet gas temperature *i.e.*, 773.15 K, is about 14 m, fixing a volume of 750 m^3. Differently – performing the design variables' values

assessment on the achieved sensitivity indices and on the GA optimization stage, *i.e.*, $L_1 = 2$ m and $L_3 = 7$ m – the high pressure economizer design features a final volume of 60.7 m^3, which leads to an HRSG's volume of about 360 m^3. Furthermore, the high pressure economizer L_2 value is equal to 4.3 m, resulting in a final HRSG length of 25.5m. The main benefit of the proposed configuration is an economic saving, about 20%.

The highest discordances are related to the temperature levels of the bottoming cycle and to the final HRSG configuration. Indeed, in spite of the similar value of the superheater high pressure temperature, the one referred to the low pressure level is about 40 K lower than the reference value. This can be explained underling that Mehrgoo *et al.* [85] proposed an exergetic modeling approach, with the aim of minimizing the entropy generation due to the temperature difference. The approach of the temperature profiles, and therefore the reduction of the pinch point temperature differences – fixing the gas-side one – leads to an increase of the steam temperature. At the same time, a reduction of the temperature difference implies an increase of both heat exchanger surface and costs. The optimization approach presented in this paper, conversely, aims at the maximum power from the steam turbine. The balance between the mass flow rate and the enthalpy output level from the superheaters is the key factor of the presented process.

Definitely, a bi-objective optimization by implementing a Pareto genetic algorithm is performed, which is not a novelty, but it represents a powerful tool that is here developed differently from previous studies. Moreover, the presented methodology combines different tools, *i.e.*, LHS, SA, GA, which are generally used separately, in order to provide a reliable and computationally cheap approach for finding robust optimal solutions, *i.e.,* the maximization of cost-effectiveness and output power, for the HRSG design. Most notably – according to the results offered by the SA – the optimal Heat Recovery Steam Generator configuration has a predominant horizontal development, with a lower height. As previously described in Fig. 4, a lower value of the height leads to a reduction in costs, unlike the width for which an increase is more suitable. All told, the outcomes show how to deal with the challenge of designing a dual pressure HRSG employing robust optimization methodologies.

4.5. Final remarks

This work proposes both a comprehensive thermodynamic design and the cost-energy optimization of a dual pressure Heat Recovery Steam Generator (HRSG). To support the optimization, a global Sensitivity Analysis (SA) is performed after

Latin Hypercube Sampling to select the possible design variables most affecting the considered objective functions, *i.e.,* global costs to be minimized and steam turbine output power to be maximized. Accordingly, six design variables are chosen for the optimization problem, and the Pareto front is achieved by running a multi-objective Genetic Algorithm (GA). Furthermore, the results show that the reduction of the ratio between gas and water mass flow rate brings to a considerable increase of the output power. With reference to the other geometry variables, *i.e.*, pitches, outer economizer's tube diameter, length of the tubes, width of each section, the recommended values are set according to the SA outcomes, without the need of the further optimization stage. Conversely, gas/water flow rate, temperature differences and condensate pump pressure values have been chosen based on the utopia optimum criterion after the GA running. According to the achieved variables' values, the high pressure economizer design is characterized by a final volume of 60.7 m^3 and a HRSG volume of about 360 m^3. The main benefits resulting from this approach are the 25.5 m length final configuration of the HRSG – with a predominant horizontal development – and thus the economic savings around 20%. Most notably, the evidence from the SA reveal that a reduction in the heat exchanger height brings to an overall cost decrease. Consequently, a limitation on the vertical development causes the HRSG sections length increase. As mentioned before, the goal of the present study is to combine the problem formulation of the heat exchangers modeling, with a robust optimization methodology. This process exhibits potential future developments, such as the detailed modeling of all sections, using – for instance – computational fluid dynamics tools.

5. Latent heat “cold” thermal energy storage

In a world handling with the challenges of climate change and the ever-increasing demand for sustainable energy sources, the search for innovative energy storage solutions has become a paramount pursuit. Among the multifaceted technologies emerging in this landscape, latent heat energy storage systems stand out as a promising frontier. These systems offer a unique approach to storing thermal energy by harnessing the latent heat associated with phase change materials (PCMs). While the concept of latent heat storage has been around for decades, recent advancements in numerical modeling techniques and optimization strategies have propelled it to the forefront of sustainable energy innovation.

This section delves into the captivating branch of latent heat energy storage, shedding light on its numerical modeling, optimization methodologies, and a profound exploration of its diverse applications. As we journey through this landscape, we will explore the potential of microencapsulation techniques in enhancing the performance and versatility of latent heat storage materials. Furthermore, we will face the intricate challenges of numerical modeling, with a special focus on a critical PCM aspect as subcooling, which plays a pivotal role in maximizing the efficiency and reliability of latent heat energy storage systems.

This section encompasses various works, *i.e.,* [J2], [J3], and [J4], developed under the same project – supported by the Italian Ministry of Economic Development, within the research project “RdS-PAR 2019-2021” – and in collaboration with ENEA.

5.1. Phase change material-based shell-and-tube heat exchanger

This section experimentally and numerically investigates the thermal performance of a vertical shell-and-tube heat exchanger, filled with a biological phase change material (PCM), linked to a water-chiller system for cold thermal energy storage. The system provides the cooling service to a 150 m^2 single-family house.

An experimental apparatus has been designed to collect the PCM temperature data through the employment of multiple thermocouples located at different heights of the heat exchanger. Starting from the experiment, a comprehensive 3D numerical model of the system has been developed based on the enthalpy-porosity method using COMSOL Multiphysics®. The PCM temperature profiles and the evolution of the solid-liquid interface location at various time instants are used as performance indicators of the model reliability and accuracy. The numerical agreement with the experimental findings is proved using statistical indices, *e.g.,* maximum values of mean absolute error (MAE) and root mean square error (RMSE) equal to 1.18 °C and 1.33 °C, respectively, with regards to central thermocouples. The results reveal that natural convection highly affects the PCM charging/discharging processes, as proved by the PCM liquid fraction, which moves from full to 51%, between two levels spaced by 0.78 m. The developed 3D model, based on the enthalpy-porosity method, allows to consider boundary conditions variability with both angle and height, which are not usually covered by simplified 2D models. Hence, this model confirms that only 39% of the PCM mass experiences the complete phase change process, proving that the current design does not allow the PCM to totally exploit the thermal storage potential, thereby making optimization pivotal and challenging.

Nowadays, a challenging issue of energy management concerns the matching between energy supply and demand, especially when renewables are exploited because of their non-programmability. Such an issue affects numerous sectors such as industrial processes, power plants, buildings, and can be tackled by using energy storage systems. Notably, thermal energy storage (TES) is an effective solution to respond to fluctuations of thermal energy demand, which can be highly floating, especially when associated to heating, ventilating and air cooling (HVAC) systems. One of the essential advantages of TES is that it can potentially reduce HVAC demand in buildings by allowing the HVAC system to operate during times when it runs more efficiently. Accordingly, the attention is here focused on cold energy storage systems, which are less popular compared to heat storage ones but equally important. In this regard, TES implementation provides more degrees of freedom in the system management [96], which entails economic benefits since traditional vapor compression chillers are highly dependent on the fluctuating grid price – more costly during the peak as compared to the non-peak hours [97]. This generally leads to a reduction in operating costs and equipment, allowing cold storage with a reduction of the chiller size, and an increase of full load-hours. Few studies have experimentally proved the effectiveness of cold storage to obtain an advantageous peak-shaving effect of the electrical load of refrigeration systems. The implemented

control strategies are various [98], as well as the storage medium used, among which the most popular are certainly chilled water and ice [99]. Providing air conditioning with ice-cold storage is among the most implemented and optimized approaches [100]. Nevertheless, the use of phase change materials (PCMs) as a storage medium in cooling systems – with higher melting temperature – is more appropriate for standard HVAC conditioning because of the heat transfer fluid (HTF) temperatures, generally above 0 °C. Hence, PCMs with a melting/solidification temperature around 5-15 °C are widespread for these applications [101]. Thus, the reliability of these systems lies in the PCM large amount of heat stored/released during charging/discharging processes, in a relatively narrow temperature interval. Therefore, in recent years, great attention has been paid to the use of PCMs for cold storage rather than ice, because of the potential to significantly reduce the size of the storage, which represents one of the main limitations of such systems [102]. As a consequence, the integration of PCMs in cold storage tanks for air conditioning purposes represents the actual challenge to ensure energy, economic and technical benefits. Moreover, the main limitations linked to its thermal properties, *i.e.,* the low thermal conductivity and the thermal expansion on melting, ask for the design of a suitable heat exchanger as a crucial component of a latent heat thermal energy storage (LHTES) system. Elsanusi *et al.* [103] studied the melting process of multiple PCMs with different arrangements in a horizontally oriented heat exchanger, whereas Wang *et al.* [104] analysed a zig-zag configuration of multiple PCMs using a two-dimensional model. Accordingly, the development of a LHTES system firstly requires the understanding of heat transfer in PCMs when these undergo solid/liquid transition. From this perspective – among the multiple alternatives – we here present the case study of PCM integration inside a shell-and-tube cold TES prototype, which provides cooling for a 150 m^2 single-family house.

The present work applies a coupled experimental and a numerical approach to analyse the charging and discharging processes of a PCM-based cold thermal energy storage. The system consists in a shell-and-tube heat exchanger filled with a biological PCM on the shell side, with cooling water supplied inside the tubes. A 3D numerical model is developed to simulate the PCM behaviour and compared with experimental results. Hence, the results – in the form of temperature profiles and graphical phase-change comparisons – are presented. The analysis of the first one reveals the differences between the numerical simulation and the PCM experimental behaviour. In addition, this study performs a qualitative comparison – to identify similarities and differences – for the melting front of the numerical result with experimental melting front, which results from the photographs during the melting of paraffin wax. In this vein, by means of them, the mushy zone, *i.e.,* the PCM region where solid phase and liquid phase coexist, is clearly identifiable. The

discrepancy between measured and simulated values of temperature is investigated as indicative of the model goodness-of-fit. Therefore, the 3D model strengths and weakness are argued.

The aim of the present work is to examine the phase change processes involving the fully vertical shell-and-tube cold storage system in order to define its reliability when coupled to a chiller system. The reviewed literature on this application shows that the thermal performance of a heat exchanger filled with biobased PCM has not been investigated from both an experimental and numerical point of view. Thus, the attempt of this paper consists in the numerical simulation of a complex system without resorting to geometrical and physical simplification, *e.g.,* 2D model, 3D model based on two concentric cylinders, or conduction-based model for the PCM side. By doing this, new useful insights about the numerical simulation of PCMs are provided, supported by new experimental results that can be used in other research studies to validate different models for the numerical simulation of macro-encapsulated PCM. To summarize, the primary objective of the present work is to present experimental data about a charging/discharging case and then to compare this with a very robust CFD model developed for the transient simulation of the energy performance of a shell-and-tube heat exchanger for cold storage with water as the heat transfer fluid.

5.1.1. Materials and methods

The architecture of the cooling system is described first, then the geometrical configuration of the vertical shell-and-tube heat exchanger (STHE), the experimental apparatus and the results are provided. Fig. 5.1 shows the layout of the cooling system used for the experimental analysis, which consists of a water chiller, a heat exchanger (user) simulating a single-family cooling thermal load, a water pump and a shell-and-tube cold storage tank. In detail, the user represents a house of 150 m^2 floor area, with daily load profiles for electrical and thermal uses taken from [105] for typical summertime schedules of Italian climatic zone E [106] (heating degree days in the range 2101-3000). As shown in Fig. 5.1, the cold storage can be fed either by using the full water mass flow rate flowing through the user, or by a fraction of it using modulating valves VM3 and VM4. In both cases, the cold storage is charged when the user's outflow temperature is lower than the PCM solidification temperature, that happens in off-peak periods, and discharged in on-peak periods when the user's outflow temperature is higher than the PCM melting

temperature. In the present work, the results used for the experimental validation of the numerical model refer to the case in which the cold storage is fed with the same water mass flow rate flowing through the user. The temperature measurements on the circuit are carried out through class 1 T-type thermocouples – with an accuracy of ± 0.5 °C – and are acquired by means of a National Instruments NI 9213 acquisition module, using the NI cRIO 9066 controller. The flow rate measurements are made by means of magnetic flow meters "Comac Flow 38 mass flow meter", with an accuracy of 2% on the recorded value and a minimum one of 0.18 m^3/h.

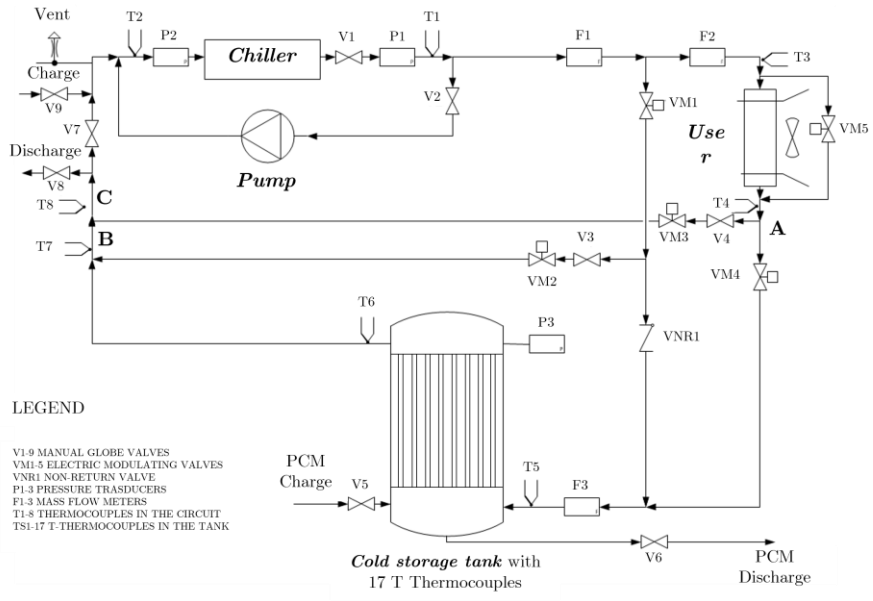

Fig. 5. 1. Layout of the chiller cooling system

Tab. 5.1 lists the properties of a commercial biological PCM, *i.e.,* PureTemp 15, designated as 100 % biobased by the U.S. Department of Agriculture bio-preferred program – as given by the producer. This material has been chosen with a melting point that guarantees to take advantage of the latent heat absorption/release. The device here presented is designed to store the cold thermal energy provided by the heat transfer fluid (HTF). Therefore, the apparatus is based on the heat transfer between the fluid in the tube-side, *i.e.,* cold water and the one in the shell-side, *i.e.,* the phase change material (PCM).

Table 5. 1. PCM properties

Properties	Values
Melting point [T_M (°C)]	15
Latent heat [L_f (kJ/kg)]	182
Thermal conductivity (W/m/ K)	
Solid phase [k_S]	0.25
Liquid phase [k_L]	0.15
Density (kg/m^3)	
Solid phase [ϱ_S]	950
Liquid phase [ϱ_L]	860
Specific heat (J/kg/K)	
Solid phase [$c_{p,S}$]	2250
Liquid phase [$c_{p,L}$]	2560
Dynamic viscosity [μ (Pa s)] at 20 °C	4×10^{-3}
Volumetric thermal expansion coefficient [β (1/K)]	3×10^{-4}

The present thermal storage tank differs from conventional shell-and-tubes heat exchanger (STHE) for the absence of plate baffles. As a result, the shell-side fluid motion – driven by the buoyancy forces inside the PCM liquid phase – develops vertically, without any obstruction. The primary fluid – cold water supplied at 1.5 bar by the chiller – enters the exchanger by means of a 19.05 mm diameter tube, externally threaded and tangentially welded to the shell. Thus, water flows through the inlet (lower) plenum, as depicted in Fig. 5.2. Once the plenum volume is totally filled, the fluid rises the shell-and-tube tubes bundle, which is realized by 66 tubes made by austenitic stainless steel (AISI 316), whose properties are listed in Tab. 5.2.

Table 5. 2. Steel thermal properties (AISI 316)

Properties	Values
Thermal conductivity (W/m/K)	17
Specific heat (kJ/kg/K)	0.502
Density (kg/m^3)	7500

In detail, pipes belong to Schedule 40 S, with an internal diameter d_{int} of 12.48 mm, an external one of 17.11 mm and a total length of 1400 mm. The tubes bundle layout is defined by a triangular pattern. Obviously, a triangular arrangement allows more tubes in a given space. All pipes are welded to the two stationary tube sheets. After flowing through the tubes, water enters the outlet plenum equipped – as well as the inlet one – by a 19.05 mm diameter tube, externally threaded and tangentially welded to the shell. Moreover, the upper plenum is integrated with a

tube-side vent valve (d_n = 15 mm) at the highest point of the heat exchanger to control inlet and outlet flow and to remove trapped air. The phase change material is surrounded by a transparent plexiglass shell with an internal diameter d_{sh} of 500 mm, a height H of 1350 mm and a thickness s_{sh} of a 5 mm. The transparency of the shell layer plays a key role for the visualization of the PCM dynamic behaviour during the thermal transient. Since the tubes bundle is longer than the shell height, the heat exchanger shows an opening – a cylindrical surface – between the shell upper edge and the lower edge of the upper plenum. This surface is highlighted in Fig. 5.2. Therefore, the shell-side fluid properties, *e.g.,* the pressure, are affected by the surrounding ambient conditions. Finally, the shell is equipped with a valve for the charging/discharging of the liquid phase PCM, placed on the lower part as depicted in Fig. 5.1.

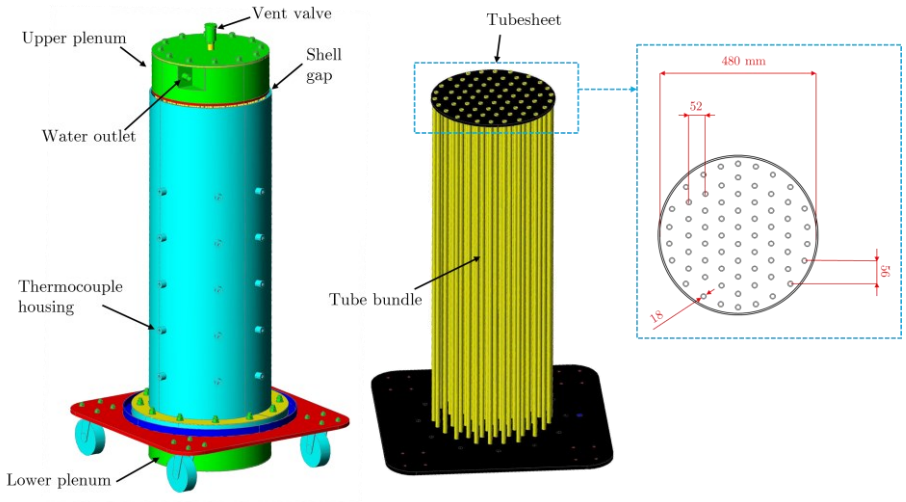

Fig. 5. 2. From left to right: Shell & Tube storage tank geometry and main features; tube bundle; tube bundle cross section

The experimental campaign has been carried out with a test facility located in the thermal storage laboratory of the department of energy technologies and smart grid (LPSAT) at the research Center of ENEA in Portici (NA). The temperature distribution of the shell-side fluid is determined by means of 17 class 1 T-type thermocouples with an accuracy of ± 0.5 °C used to measure the temperature inside the PCM. The thermocouples are run horizontally – as depicted in Fig. 5.3 – parallel to the shell surface, and arranged on 5 levels, *i.e.,* cross section, each one

spaced by 195 mm. In detail, one set of thermocouples, *i.e.,* central (CT), measures the temperature on the shell-and-tube central axis, while the second one, *i.e.,* lateral (LT), collects the data referred to the half-length of the radius, as depicted in Fig. 5.3. The central thermocouples are one on each level, instead of the lateral one – consecutively spaced about 90 degrees in counter clockwise order – arranged on Level *I*, Level *III* and Level *V*. Thus, the odd levels are equipped with 5 thermocouples (1 central and 4 lateral), while on the remaining ones there is just the central thermocouple, as in Fig. 5.3. With reference to this figure, it can be pointed out that the central thermocouples are the only ones for which the through-hole axis has a radial direction.

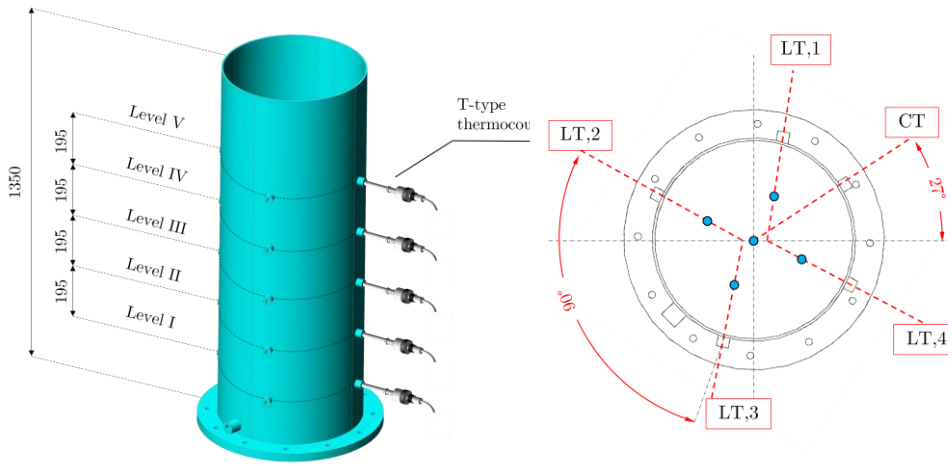

Fig. 5. 3. Thermocouples location: a) shell view b) section view

The experimental data are provided in terms of:

- Inlet/outlet HTF temperature;
- Inlet HTF mass flow rate;
- Surrounding ambient temperature;
- PCM temperature collected by the thermocouples.

As previously mentioned, the heat transfer fluid (HTF) of the storage system is supplied from a chiller which cools it down to 7 °C. As the load of the user increases/decreases, the HTF reaches the shell-and-tube storage with a lower/higher

temperature. Thus, its profile – whose trend is shown in Fig. 5.4 – is represented by a time-varying trend. Since those data are collected by a class 1 T-type thermocouple with an accuracy of ± 0.5 °C arranged on the supply line, they present a fluctuating profile by the hour that is approximated by a piecewise step function (Fig. 5.4). The mean values related to the time intervals and the deviations from them are summarized in Tab. 5.3 and illustrated in Fig. 5.4.

Table 5. 3. Mean values of water inlet temperature referred to the time intervals

Interval (h)	Temperature (°C)	Deviation (°C)	Interval (h)	Temperature (°C)	Deviation (°C)
0-7	8.68	±0.29	15-16	15.19	±0.39
7-8	9.54	±0.25	16-17	14.59	±0.41
8-9	10.3	±0.27	17-18	14.1	±0.39
9-10	11.04	±0.28	18-19	17.07	±0.45
10-11	11.83	±0.28	19-20	20.19	±0.45
11-12	12.57	±0.30	20-21	18.98	±0.55
12-13	13.22	±0.30	21-22	17.12	±0.54
13-14	13.82	±0.32	22-23	13.71	±0.49
14-15	14.43	±0.37	23-24	9.96	±0.45

Moreover, the water outflow temperature profile is here presented. When the outlet profile is above/below the inlet one, the PCM is subjected to cooling energy charging/discharging. For instance, outlet temperature is higher than inlet temperature for most of the transient regime, then it becomes lower at some points due to the heat released to the PCM by the HTF. Notably, this occurs when the HTF inlet temperature reaches the PCM melting point. Then, the inlet temperature rises as well as the user's refrigeration thermal load increases. When this happens, the PCM low thermal diffusivity does not allow the PCM to immediately perceive the temperature change, with the consequence of a gradual discharging. This is caused by the heat absorbed by the PCM, which entails a HTF outlet temperature lower than the inlet one. Therefore, at the beginning, *i.e.,* during the charging phase, the more the PCM heats up the HTF, the more the storage is correctly working. In that moment, the PCM temperature distribution along the STHE is not uniform, varying from a minimum of 16.5 °C to a maximum of 22.3 °C. This is mandatory to set the boundary conditions of the problem introduced lately. The analysis of Fig. 5.4 reveals that the HTF outlet temperature profile takes three hours to reach a quasi-stationary condition (T_{out} = 11.5 °C), thereafter the two profiles tend to get closer. At constant mass flow rate, a reduction in the HTF temperature difference can be justified by a lower heat transfer with the PCM.

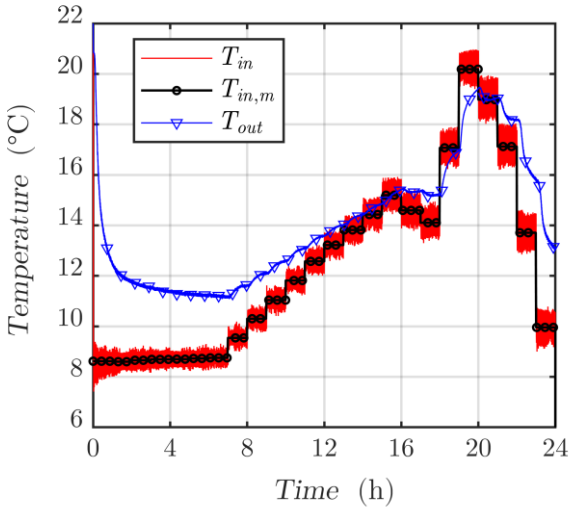

Fig. 5. 4. Temperature profiles of the heat transfer fluid (HTF): inflow; mean value referred on time intervals; outflow

With reference to the mass flow rate, the mean value of the data recorded on the thermal storage supply line is equal to 0.075 kg/s, as depicted in Fig. 5.5.

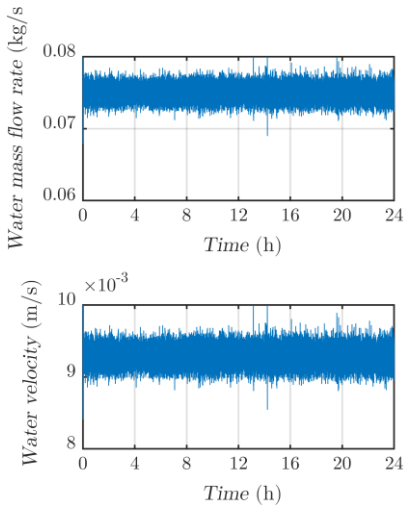

Fig. 5. 5. Above: inlet water mass flow rate; below: single-tube water velocity

Furthermore, Fig. 5.5 illustrates a single-tube HTF velocity, evaluated from: *i)* mass flow rate; *ii)* tube flow area; *iii)* number of tubes; *iv)* HTF thermophysical properties. As last experimental input – the indoor test ambient temperature profile is shown in Fig. 5.6. The latter reveals that the external temperature does not have a periodic trend, and above all – overlapping the trend observed previously in Fig. 5.4 with the present one – this trend goes along with the HTF fluid outlet temperature one.

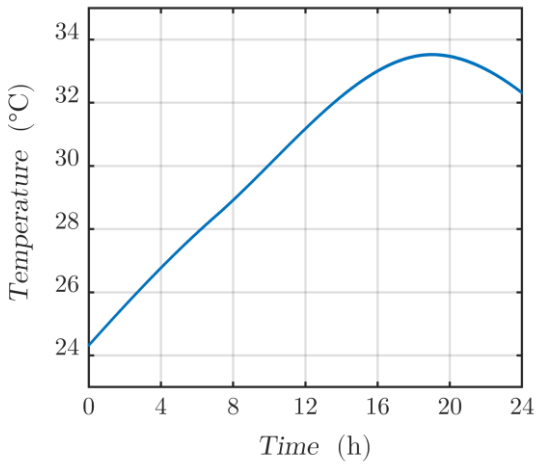

Fig. 5. 6. Test ambient temperature profile

5.1.2. Experimental setup

The results for the experimental test are here presented. Figs. 5.7 and 5.8 show the temporal variation of the PCM temperature over a period of one day. As aforementioned, the temperature data are recorded as a function of the thermocouple's location. In detail, all profiles are presented with reference to the arrangement on the cross section – from 1 to 4 – and the level – roman numerals from I to V, as shown in Fig. 5.3. Therefore, the temperature profiles of the 4 lateral thermocouples (LT) placed on the first, third and fifth level are presented in Figs. 5.7a, 5.7b, and 5.7c, respectively. Although the LT are placed on the same level, the recorded data are slightly different. This should be explained by the triangular tubes bundle pattern, which defines an asymmetric structure of the shell-and-tube heat exchanger along the angular coordinate. In detail, Figs. 5.7a-c reveal that – except for the

first level – the $LT,2$ thermocouple records higher PCM temperatures. A reason for this uneven behaviour may lie in the influence of what happens in the lower plenum influence on the first level. For instance, the HTF, when enters the tube bundle, may not enters the tubes with a uniform distribution, resulting in a different HTF mass flow rate per tube and then in an asymmetric interaction with the PCM on Level *I*. Thus, the mean value of the temperature profile ($LT,_m$) is computed for each plot referred to the LT. By doing this, a single reference profile is set for the comparison with the numerical data.

Figs. 5.7a-c show that – during the charging phase – the melting transition corresponding to the change of the PCM temperature evolution occurs in the ranges of 12.7–13.6 °C, 12.9–13.6 °C and 14.1–15.0 °C for LT_I, LT_{III} and LT_V, respectively. These temperatures stand for the melting temperature of the PCM at these positions. The difference between the values of these temperatures at different levels lies in the heat storage process of the PCM, which is affected from the natural convection phenomenon. As concerns the central thermocouples (CT), Fig. 5.8 represents the temperature profiles recorded on each tank level. Notably, the PCM initial temperature condition is not uniform along the height of the storage tank since the liquid PCM in the shell-side is affected by a density stratification, with a temperature field in a range of 17.55–21.76 °C. A further remark concerns the different temperature profiles between the central and lateral thermocouples. In depth – except for the first level CT – the CT profiles reveal a smaller deviation if compared to the LT trends. This behavior can be justified by the slight influence of the surrounding conditions on the CT points. Differently, the LT data – which are more affected by the variability of the external temperature shown in Fig. 5.6 – reach higher maximum temperatures. As an exception, the CT first level trend notably deviates from the others. This point detects a significantly lower temperature than the upper ones and shows a delay in the discharging phase that suggests a higher inertia of the PCM during the phase transition. This could be attributed to the fact that the initial temperature is not totally uniform, which is also consistent with practical cases where a uniform initial temperature distribution is very challenging especially if the device is vertically-oriented. The $CT,_I$ temperature drops faster because here there is no phase change, thus temperature drops down faster. Moreover, as regards the charging phase, it faithfully follows the tendency of the heat transfer fluid (HTF) outlet temperature. A physical explanation should be linked to the previous remarks on the thermocouple location with respect to the external condition combined with the density stratification.

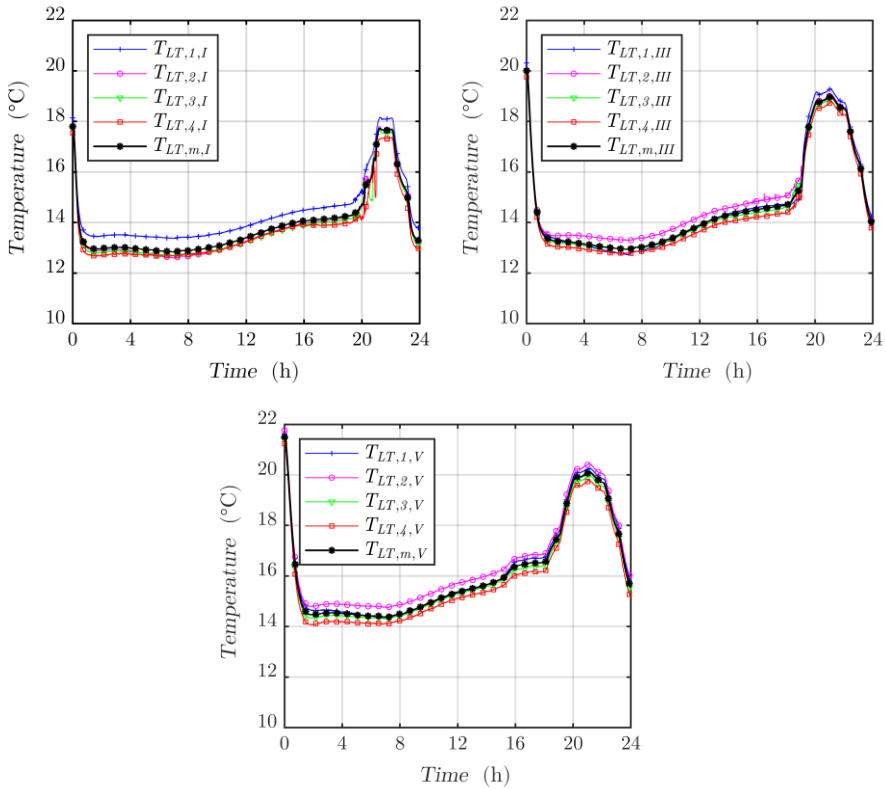

Fig. 5. 7. PCM experimental temperatures: TL on first level (I); TL on third level (III); TL on fifth level (V)

All the plots analyzed share a common feature: the initial part of the charging process presents a quick decrease of temperature in all the measurement points because of the high temperature difference between the PCM and the inlet water at the beginning of the experiment. Then, the HTF rising temperature starts the discharging process. A more exhaustive description of the phenomena involving the PCM will be subsequently investigated with the numerical results discussion.

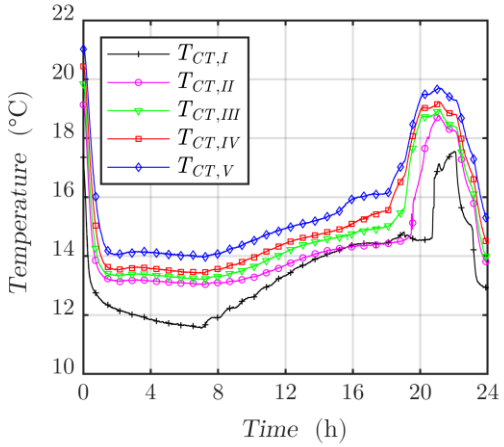

Fig. 5. 8. PCM experimental temperatures of TC for each level

For the sake of completeness, Fig. 5.9 shows hourly average value of PCM cold energy stored, determined by applying an overall energy balance for the HTF fluid.

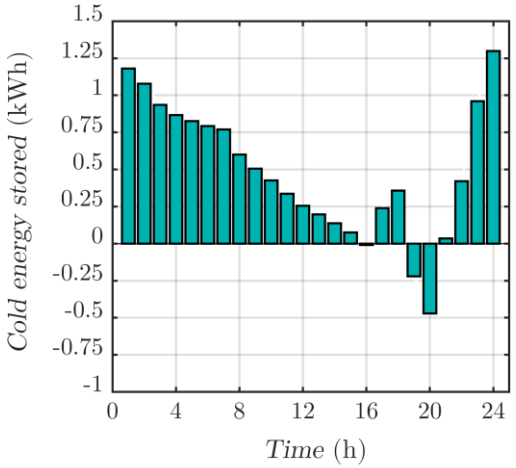

Fig. 5. 9. Hourly average values of PCM cold energy stored

Fig. 5.10 shows photos concerning the PCM dynamic evolution with reference to four time instants, captured every 6 hours throughout the day. From a first analysis it can be noticed that in the solid phase the PCM has a typical appearance of a white wax, while at temperatures above the melting one it results as a

transparent liquid. In detail, after 5 hours, the charging process starts with the PCM solidification around the pipe that are cooled by the circulated cold HTF, as depicted in Fig. 5.10a. Moreover, the amount of solid PCM around the pipes decreases with the height of the thermal storage tank due to PCM liquid convection and stratification effects. In turn, the stratification of the external temperature can also influence this phenomenon These aspects also underline the importance of a 3D model to describe the problem, as it will be shown later. Further, the heat transfer fluid HTF – which enters the storage tank from the lower plenum – performs a heat transfer with the PCM at the base of the storage system. Therefore, the PCM at higher levels will thermally interact with the HTF at a higher temperature – with temperature profiles closer and closer and consequently with a reduction of the heat transfer rate. Furthermore, this aspect suggests that a clear stratification phenomenon occurs – due to the differences in the density of the phase change material along the height of the component – based on the physical dimensions of the storage system. After 11 hours the PCM has completed the charging phase and as can be seen from Fig. 5.10b, the amount of PCM in the solid phase has increased. The gradual discharge phase starts after 11 hours. In detail, the liquefaction of the PCM, see Fig. 10c, affects the upper section of the storage system.

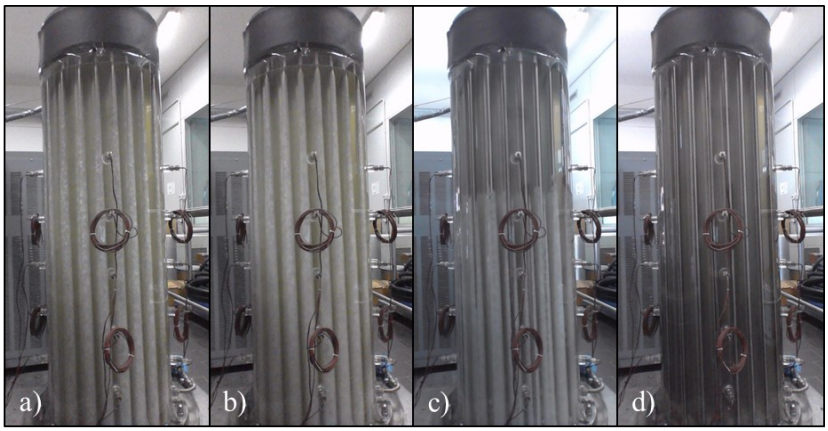

Fig. 5. 10. PCM solid/liquid transition inside the shell-and-tube thermal storage, after: a) 5 h; b) 11 h; c) 17 h; 23 h

The melting front behaves differently on the exchanger surface due to the natural convection flow developed in the liquid phase. Finally, after 23 hours the discharging process is almost completed, as shown in Fig. 5.10d. However, the PCM near the lower plenum is still in solid phase, because of the conduction heat

transfer with the upper plate of the lower plenum. To summarize, during the charging process the PCM on the shell side does not completely change phase. Thus, just a fraction of the total amount of the PCM is subjected to the solidification.

5.1.3. Methodology

A first modelling approach avoids imposing explicitly the Stefan condition at the solid-liquid interface and therefore uses a single-domain (or fixed-grid) model. Phase-field methods [107] and enthalpy methods are the most commonly used single-domain models [108]. The second modelling approach referred to as the multi-domain (or deforming-grid) method, is based on the classical Stefan two-phase model [109]. Solid and liquid domains are separated and the corresponding conservation equations are solved in each domain [38]. A third technique used to ensure a zero velocity field in the solid phase is the so-called enthalpy-porosity model [37]. In this paper the numerical simulation is carried out by means of the enthalpy-porosity method, whose description is provided in Part I.

Fig. 5.11 presents the melting/freezing temperatures of PureTemp 15, which is obtained by differential scanning calorimetry (DSC Q2000 V24.8 Build 120) under a heating/cooling rate of 1 °C/min. In detail, Fig. 5.11 shows the PCM onset/end-set, *i.e.,* intersection point of the extrapolated baseline and the inflectional tangent at the beginning/end of the melting or crystallization peak [110]. Hence, in this study – according with the DSC analysis – we assume that phase change material temperature during melting and solidification is similar, which is reasonable for the present PCM that has a melting temperature of 13 °C and a solidification temperature of 15 °C. Likewise, the phase change interval is derived from the DSC and set equal to 1.5 °C.

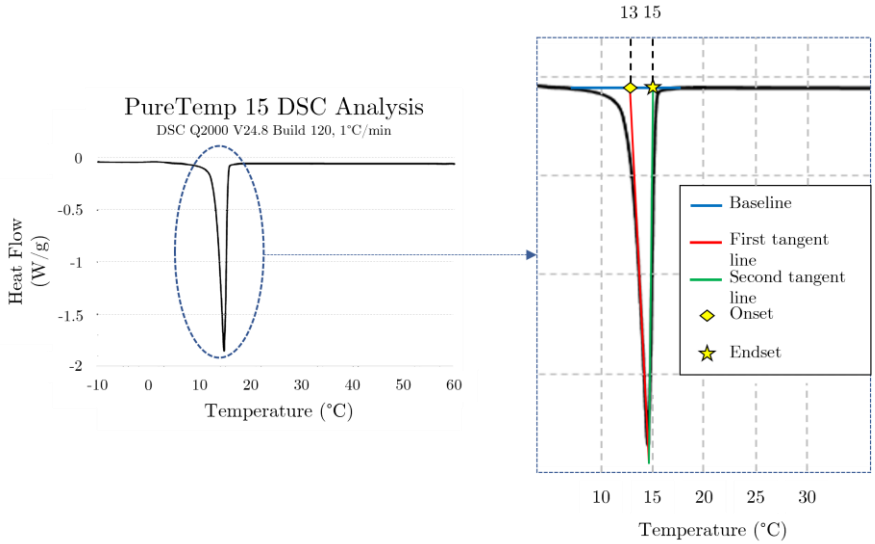

Fig. 5. 11. PureTemp 15 DSC analysis: identifying onset (13 °C) and endset (15°C) temperatures

On account of the dynamic nature of the case study, a set of initial conditions is shown below. The assessment of these conditions, however, often requires simplifying assumptions. Indeed, the finite element approach requires an appropriate compromise between the results accuracy and the computational costs.

In the previous subsection, PCM governing equations have been shown. However – based on the geometric entity concerned – the model definition has to be enriched with the equations that concern the additional components of the storage system: water and stainless steel that separates water from the PCM. For the steel domains the transient heat conduction equation is here presented:

$$k_{AISI316}\nabla^2 T = \rho_{AISI316} c_{AISI316} \frac{\partial T}{\partial t} \tag{5.1}$$

where, $k_{AISI316}$, $\varrho_{AISI316}$, $c_{p\ AISI316}$ are respectively the thermal conductivity, the density and the specific heat of the material, t is the time and T the temperature. Since modeling the HTF requires extra computational time and effort, in detail – to avoid the tube-inside flow simulation – a convective heat flux, *i.e.,* product between the convective coefficient on the water side (Eq. (5.2)) and the temperature difference between the wall and the fluid average, *i.e.,* $T_s - T_{int}$, is here defined.

$$h_{int} = 3.66\frac{k_w}{D} \qquad for\ Re_D \leq 2500 \tag{5.2}$$

We also remark that the fluid average temperature is here computed as the average between inlet and outlet temperatures T_{in} and T_{out} for each timestep considered during the simulation. As reported in Eq. (5.2), the convective heat transfer coefficient (h_{int}) is a function of the Reynolds number (Re), in turn, depending on the tubes geometry, fluid properties and velocity. For the case at issue, fixing the fluid velocity and the tubes diameter, Re_D depends just on the fluid viscosity and density. However – for the treated temperature range (7-22 °C) – these properties are such as that the Reynolds number is always below 2500, *i.e.,* laminar flow. As will be shown further on, by applying the correlation in Eq. (5.2), we assume that entrance effects are negligible, which is a reasonable assumption for the established boundary conditions. To validate this approach, in which a heat transfer coefficient is used instead of the whole tube simulation, we have run a simple 2D case of the whole heat exchanger in which we have neglected liquid convection inside the PCM, *i.e.,* only heat conduction in the PCM has been considered, with and without the CFD modeling of the HTF. The results are illustrated in Fig. 5.12, which provides clear evidence of the proposed method accuracy.

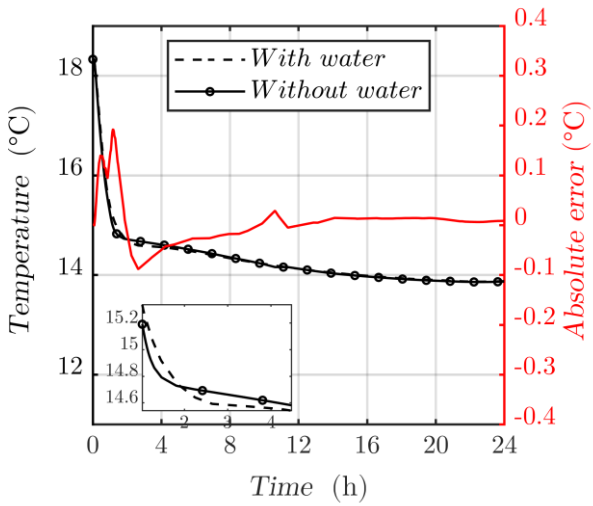

Fig. 5. 12. Comparison between the temperature profiles with and without water simulation, for a 2D single tube model

As a result, the two profiles – referred to the central thermocouple (TC) – are almost coincident, with a maximum absolute error of 0.2 °C. Thus, the slight difference between these two cases confirms that the heat transfer inside the PCM has a higher influence than the interaction PCM-HTF. As concerns the plexiglass shell, the conductive resistance R_k is far lower than the external convective one, so that it can be neglected in the model geometry. To clarify – adopting a thermal conductivity $k_{iso} = 0.19$ W/m/K – the R_k value is equal to 8.3×10^{-3}. Hence, they differ by one order of magnitude, since the external convective resistance computed is $R_c = 0.080$ K/W. As regard the air-storage system heat transfer, the coefficient (h_{est}) is evaluated as a function of the Rayleigh number (Ra), applying the classical correlation for natural convection on vertical walls – valid when the diameter of the cylinder is so large that the curvature effects are negligible [111] – under the reasonable assumption of uniform temperature, according to Eq. (5.3):

$$h_{est} = \begin{cases} \dfrac{k}{H}\left[0.68 + \dfrac{0.67 Ra_H^{\frac{1}{4}}}{\left[1+\left(\frac{0.492k}{\mu c_p}\right)^{\frac{9}{16}}\right]^{\frac{4}{9}}}\right] & for\ Ra_H \leq 10^9 \\ \dfrac{k}{H}\left[0.825 + \dfrac{0.387 Ra_H^{\frac{1}{6}}}{\left[1+\left(\frac{0.492k}{\mu c_p}\right)^{\frac{9}{16}}\right]^{\frac{8}{27}}}\right] & for\ Ra_H > 10^9 \end{cases} \tag{5.3}$$

The Rayleigh number is function of the shell-and-tube height. Finally, at the top and bottom of the PCM domain, zero-velocity and adiabatic boundary conditions are set. It is worth remarking that the air inside the volume that takes place between the PCM free surface, the lateral shell gap and the upper tube sheet act as poor thermal conductors. Thus, air obstacles the heat transfer, resulting – with good approximation – in an adiabatic condition. Because of the geometrical and physical symmetries, one can reduce the computational domain required by invoking symmetry conditions. The model geometry is represented in Fig. 5.13. The complex geometry has highlighted the need for a simplification by taking advantage of the geometric symmetry. Hence, instead of the entire volume, a portion of 30°, that correspond to 1/12 of the whole model, has been modelled. The modeling of the upper and lower plenum is neglected. All this results in a reduction of the computational burden.

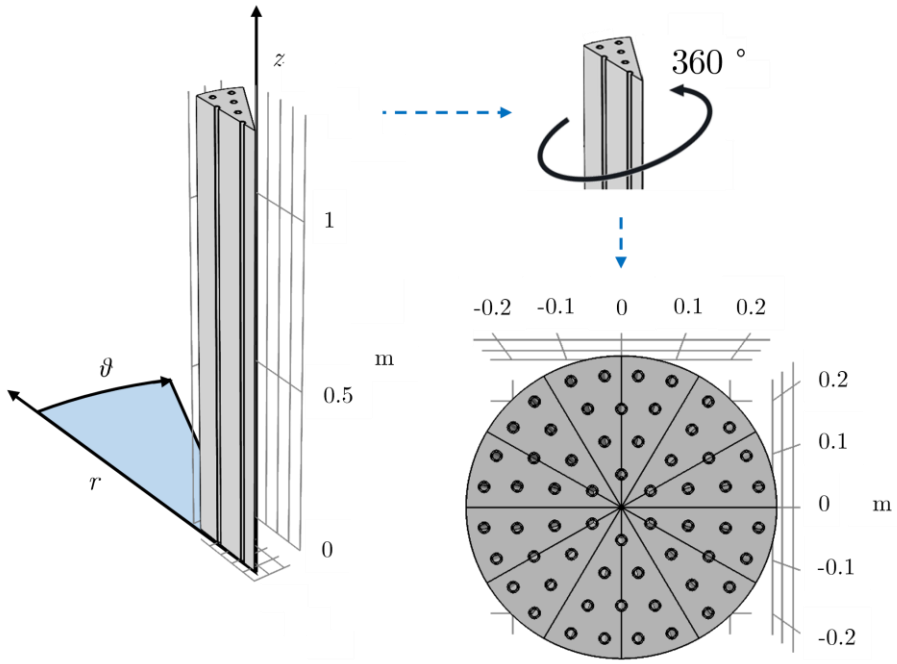

Fig. 5. 13. Geometric representation of the shell-and-tube modeled portion (1/12 of), and its composition to reproduce the real configuration

As aforementioned, at the start of the experimental test, the PCM temperature is not uniform along the heat storage height. Therefore, the temperature at time $t = 0$ along z is set by means of a curve fitting based on the experimental data, according to Eq. (5.4) reported in the following. Hence, the following initial conditions for the temperature and the velocity field are set:

$$t = 0 : \begin{cases} T_{init}\ r, z\ = c_1 z^2 + c_2 z + c_3 \\ u\ r, z\ = 0 \\ for\ 0 \le r \le r_{max}, 0 < H < H_{max}, 0 < \vartheta < \vartheta_{max} \end{cases} \tag{5.4}$$

where $C_1 = -2.33$, $C_2 = 7.47$, $C_3 = 16.43$, are derived at $t = 0$ with a non-linear regression from experimental data with a $R^2 = 0.99$. At $t > 0$, the boundary

conditions – for both charging and discharging process – are set according to the experimental tests. In the following, a resume of the heat transfer boundary conditions mathematical expressions are reported. The heat flux related to the PCM-HTF interface, *i.e.,* q_{INT}, is applied to the domains pointed out in blue in Fig. 5.14a. The second and third terms of the equations set (Eq. (5.5)) are referred to the lower and upper domains of Fig. 6.14b, whereas the face highlighted in Fig. 5.14c is exposed to the flux linked to the ambient conditions ($q_{LAT,ext}$). In detail, q_{SUP} is supposed equal to zero since it is referred to the PCM free surface, that is adiabatic for assumption as already reported. Finally, the last boundary condition is adiabatic, given the thermal symmetry. The domains subject to this condition ($q_{LAT,sym} = 0$) are the ones marked in Fig. 5.14d.

$$t > 0 : \begin{cases} q_{INT} = h_{int}(T_{int}\ t\ - T\ t, r, \vartheta, z\ ) \\ q_{SUP} = 0 \quad for\ 0 \le r \le r_{max}, z = H_{max}, 0 < \vartheta \le \vartheta_{max} \\ q_{INF} = 0 \quad for\ 0 \le r \le r_{max}, z = 0, 0 < \vartheta \le \vartheta_{max} \\ q_{LAT,ext} = h_c(T\ t, \vartheta, z\ - T_{amb}\ t\ ) \\ for\ r = r_{max}, 0 \le\ z \le H_{max}, \quad 0 < \vartheta \le \vartheta_{max} \\ q_{LAT,sym} = 0 \quad for\ 0 \le r \le r_{max}, z = H_{max}, \vartheta = \vartheta_{max} \end{cases} \tag{5.5}$$

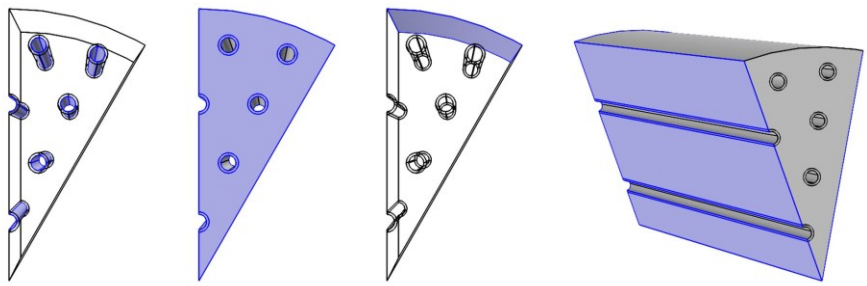

Fig. 6. 14. Computational domains selection for heat transfer boundary conditions: from left to right 1) heat flux q_{int}; 2) heat fluxes q_{sup}, q_{inf}; 3) heat flux $q_{LAT,ext}$; 4) heat flux $q_{LAT,sym}$

The mathematical expressions for the fluid dynamic boundary conditions related to the PCM are the following. Since the model definition involves the pressure only through its derivatives, a relative pressure point constraint $p_0 = 0$ is defined in order to specify a zero-reference relative pressure at least at one point, as in Fig. 15a. A no-slip boundary condition ($u = 0$) is fixed on the interface between the PCM and the shell, between the PCM and the tank basis and on the tubes' external

surfaces, according to Fig. 5.15b. Finally, a slip condition ($u \cdot n = 0$), *i.e.,* zero velocity gradient, is set on the marked surfaces of Fig. 5.15c.

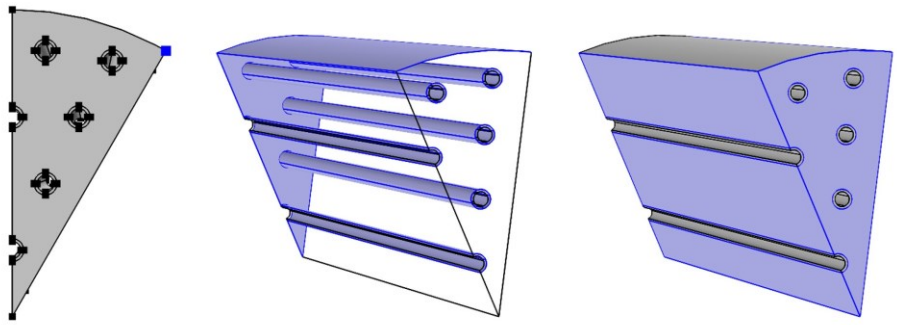

Fig. 5. 15. Computational domains selection for fluid-dynamics boundary conditions: from left to right 1) pressure point constraint; 2) no-slip condition; 3) slip condition

This section describes the computational techniques implemented in COMSOL Multiphysics® software [112]. The coupled system of momentum and energy equations introduced in Section 1.3 is integrated in time using a first-order scheme. All the terms are treated implicitly and the resulting discretized equations are solved using a Newton method [113]. Thus, the governing equations are solved using the Galerkin finite element method. The advantage of this formulation is to allow a straightforward implementation of different types of non-linearities. Therefore, the resolution of those non-linearities is achieved by means of the PARDISO solver, which operates a direct method. As previously mentioned, taking into account the geometry of the system under examination, the model created is 3D. The BDF (backward differentiation formula) is adopted for the time stepping, both for the charging and discharging phases. An initial simulation time step to 10^{-4} s is set, whereas the time step is left free to vary, up to a maximum value of 10 s. By doing this, the software itself performs an automatic maximization of the time step, resulting in a reduction of the computational efforts for the problem solving. In other words, a dynamic time step is set, evaluated by the solver at each iteration as a function of the error value of the previous iteration. The simulation time is set based on the experimental data provided by ENEA at 24 hours. Hence, the simulations are carried out with a workstation equipped with an Intel® Core ™ i7.8700K 3.70 GHz processor and 32 GB and 2133 MHz RAM. As concerns the computational grid, the complete mesh consists of 520823 domain elements, 56663 boundary elements, and 8031 edge elements. In order to perform a correct

evaluation of the properties near the walls – where the gradients are larger – a mesh refinement is implemented by increasing the resolution of the initial mesh. This computational grid is chosen starting from a mesh sensitivity analysis, by which different grid sizes are examined, *i.e.,* coarser, coarse and normal meshes, as depicted in Fig. 5.16.

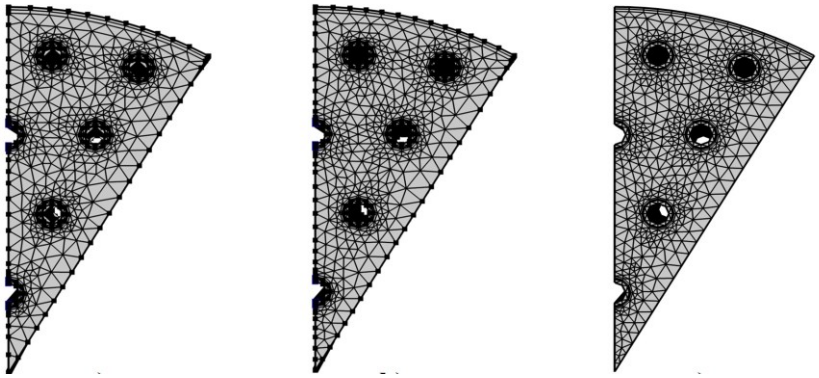

Fig. 5. 16. Computational grid horizontal section: from left to right 1) coarser; 2) coarse; 3) normal

In detail – because of the 3D model complexity – for the grid independence, a criterion of 5% maximum error with respect to the experimental data is admitted for the PCM temperature of $LT,_V$, computed at the time instant t = 7200 s, *i.e.,* 2 h of charging. From Tab. 5.4, it can be concluded that by improving the mesh quality, an error of less than 4% is obtained for the normal mesh case and equal to -3.73% if based on Richardson extrapolation calculation [114]. Moreover, comparing the numerical results varying the grid size, an increase of the mesh size leads to a reduction of the error down to 0.79%. Nevertheless – since running time is deeply affected by the number of cells – the second mesh level results as the most suitable for the present study.

Table 5. 4. Mesh independence

Mesh	Number of cells	$T_{LT,V,num}$ (° C)	$T_{LT,m,V,exp}$ (° C)	Error VS exp (%)	Error VS num (%)	Running time (min)
Coarser	372916	13.56		-9.13	-	184
Coarse	520823	13.81	14.47	-4.56	1.84	231
Normal	1021283	13.92		-3.81	0.79	475
RE		13.93		-3.73	0.07	

In order to evaluate the reliability of the mathematical model presented, an exhaustive statistical analysis is here presented in order to perform a comparison between the model outputs and experimental data. In detail, the following statistical parameters are investigated, namely the mean absolute error (*MAE*) and root mean square error (*RMSE*), estimated according to Eqs. (5.6)-(5.7), respectively.

$$MAE = \frac{1}{N_{data}} \sum_{n=1}^{N_{data}} (T_{num,n} - T_{exp,n}) \tag{5.6}$$

$$RMSE = \sqrt{\frac{1}{N_{data}} \sum_{n=1}^{N_{data}} (T_{num,n} - T_{exp,n})^2} \tag{5.7}$$

Where, N_{data} is the number of temperature values recorded in the experimental tests, and T_{num} and T_{exp} are respectively numerical and experimental temperatures related to a generic instant.

5.1.4. Results and discussions

The following subsection encompasses the presentation of the numerical results relative to the discharging and charging processes of the shell-and-tube heat exchanger (STHE). The statistical errors described in the previous section are here shown and discussed to validate the developed model. A further discussion on the melt fraction referred to three sections along the STHE height is also shown. By doing this, the comparison of the melting interface with the photographic of the heat storage is also discussed. Finally, an outline on the main outcomes and their significance is proposed.

In Fig. 5.17, temperature evolutions for the experimental and numerical profiles are presented for *I*, *III* and *V* levels. The average is employed since no significant deviations have been found, as shown before in section 5.1. Experimental measured temperature is taken as the average over the 4 lateral LT thermocouples for each level. It can be noticed that, since at the beginning of charging the PCM is all in a liquid state, during the first two hours there is a quick decrease of temperature along all the heat storage height due to the water that cools the PCM at its initial temperature. Accordingly, in these first few hours the convection at HTF-PCM interface is the predominant heat exchange mechanism as the temperature difference between them is notable. Moreover, the heat transfer inside the liquid PCM is driven by natural convection phenomenon, as the crystallization of the PCM

around the tubes has not yet occurred. Until 8 hours, due to the progressive decrease of the liquid fraction caused by the solidification, the conduction mechanism becomes the unique mechanism in the solid regions. Afterwards, the numerical temperatures are almost constant and equal to the transition one until the solidification front reaches the measuring points, that happens at different time instant depending on the level on which the lateral thermocouple is housed. In other words, since the temperature gradient between the HTF and the PCM is large, firstly there is a faster rate of heat transfer and the temperature of the PCM rapidly decreases. At the same time, as the PCM starts freezing near the HTF pipe, the heat transfer rate from solid PCM to the HTF is uniform along the axial planes, *i.e.,* vertical plane passing through the tube axis, due to conduction. Thus, the solidification front moves almost parallel to the tube axis. As seen in Section 5.1.3, the slight difference between the solid phase PCM growth around the tube from the bottom to the top of STHE is caused by the natural convection motion inside the liquid fraction. In detail, the charging process finishes after about 8, 17 and 21 hours respectively for the fifth, the third and the first level. Moreover – during that process – the PCM reaches a lower temperature in the model than in the experiments. The comparison between the 3 profiles related to the different levels *i.e., I*, *III* and *V*, confirms that the PCM behaviour changes depending on the stratification phenomena. As a result, at the first level, the PCM is not able to follow the temperature variation of the HTF, whereas the third and the fifth levels profiles exhibit a better adaptation to the experimental ones. On the contrary, as concern the melting process, the heat is transferred from HTF to solid PCM. As PCM melts, the amount of PCM near the pipes rises due to buoyancy forces caused by the natural convection motions. This natural convection loop is responsible for the difference in temperature along the height of the STHE. In order to enhance the convergence, a single T_M value is assumed for the entire model. In this frame, the numerical trends reveal a good matching with the experimental profiles. In detail, the PCM temperature at the first level remains lower than the experimental one, but globally follows the profile variation experienced by the PCM. Conversely, about the trend of Fig. 5.17b-5.17c, the numerical profiles tend intersect or stay above the experimental ones. As regard the third level thermocouple, after t = 17 h the PCM temperature rapidly increases, as a consequence of the external temperature rising. In turn, the trend is influenced by the HTF temperature – which increases drastically – and linked to the fact that the PCM is far from the phase change range. Equally, the numerical model predicts for the last level a temperature profile slightly above the experimental one, with a peak of 21.35 °C instead of the 20.12 °C recorded by the thermocouples. Given the above, it can be stated that for the discharging process the absence of the plexiglass shell in the model geometry

affects the maximum value reached by the PCM. Moreover, the profile inversion – above or below the experimental one – can be explained by the hypothesis of the absence of thermal dilatation (neglected in the model definition). When the melting process occurs, the volume of the PCM increases. Thus, without considering the thermal expansion effect, the model overestimates/underestimates the temperature referred to the upper/lower level.

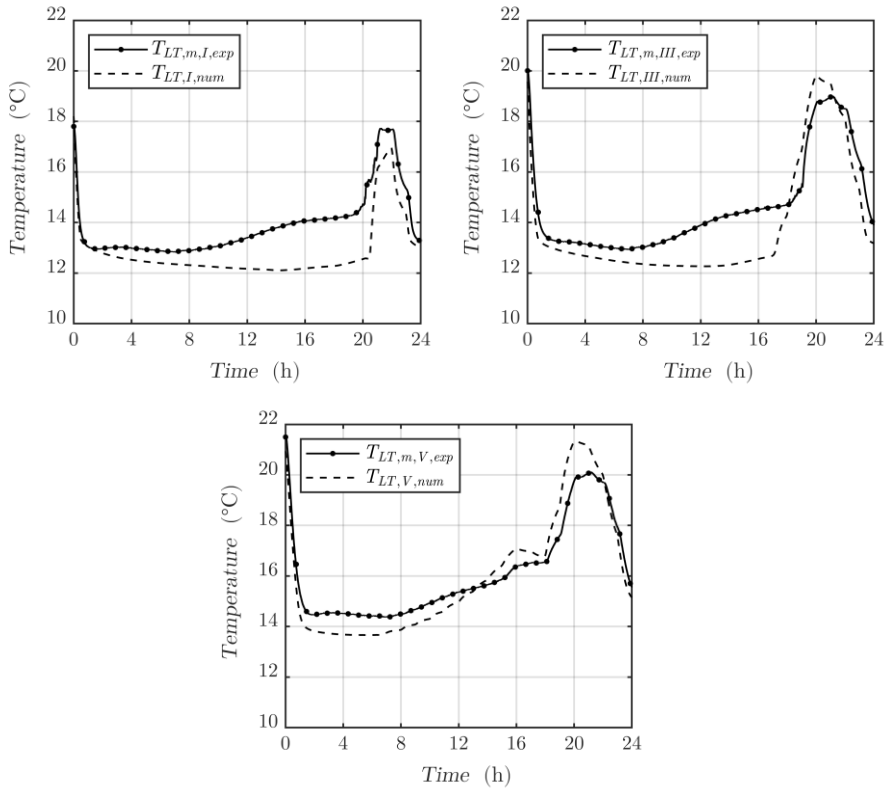

Fig. 5. 17. Lateral thermocouples temperatures temporal profiles referred to: first level (I); third level (III); fifth level (V)

Likewise, with reference to the numerical simulation related to the central axis, Fig. 5.18 shows that the experimental profiles are slightly different because of the aforementioned reasons. Moreover, in this case it can be noticed that at the

beginning the profiles tend to collide – except the one referred to the fifth level – defining a melting range more limited than the one observed experimentally. Notably, looking at the temperature evolution in the center of the tank for levels *I*, *II*, *III* and *IV*, one may notice that the model seems to not perceive the HTF temperature change until 20, 19, 17 and 14 hours, respectively. As the PCM height increases, the heat transferred with the HTF decreases and this affects the charging phase duration. Moreover, a clear evidence is the charging phase temperature difference ranging from level *IV* to level *V*. This should be explained – as aforementioned – considering that the model overestimates the natural convection with respect to the experimental behaviour.

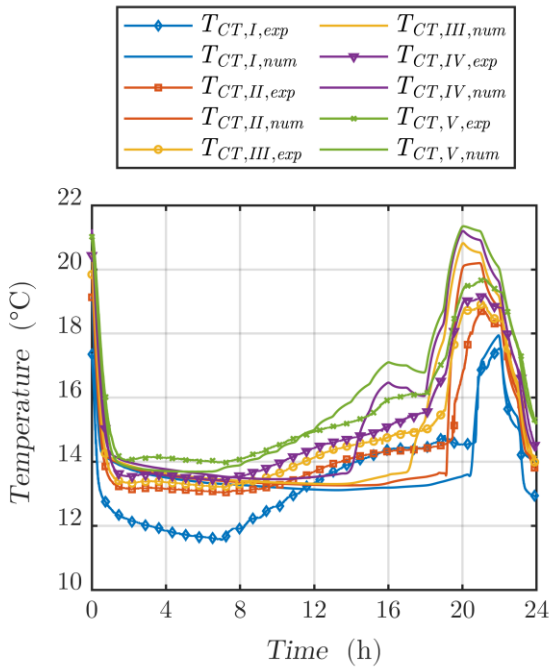

Fig. 5. 18. Central thermocouples temperatures temporal profiles

In order to assess the quality of the numerical model, the statistical parameters through the whole experiment – presented in Section 5.1.3 – are here evaluated. As a result of the previously described trends, it is expected that the model reliability enhances with the increase of the level height. Tab. 5.5 lists the values of the statistical parameters MAE and RMSE relative to the above cases and distinguished depending on the process, *i.e.,* charging and discharging. In detail, the

charging process finishes after about 8, 17 and 21 hours for the fifth, third and first level, respectively. As regards the lateral thermocouples, for both the processes the best numerical case is the one referred to the fifth level (*V*), whereas the one that differs most from the experimental trend is the third level (*III*). Indeed, the maximum mean absolute error (MAE) is referred to the PCM charging process on the third level, while the maximum deviation in terms of root mean square error (RMSE) is related to first one. Nevertheless – with reference to the charging process – the remaining cases, *i.e.,* levels *III* and *V* present a better matching with the experimental trends. In general, larger errors are observed in the last hours of the charging process for each case, when the PCM seems to pursue with the latent heat storage instead of increasing its temperature as experimentally occurs. In addition, the mean absolute error (MAE) referred to the level *V* is quite close to the absolute value of the thermocouple accuracy, *i.e.,* ±0.5, which suggests that the model results are not far from the experimental behaviour. Furthermore, it should be stressed that the comparisons are made between the numerical values and the mean value of the four thermocouples at each level.

Table 5. 5. Statistical parameters referred to the lateral thermocouples at different levels

Process	Location	MAE (°C)	RMSE (°C)
Charging	First level (*I*)	1.08	1.28
	Third level (*III*)	1.09	1.19
	Fifth level (*V*)	0.75	0.78
Discharging	First level (*I*)	0.83	1.06
	Third level (*III*)	0.84	1.04
	Fifth level (*V*)	0.61	0.73

As concerns the STHE central axis, similar findings can be highlighted from the statistical analysis based on the comparison between the simulated temperatures and the measured ones, as summarized in Tab. 5.6. The indices referred to the first level are strongly affected by the experimental temperature trend in the charging process, which clearly diverges from the others, reaching a temperature lower than 12 °C. Apart from this slight discordance of the first level, the result listed in Tab. 5.6 are confirmation of the model accuracy.

Table 5. 6. Statistical parameters referred to the central thermocouples at different levels

Process	Location	MAE (°C)	RMSE (°C)
Charging and discharging	First level (*I*)	1.08	1.3
	Second level (*II*)	1.14	1.28
	Third level (*III*)	1.18	1.33

Fourth level (*IV*)	0.97	1.13
Fifth level (*V*)	0.59	0.8

The characteristic steps of the PCM dynamic behaviour previously described are comparable with the temporal variation of the solid/liquid fraction (φ), numerically evaluated. The solid/liquid fraction evolution is a fundamental parameter since PCMs are well known to store and release energy during phase change, thus monitoring this process is very important. Therefore – consistently with the time instants illustrated – Figs. 5.18 and 5.19 show the changes referred to the temperature contours and melting fronts along the STHE height starting to the lower level ($H = 0.195$ m), through the central ($H = 0.585$ m) and up to the upper level ($H = 0.975$ m). Moreover, an additional level is depicted, *i.e.,* $H = 1.17$ m in order to promote the comparison with the experimental results. For $t = 5$ h and $t = 11$ h it is shown that the lower φ is reached close to the tube because of the lower temperature of the water in the charging phase. Conversely, for $t = 17$ h, in the same areas, the PCM experiences the discharging phase and reaches higher values of φ. The maps clearly indicate that the STHE is affected by a stratification phenomenon, as exhaustively described from Fig. 5.10. In this frame, the analysis of Figs. 5.18 and 5.19 suggests that with the exception of the last time instant *i.e.,* $t = 23$ h, where the PCM is for most fully liquid, the amount of solid PCM around the pipes decreases with the height of the STHE. In detail, the simulation results indicate that the maximum amount of solid PCM is reached after 11 hours and on the lower level, for which the average value of the melt fraction is 0.29. Conversely, at the same time instant on level *V* this value is equal to 0.37. At $t = 17$ h the melting front, starting from the top, has already reached the level *V*. The PCM at the remaining levels is still experiencing the phase change. In depth, the influence of the ambient temperature – accordingly with Fig. 5.10 – is clearly visible on the external tubes, around which the PCM oriented outwards is almost liquid. The difference between the values of φ at levels *I* and *V, i.e.,* 0.51 and 1, respectively, represents the maximum deviation along the 24 hours. Finally, at $t = 23$ h, the melting took place almost completely, except for level *I* and *II* for which the average melt fractions are 0.68 and 0.89, respectively. To summarize, the melt fraction analysis referred to STHE transversal sections clearly shows that, at the current designed configuration, the cold thermal storage does not exploit the PCM latent heat potential. Only the 39% of the PCM mass experience the total charging process, by considering the entire STHE.

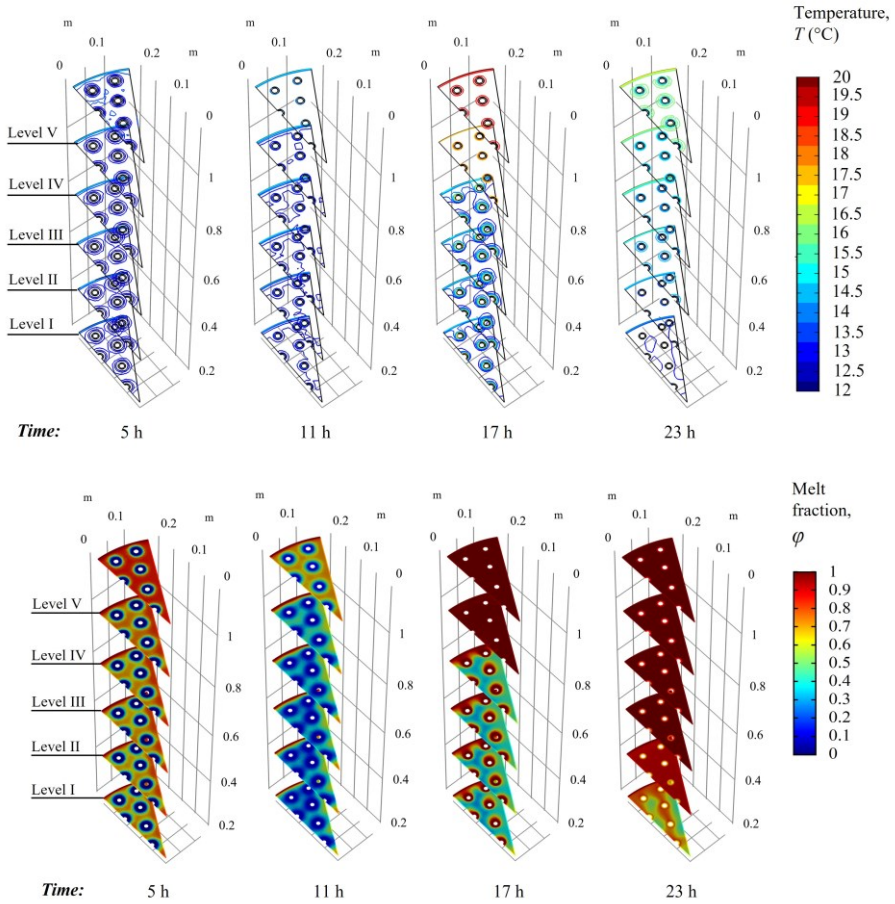

Fig. 5. 19. Temperature contours for different sections at t =5 h, t =11 h, t =17 h, t =23 h

Current solutions to describe PCM charging/discharging processes inside complex thermal storage, *e.g.,* the vertical shell-and-tube heat exchanger (STHE) here presented, are over-simplistic since they perform analysis based on substantial limitations, *i.e.,* conductive-based models, 2D analysis and so on. In this work, a robust model for the prediction of the STHE as a cold thermal energy storage is developed and then validated. Thus, the main guidelines for the model definition and for the tuning of the experimental apparatus are here provided. Therefore, this

work sheds new light on the feasibility of this kind of thermal systems for cold energy storage. The results show that with reference to the STHE geometric parameters, *e.g.,* tube size, tube dimension, shell diameter, the selected amount of PCM does not experience a fully phase change. Therefore, in order to make this storage reliable and suitable for the addressed application, several viable alternatives for improving the PCM melting process should be taken into account. For instance, since the mass flow rate of HTF is directly related to velocity or Reynolds number of the flow, it could have a significant influence on the heat transfer rate. Typically, it influences the overall heat transfer coefficient between HTF and PCM. Therefore, an increase in mass flow rate or inlet velocity of HTF could enhance the heat transfer rate, resulting in a positive effect for the PCM charging process. This should occur by means of a tube diameter variation or by acting on the chiller system. However, in this way, the difference between the inlet and outlet temperature of the HTF reduces, which may not be worthwhile. So, future works should investigate an optimum value of mass flow rate, as a compromise between heat transfer rate, energy stored, and temperature drop or rise of the HTF. Furthermore, on the PCM side, improvements over the current configuration will be aimed at overcoming the bottleneck of the melting/solidification process, represented by the heat conduction in the solid phase. It can be concluded that despite the limitations related to the model and consequently the poor results in the prediction of the first level PCM temperature profiles, our findings do however suggest that the 3D model based on the enthalpy-porosity method is suitable and consider many aspects like boundary conditions variability with both angle and height, which are not usually covered by simplified 2D models.

5.1.5. Final remarks

In this study, experimental and numerical results for a shell-and-tube heat exchanger equipped with water and PCM for cold energy storage are presented. Both charge and discharge phases are here modelled. Experimental results are presented in terms of temperatures monitored in different radial and axial locations of the heat exchanger, showing the importance of both liquid PCM natural convection and density stratification effects. Because of this, a 3D numerical model based on the enthalpy-porosity technique is presented, by studying only a twelfth of the domain with a Robin boundary condition to replace the water flow and height-variable boundary conditions at the exterior.
Based on the experimental evidence and numerical results, the following conclusions can be drawn:

- The propagation of the melt front is strongly affected by the stratification phenomena inside the liquid phase. Therefore, the solid phase distribution nearby the tubes is observed to reduce with increasing height. Furthermore, the liquid PCM does not solidify even if its temperature becomes lower than the freezing point, which limits the cold storage capacity. As a result, the numerical investigation attests that the melt fraction minimum average value – computed on the lower level (I) at t = 11 h – is equal to 0.29.
- The developed model is consistent with experimental results, since the MAE and RMSE values are equal to 1.18 and 1.33 °C, respectively, as concerns thermocouples data. The slight deviations after charging phases have been attributed to a slower response of the model in terms of thermal inertia inside the phase change temperature range. In addition, the difference in temperature along the height of the STHE can be linked to the numerical overestimation of the natural convection motion inside the liquid fraction with respect to the experimental behaviour.
- The 3D model allows to consider the influence of all boundary conditions with both angle and height. Thus, this model can help researchers to further investigate the velocity profile and temperature distribution data of PCMs at various locations for similar conditions. At the same time, the experimental results provide an accurate description of the actual performance of phase change material-based shell-and-tube heat exchanger for cold thermal energy storage, which is dependent on a variable cooling load.
- The numerical simulation confirms that the current STHE configuration does not provide an exhaustive contribution to the chiller system since the PCM on the shell side does not fully experience the phase change, *i.e.,* only about 39%. The reasons for this issue should also lie in the absence of an external insulation layer. It follows that future investigations will focus on the system optimization, by applying numerical algorithms and multi-objective approaches to address different objective functions, related to energy, environmental and economic performance.

5.2. Optimization via genetic algorithm

According to the topic treated in this work, we will mainly introduce latent heat energy storage techniques where HTF (heat transfer fluid) and PCM are not in contact, and case studies addressing air conditioning systems. In this regard, owing to the advantages offered by LHTES (latent heat thermal energy storage), PCMs are used in numerous applications including air conditioning. Some results from literature indicate that the PCM solidifies more quickly in cylindrical shell storages than in rectangular ones, and that the impact of inlet air temperature is more significant than that of air velocity on outlet temperature [115]. The effects of the temperature difference between HTF inlet and PCM melting point and of the HTF inlet mass flow rate on heat charging and heat discharging performance have been numerically studied. The HTF mass flow rate has little influence on the amount of energy stored, but greatly affects charging and discharging time [116]. A case study for replacing the conventional cooling tower using the proposed PCM thermal storage system for a water-cooled air-conditioner shows a coefficient of performance (COP) value increase of about 25.6% [117]. Combined experimental and numerical study has been performed to investigate thermal behaviour and heat transfer characteristics of Paraffin RT50 as a PCM during constrained melting and solidification processes inside a shell and tube heat exchanger. The experimental results show that by increasing the inlet hot water temperature from 70 °C to 75 °C and 80 °C, theoretical efficiency in charging and discharging processes rises from 81.1% to 88.4% and from 79.7% to 81.4%, respectively [118]. The shell and tube configuration used as a LHS unit allows to consider multiple industrial applications for latent heat storage, deals with the numerical analysis of the melting and solidification processes in three horizontal storage units for LHTS using water. In this frame, the inversion of the buoyancy forces in the PCM causes a complex recirculating motion pattern for the considered temperature range, *i.e.,* -4 °C to 4 °C [119]. New performance parameters for PCM thermal storage systems, *e.g.,* energy storage effectiveness, have been defined. This parameter can be used to optimize the design of any PCM thermal storage system to maximize the use of the storage media [120]. Moreover, the energy efficiency ratio is used to indicate the ratio of heat stored by LHSU to the energy consumed in pumping heat transfer fluid, which. It is applied to numerically investigates the characteristics of single shell-and-tube phase change heat storage unit [121].

Generally, several heat transfer enhancement techniques have been proposed, *e.g.,* dynamic melting has been experimentally tested in a cylindrical shell-and-tube heat exchanger (STHX) using water as PCM. This enhancement technique consists of externally recirculating the liquid PCM during the melting process using an external pump, thereby increasing the overall heat transfer coefficient. The experimental results showed that the phase change processes with the dynamic melting technique were 47.4%, 47.8%, and 65.3% faster than the baseline test for flow rates of 0.5, 1, and 2 l/min, respectively [122]. Moreover, inside multi-tube heat exchangers, the influence of the arrangement of inner tubes and metal foam on melting and solidification processes of PCM have been investigated [123]. Melting and solidification rates in pure PCM improve by 41% and 23%, respectively, by modifying the layout of inner tubes, while about 50 % and 33 % in metal foam/PCM composites, respectively. It demonstrates that the inner tube configuration has a greater impact on phase change inside metal foam/PCM composites. Generally, as the number of inner tubes increases, the extra effective heat transfer surface influences the bottom part of the shell, reducing total melting time by up to 29% for the four tubes MTHX [124]. Since the main barrier that restricts the use of PCMs for TES applications is their poor thermal conductivity, tee shaped fins have been suggested as an innovative fin shape to accelerate the PCM melting process in the STHX. The total PCM melting time was reduced by 33% when the tee fins were used, as compared to utilizing the longitudinal fins [125]. Melting and solidification behaviour of xylitol was examined in a vertical double spiral coil heat exchanger [126]. Due to increased convection and a considerable temperature difference between the PCM and the HTF, PCM charging time decreased as HTF inlet temperature increased. Because discharge was mostly regulated by conduction, unlike the inlet temperature of HTF, its flow rate had no substantial impact on the PCM solidification process. The rising attention on heat transfer intensification in shell-and-tube latent heat thermal energy storage units using high conducting fins is proved by the design approach using topology optimization and multi-phase computational fluid dynamics [127]. The design freedom of topology optimization allows the discovery of innovative LHTES designs and elucidates the link between design and physical processes occurring during charging/discharging [128]. A review of the literature indicates that there are many heat transfer enhancement techniques and ways to reduce melting time for LHTES systems. The primary limitation in most referenced works is that many of these enhancement/reduction techniques were analysed individually or combined with only two different methods. There is also a general lack of studies comparing the PCM melting time for different geometric configurations of the LHTES unit. However, a thorough analysis of the effects of

PCM heat transfer enhancement in combination with geometric optimization on the overall storage performance of an LHTES system has been recently addressed [129]. Nevertheless, a comprehensive analysis – based on experimental validation steps – is still lacking. This work points to define an optimization framework to increase the thermal energy storage performance of a PCM-based shell-and-tube heat exchanger. This goal is achieved by investigating the effects of varying chiller operating conditions and main geometrical parameters – via a parametric analysis – and then detecting feasible objective functions, *e.g.,* that accelerate the PCM melting process, for the optimization procedure. A fundamental step consists in the numerical evaluation of HTF inlet temperature and mass flow rate optimal values, to be validated with experimental data. Among all non-dominated solutions resulting from the Pareto front to produce the best combination of charging and discharging time, the one with the shortest geometrical distance from the ideal point that minimizes both objectives, *i.e.,* the utopia point, is selected. Thus, this optimization step is performed with the charging/discharging time as objective functions, which are here proposed as alternatives to the maximization of the energy stored during the charging/discharging phases [130]. Once the optimal operational parameters are defined, the final configuration that ensures the minimum heat transfer area is assessed through a further optimization step.

5.2.1. Experimental facility

The test facility for the experimental campaign is placed in the thermal storage laboratory of ENEA Portici Research Center in Naples (NA). It consists of an indoor equipment designed and realized to perform experimental validations of numerical models for the simulation of cold storage systems with PCMs. In detail, the water chiller provides cold water to a heat exchanger (user) that simulates a single-family cooling thermal load with a floor area of 150 m^2 and located in the Italian climatic zone E [106]. Thermal demands and daily load profiles for summer conditions are taken from Mongibello *et al.* [105]. These data are required to set the boundary conditions for the numerical problem introduced lately. The shell-and-tube cold storage tank is fed by the chiller – by means of a water pump – with the same water mass flow rate flowing through the user, as in Fig. 5.20

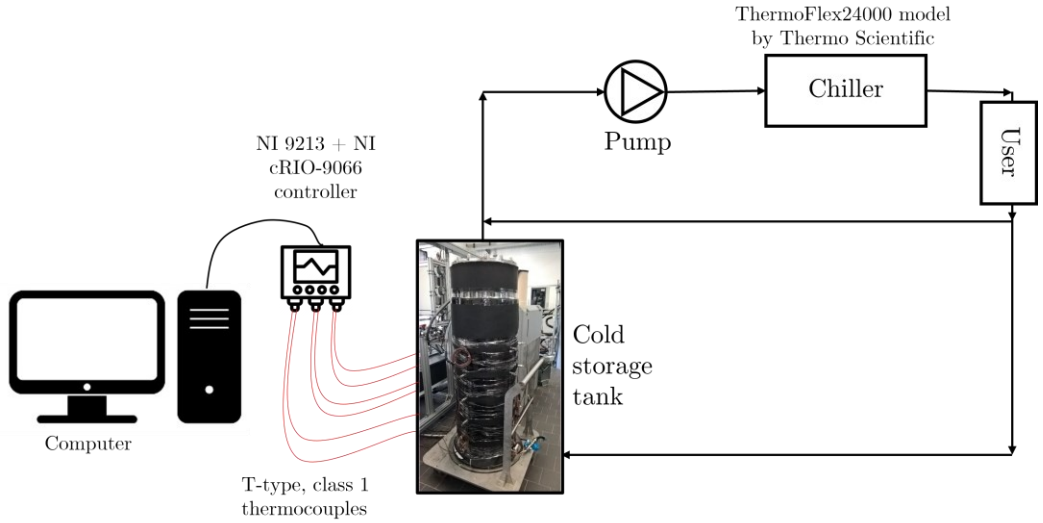

Fig. 5. 20. Schematic diagram of the chiller cooling system

The cold storage tank role is to increase the chiller performance. Without a cold storage system, for a fixed set-point value of the comfort indoor temperature, the chiller cannot work continuously whenever the refrigeration load is lower than the minimum chiller's cooling power because the controller would stop the chiller whenever the internal temperature reaches a certain set-point value. In those hours, the controller of the air conditioning system would execute various stops and restarts, which negatively affect the performance and lifetime of the system components. Therefore, the efficiency of the chiller is under the influence of user load and latent heat storage contribution. In detail, the storage thermal charge and discharge are associated with the user matching with the chiller as well as the PCM content, which results in different heat transfer performances. In other words, in presence of a cold storage system after the user, as shown in Fig. 1, the cold storage is charged when the user's outflow temperature is lower than the PCM solidification temperature, which happens in off-peak periods, and discharged in on-peak periods when the user's outflow temperature is higher than the PCM melting temperature. This helps to reduce the chiller size, reducing the maximum value of the absorbed electrical power concerning the case without cold storage. The present thermal storage tank differs from a conventional shell-and-tube heat exchanger for the absence of plate baffles. The primary fluid – cold water supplied at 1.5 bar by the chiller – enters the exchanger through a 19.05 mm diameter tube, externally

threaded, and tangentially welded to the shell. Thus, water flows through the inlet (lower) plenum. The fluid rises the shell-and-tube tubes bundle, which is realized by 66 tubes made by austenitic stainless steel (AISI 316), as specified in the previous chapter. In detail, pipes belong to Schedule 40 S, with an internal diameter d_{int} of 12.48 mm, an external one of 17.11 mm and a total length of 1400 mm. The tubes bundle layout is defined by a triangular pattern. After flowing through the tubes, water enters the outlet plenum equipped – as well as the inlet one – by a 19.05 mm diameter tube, externally threaded and tangentially welded to the shell. Moreover, the upper plenum is integrated with a tube-side vent valve (d_n = 15 mm) at the highest point of the heat exchanger to control inlet and outlet flow and to remove trapped air. The PCM is surrounded by a transparent Plexiglas shell with an internal diameter d_{shell} of 480 mm, a height L of 1350 mm, and a thickness s_{shell} of a 5 mm. The transparency of the shell layer plays a key role in the visualization of the PCM dynamic behaviour during the thermal transient. The main features of the latent heat thermal energy storage are listed in Tab. 5.7, where $T_{in}(t)$ and $T_{PCM}(z)$ are the inlet water temperature and PCM temperature distribution, defined later.

Table 5.7. LHTES parameters

System parameter	Value
Tube length (mm)	1350
Tube number	66
Inner tube diameter (mm)	17.1
Tube thickness (mm)	2.31
Mass flow rate (kg/s)	0.075
Inlet temperature (°C)	$T_{in}(t)$
Initial PCM temperature (°C)	$T_{PCM}(z)$

The PCM temperature distribution is caught using 17 class 1 T-type thermocouples with an accuracy of ± 0.5 °C. The thermocouples are placed orthogonally with respect to the shell surface and arranged on 5 levels, *i.e.,* cross-section, each one spaced by 195 mm starting from the bottom, as depicted in Fig. 2. The first set of thermocouples, *i.e.,* central (CT), measures the temperature on the shell-and-tube central axis, while the second one, *i.e.,* lateral (LT), collects the data referred to the half-length of the radius. The central thermocouples are one on each level, instead of the lateral one – consecutively spaced about 90 degrees in counter-clockwise order – arranged on Level *I*, Level *III,* and Level *V*. Thus, the odd levels are equipped with 5 thermocouples (1 central and 4 lateral), while on the remaining ones there is only the central thermocouple.

5.2.2. Materials and methods

The approaches for the numerical modeling of the PCM storage under investigation are discussed in this section. Hereafter – in distinct subsections – geometry, governing equations, boundary/initial conditions, resolution method, and the model calibration process are described. In Fig. 5.21, the layout of the 2D domain here investigated is shown.

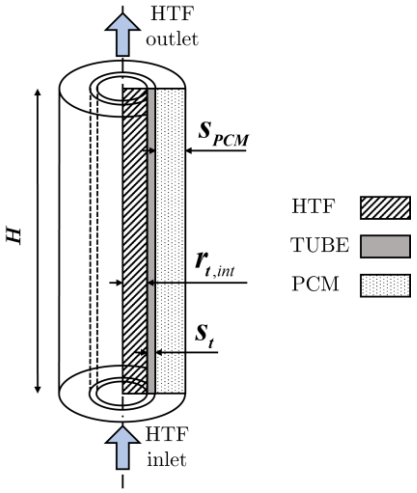

Fig. 5. 21. 2D geometry for the numerical model

The hypotheses of the 2D model are supported by this external insulation layer, *i.e.,* 2.5 cm elastomer with thermal conductivity of 0.04 W/m/K. Therefore, the thermal resistance associated with using this insulation layer of 2.5 cm thickness is equal to 0.37 K/W. In this regard, thanks to the elastomer there is a weak influence of external conditions, which cannot be considered in the 2D numerical model. The geometry considered is based on a cylindrical control volume around a single pipe of the tube bundle. The thermophysical properties of PCM, stainless steel, and water are presented in Tab. 5.8. The PCM considered is a biological material, *i.e.,* PureTemp 15, designated as 100 % bio-based by the U.S. Department of Agriculture's bio-preferred program. This PCM is mainly chosen due to its melting point, which is particularly suitable for the cold storage application of this study. The heat transfer fluid (HTF) – cold water supplied at 1.5 bar by the chiller – enters the thermal storage from below.

Table 5.8. Thermophysical properties

Properties	Value
PCM	
T_M (°C)	15
L_f (kJ/kg)	182
k_s (W/m/ K)	0.25
k_l (W/m/ K)	0.15
ϱ_s (kg/m)	950
ϱ_l (kg/m)	860
Cp_s (J/kg/K)	2250
Cp_l (J/kg/K)	2560
μ (Pa s)	4×10^{-3}
β (1/K)	3×10^{-4}
Steel (AISI 316)	
k_{AISI} (W/m/ K)	17
ϱ_{AISI} (kg/m^3)	7500
Cp_{AISI} (J/kg/K)	0.502
Water (T in °C)	
k_w (W/m/K)	$-9.45e^{-6}\ T^2 + 7.3e^{-3}\ T - 0.725$
ϱ_w (kg/m^3)	$-2.6e^{-3}\ T^2 + 1.241\ T + 861.66$
Cp_w (J/kg/K)	$-8.73e^{-4}\ T^3 + 0.097\ T^2 - 34.71\ T + 8.26e^3$

The PCM computational domain is based on the enthalpy-porosity formulation. The mathematical model is established with several reasonable assumptions:

- PCM is isotropic but not homogenous in both liquid and solid phases;
- liquid PCM is modelled as an incompressible Newtonian fluid;
- volumetric expansion during the phase changing process is not considered;
- laminar flow for both HTF and PCM is considered;
- air gap above PCM is not taken into account in the model and considered as an insulating buffer;
- thermal contact resistance at the welded interface between pipes and stationary tube sheets is neglected.

Under these hypotheses and according to the enthalpy-porosity method [37], the numerical model has been set. As aforementioned, due to radial symmetry, only a half of the tube is considered. For the thermal problem on the HTF side, a time-dependent inlet temperature $T_{w,in}$ is defined based on the experimental profile (Fig. 5.22a), and the axial boundary is considered as adiabatic [105].

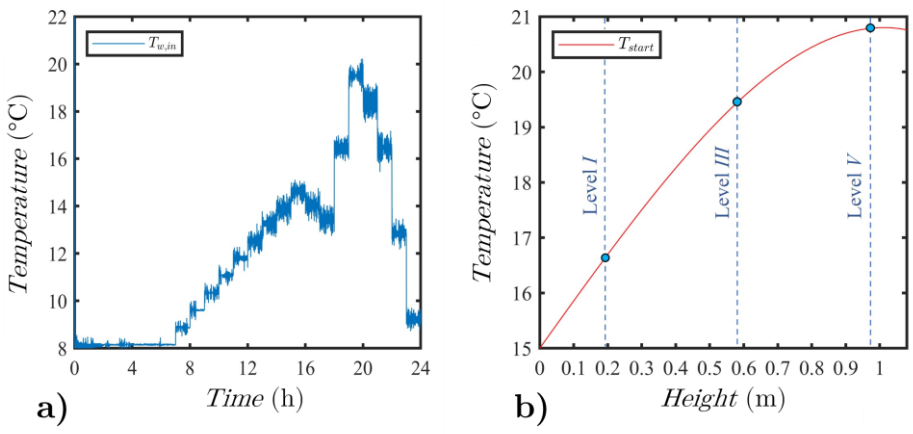

Fig. 5. 22. Temperature profiles a) water inlet and b) PCM temperature fitting

As regards the PCM region – for the sake of simplicity – we consider the horizontal and right-vertical boundaries as adiabatic. To clarify, heat transfer across the upper boundary is neglected because the air volume that takes place between the PCM free surface, the lateral shell gap and the upper tube sheet acts as a poor thermal conductor. In turn, the one related to the lower plenum is considered adiabatic because of the limited length of this part with respect to the vertical one. Since the experimental tests reveal that temperature distribution at $t = 0$ is not uniform, we fit the experimental data with cubic polynomial, with a coefficient of determination (R^2) equal to 0.99, as in Fig. 5.22b. Boundary conditions for the momentum equation resolution are consistent with the problem formulation: no-slip conditions on boundaries PCM laps stainless steel, while slip condition on the upper and lateral boundaries.

Governing equations together with the boundary conditions are numerically implemented and solved with a finite element commercial code. In detail, the coupled system of momentum and energy equations is temporally integrated according to a first-order scheme. The resolution of the model non-linearity is achieved by means of the PARDISO solver, which implements a direct method. The BDF (backward differentiation formula) is adopted for the time stepping. An initial simulation time step to 10^{-4} s is set, whereas the maximum time step is left free to vary up to 5 s. In this way, the software itself automatically maximizes the time step, which leads to a reduction in the computational effort required to solve the problem, *i.e.,* a dynamic time step is defined, which is evaluated by the solver

at each iteration of the error value from the previous iteration. A tolerance value of $1e^{-3}$ has been used, which ensures a mean absolute error (MAE) of 0.014 °C with respect to the temperature values computed on the lower thermocouple position with a fixed timestep, *i.e.,* 0.5 s. For the parametric analysis the simulation time is set based on the experimental data provided by ENEA at 24 hours, whereas for the optimization procedure a total running time of 72 hours is selected, since periodic conditions for the PCM charging/discharging phases are reached only after the end of the second day. All cases examined are calculated through a workstation equipped with an Intel Core ™ i7-10700KF 3.80 GHz processor and 64 GB and 2133 MHz RAM. Grid convergence has been verified before running validation and optimization procedure to find compromise between model accuracy and running times. Thus, three mesh levels are set for the independence test, made by boundary-layer triangular elements with boundary refinement, as depicted in Fig. 5.23.

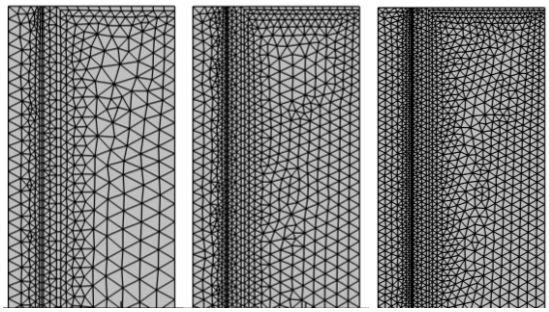

Fig. 5. 23. Computational grid for the model upper part: a) coarse level; b) normal level and c) fine level

In detail, about 19200, 31000 and 48600 elements with a minimum quality of 0.3885, 0.4259 and 0.436 are employed for coarse, normal, and fine mesh levels, respectively. Results of grid test are presented in Tab. 5.9, through a comparison on the temperature value at $y = 0.175$ m, $r = 0.017$ m, for the case with $T_M = 13$ °C and $\Delta T_M = 2.5$ °C, at the time instant $t = 8$ h.

Table 5.9. Mesh sensitivity (experimental: $T_{LT,m,I,exp} = 11.94$ °C)

Number of cells	$T_{LT,I,num}$ (° C)	$\text{Error}_{exp\text{-}num}$ (° C)	Running time (min)
19210	11.88	0.06	32
31084	11.91	0.03	45
48624	11.92	0.02	63

Tab. 5.9 clearly shows that the error for each mesh level is lower than 0.06 °C. Thus, despite all the mesh levels are suitable in terms of accuracy, the computational effort – which is crucial for the optimization procedure – considerably varies with the number of cells. As a result, the mesh level with 31084 elements is selected as a trade-off between accuracy and running times.

5.2.3. Experimental results

According to the experimental facility's description, the PCM experimental behaviour related to the lateral thermocouples is shown in Figs. 5.24 – 5.26. As aforementioned, these thermocouples are placed on three stages, *i.e.,* $H = 0.195$ m, $H = 0.585$ m, $H = 0.975$ m. Introducing the parameter $\gamma = H/L$ – where H is the actual height and L is the tubes length – Level *I*, Level *III,* and Level *V* can be associated to $\gamma = 0.14$, $\gamma = 0.43$, and $\gamma = 0.72$, respectively. The analysis of Figs. 5.24 and 5.26 reveals a marked difference between the PCM temperature trends on the same level, with reference to Level *I* and Level *III*. This difference – which reaches a value higher than 2.5 °C for $t = 7$ h on Level *I* – can be explained by referring to the influence of the lower plenum, the HTF non-uniform distribution inside the tube bundle. Notably, for $\gamma = 0.72$ these effects are mitigated, except for the influence of thermocouple accuracy, which can be clearly observed. Moreover, although the PureTemp15 PCM theoretical solidification temperature is 15 °C, the experimental results show a non-negligible sub-cooling. This means that PCM continues to store sensible heat as crystallization has not yet started. In detail, Fig. 5.26 shows that – on average – the actual melting point value is around 12 °C, and for the last thermocouple position the PCM crystallization starts at a temperature of 0.5 °C below this value. However, this sub-cooling phenomenon is small if compared to the overall temperature changes, and therefore it will be not included in the numerical model. Beyond this, the first and the last thermocouple, *i.e., LT,1* and *LT,4*, reach lower temperature values, which can be explained considering the propagation of the solidification front around the tubes. When the thermocouples hot junctions are reached by the solidification front, an evident temperature change occurs. Generally, in the first hours, natural convection is the leading mechanism. Then, the inner layers, *i.e.,* the closest to the tubes, start to crystallize thanks to the PCM mixing motions. In other words, since the liquid fraction continues to decline, conduction becomes prevalent. Therefore, looking at Fig. 5.26, *LT,1* and *LT,4* thermocouples are quickly reached from the solidification front and the material phase change on these positions does not last long due to the high value of

the phase change temperature interval. Due to the established conduction mechanism, these PCM regions are more sensitive to the water temperature variation and then after the 7$^{\text{th}}$ hour they are strongly affected by the step-trend of the water temperature inlet profile. The described phenomenon can be explained considering a water non-uniform distribution inside the tubes bundle or assuming a variation in the effective position of thermocouples. In the first case, the heat transfer should be not uniform in the plane, *i.e.*, Level *I*, and then resulting in a different PCM behaviour along the angle. In the latter case, being closest to the tube, these positions should be easily reached by the solidification front.

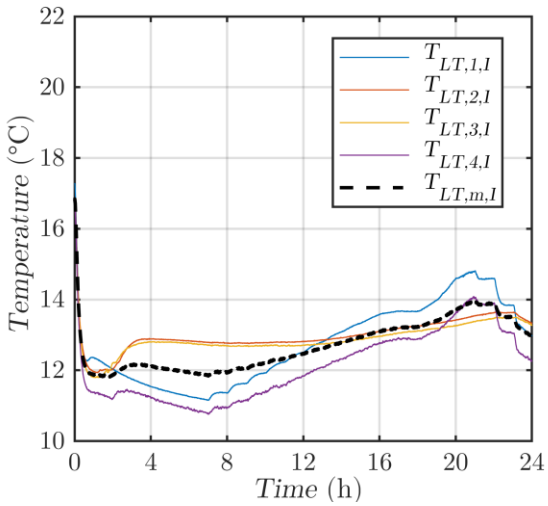

Fig. 5. 24. PCM experimental temperatures: lateral thermocouple on first level

The charging phase ends up at $t = 7$ h, after which the PCM temperature slowly rises. At $t = 18$ h – for *LT,1* and *LT,4* locations – the PCM is reached from the melting front and temperatures rise faster. Nevertheless, on average, the PCM on this stage seems to not experience an effective discharge phase. This happens because, despite the inlet water temperature ramp is changing, the propagation of heat into the medium is limited in time, *i.e.,* thermal diffusivity. Moreover, while the ramp changes the temperature distribution is not uniform. Likewise, looking at Fig. 5.25, the PCM phase transition occurs at $T = 12.5$ °C, and only a fraction of the overall material carries out a limited discharging phase. The overall trends almost reply to the ones from the lower level, which suggests that – among the possible causes for the deviation from the general trend – the most reasonable one should be a non-uniform water distribution.

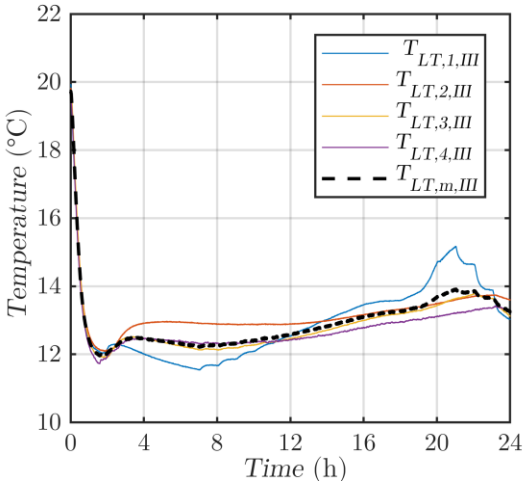

Fig. 5. 25. PCM experimental temperatures: lateral thermocouple on third level

Finally, as regards the PCM temperature profiles on the fifth stage (Fig. 5.26), the first detail that stands out is certainly almost homogenous PCM temperature evolution. This suggests the distance from the lower plenum as an additional factor that could affect the phase change process.

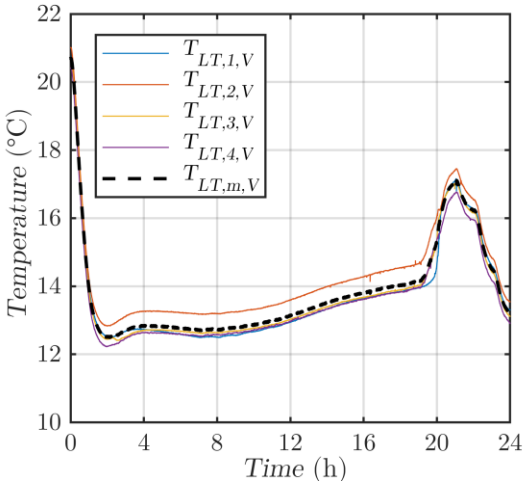

Fig. 5. 26. PCM experimental temperatures: lateral thermocouple on fifth level

The PCM farthest from the plenum is less affected by the thermal disturbance, *i.e.,* variation of the water temperature.
At the same time, heat propagation is associated either with the interaction with the pipes, or with the underlying PCM portions, characterized by low thermal diffusivity (high specific heat and low thermal conductivity). Here the average melting point results approximately equal to 12.5 °C, and the sub-cooling looks less pronounced. Moreover, differently from the above cases, all the PCM that lies on this level experiences a complete discharging phase, reaching at $t = 21$ h a mean temperature value of 16.78 °C. Since *PureTemp 15* PCM main features, *e.g.,* melting point and melting range, differ depending on the phase process, *i.e.,* charge/discharge phases [42], the calibration of these parameters is an essential preliminary step for the parametric analysis and optimization procedure. Both steps ask for a single-run process that includes the PCM charging and discharging phases. Therefore, we need for the definition of a single value of T_M and ΔT_M. This results in a trade-off between the model accuracy with respect to charging and discharging phases. To select the most suitable solution for the overall simulations, a sensitivity analysis is performed. Generally, this step – on the experimental data – is performed in terms of temperatures or energy stored. However, in this frame we analyse a 2D single pipe in the place of the entire geometry. The 2D numerical model is defined on an equivalent PCM thickness, which implies that it is not always feasible to link the thermocouples measured value to a numerical trend. In other words, we cannot arbitrarily find a value of the radius such that it corresponds to the real thermocouples position. Therefore, the model calibration is based on the evaluation of the energy stored, which ensures a higher reliability. The energy stored can be evaluated both by means of a balance on the heat transfer fluid (HTF), and with the PCM heat stored (Eq. 5.8).

$$E_{st} = \rho A \left[\int_{T_{in}}^{T_S} c_{p,S}\, dT + \int_{T_S}^{T_L} \left(c_{p,L} + L_f \frac{\partial \varphi}{\partial T} \right) dT \int_{T_L}^{T_{fin}} c_{p,L}\, dT \right] \tag{5.8}$$

where the subscript *in* and *fin* refer to initial and ending conditions, respectively, and A is the PCM area in the longitudinal section. Until the melt fraction does not become one, *i.e.,* PCM fully liquid, the last term is still zero because of the isothermal assumption on the melting process and this continues until all the solid melts. In detail, looking at the first way, it is assumed that the mass flow and the specific heat values of the HTF are constant and equal to 0.075 kg/s and 4.186 kJ/kg/K, respectively.

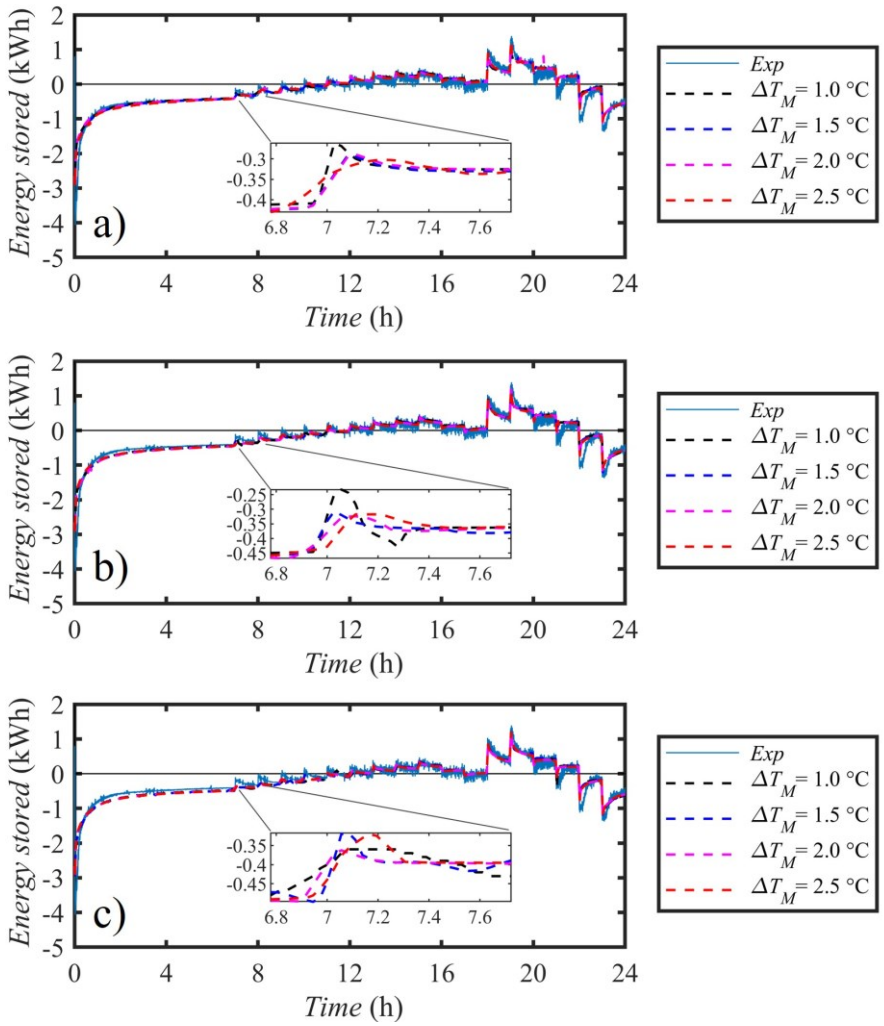

Fig. 5. 27. Cold energy stored VS melting temperature, for: a) T_M=12.5 °C; b) T_M =13.0 °C; c) T_M =13.5 °C

The calibration step aims at detecting the best solution between 3 different melting temperatures, *i.e.,* 12.5, 13.0 and 13.5 ° C and 4 melting ranges, *i.e.,* 1.0, 1.5, 2, 2.5. Therefore, the comparisons between the numerical and experimental trend of the cold energy stored are assessed and reported in Fig. 5.27.

Generally, according to the HTF inlet temperature profile, PCM has a high storage capacity in the first 2 hours thanks to the high temperature differences. The charging process occurs until the twelfth hour, after which the HTF starts to heat the PCM. At this stage the PCM undergoes the discharging phase, which continues – except for the time interval $15 < t < 18$ h – until $t = 22$ h, when the PCM starts heating the HTF again. Looking at the Fig. 5.27, it can be stated that the model is weakly influenced by the melting range (ΔT_M) variation, as confirmed by the first hours of the charging phase, *i.e.,* $0 < t < 7$ hours. As evidence, the numerical trend – fixing the melting temperature (T_M) – does not change with ΔT_M.
The differences become more evident for $t > 7$ h, because of the different PCM reaction to the temperature steps imposed by the HTF inlet temperature, as illustrated in the zoom boxes of Fig. 5.27. Conversely, T_M has a visible effect on the model accuracy, whose amplitude becomes more or less relevant depending on the time interval to which is referred. It follows that, in order to assess the values of T_M and ΔT_M for the following steps, two statistical parameters, *i.e.,* mean absolute error (MAE) and root mean square error (RMSE), referred to the trends described in Fig. 5.27 are estimated according to Eqs. (5.6) and (5.7), respectively. Where, N_{data} is the number of temperature values recorded in the experimental tests, and y_{num} and y_{exp} are respectively numerical and experimental variables related to a generic instant, which are either T or E_{st} depending on whether reference is done to temperature or energy. As seen graphically, it is expected that the model reliability enhances with the decrease/increase of T_M with respect to charging/discharging phase, respectively. In this regard, Tab. 5.10 lists the values of the statistical parameters.

Table 5.10. Statistical parameters ($y = E_{st}$)

T_M (°C)	ΔT_M (°C)	MAE (kWh)	RMSE (kWh)
12.5	1	0.0959	0.1761
	1.5	0.0953	0.1686
	2	0.0913	0.1660
	2.5	0.0943	0.1636
13	1	0.1008	0.1671
	1.5	0.0998	0.1646
	2	0.0979	0.1616
	2.5	0.0914	0.1579
13.5	1	0.1096	0.1682
	1.5	0.1074	0.1617
	2	0.1052	0.1615
	2.5	0.1016	0.1580

The MAE decreases with increasing melting range values (ΔT_M), except for T_M = 12.5 °C, for which at ΔT_M = 2 °C there is the minimum MAE value. Furthermore, the MAE decreases with T_M. Conversely – as regards the RMSE – lower values are referred to higher T_M. As aforementioned, at higher T_M the model in the discharge phase has a better fit on the experimental trend. Thus, looking at the RMSE values it means that this phase has a greater influence the charging one. Consequently, temperature and melt fraction fields of the 2D one-tube model are displayed in Fig. 5.28 to outline which of the analysed cases is closest to the dynamic behaviour of the PCM at the time instant t = 21 h. These figures are obtained with a 250 degrees revolving around the z axis of the 2D model outputs. Experimental results related to Level V (Fig. 5.28) suggest that at t = 21 h the PCM is fully liquid. As can be seen from Fig. 5.28, at t = 21 h the PCM behaviour differs in terms of temperature and melt fraction depending on the selection of T_M.

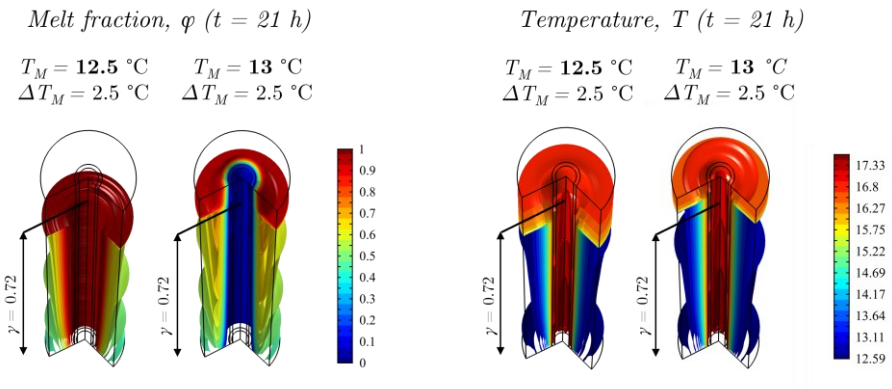

Fig. 5. 28. Iso-temperature and iso-melt fraction plots at γ = 0.72 and t = 21 h, for: T_M =12.5 °C and ΔT_M =2.5 °C; T_M =13 °C and ΔT_M =2.5 °C

For T_M equals to 12.5 °C – at γ = 0.72 – the PCM completely melts. The melt front, which gradually goes down, has already passed the *Level V,* therefore at this height the PCM is fully liquid. Accordingly – for the same T_M – the temperature field for a fixed height above the melt front is almost uniform, except near the tube wall (see Fig. 5.28). In detail, at t = 21 h and γ = 0.72, the PCM mean temperature is equal to 16.78 °C, which is in the range experimentally detected in Fig. 5.26. Conversely, for T_M equals to 12.5 °C, the PCM is going to change phase, with the melt front still above the level highlighted in Fig. 5.28. As a result, the PCM mean temperature is 13.57 °C, considerably lower than the expected value. Therefore, by

selecting T_M equals to 12.5 °C, the PCM faithfully replicates experimental evidence, while numerical simulations with T_M equals to 13 °C do not predict the phase change concurrently with experimental data. This means that for following analyses – in the light of the results of Tab. 4 and the evidence of Fig. 5.28 – the best case is the one with $T_M = 12.5$ °C and $\Delta T_M = 2.5$ °C.

5.2.4. Parametric analysis and multi-objective optimization

The aim of the parametric analysis and the subsequent system optimization is to investigate the influence of each parameter on the model evolution and then identify the configuration that increases the storage performance. Fig. 5.29 shows the flow chart pursued along this work.

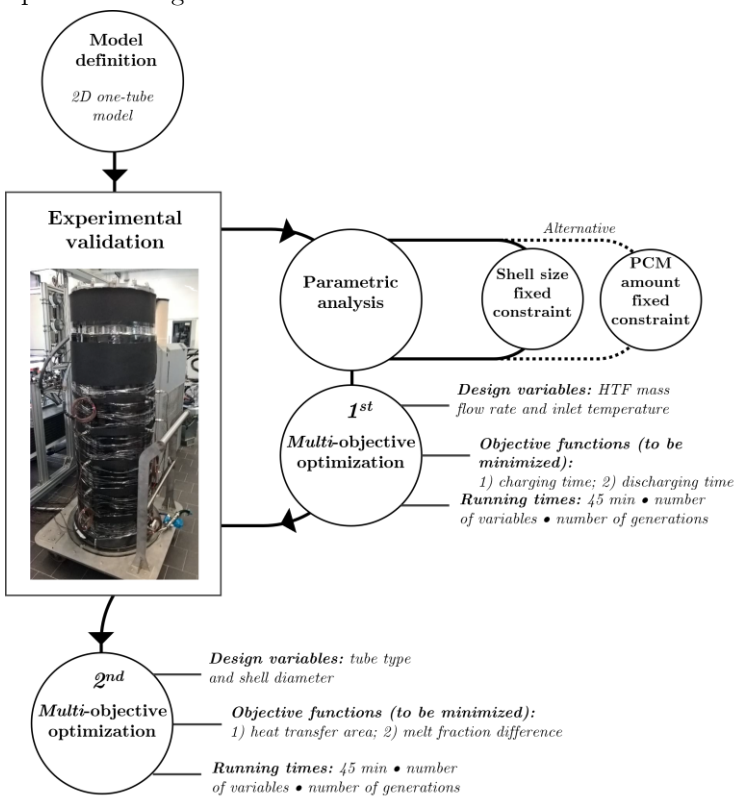

Fig. 5. 29. Flow chart of alternatives for the optimization procedure

It that starts with the definition of the 2D one-tube equivalent model and a first validation process is performed. Thereafter, parametric and optimization procedures are carried out, respectively, followed by another experimental test aimed at proving the procedure reliability. In depth, this graph elucidates two feasible alternatives to make the parametric analysis, which differ depending on whether it is fixed the heat exchanger shell size or the PCM volume. In the first case, the aim is to understand how close the current configuration is to the one that increase the storage performance by fixing the maximum volume made available by the shell. On the other hand – fixing the total amount of PCM – the LTHES geometry is free to vary after defining a certain pipe ratio (γ). As highlighted in Fig. 5.29, this study focuses on the first case, which is mandatory for the successive optimization step. Parametric analysis in the aspect of thermodynamic performance is first conducted to investigate the influence of several design parameters, and then to detect which of them mostly affect the system performance, providing the design variables to be optimized. In depth, genetic algorithm (GA) is employed in this study to perform a multi-objective optimization to maximize the LHTES performance. This goal is achieved by selecting as objective functions (OFs) the charging and discharging times, both to be minimized. By doing this, PCM solidification and melting processes – referred to the periodic conditions – are optimized according to the HTF temperature profile, *i.e.,* maximize the PCM cold storage speed during the charging and the released heat in the discharging phase. The latter have been already selected as OF for the multi objective geometric optimization of PCM-based cylindrical heat sink [131]. However, in such a case, in order to have contrasting OFs, charging and discharging times were maximized and minimized, respectively. Finally, finding the minimum heat transfer area, while allowing the shell diameter and tube type to vary, is the last stage performed in this work to fully exploit the PCM optimum quantity. Therefore, the heat transfer area (to be minimized) and the difference between the melt fraction higher and lower values of the third day (to be maximized) are chosen as the contrasting objective functions.

Tab. 5.11 shows LHTES thermophysical properties used for parametric analysis. The range of each parameter is determined after performing an exhaustive literature review and several preliminary simulations. As concerns the geometrical parameters, we consider only commercially available pipe typologies. The range for pipes' number is chosen as a trade-off between their volume and the volume made available from the shell. The pipe height is seen as the maximum elevation for which the PCM skirts the pipe itself. Finally, each of the parameters linked to the chiller systems is varied based on system regulation criteria, *e.g.,* user load, pipes maximum flow rate, chiller size. In this regard, the mass flow rate is free to vary

from 0.05 to 0.1 kg/s, whereas the water inlet temperature can be reduced about 2 °C, shifting down the entire HTF inlet temperature profile. To elucidate – based on the chiller operation principle – with a fixed user thermal load, a reduction in the HTF temperature provided by the chiller is perceived from the thermal storage as a global reduction of the temperature profile. Therefore, we vary this parameter from the actual value to the lower one to investigate its influence on the thermal storage system. Looking at Tab. 5.11, the parameters are varied in the given ranges while keeping the other ones fixed at the default value.

Table 5. 11. Ranges for parametric analysis

LHTES parameters	Unit	Default	Range	Step
Pipes type	-	3/8 sch 40s	1/4 sch 40s, 1/4 sch 30, 3/8 sch 80s, 1/2 sch 80s	-
Pipes number	-	66	from 62 to 86	4
Pipes height	m	1.08	from 0.88 to 1.23	0.05
Water mass flow rate	kg/s	0.075	from 0.05 to 0.1	0.0025
Inlet temperature difference	°C	$\Delta T_{HTF}(t)$	from 0 to -2	0.25

Therefore, the parametric analysis is based on preliminary hypotheses: we assume that the diameter of the Plexiglas shell is constraint, so that a change in the pipe type implies a variation in the PCM volume around the pipes and thus a different PCM equivalent thickness. In other words – fixing the maximum height of the PCM column (H) – an increase in the pipes' diameter or in their number leads to a reduction in the PCM-equivalent thickness, as shown in Fig. 5.30.

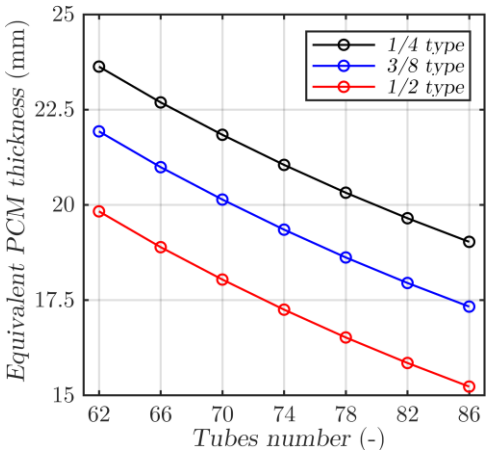

Fig. 5. 30. Equivalent PCM thickness

From a fluid-dynamic point of view, a further limitation is defined by the variation of the HTF flow regime as the selected parameters vary. To apply the hypothesis of laminar flow in the parametric analysis the Reynolds number (Re) must be lower than limit threshold for the transition to turbulent regime, *i.e.,* 2300, in the considered ranges. Given the minimum number of pipes, the minimum internal diameter (1/4 sch 40s), the maximum HTF mass flow rate (0.1 kg/s) and evaluating the properties of HTF at a temperature of 20 °C, the Re is equal to 224.31, which is far smaller than the transition Re.
Multi-objective genetic algorithms (GAs) are powerful tools to achieve optimal Pareto-solutions that enable to perform trade-off analyses under complex conditions. By doing this, users can conduct extensive design investigations in a short period of time based on massive results. GAs are extensively used in various engineering fields, *e.g.,* power generation [132], thermal management [133], energy storage [134]. In this study – to run the GAs – the pre-programmed functions available under MATLAB [78] environment are used and coupled with COMSOL Multiphysics [72] via the COMSOL tool LiveLink™ for the evaluation of the objective functions. The crossover and mutation functions have been modified, and further lines of code have been added to the MATLAB script to save the outcomes of all GA generations. The GA parameters chosen in accordance with earlier research are the following: (i) the population size is chosen to be four times the number of design variables; (ii) the crossover fraction is set equal to 0.6 [132]; (iii) the mutation probability is set equal to 0.1 [132]; (iv) 5% of individuals are selected as elite [132]; (v) the tolerance is left unchanged from the MATLAB default value, *i.e.,* 10^{-6} for multi-objective GA; (vi) the maximum number of generations is set equal to 50.
Performing the GAs allows to save substantial computational times compared to exhaustive research, which are not feasible in this case because each finite element code's simulation requires around 44 minutes, by using a machine equipped with an Intel Core ™ i7-10700KF 3.80 GHz processor and 64 GB and 2133 MHz RAM. Exhaustive research on operational variables, *i.e.,* HTF inlet temperature and mass flow rate, in accordance with the steps listed in Tab. 5.11, requires 21·9·44 = 8316 minutes of simulation, which means fewer than 6 days. By enhancing the design variables' number this value drastically increases. Moreover, the optimization procedure is performed with reference to period conditions that are reached only after the end of the second day of simulation. Thus, the running time is three times a single day run, *i.e.,* 135 minutes, which multiplied by the design variables' combinations amounts to more than 17 days. Therefore, the goal of the genetic algorithm employment lies in a substantial computational saving, as proved hereafter.

5.2.5. Results and discussions

This section elucidates the results concerning the multi-objective optimization performed in this study. For the parametric analysis look at [J2]. Results of the optimization procedure are illustrated and discussed, including their experimental validation. Finally, the configuration with the minimum heat transfer area is determined and investigated, proving deep insights about PCM-based shell-and-tube heat exchangers.

Standards sensitivity analysis, *e.g.,* based on monotonic non-linear correlations are commonly performed because – varying from 0 to 1 – they exhibit how influential are the input parameters on the output functions. The magnitude of the influence – growing from 0 to 1 – is estimated to assess how the variation of the treated parameters affects the objective functions. In this case the parametric analysis allows to discard variables for which the energy stored and melt fraction have varied less. As a matter of fact, while it is evident that the tubes height (H) needs to be increased for obtaining better performance, for the mass flow rate, it is more complicated to determine how much it needs to be changed. Furthermore, in the parametric analysis, each variable is changed while the others stay constant, so the interaction between them is not considered. By choosing mass flow and inlet temperature as design variables, it is also possible to assess the extent to which these two variables interact. Consequently, these variables are chosen to be varied into the genetic algorithm procedure. Fig. 5.31 shows the Pareto front that results from the optimization procedure, considering as objective functions the time to discharge (to be minimized) and the time to charge (to be minimized), both evaluated with respect to periodic condition, *i.e.,* day 3. The optimal point, *i.e.,* $\Delta T_{HTF} = -1.25$ °C, $\dot{m}_{HTF} = 0.095$ kg/s – selected using the utopia criterion – is evaluated as a trade-off between charge and discharge times. The selection of the aforementioned objective functions is driven by the need to consider – at the same time – the benefits of the inlet temperature reduction ($T_{w,in}$) on the charging time, and the disadvantage on the discharge time. Accordingly, shifting down the inlet temperature profile causes a reduction in both the minimum and maximum water temperature, which facilitates the charging process to the detriment of the discharging one. With reference to the Pareto front, the actual start of the charging process is set as the starting instant, rather than the beginning of the day. In this way once the periodicity is reached, the sum of the time intervals, *i.e.,* charge and discharge, is always 24 h.

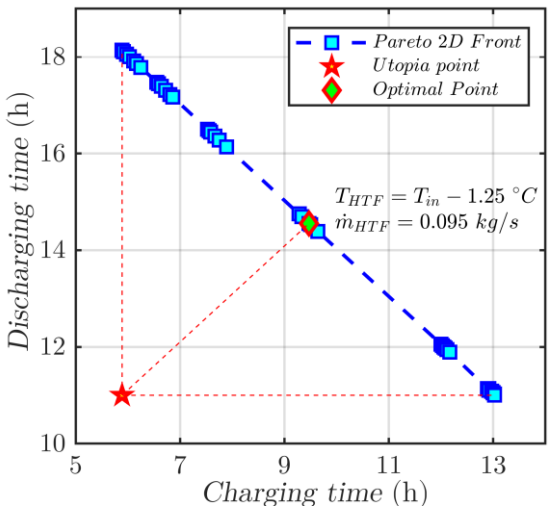

Fig. 5. 31. Pareto front for minimize charging and discharging times

With reference to periodic conditions, Fig. 5.32 shows the results of the optimization procedure applied to the energy stored by the LHTES. In detail, from the analysis of Fig. 5.32, one can note that the minimum value of the energy stored from the initial configuration ($E_{ini,min}$) is – in absolute value – equal to 0.98 kWh, while the optimal one ($E_{opt,min}$), is 1.37 kWh, resulting in a difference of 0.39 kWh. Therefore, the configuration with the optimal design variables reaches a percentage increase of the cold energy stored about 40%. At the same time, with reference to the discharging process, the maximum value reached by the energy stored from the initial configuration ($E_{ini,max}$) is – in absolute value – equal to 0.79 kWh, while the optimal one ($E_{opt,max}$), is 0.87 kWh, resulting in a difference of 0.08 kWh. In this frame, the optimization process leads to a worst result, because of the compromise between charging and discharging processes. Globally, for the initial configuration the difference from the minimum and maximum values is 0.19 kWh, whereas for the optimal configuration is 0.5 kWh.

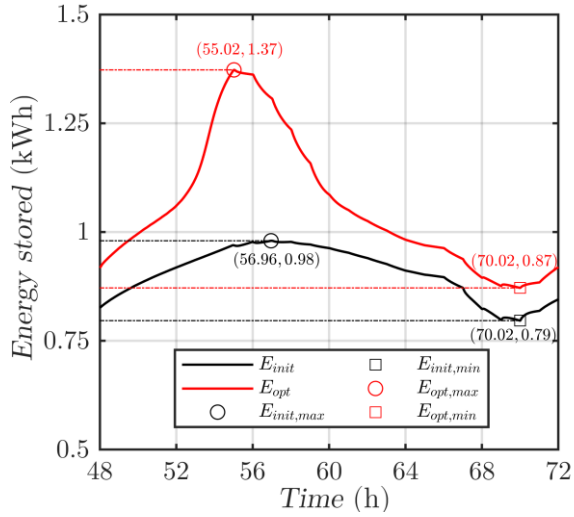

Fig. 5. 32. Cold energy stored comparison

For sake of completeness, we report below the PCM melt fraction with reference to the optimal design variables (see Fig. 5.33). Here are shown several times instant useful to understand the PCM behaviour, *i.e.*, charging start, third day start, charging end, discharging end. In detail, the PCM spends 9.4 hours to fully charge and 14.6 hours to reach the final discharge point. The main outcome derives from the difference between the minimum and maximum melt fraction values, around 0.4 kWh. This means that the amount of PCM that experience a complete cycle of charging and discharging is the 40% of the initial one. Consequently, the next step shown in the following section consists of find the configuration that brings to a complete usage of this 40% of PCM.

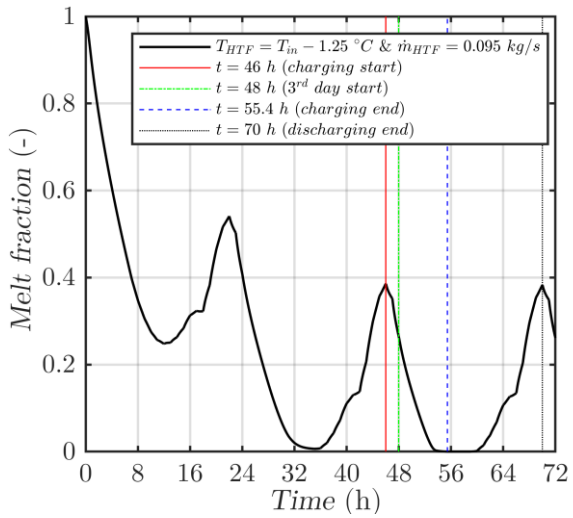

Fig. 5.33. Melt fraction trend for the optimal configuration

5.2.6. Validation and results

Before the evaluation of the minimum surface for the considered thermal storage, a further experimental validation of the procedure for the minimization of charging/discharging time is performed. In detail, Fig. 5.34 shows the temperature trend related to the lateral thermocouples on the intermediate level, *i.e.,* 0.585 m, compared with the analogous numerical data. Furthermore, this figure provides the PCM melt fraction distribution computed every 8 hours. Notably, since a scale factor is applied to these plots in order to make them more compact, they do not represent the effective proportion between tube height and diameter. Looking at the temperature evolution, we can see that the agreement between numerical and experimental trends increases from the first to the last day. This derives from the influence of the environmental conditions, which becomes less relevant over time. Generally, the numerical model tends to underestimate the temperature, especially at the end of the charging phase. Moreover, as further difference, the PCM numerical trend displays a slight delay with respect to the experimental one. The model goodness is proved by the low values of MAE and RMSE, 0.53 °C and 0.70 °C, respectively. To catch PCM phase evolution during the simulation, melt fraction

fields are also presented in Fig. 5.34, for different time instants. In all time instant considered, melting front distortion caused by natural convection makes the field not be orthogonal to the heat flux from the HTF. The amount of PCM that undergoes the solidification process at the end of the charging phase widely varies. According with the melt fraction evolution of Fig. 5.32, at $t = 8$ h the melt fraction is near 0.25, while at $t = 56$ h it is 0.

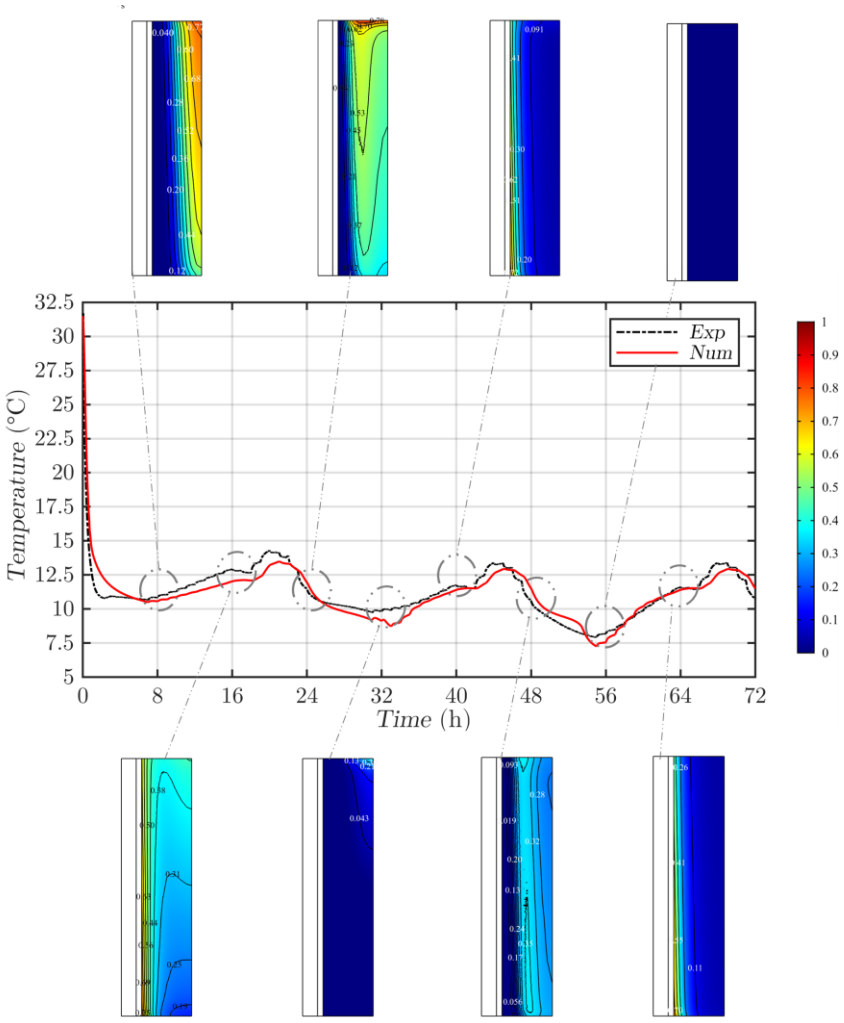

Fig. 5. 34. Validation of the optimized case: temperature distribution on mid-height thermocouple position, and PCM iso-fraction plots every 8 hours

5.2.7. Assessment of minimum heat transfer area

We have found that only the 40% of the PCM experiences a complete charging/discharging process – which is crucial for the system performance. The amount of PCM initially estimated for the storage system is more than enough or, equivalently, the heat transfer surface area is oversized with respect to the PCM and the application. Therefore, the final step consists of finding the minimum heat transfer area that allows to exploit the full potential of the PCM optimized amount, *i.e.,* 40% of the initial one, allowing the shell diameter and the type of tube to vary. By setting all the parameters and increasing/reducing the shell diameter, a reduction/increase in the height of the PCM column around the pipes is obtained. As the shell diameter rises – if the ratio between the distance of the pipes and the shell diameter (L/D) is fixed – this leads to an increase in the equivalent thickness of PCM around the pipes and this negatively affects the charging time (increases) and discharge (decreases). Conversely, if the diameter decreases, the heat transfer surface increases due to a greater PCM height, but a smaller equivalent thickness is defined as it is assumed that (L/D) is fixed. It results in a clear trade-off between the heat transfer surface (to be minimized) and the amount of PCM that melts/solidifies (to be maximized). The effects of the shell diameter size are summarized in the sketch (see Fig. 5.34).

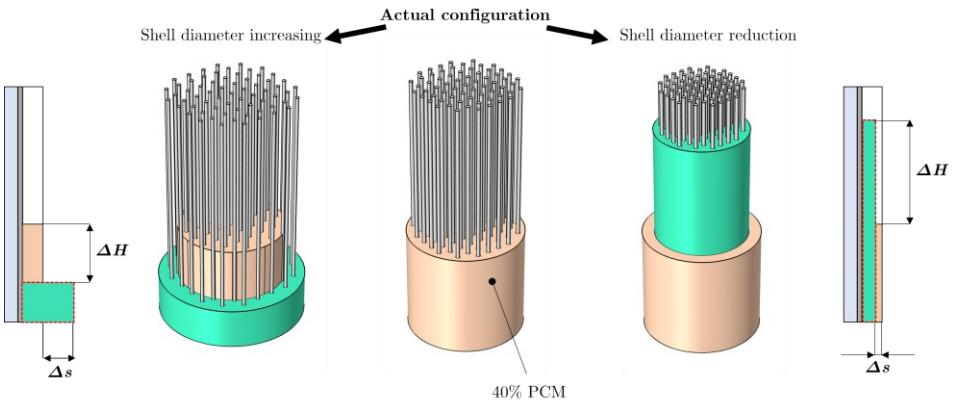

Fig. 5. 35. Influence of the shell diameter's variation on PCM height (ΔH), and equivalent thickness(Δs)

Searching for the minimum heat transfer surface is not a trivial claim since it is strictly linked to the latent heat storage affordability. A reduction in the PCM height brings to the need of shorter pipes, and then to lower costs. Based on the previous factors, we assess the minimum value for the shell diameter – represented by a constraint on the sum of the pipes volume and the PCM one, to be lower than the shell volume. By doing this, the resulting range is from 0.30 to 0.60 m, where the higher value is arbitrarily defined. Moreover, the other design variables are the tube diameter and thickness. Following the commercial availability, seven tube types are identified, as already mentioned in Tab. 5.11. The objective functions selected in this frame are the minimum heat transfer area (to be minimized) and the difference between the melt fraction higher and lower value of the third day (to be maximized). For the sake of completeness, we specify that in the place of the melt fraction difference – to improve the system performance – other alternatives can be performed as objective functions, *e.g.,* feed speed of the melt front, melt fraction daily average value. Fig. 5.35 shows the Pareto front that represents the trade-off between the heat transfer area and the melt fraction difference.

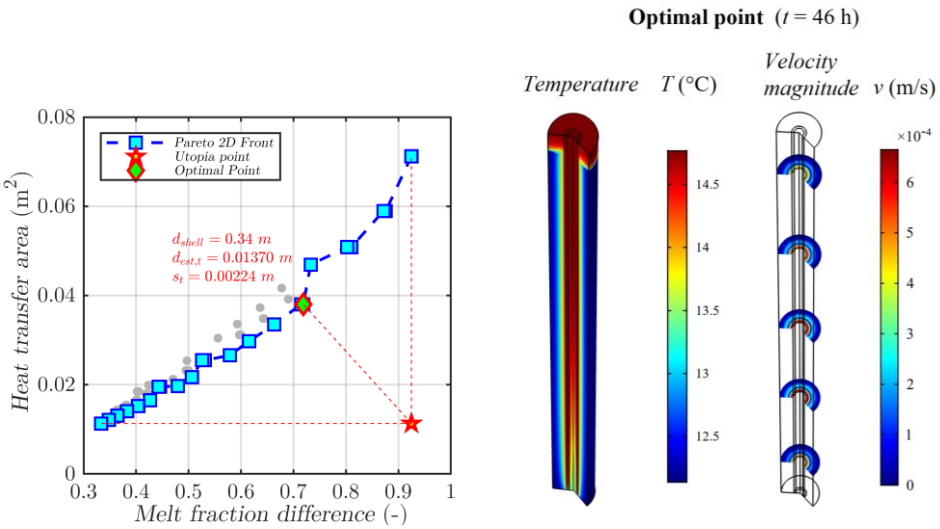

Fig. 5.35. Pareto front for the minimum surface area detection and temperature/velocity magnitude referred to the optimal point at t = 46 h

Among the optimal point detected by the front, the one selected by the utopia criterion is highlighted, and the related values of the design variables are revealed.

This optimal point is identified by a heat transfer area and melt fraction difference equal to 0.038 m^2 and 0.72, respectively. Moreover, in Fig. 5.35 are highlighted the configurations for which the heat transfer area and the melt fraction difference are minimized and maximized, *i.e.,* P_1 and P_2, respectively. In accordance with the premises, the optimization procedure has confirmed that lower heat transfer area – expected for higher shell diameters – involves lower usage of the PCM potential. Conversely – to exploit the 72% of the PCM capacity – a reduction in the shell diameter value is required, down to 0.34 m. Among all the tube types analysed, the optimal one results to be the 1/2 sch 80s. For the sake of completeness, the temperature and velocity magnitude contours referred to the optimal point at $t =$ 46 h are also depicted in Fig. 5.35, allowing the location of the PCM to be identified around the pipes. Tab. 5.12 resumes the main features referred to the three points, *i.e.,* optimal point, P_1 and P_2, that derive from the Pareto front and the initial one, showing the actual impact of varying shell diameter and pipe type.

Table 5. 12. Main design configurations deriving from the Pareto front

Case	Heat transfer area	Melt fraction difference	Tube type	Shell diameter
Optimal point	0.038 m^2	0.720	1/2 sch 80s	0.340 m
P_1	0.011 m^2	0.338	1/4 sch 40s	0.600 m
P_2	0.070 m^2	0.920	1/2 sch 40s	0.320 m
Starting point	0.023 m^2	0.400	3/8 sch 40s	0.480 m

Looking at the data in Tab. 5.12, it can be seen that although the optimization was aimed at reducing the transfer area, the optimal solution is characterized by a higher value than the initial condition. To fully understand the benefits of the implemented procedure, the changing/discharging times and melt fraction difference with respect to the dimensionless heat transfer area, *i.e.,* actual value (A) scaled from the initial value (A_0) are shown in Fig. 5.36.

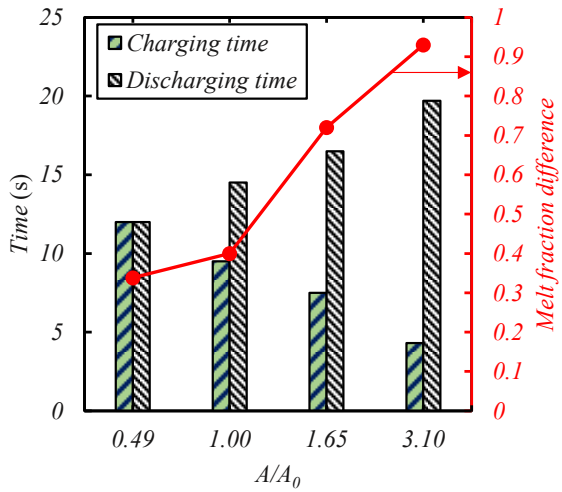

Fig. 5.36. Charging/discharging time and melt fraction difference for different dimensionless heat transfer areas

In the first optimization step, minimizing the charging and discharging time has been resulted in the configuration with $A/A_0 = 1.00$, characterized by a melt fraction difference value of 0.4. A reduction in the heat transfer area, *i.e.*, $A/A_0 = 0.49$, leads to a reduction in the discharge time and a consequent increase in the charge time. The global effect is a reduction in melt fraction difference. Conversely, increasing the heat transfer area to the limit, *i.e.*, $A/A_0 = 3.10$, results in a very fast charging phase to the detriment of a very slow discharge. The increase in melt fraction difference is considerable. The trade-off between the various configurations is represented by the optimum point, *i.e.*, $A/A_0 = 1.65$, which allows for an increase in the melt fraction difference over the starting case of 80%.

5.2.8. Final remarks

The proper design of a LHTS can be not sufficient to ensure the fully exploitation of the PCM potential. Depending on the user demand, thermal load profiles can vary and consequently affect the system reliability. As a proof, we have experimentally found that the PCM does not appear to have a successful discharge phase, on average. This occurs because, despite the inlet water temperature ramp is changing, the diffusion of heat into the PCM, *i.e.*, thermal diffusivity, is limited in time. As a result, just a small portion of the total PCM goes through a partial discharging phase. In this regard, this paper presents a comprehensive approach to optimize

the performance of a PCM-based shell-and-tube cold energy storage, making the charging/discharging phases more effective. The proposed methodology has handled this issue by employing a multi-step approach that allows to identify solutions able to minimize the time required for charging/discharging processes and to assess the configuration that ensures minimum heat transfer area. This approach has been applied to a chiller system that provides cold water to a heat exchanger (user) for a single-family cooling thermal load simulation. The main originality of this paper, beyond the experimental contribution, concerns the introduction of a multi-step methodology for the multi-objective optimization applied to latent heat thermal energy storages. The following main conclusions and insights about PCM-based shell-and-tube heat exchangers can be drawn:

- Even though the PureTemp15 PCM predicted solidification temperature is 15 °C, experimental results reveal a pronounced sub-cooling. The real solidification point is around 12 °C, and PCM crystallization begins at a temperature of 0.5 °C below this value for the last thermocouple position.
- The parametric analysis is mandatory to select proper design variables for the optimization procedure. This allows, among the possible combinations, to perform the simulations of the most influencing one, by reducing drastically the computational effort, and by showing – among the solutions of the Pareto front – also a valid decision-making criterion.
- The performance of the system is optimized by coupling a finite element numerical model with MATLAB and minimizing PCM charge/discharge time by changing the operating conditions of the chiller. The best results are obtained with a water mass flow rate of 0.095 kg/s and a water inlet temperature reduction of 1.25 °C. The obtained results are further verified by experimental tests and PCMs transient evolution is discussed looking at melting and solidification processes.
- As a major result of storage system optimization, it is estimated that the maximum amount of PCM that can be fully utilized is 40% of the original. Therefore, based on this value, a further optimization stage is carried out to assess the minimum heat exchange surface of the storage system, reducing the shell diameter by 12 cm and adopting 1/2 sch 80s tubes to exploit 72% of the PCM potential. This optimal solution implies a 69% increase in minimum heat transfer area.
- Definitely, the proposed methodology ensures at least two benefits: a) an economic one linked to the optimization of the amount of PCM inside the energy storage, followed by the reduction in the system size; b) an

environmental one resulting from the higher energy stored from the PCM as a consequence of the multi-objective optimization, which leads to a saving of primary energy demand.

In conclusion, the proposed multi-objective and multi-step optimization framework reveals excellent potentials. It couples the time-saving properties of genetic algorithms with the accuracy of experimental validations, enhancing by far the latent heat storage capability. However, as from the results section, there is still room of improvement for the PCM exploitation, *i.e.,* fill that 28%. Further research is recommended to reach that goal and investigate the influence of heat transfer enhancement techniques, *e.g.,* fins, nanoparticles, on both actual and optimal configurations.

6. Wall type heat recovery and ventilation system

The content here presented were published in Applied Energy [J5].

This work applies multi-objective optimization based on a genetic algorithm to design a wall-type heat recovery and ventilation (HRV) unit equipped with a phase change material (PCM) to show the benefits of using this thermal energy storage in buildings. The initial design – taken from a reference work – consists of an airflow driven by a fan through a copper tube bundle filled with PCM. Starting from this, a thermo-fluid dynamic 3D model is developed to assess the natural convection negligibility inside the PCM. Then, a 2D model is solved with a commercial finite element code and validated. Once the validation is assessed, this model is coupled with MATLAB® to perform the multi-objective optimization procedure. Optimal system configurations (tube diameter, thickness, pitches) and operational variables (fan velocity, cycle time, PCM melt temperature) are achieved on a 3D Pareto surface that collects the non-dominated solutions, i.e., minimizing costs and pressure drop (air side), and maximizing the average storage rate. The 3D Pareto approach enables to find solutions that outperform the initial configuration, i.e., the average storage rate is increased by 28.4%, simultaneously improving the other two objective functions. Finally, two sub-optimal solutions from the 2D fronts are numerically compared to show the difference in the air stream distribution across the new tubes' arrangement and the PCM melting evolution. The HRV efficiency is enhanced from 37.5% to 44.4%, confirming that the proposed approach provides an economically-feasible solution, while reducing energy consumption and maintaining good indoor air quality.

6.1. Introduction

All the efforts to design and optimize energy systems must actually support sustainability, meant as the ability to take advantage of all free sources without

creating environmental damage. Regarding buildings, this concept can be applied to several fields, *i.e.,* heating, cooling, and electrical power supply [135]. The literature background on most of them provides several contributions that offer clear guidelines to improve system performance granting multiple benefits, *e.g.,* energy, economic and environmental [136]. Modern buildings are designed to reduce heat losses via low thermal transmittance values of envelope components. However, increasing the thermal insulation of windows can inhibit air circulation. Heat recovery and ventilation (HRV) systems can provide both heat recovery and ventilation to prevent issues such as mold formation and low air quality [137]. The presence of a large temperature difference between indoor and outdoor air can decrease thermal efficiency due to air changes [138]. Hence, thermal storage in ventilation systems has been introduced to reduce the amount of energy required by heating and cooling devices. The selection of the energy storage system depends on many factors such as storage period, operating conditions, and economic feasibility [138]. The most comprehensive classification of HRV concerns the principle that regulates heat transfer: regenerative and recuperative [139]. The former is based on metal surfaces that cyclically store/release heat when exposed to either supply or exhaust airstream, while the latter transfers heat across a dividing plate by means of thermal conduction or by means of an intermediate fluid. In addition, among the several classifications of HRV, one can differentiate between centralized and decentralized ones [140]. The former heat recovery ventilator requires adequate ducting for air distribution installation and generally covers the need of the whole building. Conversely, the decentralized one is created to be fitted directly in the wall, *i.e.,* wall-type, in contact with the outside and is effective just for one space. These systems can be further classified as sensible heat recovery and total heat recovery, which comprises both sensible and latent heat. The most common sensible heat exchangers are chilled-water systems [138], and rock beds [141], while the latent heat ones are air-PCM (phase change material) heat exchangers [142]. Based on the previous classifications, this work focuses on recuperative, decentralized, and total heat recovery systems. This type can be traced back to single-room heat recovery units, also known as wall-type ductless HRV systems, particularly recommended when a standard mechanical ventilation system with heat recovery cannot be installed, *i.e.,* existing building with no space for additional ducts, retrofitting and refurbishment applications. As aforementioned, this kind of systems relies on latent heat thermal energy storage (LHTES), which provides attractive solutions because of the high storage potential, *i.e.,* 5 to 14 times greater than that of a conventional sensible heat storage system [143]. The operation is based on PCMs, which are widely used for the storage of sensible and latent heat in building structures [144]. Indeed, PCMs can store and release thermal energy through the cyclic

change of state between solid and liquid. This phase change generally occurs in a well-defined temperature range, which makes the choice of the correct PCM essential for the final application. In detail, the melting and freezing points of PCMs must be precisely matched to local climate conditions to ensure maximum system efficiency [145]. The most popular and investigated PCM type is paraffin wax [146]. Its usage is favoured by the wide range of melting temperatures, *i.e.,* from 10 to 90 °C, and due to their promising properties as phase change materials. Paraffin wax is safe, reliable, predictable, less expensive, and non-corrosive, but at the same time it has low thermal conductivity, and it is affected by large volume changes that can limit its use. However, these effects can be eliminated by modifying the wax and storage system through methods such as direct incorporation into polymers or encapsulation [147]. When these approaches are not viable options, the most valuable alternative is to increase the system performance optimizing it. From a general perspective, the optimization process consists of adapting a process to enhance a specified set of parameters without violating a few constraints [148]. With reference to thermal systems, and specifically to HRV, this means modifying the HRV design consistently with predefined objective functions, varying the main affecting variables.

The performance of HRV has been deeply investigated through the years. Experimental investigations and numerical simulations on HRV units for single room ventilation have been presented, focusing on airflow distribution, HRV unit position, and design optimization. Depending on the type of HRV, different approaches have been pursued and sometimes conflicting results obtained. In detail, with reference to the regenerative type, Manz *et al.* [149] showed that even with small units, high-temperature efficiencies can be obtained. Further, they proved that, generally, the most critical issue for successful applications of single-room ventilation units is the acoustic, because of the high indoor sound pressure levels. Concerning heat recovery through enthalpy exchangers, Liu *et al.* [150] found the weighted coefficient equations for defining the performance of an energy recovery ventilator (ERV) based on the link between sensible heat, latent heat, and enthalpy efficiency. They showed that to improve energy performance, more efficient enthalpy exchange materials and more powerful fans must be explored. More recently, rotary heat recovery devices have been proved to be effective when coupled with a roof mounted multi-directional wind catcher system [151], addressing the challenge of the heat transfer from one flow to another while maintaining the momentum required for adequate ventilation. Furthermore, parameters that affect membrane based ERV used in HVAC (heating, ventilating and air conditioning) systems have been numerical studied to assess their effects on overall efficiency, *i.e.,* supply and

exhaust air velocity variations, membrane spacing and thickness, water diffusivity through the membrane, outdoor air temperature and humidity on the HRV performance [152].

6.1.1. Aim and originality of this study

The literature survey underscores the potential for relying on HRVs as effective devices in the ventilation of air-conditioned environments and highlights the use of PCMs as latent heat energy storage media in various applications [153], [154]. While there have been several proposals for optimizing heat recovery systems with embedded PCMs [155], [156], a significant knowledge gap has been emphasized regarding the optimization of wall-type HRV systems. These systems differ from others in their compactness – presence of an air fan upstream or downstream of the tube bundle – and a heat exchanger that can include different kinds of storage media, *e.g.,* PCMs. The present work aims to fill the lack of how to set up an optimization approach to effectively integrate PCMs into HRVs, focusing on several aspects that affect the overall efficiency, *i.e.,* fan speed, PCM phase change temperature, tubes arrangement. Thus, as per our knowledge, this contribution represents one of the few attempts to optimize a decentralized PCM-based HRV system and aims to provide a methodology to address this objective, considering the nature of heat transfer and fluid-dynamic mechanisms that govern the operation of such systems. Specifically, in this work a numerical model of the decentralized PCM-based wall-type heat recovery unit is first developed and then validated against the experimental data provided in the reference paper [157]. Combining the current knowledge gap already evidenced with the enormous potential of numerical simulation and optimization – which mainly lies in time and money saving with respect to experimental campaigns – the target is to show new useful insights on the optimization procedure for enhancing the thermal performance, *i.e.,* average storage rate of wall type heat recovery systems, simultaneously reducing the investment costs and the pressure drop. This multi-objective approach is performed by means of a NSGA-II genetic algorithm, which ensures high computational performance, *i.e.*, trade-off between computational burden and results robustness [132]. This benefit becomes even more relevant with the increase in the model complexity, as with optimization procedures involving CFD simulations, especially when computationally-expensive PCM-based models are addressed.

6.2. Materials and methods

This section is devoted to the definition of the wall-type HRV features, the mathematical approach used to solve the CFD problem and the further definition of the optimization process. Most applications linked to PCM usage are affected by natural convection phenomena, which derive from the phase change process and strongly influence the dynamic evolution of the melt front. Therefore, the numerical models generally require appropriate terms to predict the correct phase change evolution. Nevertheless, for specific cases – such as the present one – natural convection is almost absent and therefore negligible [158]. This happens because of the low relevance of recirculating motions, which are clearly affected by geometry and PCM properties [121]. Since studies that deal with natural convection have been mostly limited to specific geometries or PCM types, in this work a 3D conduction-convection model is firstly defined to quantify the magnitude of natural convection inside liquid PCM and whether it plays a significant role in the PCM melting/solidification process. This is mandatory to assess if the 3D problem can be reasonably simplified with a 2D approach that considers the thermo-fluid dynamic evolution on a horizontal cut plane. The remaining of this section is organized as follows: the model geometry and parameters are showed in subsection 2.1. Then, the numerical model is presented in subsection 2.2, together with the initial and boundary conditions, *i.e.,* subsection 2.3. The grid and time-step independence are assessed in subsection 2.4 to find the optimal model features before running the multi-objective genetic algorithm (MOGA), whose details are unveiled in subsection 2.5.

6.2.1. Case study

Number of occupants, climate, and volume of the building that needs to be ventilated strongly affect the choice of a heat recovery ventilation (HRV) system. Thus, focusing on the single-room type, its electrical power consumption can range from 5 W to 100 W depending on the type, while the investment cost may approach 10^4 €, including the whole installation [137]. In this work, a decentralized ventilation system (DVS) is considered, with a tube bundle prototype as heat exchanger. This kind of HRV unit is integrated into the wall, one per room, differently from whole-house ventilation systems, where the unit is installed in a utility room. Fig. 6.1 shows the overview of the wall-type HRV experimentally analysed by Pekdogan *et al.* [157] – which will hereafter be referred to as the reference design – whose

main parts are: two covers for indoor and outdoor air release, an air filter, an axial fan, and a tube bundle heat exchanger unit with a staggered arrangement. The working principle can be explained by looking at two main objectives: enhance air quality, heat recovery. As regards the first one, thanks to the presence of an axial fan, the airflow is forced to pass through a filter, which removes foreign particles like dirt, dust, and grit from the air.

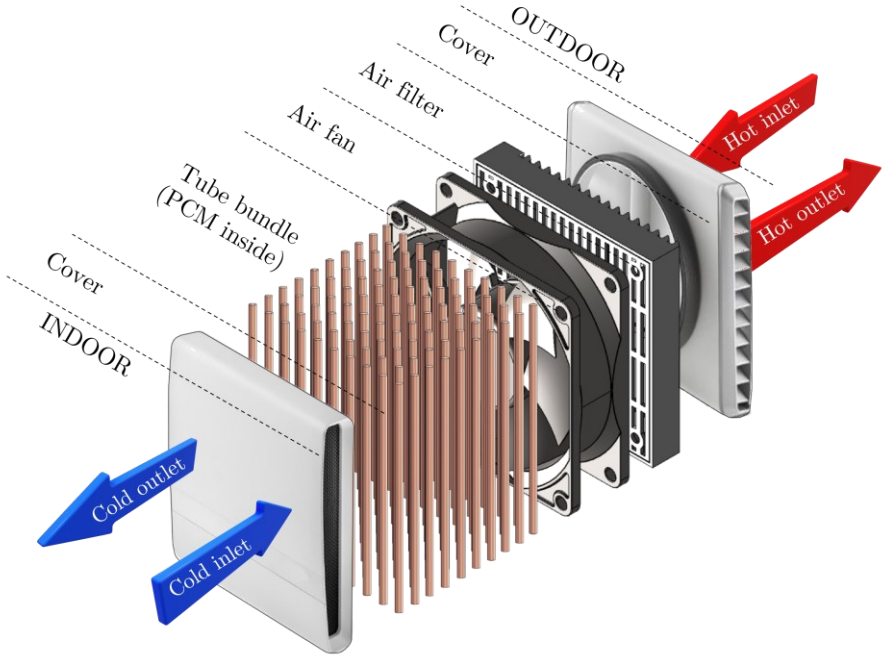

Fig. 6. 1. Heat recovery and ventilation unit here investigated.

This happens alternatively, depending on the airflow direction, which can be taken from inside/outside. Looking at the heat recovery, the air to be warmed/cooled up flows over the tube bundle heat exchanger unit with inside the PCM, which is at a higher/lower temperature with respect to the air. Thus, the working principle of this wall-type HRV system relies on the temperature differences between indoor/outdoor environments and PCM melting temperature. With reference to summer conditions, the melting temperature of the PCM is set to be greater than the indoor temperature and lower than the outdoor one. As a result, looking at Fig. 6.1, when warm air from outside (hot inlet) flows over the heat exchanger cools down (cold outlet) because it transfers heat to the PCM inside the tubes.

Conversely, when air from the inside (cold inlet) flows around the tubes, it cools the PCM as its temperature is lower than the PCM melting one and exits the system warmer (hot outlet). The geometrical characteristics of the heat recovery unit and of the tube bundles, together with the PCM thermophysical properties are listed in Tab. 6.1. As reported in [157], the PCM initially considered is the RT27, *i.e.,* a paraffin with a melting point of 27 °C, which has been here selected as PCM inside the tube bundle.

Table 6. 1. Heat recovery unit characteristics and PCM RT27 thermophysical properties.

Parameters	Value
HRV characteristics	
Tube height, H (cm)	15.0
Tube bundle length, L (cm)	15.0
External diameter, d_{ext} (cm)	0.48
Tube thickness, s_t (cm)	0.03
Transversal pitch, X_{tr} (cm)	1.40
Longitudinal pitch, X_l (cm)	1.40
Diagonal pitch, X_d (cm)	1.57
Tube inner volume, V_{inn} (m^3)	$2.04e^{-6}$
PCM mass per each tube, $m_{PCM,t}$ (g)	1.60
PCM properties	
Melting point, T_M (°C)	27.0
Melting range, ΔT_M (°C)	2.00
L_F (J kg^{-1})	1.84 e^5
ϱ_L (kg m^{-3})	760
ϱ_S (kg m^{-3})	880
μ_L (Pa s)	2.00 e^{-3}
β (K^{-1})	3.09 e^{-4}
c_{pS} (J kg^{-1} K^{-1})	180
c_{pL} (J kg^{-1} K^{-1})	256
k_S (W m^{-1} K^{-1})	0.20
k_L (W m^{-1} K^{-1})	0.20

Based on the reference design, the three-dimensional configuration (Fig. 6.2) of the tube bundle is firstly modelled. Because of the high computational cost, the simulation of such geometry is not always feasible, particularly if this model has to be iteratively run by the optimization process. Therefore, from that geometry, two simplified designs can be analysed: the first considers the minimum longitudinal

section of the 3D domain, *i.e.,* simplified 3D model (Fig. 6.2), while the second one is a 2D horizontal section that considers three columns, *i.e.,* the inner tubes of the bundle. As depicted in Fig. 6.2, the reference design bundle is characterized by 10 columns and 10 rows of tubes. Because of the staggered tubes arrangement, each tube lies halfway between the two adjacent tubes in the following tube row.

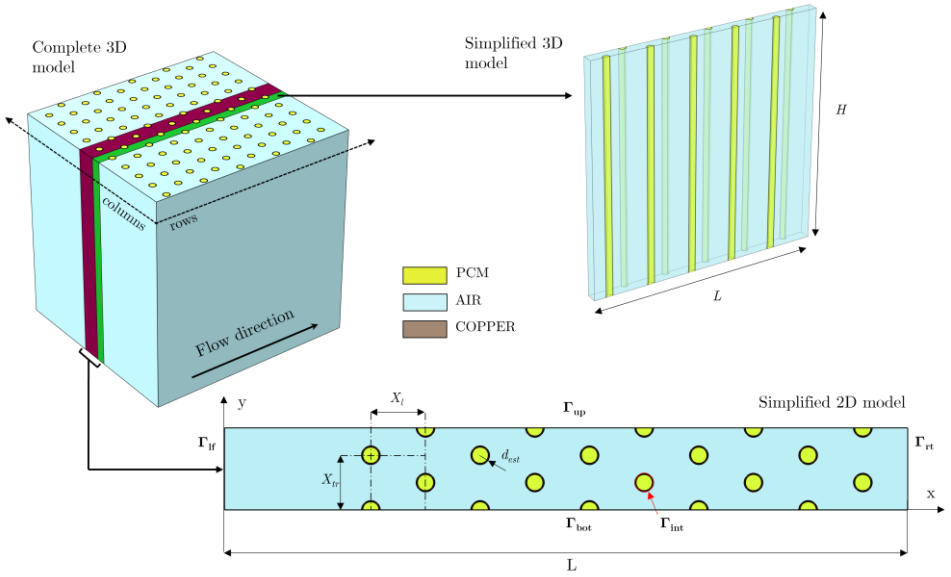

Fig. 6. 2. Complete 3D model, simplified 3D model, and simplified 2D model

6.3. Numerical model

Three domains – air, tubes, and PCM – are here considered to solve the heat transfer and fluid dynamics problem. However, the tubes are only interested by conduction as heat transfer mechanism. Thus, only the governing equations for air and PCM domains and the associated boundary and initial conditions are here presented. Their formulation is valid for both 2D and 3D transient models.

6.3.1. Airstream model

The problem here treated is about air forced convection outside a tube bundle. The fluid is treated as a non-isothermal, incompressible laminar flow, meaning that the governing equations –continuity, momentum, and energy – are as follows [152]:

$$\nabla \cdot \boldsymbol{v} = 0 \tag{6.1}$$

$$\rho_{air}\left(\frac{\partial \boldsymbol{v}}{\partial t} + \boldsymbol{v}\nabla \cdot \boldsymbol{v}\right) = -\nabla p + \mu_{air}\nabla^2 \boldsymbol{v} \tag{6.2}$$

$$(\rho c_p)_{air}\left(\frac{\partial T}{\partial t} + \boldsymbol{v} \cdot \nabla T\right) = \nabla \cdot (k_{air}\nabla T) \tag{6.3}$$

where ϱ_{air}, k_{air}, μ_{air} and $c_{p,air}$ are the thermophysical properties referred to air, t the time, T the temperature, p the pressure, and v the velocity vector. The arrangement of the tubes is staggered, as shown in Fig. 6.2, so that the mean fluid velocity, for incompressible flow, varies along the tube bundle with the cross section. The Reynolds number (Re) is conventionally referred to the external diameter (d_t), and to the maximum air velocity (v_{max}), which can be computed from Eq. (6.5) [159]:

$$Re = \frac{\rho v_{max} d_t}{\mu} \tag{6.4}$$

$$v_{max} = \begin{cases} \dfrac{v_\infty}{2}\dfrac{X_{tr}}{\left[\left(\frac{X_{tr}}{2}\right)^2 + X_l\right]^{\frac{1}{2}} - d_t} & if \dfrac{X_{tr} - d_t}{2} > X_l - d_t \\ \dfrac{v_\infty}{2}\dfrac{X_{tr}}{X_{tr} - d_t} & if \dfrac{X_{tr} - d_t}{2} < X_l - d_t \end{cases} \tag{6.5}$$

In this study, referring to summer conditions, air enters the domain at a variable inlet temperature (T_{in}), *i.e.,* from 20 to 35 °C, and with a uniform inlet velocity

(v_∞), *i.e.,* from 0.25 to 0.35 m/s. Considering the actual system configuration, *i.e.*, $X_{tr} = X_l = 1.4$ cm, and $d_t = 4.76$ mm, and thus using the second relation expressed in Eq. (6.5), $v_{\max}$ is equal to 0.53 m/s. Under these conditions and evaluating air properties at a mean temperature ($T_{in} = 27.5$ °C), the Reynolds number is equal to $Re = 164$, which is far from the transition to turbulent flow and allows to consider a laminar flow model for the air.

6.3.2. PCM model

The PCM mathematical formulation is based on the enthalpy-porosity approach [13], which is based on several reasonable assumptions. Firstly, the PCM is treated as isotropic but not homogenous in both liquid and solid phases. The incompressible Newtonian fluid hypothesis is used to model the liquid phase once the temperature becomes higher than the liquid transition temperature. In this case, the phase change is analysed without considering the associated volume change, which is reasonable due to the small temperature gradients and PCM composition [160]. PCM is modelled under the assumption of laminar flow, and finally, the thermal contact resistance at the welded interface between tubes and support base is neglected, since it is roughly equal to 10^{-6} m^{2}K/W, which is far smaller than the other thermal resistances involved. As aforementioned, in this case the variation in PCM density is considered only in the buoyancy terms of the momentum balance equations, through the Boussinesq approximation, which is a standard whenever natural convection should be significant, and the temperature changes are small. These assumptions allow the governing equations to be written as already presented in Chapter 1.

6.3.3. Boundary and initial conditions

Exhaust and supply temperature profiles, T_{exh} and T_{su}, are derived from the experimental data of the reference work [157] and displayed in Fig. 6.3. They are used as boundary conditions to facilitate comparison with the experimental results of the reference work. Likewise, the fan speed in the exhaust mode, v_{exh} is set equal to 0.344 m/s, while in the supply mode v_{su} to 0.282 m/s. As already stated, the airflow must alternately pass through the tube bundle to make the PCM inside the tubes able to release/store heat to/from the indoor/outdoor environment.

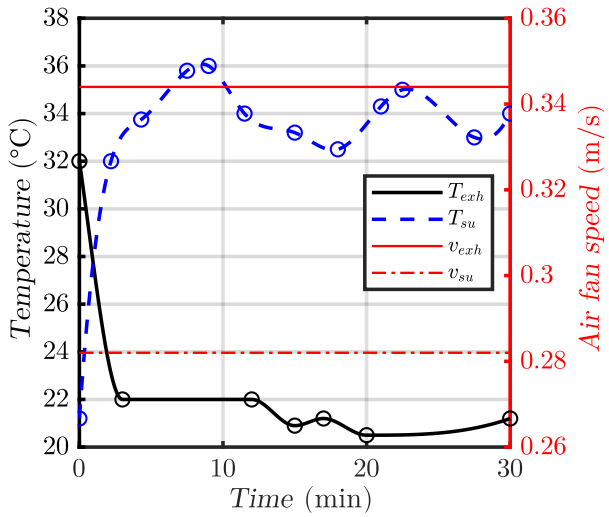

Fig. 6. 3. Exhaust and supply temperature profiles.

Therefore, indicating with t_c the total operating time interval of the system, in the first half (exhaust mode) the airflow proceeds from left to right, while the opposite occurs for the second half. Furthermore, it is assumed that at the initial state ($t = 0$), the device has a uniform temperature ($T > T_M$) such that the PCM is in the liquid phase, and there is no motion inside the domain. Although the problem analysed is highly dynamic, assuming a uniform distribution is not a limitation. To this end, for the same operating time of the reference work, the temperature values along the rows are quite similar. As regards the boundary conditions – with reference to Fig. 6.2 – on the air side, a slip condition is set on the upper (Γ_{up}) and bottom surface (Γ_{bot}), which also translates in the stress continuity ($\boldsymbol{\tau}_{jk} = 0$). On the PCM side, the same condition is set on Γ_{up} and Γ_{bot}, while a no-slip condition is applied where the fluid is in contact with the inner pipe wall. Accordingly, the initial and boundary conditions are resumed in Tab. 6.2.

Table 6. 2. Initial and boundary conditions

	$t = 0$	$0 < t \leq t_c/2$	$t_c/2 < t \leq t_c$
Heat transfer	$T = 30$ °C	$T = T_{exh}(\text{t})$ on Γ_{lf}	$T = T_{su}(\text{t})$ on Γ_{rt}
		$\partial T/\partial n = n \cdot q_t$ on Γ_{int}	$\partial T/\partial n = n \cdot q_t$ on Γ_{int}
		$T_{air} = T_t$ on Γ_{int}	$T_{air} = T_t$ on Γ_{int}
Air flow	$v = 0$ in $\boldsymbol{\Omega}$	$v = v_{exh}$ on Γ_{lf}	$v = v_{su}$ on Γ_{rt}

		$p = p_0$ on Γ_{rt} $\quad$ $p = p_0$ on Γ_{lf}
		$\begin{cases} \boldsymbol{v} \cdot \boldsymbol{n} = 0 \\ \boldsymbol{\tau}_{jk} = 0 \end{cases}$ on Γ_{up}, Γ_{bot}
PCM flow	$v = 0$ in $\boldsymbol{\Omega}$	$\begin{cases} \boldsymbol{v} \cdot \boldsymbol{n} = 0 \\ \boldsymbol{\tau}_{jk} = 0 \end{cases}$ on Γ_{up}, Γ_{bot}
		$v = 0$ on the internal tube walls

6.3.4. Grid and time-step independence

To ensure that the numerical model is independent on grid density, the temperature evolution at the 2nd row for both exhaust and supply processes is evaluated for different numbers of elements (cells), as shown in Fig. 6.4. The axis of the tube in the second row is chosen as the point for evaluating the mesh independence because it is subject to large temperature gradients. The number of elements varies from 85066, *i.e.,* fine mesh, to 31204, *i.e.,* coarse mesh, and the time step is set to 0.1 s. Fig. 6.4 shows a zoomed-in view of the mesh resulting from the commercial software physics-induced sequence, which accounts for the boundary layer meshing. Moreover, Fig. 6.4 reveals that no significant change occurs in the evaluation of the temperature profiles – especially for the charging phase where profiles are almost identical – when the number of elements is changed.

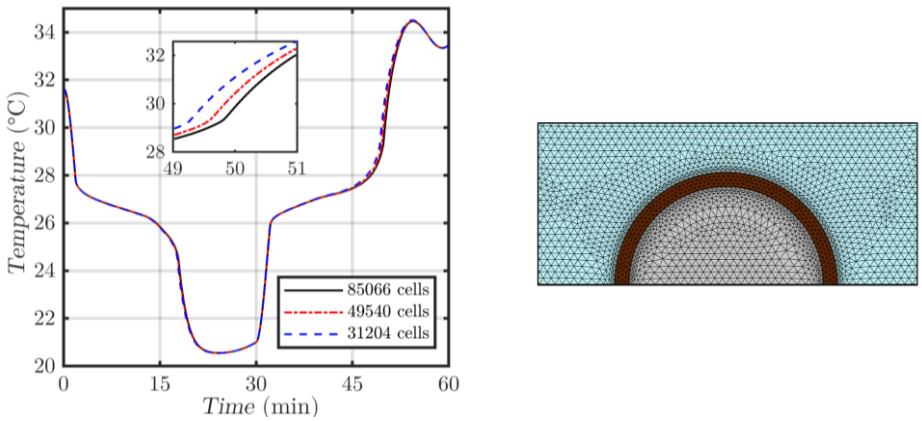

Fig. 6. 4. Grid independence test on the 2nd row tube temperature and a detail of the mesh structure

As regards the supply phase where the PCM melts, the zoom-in box highlights that passing from 31204 cells to the 49540 ones, the difference with the higher quality grid profile decreases, proving that the normal mesh should be selected as the most appropriate one since it represents a good trade-off between accuracy and computational efforts. Therefore, the triangular mesh used is provided in Fig. 4, with a maximum element size of 1.5 e^{-4} m. As regards the time step, diffusion-convection problems are typically handled using the backward differentiation formula (BDF) approach with free time stepping. When employing adaptive time stepping, the software, *i.e.,* COMSOL Multiphysics®, adapts the time step to satisfy the required relative tolerance, here set equal to 10^{-4}. As a result, comparing this approach with a fixed timestep one, *i.e.,* 0.05 s, there is a negligible temperature variation, whose maximum value during the time evolution is 0.1 °C.

6.4. GA multi-objective optimization approach

The optimization framework to evaluate appropriate geometrical features and boundary conditions for the heat recovery unit is resumed in the flowchart of Fig. 6.5. The problem resolution starts with the definition of design variables, equations, and constraints. All these data are set according to the model definition and then processed by a MOGA (multi-objective genetic algorithm), an upgrade of NSGA II, which is a population-based optimization technique that is inspired by natural selection, genetics, and evolution to find the optimal solution for a given problem. The search starts from an initial population that is generated randomly via the creation process. Each individual is considered as a potential solution candidate. Individuals are assessed against an objective function at each evolutionary stage. The resolution of the governing equations presented in subsection 6.2.2 is performed through the commercial CFD software COMSOL Multiphysics®. The individuals produced in each generation by means of the MATLAB® codes are fed to the CFD simulation tool thanks to the COMSOL Multiphysics® LiveLink™ (6.0) for MATLAB®. By doing this, the fitness function provided by the finite element method (FEM) analysis is then transferred to the MOGA, which thanks to the conversion, mutation, and selection functions, performs the evolution process. Selection involves the removal of a particular percentage of the population based on the probability-based "survival of the fittest". By optimizing random changes in

variables, mutation allows for the discovery of new parts of the evolving population. To identify a useful response, the GA iteratively improves a set of tentative solutions utilizing the above processes. By default, it is not possible to find a solution with all objective functions at their optimal values when there are many conflicting objective functions in the optimization problem. When solutions cannot be improved in any of the objectives without deteriorating at least one of the others, they are identified as Pareto solutions. Depending on whether two or more objective functions are used, the MOGA execution produces a curve/surface of non-dominated solutions. Those solutions provide the best trade-offs for the addressed objective functions. In order to achieve a good front/surface from the optimization procedure, appropriate parameters have to be established. At the end of the process, a solution will be picked from the Pareto front, adopting the so-called multi-criteria decision-making, which can be done in a variety of ways based on the needs and desires of the stakeholders. The utopia point technique, for example, can be used if equal weights are given to the objective functions. This latter provides the Pareto solution that minimizes the distance from the utopia point (after the objective functions have been normalized to their minimum and maximum values), which is the ideal point that delivers the best values (minimum or maximum) of the objective functions.

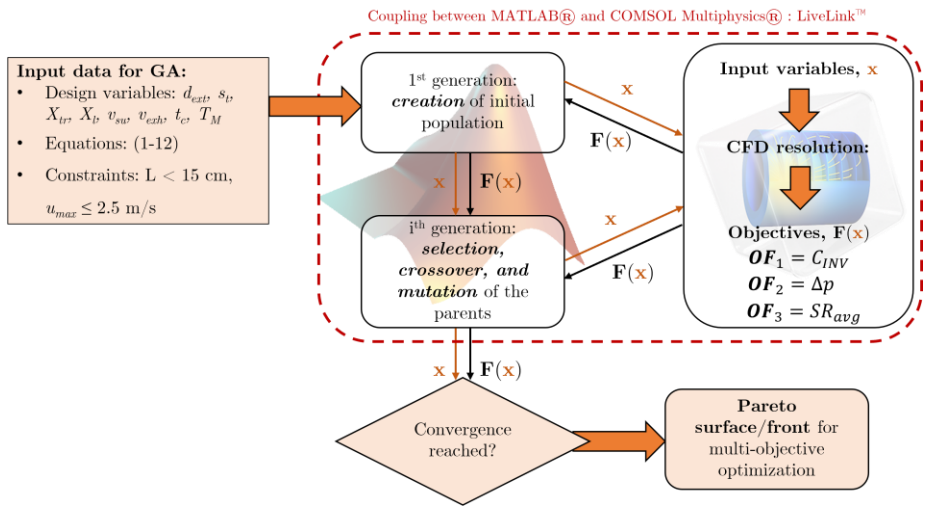

Fig. 6. 5. GA multi-objective optimization flowchart

6.4.1. Objective functions

The definition of the optimization problem is made under several assumptions:

- fan and air filter purchase costs are neglected because they are 1 or 2 orders of magnitude lower than the investment costs for pipes and PCM;
- maintenance fees related to the device are neglected [155];
- fixed total volume of the tube bundle heat exchanger.

Based on the results derived from the 2D model validation, some geometrical/thermophysical variables can affect the model performance, *e.g.,* the efficiency/average storage rate of the heat recovery prototype for different working conditions, and the costs, *i.e.,* investment and operational ones. In detail, since the PCM needs to quickly respond to the external loads, one of the objective functions is to minimize the melting/solidification time with respect to the running time. On the other hand, to accelerate the process, the heat transfer mechanism on the air side has to be enhanced. However, faster airstream means higher costs linked to run the fan. Therefore, another objective function to be selected should be related to the pumping power of the fan, which is dependent on the pressure drop of the airstream through the tube bundle. Clearly, these objective functions are in contrast, so that a benefit in one direction happens to the detriment of the other. This means that an optimization procedure can help to select an appropriate trade-off between these objectives. At the same time, the heat exchanger itself has a certain cost, *i.e.,* investment one, which is the sum of two contributions: PCM and tubes prices. Since the fan speed is generally limited by the emission of noise into the indoor space, a viable and more general approach consists of fixing a constraint on the fan speed value – based on limits imposed by regulations and acceptable noise levels – and therefore considering the operational costs separately from the investment one. By doing this, tubes and PCM costs can be separated from the costs linked to the electricity required to run the fan, which notably differ from each other by 1 or 2 order of magnitude, depending on whether the investment cost is capitalized or not. In such a case, the optimization problem can be formulated with three objective functions, *i.e.,* investment costs ($OF_1 = C_{INV}$), pressure drop ($OF_2 = \Delta p$), and average storage rate ($OF_3 = SR_{avg}$), where the first one considers the variation in the quantity of PCM, the number of tubes and their size, the second one directly influences the system operating costs, and the third one describes on average the heat rate transferred between air and PCM. It is worth noting that the aim is to

maximize the OF_3 and minimize the others. In this work the main reason for choosing the pressure drop instead of pumping power is linked to the choice of the design variables: the inlet velocity (for both supply and exhaust phases) is set as design variable and then is free to vary. Further, our aim is also to check and control during the optimization process the evolution of pressure drop, since high pressure losses and strong recirculation behind the last tube could take place, caused by a noticeable reduction of the free area for the flow. Moreover, in this work, the pressure drop is preferred to the operational costs as we do not consider a periodic operation of the system. As stated before, the investment cost (C_{INV}) is computed as the sum of PCM cost (C_{PCM}) and tube bundle cost (C_{TB}):

$$OF_1 = C_{INV} = C_{PCM} + C_{TB} \tag{6.6}$$

As specified in the assumption, the fan investment cost is neglected, as well as the maintenance fees. The purchase cost (in €) of the copper tube bundle heat exchanger can be expressed as a function of surface area using the following relation [161]:

$$C_{TB} = (cA_t^b)/r_{€\$} \tag{6.7}$$

where $r_{€\$}$ is the dollar to euro exchange rate, supposed equal to 1.09, A_t is the total tube outside heat transfer area, c and b are the cost coefficient constants, which depend on material type and heat transfer area [161]. In this case, since the heat transfer area is always lower than 9 m^2, these constants can be set equal to $c = 3728$, $b = 0.472$. Therefore, in the initial configuration C_{TB} is equal to € 1688. As regards the PCM cost, the Rubitherm RT 27 price is not available from the data sheet. Therefore, since this PCM type is a paraffin wax, looking at a similar composition [162], it is generally sold in different formats depending on the PCM mass desired, *e.g.,* 25 or 100 g formats. It has been verified that as the melting temperature changes, the cost does not change significantly. Large quantities of product allow making scale economies in the purchase, leading to a cost reduction. In order to accommodate this phenomenon, the PCM cost can be established from the following step cost curve depending on the desired PCM mass:

$$C_{PCM} = \begin{cases} € \ 32.34 & m_{PCM} \leq 100 \ g \\ € \ 91.40 & m_{PCM} > 100 \ g \end{cases} \tag{6.8}$$

These data have been established by viewing the seller sheet on 21st May 2022. The mass of PCM can be computed as follows:

$$m_{PCM} = \rho_{PCM} V_{PCM} N_t \tag{6.9}$$

In the reference configuration, each tube contains 1.6 g of PCM, which multiplied by 100 tubes implies a total PCM amount of 160 g. This leads to a PCM cost of € 188.6. The second objective function (OF_2) is the pressure drop, defined as the difference between the pressure at the inlet surface minus the pressure at the outlet one. Finally, the last objective function (OF_3) is the average storage rate, computed through an energy balance on both charging and discharging processes on the air side between inlet and outlet (Eq. (6.10)), making its evaluation independent on the number of PCM tubes, which varies during the optimization.

$$\begin{aligned} OF_3 = SR_{avg} = m_{air} c_{p,air} \ T|_{x=L} - T|_{x=0} \ |_{ex} \\ + m_{air} c_{p,air} \ T|_{x=0} - T|_{x=L} \ |_{su} \end{aligned} \tag{6.10}$$

The values in the baseline are the following, depending on the cycle time: 17.1, 22.05, and 15 W for 30, 40 and 60 minutes, respectively. Differently from the system actual running period, the heat storage rate is a crucial evaluation index as it relates the potential of the PCM in terms of storage to the actual time available to realise it. Furthermore, SR_{avg} represents a suitable OF for this optimisation as, being evaluated on air-side, it does not need to be computed at the interface with the PCM, which varies along the optimization.

6.4.2. Design variables

Once the objective functions have been identified – when designing and optimizing the tube bundle – it is useful to differentiate between two groups of independent variables, *i.e.,* decision variables and parameters. While the former can be changed during the optimization process, the parameters are fixed. The remaining, *i.e.,* dependent variables, are derived from the independent ones by means of thermodynamic and geometric relationships. Thus, the decision variables and the related constraints have been defined and set in the genetic algorithm MATLAB® optimization toolbox. All geometrical variables affecting the size of the tubes, *i.e.,* external diameter d_{ext}, tube thickness s_t, transversal, and longitudinal pitches X_{tr}, X_l, can influence both the amount of PCM inside the tubes and the fluid dynamics of the air outside the bundle, and they consequently are taken as design variables. On the air side, the variables that mostly affect the performance of the HRV unit are the fan speeds in exhaust and supply mode v_{exh}, v_{su}, respectively. The fan speed has been constrained to a maximum value of 2.5 m/s based on previous studies [152]. Finally, the cycle time t_c, and the melting temperature T_M have been left to

vary to define the most suitable operation for the application here investigated. The design variables for the optimization process are displayed in Tab. 6.3, where the ranges of variation of the variables themselves are highlighted. The ranges corresponding to the first four variables, which are linked to the system geometry, are defined in such a way as to preclude domain overlapping and to ensure that at least one column of tubes appears in the considered 2D domain. The ranges for fan speeds are established both in relation to physical considerations (as discussed in subsection 2.2.1) and by referring to values used in technical practice [152]. Finally, the cycle time range is set according to the specified operating time cycles of the reference work, which are 15 min, 20 min, and 30 min, and the melt temperature range based on the airstream temperature fluctuations during operation.

Table 6. 3. Design variables of the GA

Design variables	Initial value	Range	Step
External diameter, d_{ext} (mm)	4.76	3.00-7.00	0.20
Tube thickness, s_t (mm)	0.300	0.20-0.80	0.01
Transversal pitch, X_{tr} (mm)	14.0	8.00-20.0	1.00
Longitudinal pitch, X_l (mm)	14.0	8.00-20.0	1.00
Exhaust fan speed, v_{exh} (m/s)	0.344	0.10-2.50	0.10
Supply fan speed, v_{su} (m/s)	0.282	0.10-2.50	0.10
Time interval, t_c (s)	3600	1800-3600	100
Melt temperature, T_M (°C)	27.0	23.0-30.0	1.00

It is worth pointing out that the temperature initial condition has been varied in relation to the melting temperature implemented by the algorithm in order to ensure that the PCM is completely liquid at the start of the exhaust phase, based on the reference work. As regards the dependent variables, the diagonal pitch, tubes inner volume and PCM mass/tube can be easily derived. At the same time, the tubes number N_t can be obtained from the following equation [159]:

$$N_t = \frac{L_{tr}}{X_{tr}} \frac{\frac{L_l}{X_l} + 1}{2} + \left(\frac{L_{tr}}{X_{tr}} - 1 \right) \frac{L_l / X_l - 1}{2} \tag{6.11}$$

where, L_{tr} and L_l are the heat recovery length in the transversal and longitudinal directions, respectively. Then, the total heat surface area is computed as:

$$A_t = \pi d_{ext} H N_t \tag{6.12}$$

Based on how the design variable ranges of variation have been set, the total number of possible combinations (exhaustive search) is equal to 1.11^{10}. With a

simulation time of 10 minutes on average, this would require several years of simulations. The advantage of the genetic algorithm is indeed the substantial reduction in the computational time, which is of the order of 10 days. Tab. 6.4 lists all the settings of the aforementioned MOGA features, referred to as tuning parameters, and evaluated on the basis of the authors' experience.

Table 6. 4. MOGA tuning parameters

Tuning parameters	Value
Population size	80.0
Maximum no. of generations	50.0
Minimum function tolerance	$1.00e^{-5}$
Probability of crossover (%)	60.0
Probability of mutation (%)	10.0
Number of crossover point	2.00
Selection process	Tournament
Tournament size	2.00

6.5. Results

The primary goal of this work is to design a tube bundle that maximizes heat transfer while minimizing air pressure drop and investment costs. However, as the geometrical structure of the heat exchanger is modified to optimize heat transfer, the pressure drop of air increases as well. Further, by changing the PCM amount and tube size to improve the storage rate, investment costs rise. As a result, since the best solution for all objective functions cannot be concurrently obtained, the analysis of the resulting 3D Pareto surface is hereafter discussed. Therefore, this section shows different approaches to select the most suitable solution from the ones collected by the Pareto front. Then, it shows the benefits resulting from the optimization comparing – both qualitatively and quantitatively – the results obtained here with the reference design.

6.5.1. Model validation

This step consists of the comparison of the CFD model results with the dataset provided by the reference work. This validation process, performed on the 2D

model, is essential since it allows the numerical model to be used both to investigate the thermal performance of the heat recovery unit and then to be further optimized. Thus, this step mainly deals with the comparison between the present work (numerical) and reference (experimental) PCM temperature evolutions during the melting and solidification processes. A propaedeutic phase for the model validation is represented by the calibration of the PCM melting range (ΔT_M). This step involves the variation of the ΔT_M value – in a reasonable range – to detect which of them ensures the best fitting to the experimental dataset [163]. In detail, ΔT_M has been varied from 1 to 2 °C, and the PCM numerical profiles resulting from this analysis are showed in Fig. 6.6 For the sake of simplicity, the experimental temperature profiles used for the comparisons are referred to the tubes in the 2$^{\text{nd}}$, 6$^{\text{th}}$ and 10$^{\text{th}}$ rows, in order to investigate the entire domain uniformly. Fig. 6.6 shows the model behaviour on the different points of measure, varying the melting range value. Looking at the discharging phase, all the PCM temperature trends depicted share a delay in the solidification process, differently from the experimental case for which the temperature decrease is smoother than the numerical one. This suggests that the numerical model tends to make the phase change lasting longer than the experimental one, which can be attributed to several reasons, *e.g.,* model evolves more slowly, lower thermal diffusivity. Another evidence that results from the comparison between experimental and numerical trends is the temperature reached at the end of the discharge phase, which is slightly lower for the numerical case. As regards the charging phase, the simulated PCM temperature rises faster than the experimental one, as a consequence of the boundary conditions adopted. Then, the charging phase is quite similar for the three analysed cases. The higher discrepancies are related to the last 15 minutes, where the high fluctuations in the air temperature influence the model behaviour, resulting in an underestimation of the final PCM temperature. In detail, the major differences are showed in the 2$^{\text{nd}}$ row case, whereas moving to the following rows these discrepancies tend to decrease.

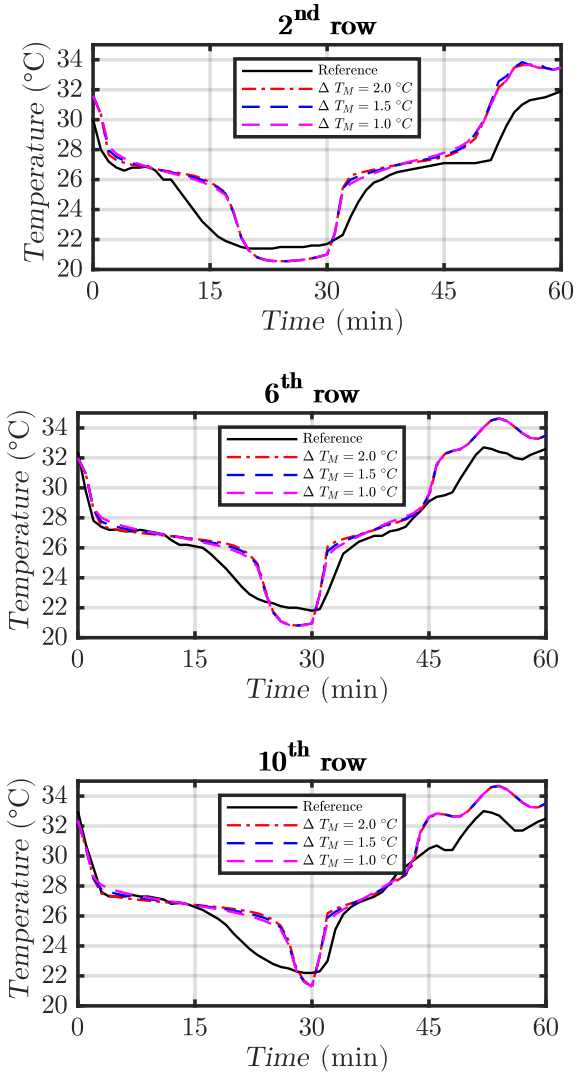

Fig. 6. 6. Melting range calibration on experimental data

The reason of these profiles is linked to the airflow direction: during the discharging phase air skirts the 2nd row before reaching the lasts two, while the opposite happens for the charging one. Therefore, the 2nd row cools down quicker than the 10th one in the discharging phase and warms up slower in the later phase. Looking at

the effects of the melting range variation, it seems that it weekly affects the model accuracy, as proved by the statistical indices listed in Tab. 6.5, *i.e.,* mean absolute error (MAE) and root mean square error (RMSE), evaluated against experimental results.

Table 6. 5. Statistical indices referred to PCM temperature profiles (the lowest values are in bold)

Row	ΔT_M (°C)	MAE (°C)	RMSE (°C)
2nd	1.00	1.50	2.00
	1.50	1.51	1.98
	2.00	1.51	1.96
6th	1.00	1.05	1.34
	1.50	1.04	1.30
	2.00	1.03	1.27
10th	1.00	1.05	1.40
	1.50	1.01	1.36
	2.00	0.99	1.31

The model accuracy is proved by the limited values of these indices, if compared to similar case studies [164]. In detail, as in [164] the comparison between numerical and experimental data is provided for three different PCM tubes at different locations, and therefore the current model is thought to be reasonably accurate. From Tab. 6.5, it can be seen that except for the MAE values referred to the 2nd row, a melting range value equal to 2 °C ensures a higher consistency with experimental results, *i.e.,* minimum MAE and RMSE values. Therefore, this calibrated value is used hereinafter. The 3D model has been built considering only a channel that represents the tenth part of the entire geometry. This choice is justified by the excessive computational effort that would be required to model the entire system. In this way, two useful insights on the dynamic behaviour of the PCM within the tubes can be derived: i) the first concerns the difference in the PCM phase as the row changes, *i.e.,* from the 1st to the 9th rows; ii) the second is the distribution of the liquid phase in each tube. In detail, Fig. 6.7 represents the melt fraction fields inside the tube bundle at $t = 15$ min, *i.e.,* the middle part of the discharging phase. The cold air stream (from left to right) gradually cools the (previously liquid) PCM to solidification. As shown by the different colours indicating various melt fraction values, part of the PCM is still experiencing the phase change (last rows), while the PCM inside the first tubes row is already solid. Looking at the melt front of the 8th and 10th rows, we find out that no effects about the natural convection can be detected in the model since the melt front propagates parallel to the tube axis. This means that the heat conduction in the radial direction is prevalent to the convection in vertical direction, as a consequence of the little tube radius.

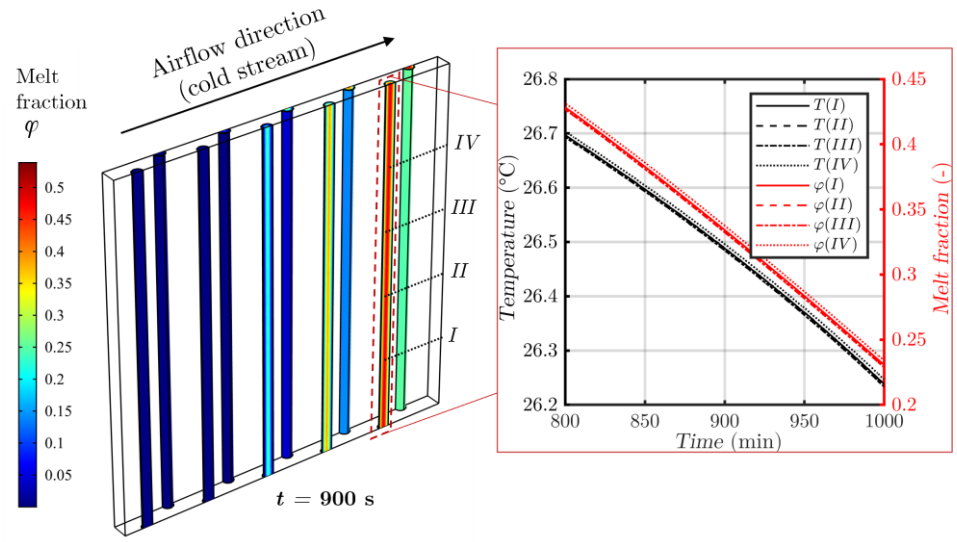

Fig. 6. 7. PCM melt fraction fields inside tube bundles (I, II, III, IV refer to different heights equally spaced)

Furthermore, confirming what seen from the graphical melting front analysis, the temperature and melt fraction for the tube in the 9th row are also depicted in Fig. 6.7. At different heights – equally spaced – *i.e.*, *I*, *II*, *III*, *IV*, and at the same radius, these quantities remain almost unchanged, remarking the negligibility of buoyancy effects in the liquid PCM.

6.5.2. Optimized design

The multi-objective genetic algorithm (MOGA) result is a set of non-dominated, optimal Pareto solutions. One 3D Pareto front and three 2D Pareto fronts – one for each couple of objectives – can be used to depict these solutions. Starting from this set of solutions – when applicable – several constraints can be identified to bound the regions (volumes/planes) that improve the objective functions compared to a certain reference case. By doing so, irrelevant solutions can be excluded in order to improve performance compared to the base case, both from an economic and thermos-fluid dynamic point of view. Hence, the 3D unconstrained Pareto front, which collects all solutions explored by the GA, *i.e.,* 1900, and the ones defining the optimal surface, *i.e.,* 368 non-dominated individuals, is depicted in

Fig. 6.8. To facilitate the comparison with the initial design, the reference points have been added in Fig. 6.8. The distribution of the points on the optimal surface roughly agrees with an ideal distribution: an improvement in the average storage rate (OF_3) happens to the detriment of the investment costs (OF_1). On the other hand, the thickening of the optimal points for low values of pressure drop (OF_2) shows how slightly they correlate with the investment cost.

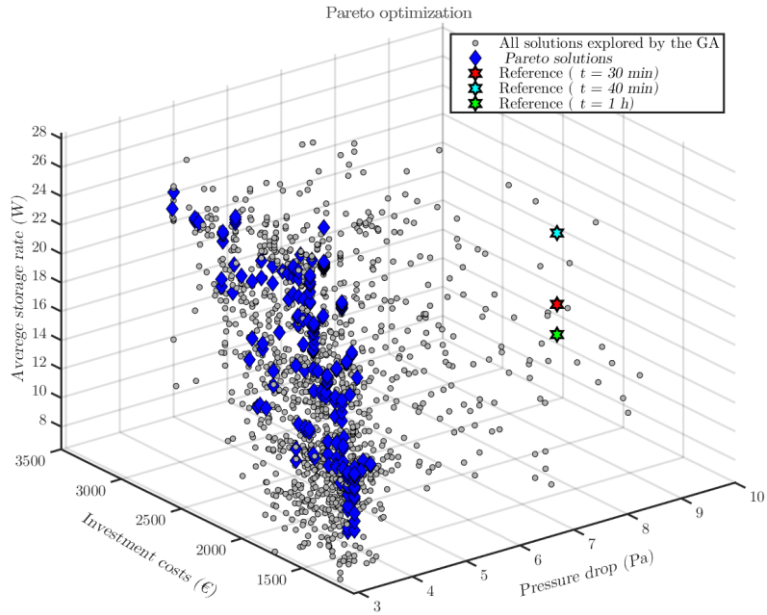

Fig. 6. 8. GA unconstrained 3D Pareto front and reference solutions

This means that a considerable change in pressure drop is related to different pitch values, rather than to the size of the pipe diameter, which would imply a more significant increase in investment cost. Looking at the pressure drop, the solutions processed by the GA show significantly lower values than the reference ones, *e.g.,* from 8.5 Pa of the reference design to an average value of 4 Pa of the optimal surface. This indicates that it is possible to achieve approximately a halving of the pressure drop. For the remaining variables, it can be seen that the distribution is more spatially uniform, particularly for the average storage rate. For the investment costs, on the other hand, a thickening of the values towards the lower limit of the objective function, *i.e.,* around 1000 €, can be observed. However,

understanding the results for the other variables is more laborious just looking at Fig. 6.8, and therefore to address this need, a first constrained Pareto front has been depicted in Fig. 6.9. At this stage, the constrained *OFs* are pressure drop and investment cost – cyan and yellow planes, respectively – while the average storage rate is free to vary. This results in the exclusion of a large portion of the solutions investigated by the GA, with the remaining individuals continuing to improve both objectives, *i.e.,* pressure drop lower than 8.5 Pa and investment costs lower than 1880 €.

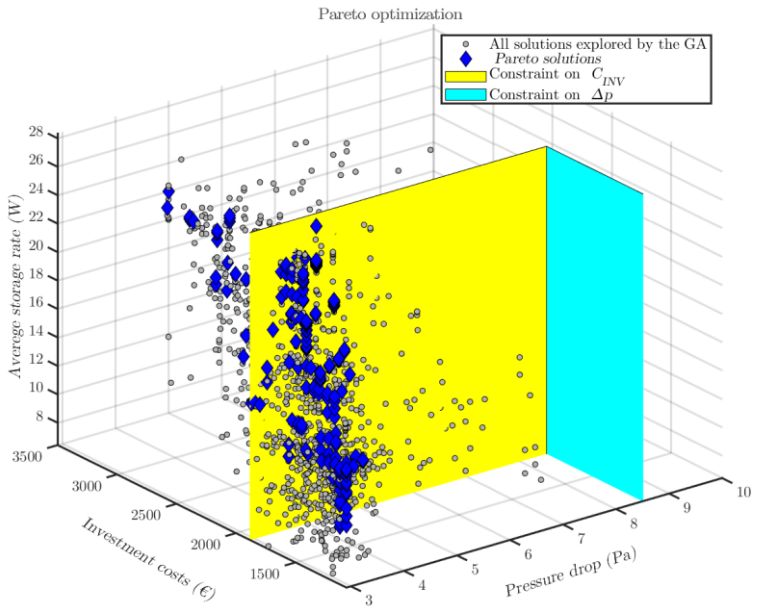

Fig. 6. 9. Constrained 3D Pareto front, excluding solutions with higher pressure drop than 8.5 Pa, and higher investment cost than 1880 € (reference values)

Generally, the Pareto approach identifies existing trade-offs, but it also identifies a set of potential solutions for various weighting and scaling strategies connected with the criteria of interest, *e.g.,* utopia optimum. Since the aim is to increase the storage performance of the HRV system, hereafter (Fig. 6.10) a second constrained 3D Pareto front is analysed to highlight the solutions that fulfil the inequality: average storage rate (SR_{avg}) > $SR_{\text{avg,ref}}$, having excluded solutions with higher pressure drop than 8.5 Pa and higher investment costs than 1880 €. The solution that

maximizes the SR_{avg} under the mentioned constraints is the one with $SR_{\text{avg}} = 28.32$ W. This value outperforms the reference one by 28.4%. By doing this, the constrained solutions effectively increase the performance of the HRV unit for all the objective functions, compared with the reference case.

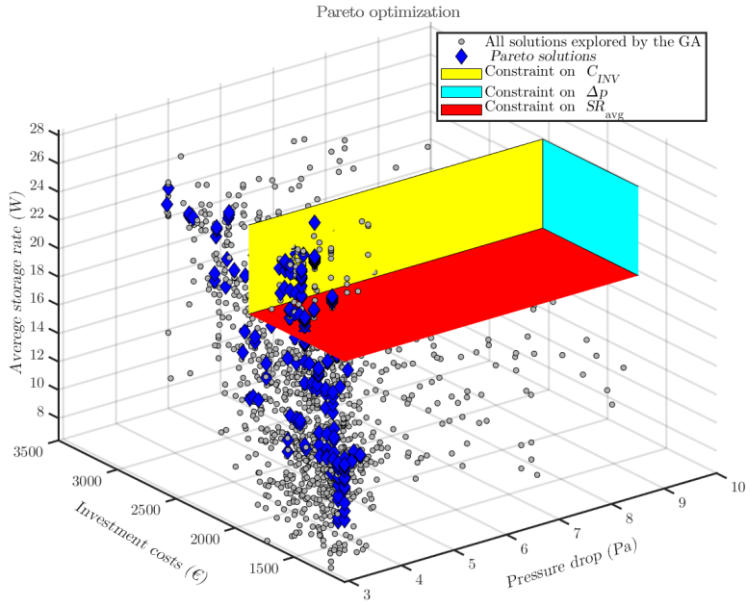

Fig. 6. 10. Constrained 3D Pareto front, excluding solutions with higher pressure drop than 8.5 Pa, higher investment cost than 1880 €, and lower average storage rate than 22.05 W (reference)

Fig. 11 depicts the distributions of the design variables selected by the evolutionary mechanism performed by the GA. The scatter-plots have been coupled with the histograms to highlight the preferences of the algorithm in the selection of certain variable values. In detail, the third variable, *i.e.,* the transversal pitch, repeatedly assumes the maximum value of the identified range, *i.e.,* 20 mm. Equally, the seventh one, *i.e.*, the cycle time, is predominantly equal to the lower value 1800 s. In the first case, this can be explained by looking at the pressure drop, which decreases significantly as the cross-sectional area increases. In the second case, the cycle time is mainly distributed close to the lowest value since the PCM phase transition occurs in a limited time interval, generally lower than the half of the time cycle. As the phase change is completed, for the remaining time the PCM transfers heat to/from the air in a sensible form, which is not effective for the

storage purpose. Therefore, the GA adapts to this behaviour, keeping the time to the minimum needed.

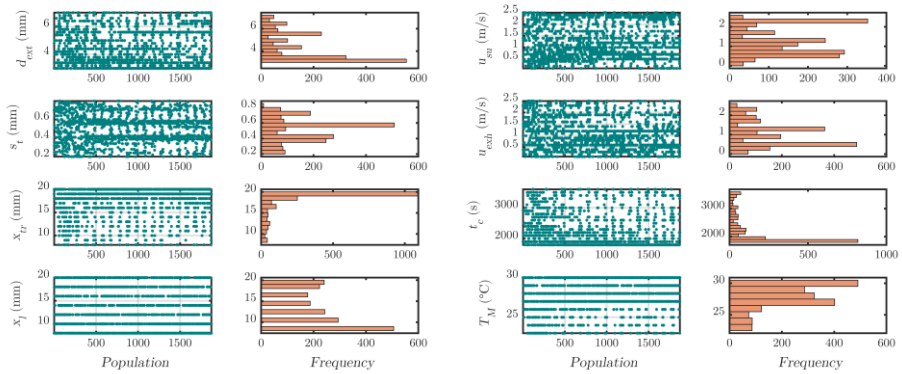

Fig. 6. 11. Scatter plot and distribution of GA multi-objective optimization design variables

Generally, what has been seen for X_{tr} and t_c suggests that their values could have been assigned in advance, reducing the number of variables to be analysed to 6. For the remaining variables, similar considerations cannot be made, as the frequency of the distributions is much more homogeneous over the range considered. The diameter of the tubes settles at the lower limit of the selected range, indicating the need to reduce the investment cost and the pressure drop. At the same time, this suggests that a thicker pipe does not lead to any benefit in terms of heat transfer, which is confirmed by the frequency of the values assumed by the second decision variable, *i.e.,* s_t, which prefers intermediate values in the range considered.

6.5.3. Analysis of 2D fronts

At this stage, to further investigate the optimization results, the 2D unconstrained Pareto fronts are discussed, as they represent possible scenarios for the selection of the optimal points. The MOGA result is a collection of optimal Pareto solutions that are non-dominated because no other solutions allow for simultaneous improvement/reduction of the considered objective functions. These solutions, which offer optimal design scenarios for multi-objective optimization, can be represented on three 2D Pareto fronts – the projection of the 3D one for each pair of

objectives – and one 3D Pareto front. This is mandatory to assess the convergence of the GA procedure, which is achieved when a certain criterion is satisfied. In detail, when a stop requirement is met, *e.g.,* negligible changing in the Pareto front appearance over the generations evolution or reaching the maximum number of generations, the GA outcome can be considered reliable. For each of the fronts depicted in the following, the utopia optimum is also presented, *i.e.,* the point that ideally identifies the best solution from the Pareto optimal set. 2D fronts will be referred to as follows:

- $2D_{12}$: investment costs (OF_1) vs pressure drop (OF_2);
- $2D_{23}$: pressure drop (OF_2) vs average storage rate (OF_3);
- $2D_{13}$: investment costs (OF_1) vs average storage rate (OF_3).

In detail, Fig. 6.12 shows the Pareto front resulting from the investment costs vs pressure drop analysis ($2D_{12}$). In this case, compared to the 3D case, only one scenario is mentioned as the reference condition*, i.e.*, the one with the highest SR_{avg} value. Each circle represents one of the 1900 solutions, *i.e.*, combinations of the design variables, whose colour gradually varies according to the generation to which it refers (from white to black). Then, it follows that there is a convergence of the algorithm towards the optimum value as black dots tend to accumulate around it. Despite this, there are darker spots also far from the optimum point. This is related to the influence of the mutation function on the algorithm, which allows to preserve genetic variety from one generation to the next. Fig. 6.13 depicts the Pareto front obtained when comparing the pressure drop and the average storage rate, *i.e.,* $2D_{23}$. In this frame, the collection of optimal solutions can be clearly seen. This front includes all the points with a pressure drop between 2.92 and 3.71 Pa, and an average storage rate between 13.8 and 28.32 W.

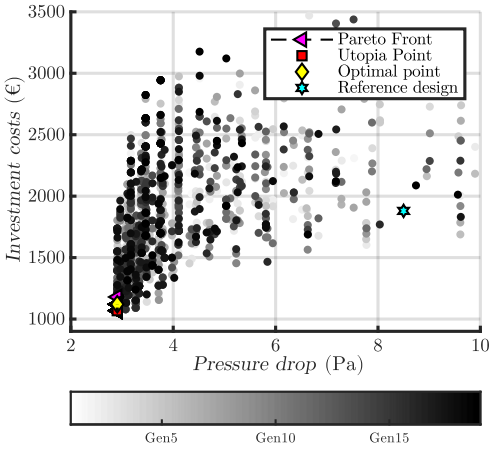

Fig. 6. 12. Investment costs vs pressure drop: 2D optimal solution ($2D_{12}$)

The latter value is precisely the one that can also be appreciated with reference to the 3D plot.

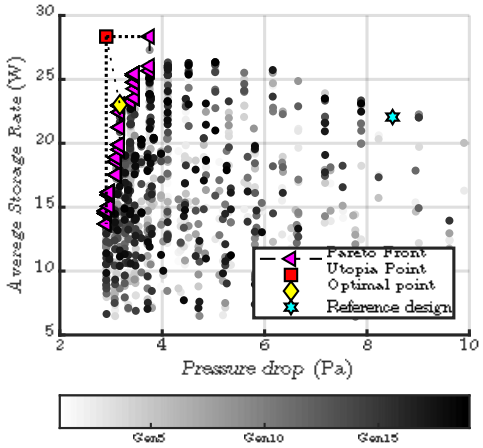

Fig. 6. 13. Pressure drop vs average storage rate: 2D optimal solution ($2D_{23}$)

Finally, Fig. 14 shows the last couple of objective functions, *i.e.*, $2D_{13}$.

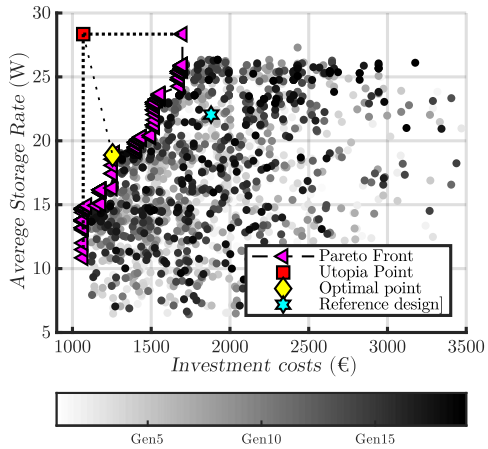

Fig. 6. 14. Investment costs vs average storage rate: 2D optimal solution ($2D_{13}$)

Here too, the Pareto front is well defined and among all the possible solutions, the one provided by the utopia criterion is chosen as the trade-off. As in the previous cases, the highlighted optimal points substantially improve the performance of the system compared to the reference case.The objective functions and design variables values related to the optimal solutions in the three 2D cases are listed in Tab. 6.6.

Table 6. 6. Objective functions value from the 2D front analysis

Case	OF_1, C_{INV} (€)	OF_2, Δp (Pa)	OF_3, SR_{avg} (W)	Design variables, x							
				d_{ext} (mm)	s_t (mm)	X_{tr} (mm)	X_l (mm)	v_{exh} (m/s)	v_{su} (m/s)	t_c (s)	T_M (°C)
$2D_{12}$	1119	2.92	10.4	4.00	5.80	20.0	18.0	0.70	1.20	1800	27
$2D_{23}$	1447	3.16	23.8	5.00	7.20	20.0	14.0	0.70	1.00	1800	29
$2D_{13}$	1252	3.74	18.0	3.60	5.60	20.0	10.0	2.40	0.70	1800	30

The $2D_{13}$ and $2D_{23}$ cases are taken as solutions for the following performance comparison.

6.6. Discussion

In this section, the main findings of the presented approach are discussed through a qualitative and quantitative approach. In detail, performance

comparison is presented for reference and optimized cases, separately, for two phases, *i.e.,* exhaust and supply. The aim is to describe the air-tubes-PCM interaction. Then, the HRV efficiency is presented and discussed to provide a proof of the approach's effectiveness.

6.6.1. Performance comparison

Fig. 6.15 shows how the airstream velocity changes depending on the phase, *i.e.,* exhaust or supply mode, and on the solution, *i.e.,* reference design, optimized one $2D_{13}$, optimized one $2D_{23}$. The optimized $2D_{12}$ design requires no further analysis because, as evidenced by the 3D analysis, it has very limited average storage rate values. In the initial design, both phases last 30 min, whereas for the optimized ones the half. Looking at the reference design, although the fan provides the two phases for the same time interval, the discharge direction operates with a lower flow rate than the exhaust direction. As expected, the tubes arrangement causes a deviation of the air flow, which on the one hand increases pressure drop and on the other improves heat exchange. Compared with the reference tube bundle, the $2D_{13}$ shows an increased number of tubes with lower diameter, reduced longitudinal pitch and increased transversal one. Conversely, the $2D_{23}$ configuration presents tubes with bigger diameter, higher tube thickness, equal longitudinal pitch but higher transversal one. The result in the first case, *i.e.*, $2D_{13}$ is a less staggered configuration, which makes the velocity magnitude between the tubes' columns higher. Moreover, this happens also because of the different inlet velocity, which passes from 0.7 to 2.4 m/s. In the second case, the airstream is quite similar in the distribution pattern, and it differs only for the velocity magnitude, from a maximum of 0.8 to 2.0 m/s. Therefore, the configuration $2D_{13}$ shows a lower value of pressure drop if compared with the $2D_{23}$.

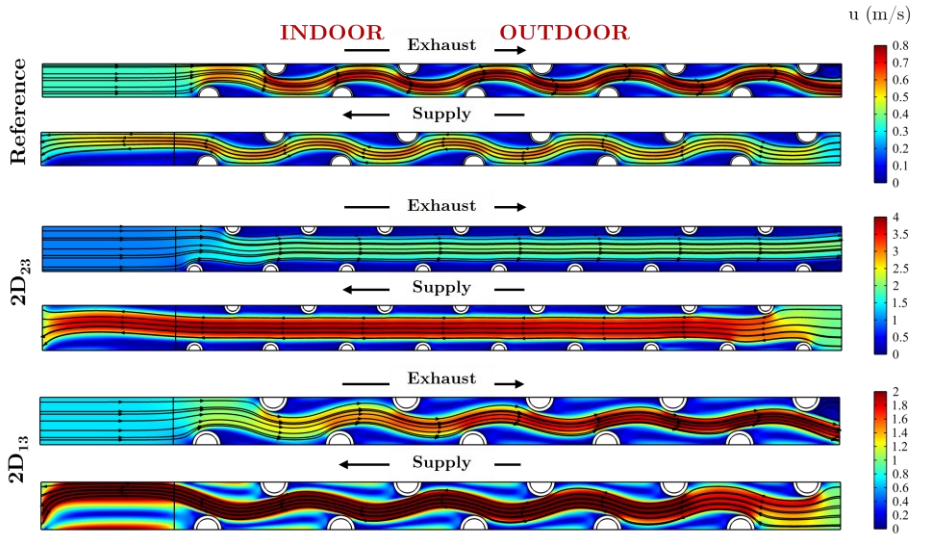

Fig. 6. 15. Airflow velocity modulus fields in exhaust and supply modes before and after the optimization

Fig. 6.16 and 6.17 show the comparison of the PCM melt fraction distribution inside the tubes in the reference and optimized cases, for the exhaust mode and supply mode, respectively. Remarkably, the outlet section, *i.e.,* the outdoor environment, is on the right side and the inlet section, *i.e.,* the indoor environment to be cooled, is on the opposite side. In detail, in the charging phase (Fig. 6.16), cold air taken from the inside passes through the tube bundle absorbing heat from the PCM, and then flowing to the outside at a higher temperature; on the other hand, in the discharge phase, air will be taken from the outside environment passing through the tube bundle releasing heat to the tubes containing the PCM and entering the inside environment at a lower temperature. As it can be observed in the first minutes of the reference design, when the HRV unit is in the charging phase the first rows gradually solidify while the last ones, which are reached by progressively colder air, take longer to solidify, *i.e.,* more than 20 min. Due to the conduction-dominated problem, the solidification front propagates in a radial direction during the phase transition.

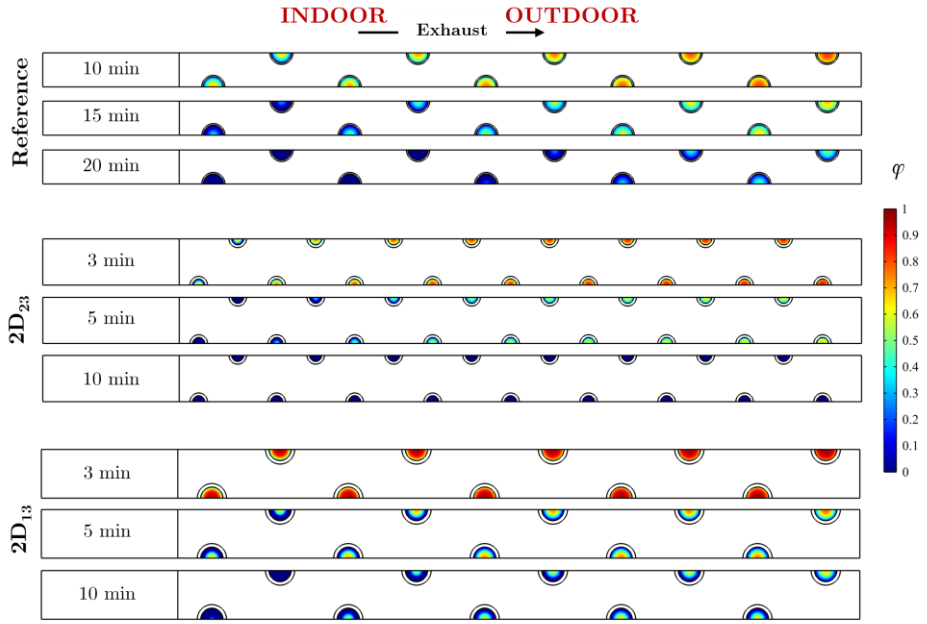

Fig. 6. 16. PCM melt fraction fields in exhaust mode before and after the optimization for different time instants (airflow from left to right)

On the contrary, in the charging phase of the first optimized case, *i.e.,* $2D_{13}$, the first rows are starting to melt at $t = 3$ min while the last ones solidify at $t = 10$ min, for which in the reference configuration the PCM in the front rows has just started to solidify. Thus, the thermal transient related to the phase change is much faster than the initial design. This does not occur in the $2D_{23}$ configuration, which shows a slower evolution of the PCM melting/solidification. In detail, the charging phase starts after $t = 3$ min, for which the appearance of the mushy zone spread is beginning to be visible near the walls of the first rows. The solidification of the PCM, which in the previous case could be considered to have been completed by $t = 10$ min, in this case is still taking place. The charging phase can be considered completed, *i.e.,* the last row has completely solidified, at time $t = 14$ min.

Looking at Fig. 6.17, similar considerations can be made about the melting phase of the PCM. Again, the thermal transient occurs faster in the optimized configurations, specifying that the discharge phase of the PCM in the second case, *i.e.,* $2D_{23}$ ends exactly with the end of the cycle time. This emphasises that in the

optimized case, the phase transition of the PCM and – thus its potential – is exploited in the best possible way.

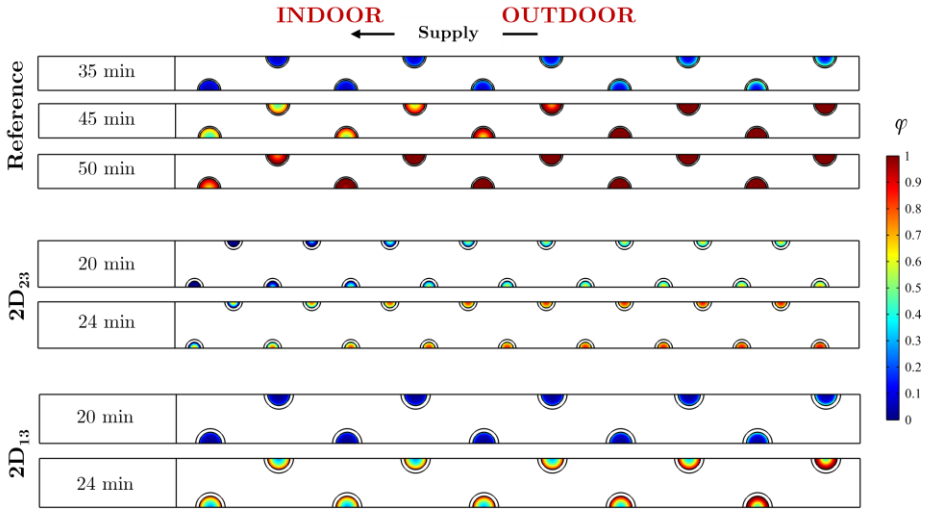

Fig. 6. 17. PCM melt fraction fields in supply mode before and after the optimization for different time instants (airflow from right to left)

Finally, the quantitative comparison between the optimal points detected in the optimization procedure and the reference one has been performed. In this frame, the efficiency of the heat recovery unit computed on these working conditions is evaluated according to the following procedures described in European Standard EN 13141-8:2014 for non-ducted units to measure the temperature ratio on the supply air side [165]. The standard definition is based on the difference between the supply air temperature after heat recovery and the outdoor air temperature, divided by the exhaust air temperature before heat recovery and the exhaust air temperature after heat recovery. For PCM-based units, air tends to reach the PCM temperature along the tube bundle. Therefore, compared with the classical definition, the efficiency can be rewritten as:

$$\eta(t) = \frac{T_{air}\ 0,t\ - T_{air}(L,t)}{T_{PCM}\ 0,t\ - T_{air}(L,t)} \tag{6.13}$$

which express the ratio between the real and the ideal maximum transferred thermal power. T_{air} and T_{PCM} are the temperature of air and PCM, respectively, evaluated at the initial/final position (0 or L) and at the time, t, depending on the

case. Thus written, the efficiency of the recuperator refers to the formulation of Peclet's number (Pe), which relates convective and diffusive transport phenomena, and thus physically represents the change in enthalpy divided by the driving force. The time-averaged heat recovery efficiency used in this work can be divided in two contributions, depending on whether the supply or exhaust air side efficiency ratio is considered:

$$\begin{cases} \eta_{exh} = \dfrac{1}{t_{exh}} \displaystyle\int_0^{t_{exh}} \dfrac{T_{air}\ L,t\ - T_{air}(0,t)}{T_{PCM}\ L,t\ - T_{air}(0,t)} \\ \eta_{su} = \dfrac{1}{t_{su}} \displaystyle\int_0^{t_{su}} \dfrac{T_{air}\ 0,t\ - T_{air}(L,t)}{T_{PCM}\ 0,t\ - T_{air}(L,t)} \end{cases} \tag{6.14}$$

Based on this definition, the efficiency depends on several factors: the fluid, the type of heat exchanger, the size and heat transfer properties of the heat transfer surfaces. Starting from the set of Eq. 6.14, the mean efficiency – as sum of charging and discharging process – is computed as follows:

$$\eta\ t\ = \frac{\sum_1^n (\eta t_i)}{\sum_1^n t_i} = \frac{\eta_{exh} + \eta_{su}}{2} \tag{6.15}$$

Generally, the efficiency is computed as the weighted average of efficiency of the process on the time of each process, here shortened in an arithmetical average because both processes last equally. Hence the results of the HRV efficiency are resumed in Tab. 6.7. This comparison is made with all assumptions/constraints of the model held constant, *e.g.,* total volume of the storage system. Our numerical results about the initial design show a discrepancy with the reference work about 5.7 percentage points on the exhaust mode and 1.5 percentage points on the supply mode. Therefore, accordingly with the temperature distribution gaps highlighted in Fig. 5, the model predicts the experimental trend quite accurately. The initial design results – referred to a $t_c = 30$ min – are then compared with the optimized one, referred to both 2D and 3D results. As it can be seen, the $2D_{13}$ configuration fails to improve system performance, as a consequence of the low average storage rate. Despite this, it has significantly lower investment costs (33.3% reduction). Conversely, the $2D_{23}$ and the 3D one shows an increase in the HRV efficiency. In the first case the difference with the initial design is really slight, while in the letter case it is considerable, *i.e.,* 6.7 percentage points.

Table 6. 7. HRV efficiency: reference VS optimized model

Case	η_{exh}		η_{su}		η
	Ref	Present work	Ref	Present work	Present work
Initial design • 30 min (each phase)	0.467	0.524	0.246	0.231	0.375
Optimized $2D_{13}$		0.373		0.275	0.324
Optimized $2D_{23}$		0.498		0.296	0.397
Optimized 3D (max OF_3)		0.543		0.346	0.444

6.6.2. Cost effectiveness of optimized HRV

HRV units can be a cost-effective solution to save energy and improve indoor air quality. When used and maintained correctly, HRVs in energy-efficient buildings can increase filtration and remove micropollutants, leading to better indoor air quality. This can provide more comfort for those living in the building and reduce health issues. However, the cost-effectiveness of an HRV unit depends on several factors such as climate, house sizes, as well as occupants' number. Further, as emphasized in this work, the overall cost for a single decentralized device that includes a phase change material as latent heat storage media can range from € 1100 to € 1450. This cost has to be summed to the one related to the ventilation, which depends on the air changes per hour (ACH) and thus on air fans' consumption. In this work, the optimization of the decentralized wall-type HRV has investigated the reduction of pressure drop – directly linked to pumping power – while seeking maximum thermal storage in the PCM. Based on the maximum pressure drop values and on the inlet velocity for supply and exhaust phases – considering commercially available fans – an electric power of 15 W is recommended (and plenty). Consequently, using an average electricity price for European Union of 0.253 €/kWh (including taxes, for household consumers, first half of 2022) [166], a comparison between HRV annual electricity consumption and household appliances is provided in Tab. 6.8.

Table 6. 8. HRV energy consumption/year compared to household appliances

Device	Working hours/day (h)	Energy required/year (kWh)	Cost/year (€)
Wall-type HRV	24	132	34.3
Home Refrigerator	-	550 [167]	139
Dishwasher	-	300 [167]	75.9
Audiovision	-	600 [167]	152
Washing machine	-	150 [167]	38.0

Therefore, as shown in Tab. 6.8, the wall-type HRV annual cost aligns with common household appliances and thus makes the HRV itself an economically feasible solution in terms of electricity consumption. It can also be noted that, by providing the cooling demand for ventilation [168], one can define the savings in terms of thermal energy and then determine (once the average EER has been set) an average value for electricity savings and consequent impact in terms of CO_2-eq. As remarked from the presented results, although a heat recovery and ventilation system can provide significant energy savings, it may not always be an effective solution. With numerous solutions available, determining the most suitable one is not a trivial task, especially if one has to choose at the same time the operating conditions to be used. Research focus is often on assessment methods to display the highest efficiency. However, neglecting device energy consumption and costs can lead to overestimation of the device feasibility. Decentralized devices with one fan, located on the building facade, are particularly sensitive to these aspects, as proved in this multi-objective optimization. Therefore, it's crucial to find a phase change material that fits the application, while using a single and comprehensive method that considers all these aspects simultaneously.

6.7. Final remarks

This work introduces a framework for the multi-objective optimization of a wall-type heat recovery and ventilation (HRV) unit, which stores latent heat thermal energy through a phase change material. The initial design of a recuperative, decentralized, and latent heat recovery system is taken from a reference work [26]. Then, a CFD model has been defined based on the alternating operation, *i.e.,* supply and exhaust modes, and has been optimized via a multi-objective genetic algorithm (MOGA) once 8 design variables, equations and constraints have been

set. The validation of the storage system has been carried out using the enthalpy-porosity method for modelling the PCM. The main results of this work are the following:

- The reference design can be modelled with a 2D conduction-based model, *i.e.,* neglecting natural convection inside PCM, without losing model accuracy, as proved by the limited values of the RMSE, *i.e.,* lower than 1.8 °C;
- The optimal design, which can be recognized looking at the 3D Pareto front (368 non-dominated solutions), outperforms the reference one by 28.4% with respect to the third objective function, *i.e.,* average storage rate, having fixed the total volume of the heat exchanger;
- The most suitable solution from an economical point of view shows a cost of the HRV system of 1119 € – which is far less than the baseline one – and also implies a low value of pressure drop, *i.e.,* 2.92 Pa, and a limited heat storage rate of 10.4 W;
- Computing the HRV efficiency – as from the European Standards – two over the three, *i.e.,* $2D_{23}$ and 3D configurations improve the system performance. This implies that in order to increase the efficiency of heat recovery, it is essential to increase the fan speed, the transversal pitch, and the diameter of the tubes, at the half of the operating time. The 3D Pareto approach shows solutions that outperform the initial configuration, with a 28.4% higher average storage rate while improving the other objective functions. Two solutions from the 2D fronts have been compared to show the difference in air flow distribution and PCM melting evolution. The HRV efficiency has increased from 37.5% to 44.4%, proving that the proposed approach helps to find solutions that reduce energy consumption;
- The analysis of the distribution of the design variables selected in this study shows that 2 out of 8 variables can be assigned a priori, *i.e.,* X_{tr} and t_c. This suggests that for future studies, a sensitivity analysis can be carried out to predict this result and lighten the optimization algorithm.

From the presented outcomes, it follows that the operating costs related to the optimized configuration identified in this contribution are comparable with yearly household appliance costs. However, the cost-effectiveness of this wall-type HRV system should be explored in depth by evaluating the savings in terms of thermal energy. The increasing popularity gained by PCMs – with the resultant gradual cost reduction – as well as the various types of system configurations that can be used, *i.e.,* plate-fin heat exchangers, make HRV with latent storage media a viable solution for the challenges of the future. In this frame, experimental research on

various phase change materials in varying indoor and outdoor settings is required, *e.g.,* winter conditions. Moreover, different storage media, *e.g.,* microencapsulated PCMs, should be tested to define which is desirable for such application. To ensure better heat diffusion in the PCM, the geometry of the tube bundle should also be changed, *e.g.,* using non-uniform pitches or fins on the tubes. Finally, additional research is needed to explore the balance between choosing a PCM for the winter and summer seasons.

7. Thermal insulation in rectangular enclosures

The content here presented is part of [P1], and [C5]

7.1. 3D printed walls

The global challenge of the energy transition demands the attention of every nation, as it is vital for the preservation of our planet's ecosystem. This imperative arises from the unchecked surge in greenhouse gas emissions across all sectors, including residential, industrial, and tertiary. Notably, the residential sector stands out as a major energy consumer, bearing a significant responsibility for the release of air pollutants and substances that alter the climate. These consumption patterns are largely attributable to the inefficient energy design of our built environment. One of the primary culprits behind energy inefficiency is the subpar design of building envelopes, which leads to substantial heat losses or gains and subsequently increases thermal loads. To counterbalance these loads, considerable energy consumption is required through suitable air conditioning systems. Today, global electricity production remains heavily reliant on non-renewable fossil fuels. Consequently, the inefficiency of any component within our built environment can significantly contribute to pollution and climate change.

In response to this challenge, various measures are currently being implemented to rejuvenate our building infrastructure. In most cases, these measures prioritize the installation of thermal insulation as a pivotal intervention, aimed at bolstering the thermal resistance of the building envelope. Conversely, for new constructions, the design phase includes a thermal analysis of the building to ensure compliance with current regulations and minimum energy performance requirements. Despite these efforts, several studies have underscored critical issues inherent in current construction techniques, such as material and labour costs. This highlights the pressing need to reevaluate and reform the processes involved in constructing buildings. In this context, the quest for innovative techniques in designing and constructing building envelopes has gained significant momentum. At the forefront of this movement is "Additive Manufacturing," encompassing a range of methods for

creating objects from computerized 3D models by layering materials. This approach offers numerous advantages over traditional production techniques, including the ability to transform complexity from a limitation into an asset, ensure material uniformity, reduce production steps, and lower costs [169].

However, the evolving regulatory landscape presents challenges even for innovative production methods like 3D printing. One of the most complex challenges is improving thermal performance, which involves reducing thermal transmittance (U) below specified limits depending on the climatic zone. Solutions to reduce heat transfer through printed walls have drawn inspiration from methods used to enhance the performance of building envelopes [170]. Specifically, researchers have explored the benefits of applying external insulation layers to printed modules [171] and introducing loose materials within the air cavities formed between layers of cement mortar. In both cases, the goal is to create barriers to heat transfer, akin to the use of foams and low-conductivity compounds. However, these approaches compromise one of the fundamental innovations brought by 3D printing techniques, which is the ability to produce a final product using a single material. Additionally, incorporating insulating materials increases production costs and introduces challenges related to deterioration and chemical incompatibility with cement mortar, which differs in chemical composition from the cement used in traditional construction techniques [172]

As a result, extensive research is often conducted to optimize the thermal properties of walls, aiming to eliminate the need for these solutions [173], [174]. These studies focus on enhancing thermal performance by adjusting the geometric configuration of modules or conducting numerical analyses that predict the actual thermal behavior of the wall before the printing phase begins.

In the context provided by the introduction, the subject of the patent application is an innovative cement mortar wall to be produced through "Additive Manufacturing" (3D printing), optimized from a thermofluid dynamics perspective, and combined with low-emissivity and thermal-insulating paints to minimize thermal transmittance (U). This wall has been named LUW3D ("Low U Wall via 3D printing"). The printing phase of the prototype takes place after a thermofluid dynamics optimization process aimed at improving thermal performance. In detail, by studying the fluid dynamics and heat exchange occurring within the air cavities inside the prototype, the optimal values of design parameters are identified to minimize thermal transmittance, as defined by UNI EN ISO 6946. Therefore, by combining the benefits of Computational Fluid Dynamics (CFD) analysis with Computer-Aided Design (CAD) virtual prototyping, it is possible to identify the optimal configuration, both structurally and energetically. Heat transfer within cavities is

governed by two phenomena: convection and radiation. The reduction of thermal transmittance can be pursued by reducing air recirculation phenomena within the cavities, which cause increased heat exchange by convection, and by limiting the radiative portion exchanged between the internal cavity surfaces. While adjustments to cavity geometry can address convection, radiative effects depend on temperature and emissivity (or emittance) of the material in the infrared wavelength band. Since we cannot modify the former, attention is directed towards limiting emissivity by applying paints with appropriate shielding properties. Specifically, by applying thin layers of low-emissivity material, radiative heat exchange can be significantly reduced. Finally, the addition of thermal-insulating paints, which introduce additional non-negligible thermal conductive resistances, allows achieving thermal transmittance values in line with the limits recommended by Ministerial Decree 26/6/15.

The prototyping of the artifact, which is constructed in modules, proceeds through multiple phases. A detailed representation of the logical process underlying the wall design is provided in the flowchart in Fig. 7.1. Here, the steps defining the path to achieve a transmittance value lower than the limit (U_{lim}) are described. Specifically, this technology involves initializing geometric data related to the wall (*e.g.,* height, length, thickness) and the printing process (e.g., layer thickness, spacing, height, extrusion profile, etc.). The printing process imposes specific construction constraints that must be considered from the initial design phase, such as maximum overhang. Once these parameters are identified, the limit value below which the artifact's transmittance is desired is defined, depending on the climatic zone. All steps are then determined based on this set value. The modeling of internal geometry occurs after an implicit step (not shown in the flowchart) that involves defining the profiles of the external partitions. Specifically, external profiles can replicate the classic configuration of walls found in residential buildings, such as vertical walls, or assume curvilinear forms, always in accordance with geometric and construction constraints. Therefore, external partitions are not necessarily planar but can be defined by envelope surfaces of curvilinear profiles. The prototyping of the wall aims to limit three simultaneous mechanisms of heat exchange: conduction, convection, and radiation. To address the first two components, it is necessary to properly model the internal geometry (partitions and cavities) or consider the application of thermal-insulating paints. Conversely, reducing the radiative portion can be achieved by using low-emissivity paints. The internal geometry features a series of cavities and partitions made of cement mortar, properly shaped, and spatially located to inhibit natural circulation and limit conductive heat exchange. The partitions can be spaced at a constant or variable pitch, such as according to a geometric series. They are defined based on functions of any nature, such as

linear, quadratic, sinusoidal, etc. Prototyping aims to create cavities that ensure transmittance is below the limit value. It is possible that, depending on the defined geometry, this constraint may not be met. This implies that actions to limit convection are insufficient to reduce transmittance. In such cases, the use of thermal-insulating paints is planned, defining a layer of thermally resistant material that adds to the conductive resistance of the cement mortar. These paints are to be applied uniformly to the surface of the partitions.

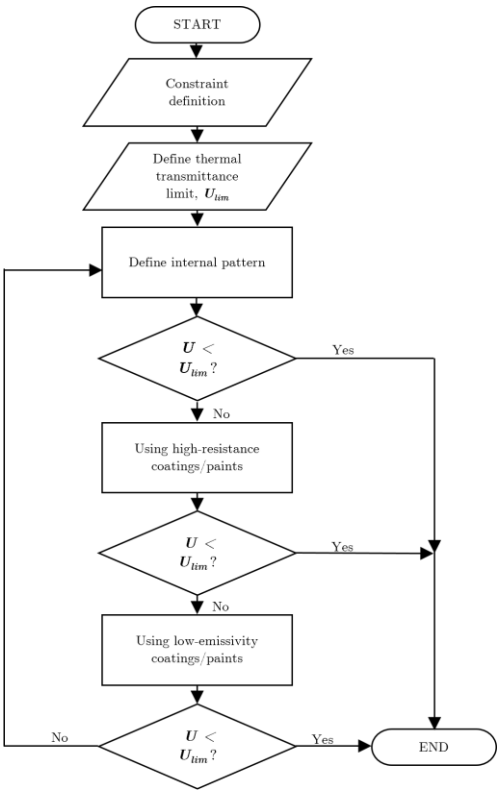

Fig. 7.1. Flow chart of thermal transmittance reduction

These paints are to be applied uniformly to the surface of the partitions. If this solution also fails to meet the constraint on thermal transmittance, it is necessary to apply a low-emissivity paint that inhibits heat transmission by radiation. The three-dimensional (3D) model prototyping is carried out using CAD software. The

geometry thus created is imported into thermofluid dynamics simulation software (CFD), through which the model's performance is evaluated by defining appropriate boundary conditions. The materials used for the prototype are as follows: (i) cement mortar suitable for meeting the requirements of 3D printing technologies for extrusion; (ii) low-emissivity paint; (iii) thermal-insulating paint. The mortar is produced from a dry premixed powder composed of selected sands with the addition of water. The mixture, obtained respecting appropriate proportions, possesses mechanical characteristics that enable self-support during the printing phase, ensuring maximum fidelity to the original 3D model. An experimental evaluation was conducted in the thermal insulation materials analysis laboratory (IMATlab) at the University of Federico II, using the NETZSCH Guarded Hot Plate (GHP) 456 Titan® instrumentation, from which a thermal conductivity value of the material (k) equal to 1.05 W/m K was derived.

The examined prototype involves the application of 2 layers of shielding low-emissivity paint. Specifically, this paint ensures a reduction in the emissivity of the cavity walls, resulting in a reduction in thermal power transferred by radiation. Currently, low-emissivity paints are available on the market, capable of providing an emissivity value of 0.2 in the infrared band. The module, in fact, emits thermal radiation in the far-infrared band when it reaches temperatures close to ambient temperatures. Since the thermal power emitted by a surface is proportional to its emissivity, the use of such paints - based on aluminium powders - with reduced emissivity leads to a reduction in emitted radiation. Furthermore, the method under consideration includes the application of thermal-insulating paints, in addition to the use of low-emissivity paint. These paints, in fact, have the benefit of increasing the thermal resistance of the module. Specifically, among the products currently available on the market are paints based on hollow glass microspheres, which offer excellent insulating properties. Therefore, by applying an appropriate number of layers of paint to the external and internal surfaces of the module, the thermal transmittance value (U) can be further reduced. The optimization phase of the geometry precedes the creation of the prototype. In detail, the optimization process involves parameterizing the model based on the geometric constraints set during the design phase. Each geometric variable can take discrete values within a range defined in relation to the identified geometric constraints. Among the main geometric variables that influence the objective function to be minimized, *i.e.,* thermal transmittance (U), are the thickness of the module and the layers of cement mortar, angular offset, i.e., overhang, and the thickness and height of the cavities. The ranges of variation for each variable are reported in Tab. 7.1. Experimentally, it has been observed that the stability of the material during deposition is influenced

by this parameter. In detail, greater stability is achieved in the case of a nozzle of 0.04 m.

Table 7.1. Main constraints for 3D printing

Maximum values		
X (m)	Y (m)	Z (m)
0.6	3	3
Minimum values		
X (m)	Y (m)	Z (m)
0.4	-	-
Layers properties		
Overhang	Bending	Texture
15°	Single/double	Thin/thick
Layers dimension		
Thickness (cm)		Height (cm)
4 – 6		1 – 1.5

The prototype of the LUW3D wall, resulting from optimization, is depicted in Figure 7.2. The overall thickness is 50 cm. The section is square (1m x 1m), and the thickness and height of the cement mortar layer are 0.04 m and 0.01 m, respectively.

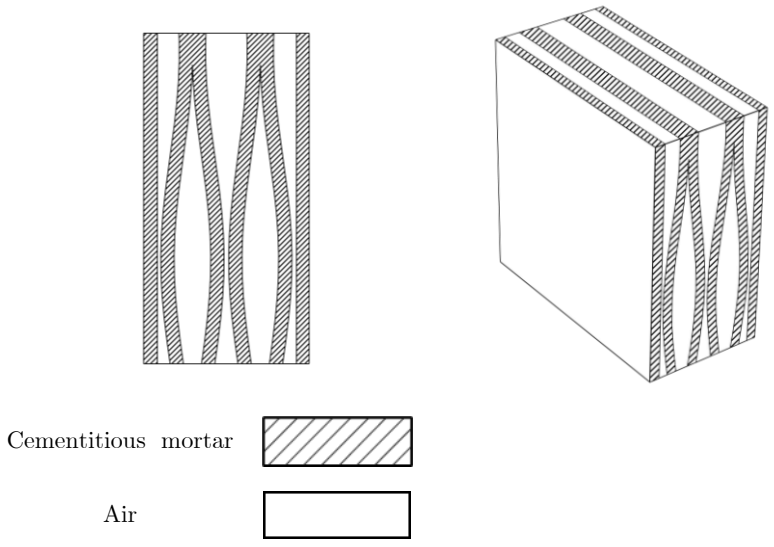

Fig. 7.2. 2D and 3D views of the prototype

The height of the cavities is optimized to limit the increase in the convective heat transfer coefficient caused by natural convection. The profiles describing the development of the external surfaces are linear, while the characteristic surface of the dividing partitions is generated by the composition of two perpendicular sinusoids. The profiles are pairwise symmetric with respect to the vertical axis. The artifact, including internal and external profiles, is created in a single solution through the cement mortar deposition process. Depending on the type of geometry defined during prototyping, the system deposits material through the nozzle - using pneumatic, mechanical, piston, or worm drive mechanisms - initially printing along the outer contour and subsequently defining the internal pattern. The thermal transmittance (W/m^2K) (U) is given - according to UNI EN ISO 6946 - by the reciprocal of the sum of specific thermal resistances [m^2K/W]. In detail, this sum consists of 4 terms: the internal and external boundary resistances (R_{si} and R_{se}), the resistance of non-homogeneous layers (R_{nh}), and that related to homogeneous material layers (R_h). R_{int} and R_{est} are equal to the reciprocal of the convective heat transfer conductance of the air, R_h is equal to the ratio of the material thickness to its thermal conductivity, while R_{nh} can be obtained by simulating the behavior of the fluid. Therefore, thermal transmittance varies significantly depending on ambient conditions, which are considered by evaluating the resistances R_{int} and R_{est}. They should be assessed consistently with what is reported in the regulation. If you want to analyze the thermal exchange related to the wall alone, it is necessary to refer to conductance (C). For non-homogeneous elements, *i.e.,* characterized by non-uniform thermal properties, such as air cavities, it is necessary to refer to the conductance, C, of the layer, expressed in W/m^2K. The conductance values are reported in the relevant reference standards or can be obtained through laboratory tests or finite element numerical simulations (as in the present case). Through C, it is possible to decouple from considering the interaction between the wall and external conditions - which vary depending on the location - and consider only the thermal performance of the module. The obtained values of conductance (C) and thermal transmittance (U) for the LUW3D module are 0.355 W/m^2K and 0.335 W/m^2K, respectively. The substantial contribution to achieving these values is ensured by the application of thermal-insulating and low-emissivity paints. In detail, the order of application of the different products is illustrated in Fig. 7.3.

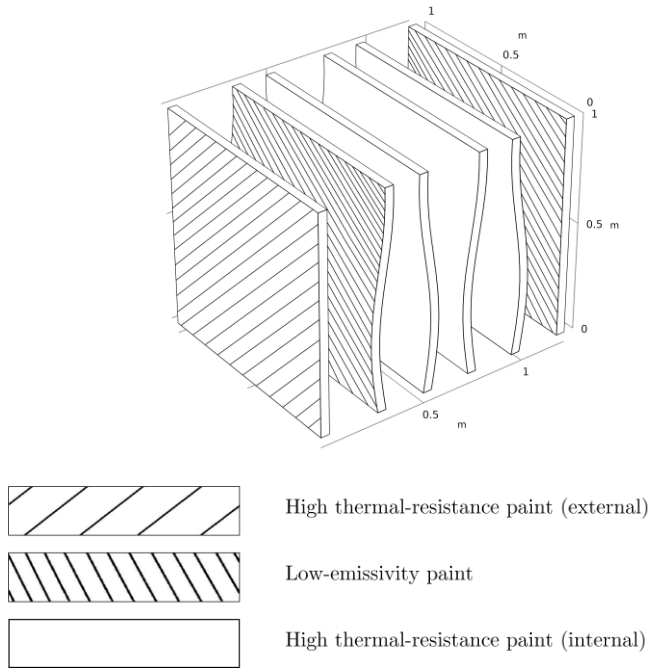

Fig. 7.3. View of all layers and paints to be used for each of them

The thermal-insulating paints are placed externally to the module and internally on the sinusoidal profiles. In contrast, the low-emissivity paint is applied to the internal surfaces of the external partitions and the external surfaces of the lateral sinusoidal profiles. The application of the paints is ensured by an airbrush with an extension. In particular, through appropriate holes, the extension can be inserted inside the cavities, allowing for the correct painting of surfaces, ensuring a homogeneous and uniform distribution. The placement of low-emissivity paints in the outermost cavities limits the propagation of infrared radiation inside the module. On the other hand, thermal-insulating paints increase the surface resistance of the internal partitions, ensuring lower heat propagation tendency.

With reference to the optimal configuration of the LUW3D prototype, the velocity and temperature fields, related respectively to convective motions inside the cavities and the entire prototype, are shown in Fig. 7.4 below.

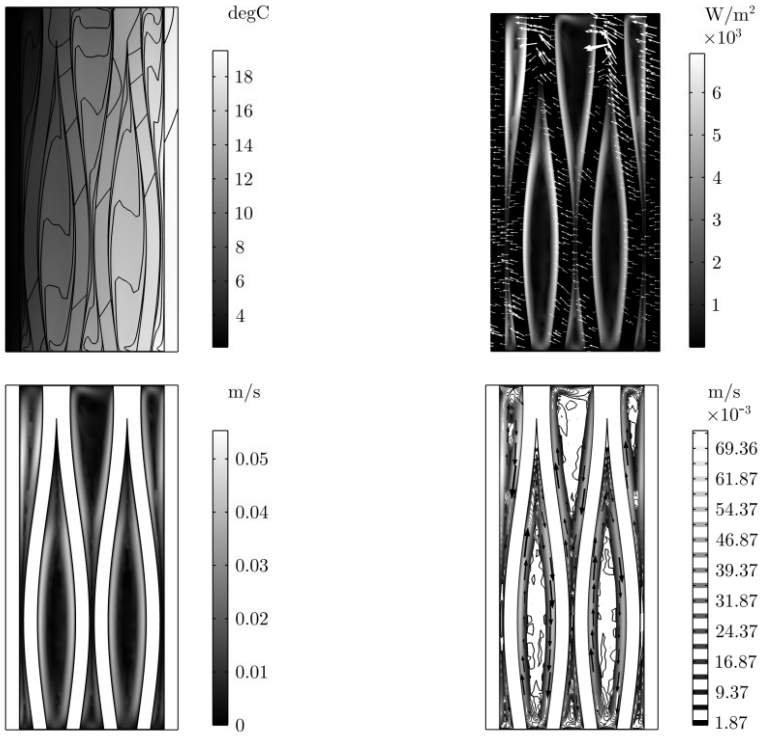

Fig. 7.4. Temperature field; heat flux magnitude; velocity magnitude field and vorticity contours

In-depth analysis of Fig. 7.4 reveals the presence of air recirculation within the cavities, exerting an influence on the propagation of heat through the wall and consequently shaping the resulting temperature field as depicted in Fig. 7.4c. Moreover, Fig. 7.4d highlights the thermal flux vectors, and their uneven distribution within the prototype suggests the emergence of preferential pathways for heat diffusion. Notably, the conductive heat transfer mechanism, which affects the regions of cement in contact with each other, encounters resistance due to the presence of air cavities acting as a barrier to heat transmission. This rationale underpins the decision to prevent direct contact between the internal vertical surfaces of the external panels and the sinusoidal surfaces, thereby allowing air to intervene and curtail heat exchange.

7.2. Thermo-hygrometric problem

The evaluation of the thermal and hygrometric performance of the 3D printed wall is divided in 3 different studies: buoyant flow, radiative heat transfer (non-isothermal flow) and moisture transport (in building materials, in air) in confined cavities. All these points are achieved simultaneously because of their mutual influence, as depicted in Fig. 7.5.

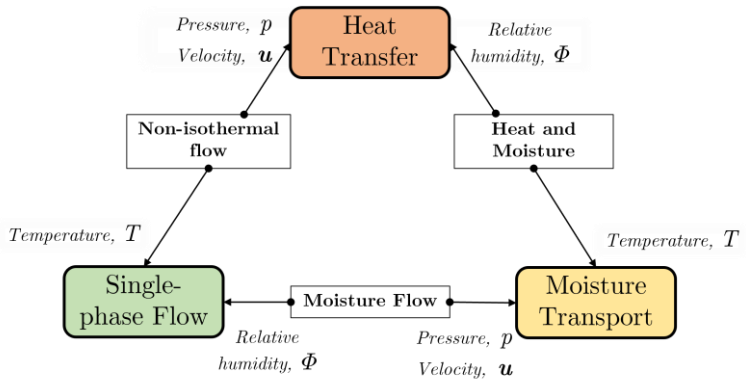

Fig. 7. 5. Problem definition

Among the several benefits of 3D printing techniques, one of the most relevant is the design of low-weight structures, which results in the presence of air gaps. Leaving an air gap between two layers in a wall allows the air being poor heat conductor, responding as a barrier to heat transfer. Free convection is typically the main driving force of the resulting recirculating flow. Different approaches have been developed, starting from using the Boussinesq approximation and variable viscosity [175], while performing a linearized approach and reported results for moderate Rayleigh numbers [176]. The problem under analysis is depicted schematically in Fig. 7.6.

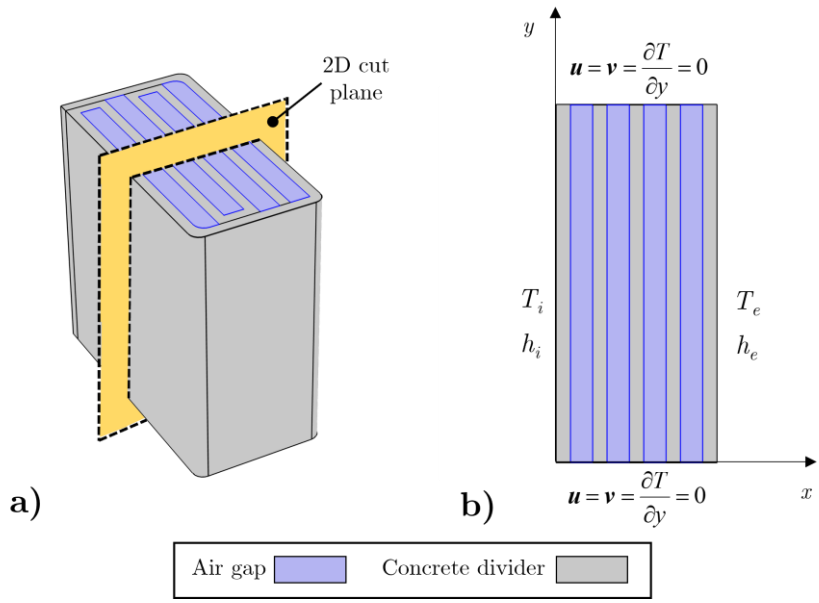

Fig. 7. 6. Problem model: a) 3D sample; b) 2D section

The flow domain is the interior of a 2D rectangular cavity with a fixed aspect ratio. The horizontal surfaces of the cavity are assumed to be perfectly adiabatic, while the vertical walls are surrounded by air, so that convective heat flux is assigned. Parameters T_i, h_i and T_e, h_e are temperatures and convective heat transfer coefficients for internal and external environment, defined for the left and right walls, respectively. Owing to heat transfer through the vertical walls, density changes result in a recirculating flow, in a range where the flow remains in a laminar regime. To perform a comparison of the evaluation methods, the moisture problem is modelled according to the EN ISO 13788 [177] standards. Thus, the methodology is applied for the design of a building envelope prototype for the winter climatic conditions of Naples, which corresponds to an outer temperature $T_e = 2$ °C and $\phi_e = 92\%$, and an inner temperature $T_i = 20$ °C, with $\phi_i = 55\%$. So, the simulations are performed under a temperature difference of 18 °C. In the hypothesis of stationary flow, elements with a simple flat geometry – made from a sequence of homogeneous and isotropic layers, including air layers – and isothermal surfaces outside the wall, thermal transmittance is a regulated parameter to evaluate the thermal performance [178]:

$$U = \frac{1}{\frac{1}{h_i} + \sum_{i=1}^{n} \frac{s_i}{k_i} + \sum_{j=1}^{m} R_j + \frac{1}{h_e}} \tag{7.1}$$

The evaluation of the convective coefficients h_i and h_e is achieved from UNI EN ISO 6946 [178], which specifies the conventional values of surface resistance. Indeed, for the external convection the air velocity is assumed to be 4 m/s [8]. Since transition in a free convection boundary layer depends on the relative magnitude of the buoyancy and viscous forces in the fluid, a parameter used to compare the thermal gradient with the viscous resistance is the dimensionless Rayleigh number, which is the product of the Grashof and Prandtl numbers and measures the ratio of the buoyancy forces with respect to the viscous forces:

$$Ra = GrPr = \frac{g\beta\ T_S - T_\infty\ L^3}{\nu\alpha} \tag{7.2}$$

Where L is the characteristic length, *i.e.,* the height. Depending on the Rayleigh number the flow can be categorized as turbulent or laminar [179]. For rectangular enclosures, Rayleigh numbers less than 10^8 indicate a buoyancy-induced laminar flow, with transition to turbulence occurring over the range of $10^8 < \mathrm{Ra} < 10^{10}$ [180].

Governing equations

To solve the non-isothermal flow – which occurs in natural convection problems – the Boussinesq approximation is performed. The unknown parameters that appear in the following equations are the fluid velocity vector $\boldsymbol{u}$, the pressure p and the temperature T:

$$\nabla \cdot \boldsymbol{u} = 0 \tag{7.3}$$

$$\rho\ \boldsymbol{u} \cdot \nabla \boldsymbol{u}) = -\nabla p + \mu \nabla^2 \boldsymbol{u} - \rho\beta(T - T_0\ \boldsymbol{g} \tag{7.4}$$

$$\rho c_p (u \cdot \nabla T) = \nabla \cdot (k \nabla T) \tag{7.5}$$

Where, ρ is the fluid density, μ the fluid dynamic viscosity, β the coefficient of thermal expansion, k the thermal conductivity, c_p the specific heat at constant pressure, $\boldsymbol{g}$ the acceleration due to gravity, and T_0 the reference temperature.

As regards the coupling between heat and moisture transport through the building material, the equations implemented in this study are here presented, under

the hypothesis of steady state flow, 2D model, thermophysical properties dependent from temperature, absence of heat and moist sources, in accordance to the European Standard EN 15026 [181]:

$$-\nabla\cdot\left(k_{eff}\nabla T + L_v\delta_p\nabla\ \Phi p_{sat}\ \right) = 0 \tag{7.6}$$

$$\nabla\cdot\left(-\xi D_W\nabla\Phi - \delta_p\nabla\big(\Phi p_{sat}\ T\ \big)\right) = 0 \tag{7.7}$$

Where k_{eff} is the effective thermal conductivity, L_v is the latent heat of evaporation, δ_p is the vapor permeability, Φ is the relative humidity, p_{sat} the vapor saturation pressure, ξ is the moisture storage capacity, D_W is the moisture diffusivity. For moist air, heat transfer and moisture transport – by diffusion and convection – are modelled trough the following equations:

$$\rho c_p\boldsymbol{v}\cdot\nabla T + \nabla\cdot\boldsymbol{q} = 0 \tag{7.8}$$

$$M_v\boldsymbol{v}\cdot\nabla c_v + \nabla\cdot\boldsymbol{g}_v = 0 \tag{7.9}$$

$$\boldsymbol{g}_v = -M_v D\nabla c_v \tag{7.10}$$

Where M_v is the molar mass of water vapor and D is the vapor diffusion coefficient in air. For the thermal radiation problem, the surface-to-surface model is implemented, where each wall of the cavity is opaque to thermal radiation – the emissivity of cementitious materials is equal to 0.9 – and the fluid is deemed to be transparent and not participating in radiative heat transfer.

Glaser Method

Glaser method consists of the detection of water condensation inside or on building materials surfaces, through a graphic comparison between the saturation pressure and the partial steam pressure. The building envelope, dividing environments with different temperatures and relative humidity, is subject to heat and moist transfer, which is caused by the difference between vapor partial pressure of the two environments – determined by Eq. 7.11 – and by the wall vapor permeability.

$$p_{vap}(\varphi, T)\ =\ \varphi\ \cdot\ p_{sat}(T) \tag{7.11}$$

Condensation should occur if $p_{vap} = p_{sat}\ (T)$, where the distribution of partial pressure of vapour is determined by means of the Fick's law. By neglecting heat and moisture storage, latent heat effect and capillary transport of liquid moisture, the following equations are obtained for heat and moisture transport:

$$\nabla \cdot (k_{eff} \nabla T) = 0 \tag{7.12}$$

$$\nabla \cdot \left(\delta_p \nabla \left(\Phi p_{sat}\ T\ \right)\right) = 0 \tag{7.13}$$

Moreover, Glaser method does not consider some important physical phenomena, *e.g.,* the dependence of thermal conductivity on the moisture content, the variation of the properties of the materials as a function of the moisture content, the air flows through cavities, and therefore it generally overestimates the condensation risk. Based on this value and on the governing equations, the thermophysical properties implemented in the FEM model are listed in Tab. 7.2.

Table 7.2. Thermophysical properties

Cementitious mortar properties	Value
Density, ρ (kg/m^3)	2000 kg/m^3
Specific heat, c_p (J/kg K)	880 J/(kg K)
Water content, w (kg/m^3)	$w = \frac{146}{(1 + (-8 \cdot 10^{-8} \cdot R_{H_2O} T_{ref} \rho_w \ln(\Phi)^{1.6})^{0.375}}$
Thermal conductivity, k_{eff} (W/m K)	$k_{eff} = 1.2 + \frac{12.64}{1000} w$
Vapour permeability, δ_p (kg/(m s Pa))	$\delta_p = f(w(\Phi))$
Moisture diffusivity, D_w (m^2/s)	$D_w = f(w(\Phi))$

Grid independence

A well-tuned mesh is needed to capture the solution, especially the temperature and velocity changes near the walls. COMSOL Multiphysics® provides 9 levels mesh *i.e.,* from extremely fine (1) to extremely coarse (9). The full mesh, extremely fine (1), consists of 97580 tetrahedral elements. To reduce the computational burden, a grid independence test is performed on the thermal transmittance value (U), as in Fig. 7.7. The final mesh level, *i.e.*, finer (as in Fig. 7.7), represents a compromise between the thermal transmittance value, the percentual deviation and the running time. To validate the results obtained by the simulations, standard values

of transmittance are calculated, using the method provided by international regulation (ISO 6946:1996, 1996). The validation approach must be referred to cavity thicknesses less (or equal) than 30 cm. Indeed, the enclosure thickness is assumed to be of 10 cm. The transmittance value obtained is 2.3904 $W/m^2 K$, against the 2.3998 W/m^2K of ISO 6946. To provide the verification of the model built in COMSOL Multiphysics®, a numerical study on the assessment of thermal transmittance of hollow concrete blocks has been selected as reference work [182]. The mentioned study solves the natural convection problem of two parallel isothermal walls at different temperatures. Both the cases – with and without radiation – are considered, to evidence how the percentage deviation is amplified including the radiation.

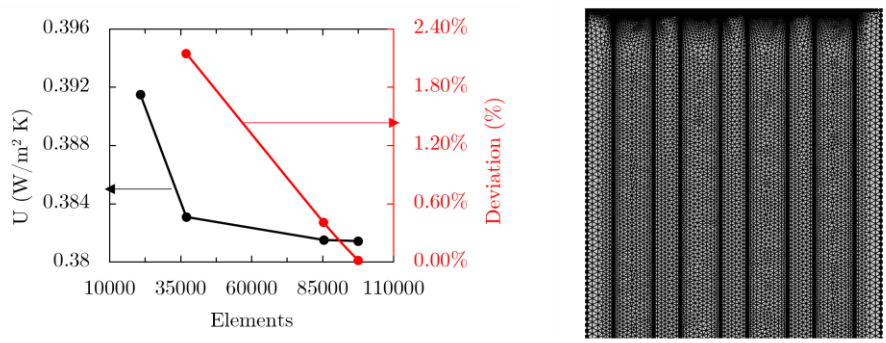

Fig. 7. 7. Grid independence: a) test on thermal transmittance; b) final mesh configuration

As itemised in Tab. 7.3., the model results are quite the same for the case without radiation, while a higher (but still limited) difference outcomes from the second case, which accounts for air contribution as participating media for radiative heat transfer through discrete ordinate method (DOM).

Table 7.3. Comparison between present work and reference thermal transmittance

Study	Thermal transmittance, U (W/m^2K)	
	No-radiation	DOM
Present work	2.898	5.7
Reference	2.895	5.85
Difference (%)	0.1	2.56

The comparison between the Glaser method application and the thermo-fluid dynamic one is now discussed. Specifically, a first comparison between the Glaser Method results for the 1D case and the 2D CFD model with the same assumptions, *i.e.,* 2D simplified, is assessed. Then, the Glaser method limitations are exhaustively highlighted. Moreover, a brief comment on the thermal transmittance is here

provided. Thus, as starting point, results are presented in terms of temperature distribution (Fig. 7.8a), and comparison between the trends of saturation pressure vs partial pressure over the geometry previously described (Fig. 7.8b). In detail, the diagrams have been obtained implementing Eq. (7.11) for partial vapour pressure, and saturation pressure (p_{sat}) is evaluated following the EN ISO 13788 standard. Fig. 7.8 shows that the saturation pressure is linear in the 1D case, while it is affected by the recirculating flow inside cavities in the 2D case. Nevertheless, values at the interfaces are almost equal. Moreover, the slope of the curves does not match perfectly in the concrete region because of the definition of the effective thermal conductivity, dependent on the water content (see Tab. 7.2).

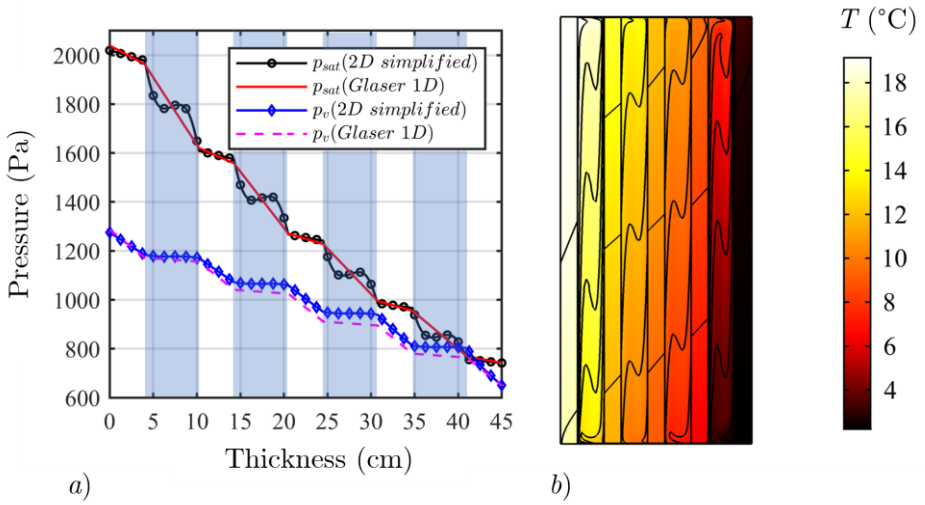

Fig. 7. 8. a) Comparison of saturation and partial pressure between Glaser 1D and 2D simplified model; b) 3D wall temperature field

As concerns the partial vapour pressure – since the Glaser method considers the vapour transport in the building materials only by diffusion – the small deviations between the curves in the concrete regions are influenced by the vapor permeability trend. The higher $\delta_{p,}$ the lower the water content, which increases from left to right according with the boundary conditions.

Therefore, the 2D trend is a flatter on the left compared to those on the right. At this stage, we consider the results of the model with the contribution of latent heat and, specifically, the transport of moisture by capillarity within the concrete

layers. Diagrams in Fig. 7.9 show the trends of p_{sat} and p_v obtained at first for the model with Glaser method limitations, then without it, *i.e.,* 2D complete.

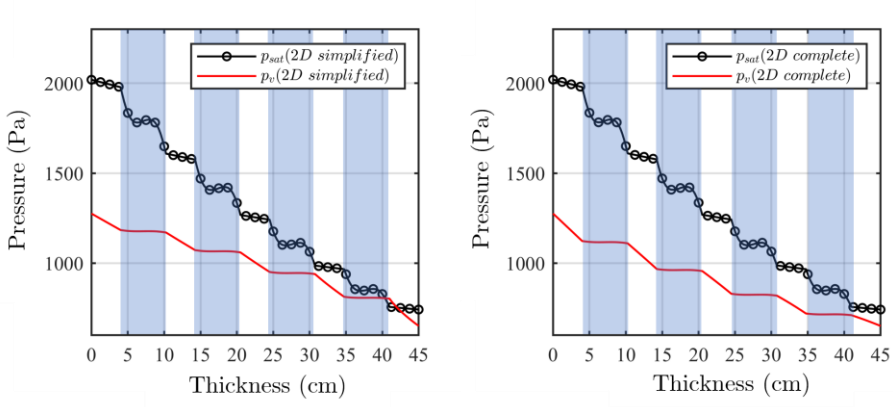

Fig. 7. 9. Difference between condensation risk detection of 2D simplified model (left) and 2D complete model (right)

Based on pure observation – under the tested environmental conditions – interstitial condensation occurs adopting the hypothesis of the Glaser method, as confirmed by the intersection between the partial pressure of vapour and the saturation pressure. Conversely, it does not occur when we consider the contribution of latent heat and the moisture transport by capillary suction – which is quite relevant for high relative humidity values – and depends on the moisture diffusivity.

8. Heat sinks: from traditional to microchannel TO-based

The content here presented is part of [C1], [C2] and [C4].

8.1. Heat sink design with phase change materials

Thermal management is considered to be one of the main bottlenecks in the growth of innovative microprocessors technologies [183]. In this vein, one of the current research challenges is to find compact and economically feasible devices able to dissipate large amount of heat under appropriate constraints [133]. The need to remove heat fluxes at a rate equal or greater than the generated one is linked to their temperature increase, which can lead to reduction of the reliability and performance, and at worst to a failure. In several electronics cooling applications, *e.g.,* temperature stabilization during pulsed operation, short term thermal storage, and protection from failure during loss of coolant scenarios, PCM-based heat sinks can be well suited solutions because of their capability of absorbing the generated waste heat in the absence of high thermal gradients [184]. These passive devices take advantage of the PCM latent heat, at least two orders of magnitude higher than the sensible energy that can be stored by other materials. Moreover, while absorbing thermal energy, PCMs guarantee a minimal temperature rise during the phase transition. Generally, having defined a suitable PCM for an application, this kind of heat sink can reduce system size, cost, maintenance, and power requirement [185]. Nevertheless, common trade-offs between thermal storage capacity and temperature differences can emerge, *e.g.*, fins number effects thermal gradient and meanwhile the PCM amount, and thus the thermal storage capability. New solutions should be able to survive massive heat production while keeping the space and safety constraints. In this frame, optimizing heat sinks with numerical approaches is a topic of general interest, as proved by several studies that went through potential thermal management solutions in depth. Numerical optimization approaches based on topology optimization would be very useful to find optimum solutions for the additive manufactured heat sinks [62]. For instance, Sigmund *et al.* [186] improved the performance of a liquid-cooled heat sink with topology optimization by a peudo-3D model resulting in a modified air foil fin shape. Iradukunda *et al.* [187] used topology optimization to generate optimal heat spreading

structures that can be coupled with PCM to enhance the heat transfer rate. Specifically, under a pulsed load of 50 W, the hybrid heat sink exhibited the capacity to lower peak temperature by up to 18.9 °C relative to a benchmark plate fin design of similar dimensions. There are still many practical challenges that need to be addressed to achieve volume or mass-optimized, fully functional, and highly reliable PCM heat sink designs. This work points to provide a further example of topology optimization, starting from an existing geometry [188] and proving the benefits of this process. Specifically, the main contribution of this work is to enhance heat transfer mechanisms in the PCM-based heat sinks with an innovative metal structure and contribute to the knowledge gap-filling on thermal analysis of heat sinks for thermal management employing innovative – but well established – optimization tools.

A half plate-fin (*PF*) PCM-based heat sink for electronic cooling is illustrated in Fig. 1, together with a topology-optimized one (*TO*). Both geometries are made of a conductive metal structure, *i.e.,* aluminium. The traditional one is taken from a reference work [188], as well as the materials thermophysical properties, while the topology-based is achieved through steps described later. All the walls of the PCM-based heat sink are adiabatic except for the heat source area where a constant temperature of 44 °C is applied [188]. Therefore, heat is acquired from the hot wall (T_w) to which the plate fins are attached, and then transferred into the PCM for temporal heat dissipation. The initial temperature of the computation domain is set at 20 °C.

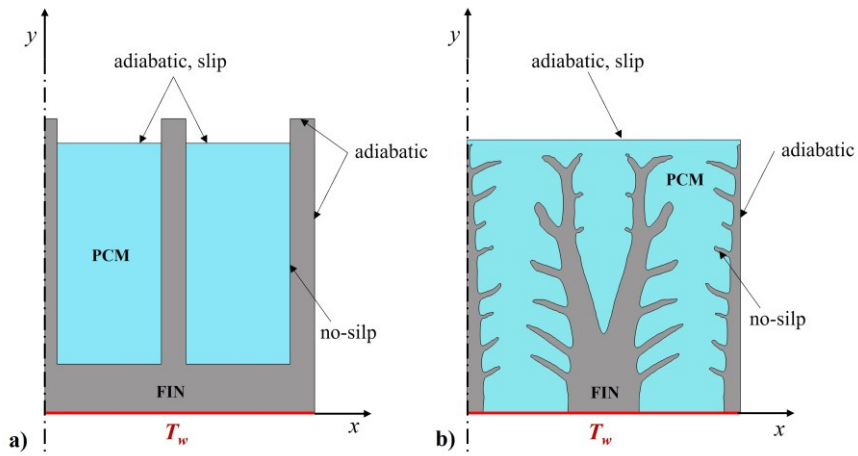

Fig. 8. 1. Heat sink geometry: a) plate fin (PF), topology (TO)

The PCM is demanded to absorb heat from a metal structure – aimed at enhancing heat diffusion – and then to overcome the low thermal conductivity of PCM. Under a fixed metal volume fraction, the optimization effort is worthwhile in designing a highly efficient conductive thermal structure in a PCM-based heat sink. The aim of this optimization problem is to design a conductive heat sink (Fig. 8.1) that enhances the heat transfer via diffusion between the domain and the constant temperature boundary. To balance the heat rate in the design domain, an artificial volumetric heat source term (Q) is introduced on the right-hand side of Eq. (8.1) to mimic the heat absorbed by the PCM during the phase change process:

$$-k\nabla^2 T = \ Q \quad on\ \Omega \tag{8.1}$$

To simulate the electronic heat source, a constant wall temperature (T_0) – above the PCM melting temperature – is prescribed, while remaining boundaries are assumed to be adiabatic:

$$T = T_0 \quad on\ \Gamma_D \tag{8.2}$$
$$\nabla T \cdot \boldsymbol{n} = 0 \quad on\ \Gamma_N \tag{8.3}$$

To find the optimal topology for given objective functions and constraints, the density method is used [189]. For this purpose, a design variable, *i.e.,* design density (γ) is defined, which can assume for each finite element values between 0, *i.e.,* no material or fluid, and 1, *i.e.,* solid material. The solid isotropic material with penalization (SIMP) method is used to influence the material distribution such that intermediate design values are repressed, and a well-defined material distribution is achieved, *i.e.,* replaces the discrete variables with continuous ones. In this frame, using the SIMP method, the thermal conductivity of (8.1) is replaced by:

$$k_{SIMP}\ \gamma \ = k_{min} + (k_{max} - k_{min})\gamma^n \tag{8.4}$$

where k_{min} and k_{max} are the thermal conductivities of the poor and the high conductors, respectively, while n is the penalization factor, set equal to 8. The limit on the solid fraction is defined based on the reference case, *i.e.,* 35 % of the total area. From a topological point of view, the design objective is to find the optimized material distribution that minimizes the global temperature distribution of the domain. At the same time, to avoid geometries with low-scale parts – to be hardly achievable with 3D printing techniques – manufacturing constraints are also

considered in the optimization approach [190]. The mathematical problem can be drawn as following:

$$\begin{cases} minimize\text{: } f\ \gamma\ = \displaystyle\int_{\Omega} \nabla T\ k\ \gamma\ \nabla T\ d\Omega + \frac{h_0 h_{max}}{A} \int_{\Omega} |\nabla\gamma(x)|^2 d\Omega \\ s.t.\ :\ \int_{\Omega} \gamma\ d\Omega < \delta A \\ 0 \leq \gamma \leq 1 \end{cases} \tag{8.5}$$

Where h_0=0.3 mm and h_{max}=0.05 mm are the parameters that govern the size of details in the solution and the mesh size, respectively. A is the domain surface, and δ is the solid material fraction, *i.e.,* 35 %.

Several papers performed an analysis with a topology-based structure considering the PCM during the optimization process. However, the resulting geometry bears a close resemblance to the TO structure obtained considering pure conduction without PCM motion. Therefore, in the present study, the optimized structure is derived neglecting the PCM presence. Two conductive metal structures, *i.e.,* the conventional plate-fin and optimized tree shape structures deriving from the topology optimization process are investigated.

The following assumptions are set for the PCM thermal model definition: PCM is isotropic but not homogeneous; phase change during solidification/melting occurs in a temperature range established in [188]; volume reduction/expansion during the phase change is ignored, together with air gaps caused by this; laminar flow model for PCM liquid phase, which is treated as a Newtonian fluid; Boussinesq approximation to include the buoyancy effects. The phase change modelling is based on three distinct regions, *i.e.,* a totally liquid region, a solid one and a mushy zone, where both phases coexist.

Each numerical simulation solves the enthalpy-porosity approach for the PCM numerical analysis. In particular, the energy and momentum equations are discretized using the fully coupled solver. The convergence criteria for the continuity and momentum equations and energy equation are applied, performing mesh independence study and time step evaluation to ensure the numerical accuracy, as in Fig. 8.2.

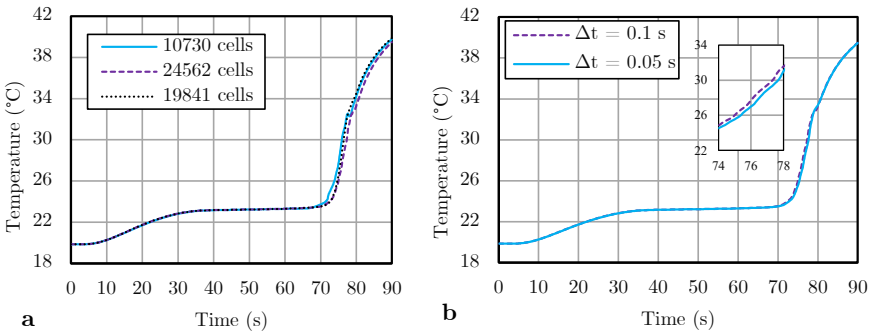

Fig. 8. 2. a) grid convergence test at time step of 0.1 s; b) time step convergence test at cells number of 24562

Looking at these trends, further increasing the numbers of elements – with respect to 10730 cells – has negligible effects on the simulation results. At the same time, the time steps independence is assessed, selecting at first a $\Delta t = 0.05$ s and then equal to 0.1 s. The second one represents a suitable trade-off between acceptable computational costs and model reliability. Once optimal grid and time step have been defined, a validation step is performed with respect to the reference case (Fig. 8.3). The comparisons are made in terms of temperature evolution – at the point P = ($7.8e^{-3}$, $5e^{-3}$) with reference to the axis position in Fig. 8.1 – and PCM melt volume fraction, varying the phase change interval ΔT_M. In both cases, except for a slight difference in the PCM response to the liquid phase transition, the model confirms the reference trends. However, the case with ΔT_M seems to be more accurate.

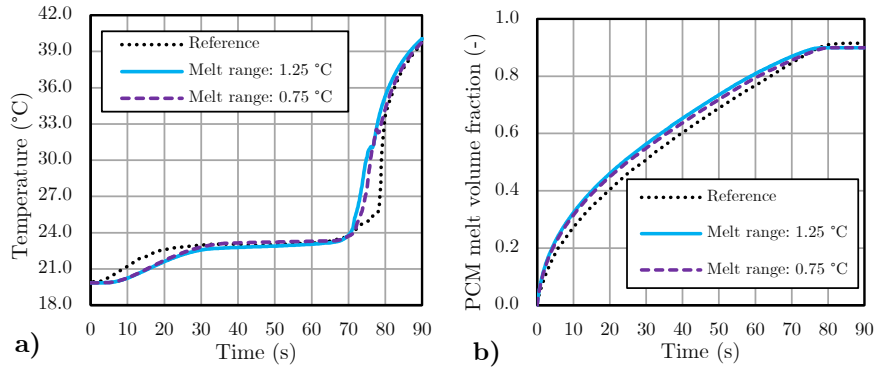

Fig. 8. 3. Model validation varying PCM melt range: a) temperature profile at P = (7.8e-3, 5e-3) m; b) PCM melt volume fraction

After the model validation, the optimized tree-shape structure has been obtained according to the density-based topological optimization approach. The performance of this shape, supposed to have the so-called optimal heat conduction path from the heat source into the PCM domain, have been compared with the conventional one, looking at temperature and melt fraction evolution. Finally, remarks on the heat flux spread by the two heat sinks are proposed.

Fig. 8.4 presents the temporal evolution of the heat sink temperature, for 3 time instants, *i.e.,* 10, 20 and 40 s. These values are selected to catch the main differences between the heat diffusion inside the heat sink, until the PCM of the *TO* case is fully melted. As can be seen, the temperature evolution inside *TO* PCM-structure is strongly affected by the shape of fin structures. They act as heat spreaders due to the high thermal conductivity and high surface area and mitigate temperature gradients faster than the conventional geometry. Conversely, the thickness of the PCM in the plate-fin heat sink makes the heat diffusion slower.

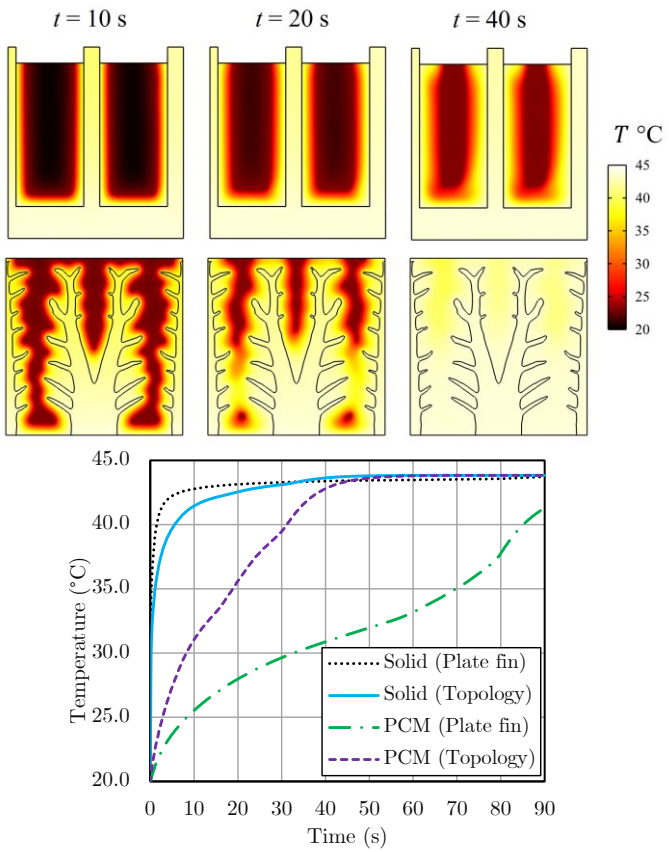

Fig. 8. 4. Comparison of heat sink temperature field at 3 time instants: t = 10 s, 20 s and 40 s; average temperature evolution for solid (aluminium) and PCM

After 40 s, the PCM inside the *TO* heat sink has reached an almost uniform temperature distribution, while the one in the *PF* heat sink is still changing phase. At the same time, looking at the average fin temperature (Solid), the *TO* configuration exhibits a slower temperature rising due to the absence of a base plate, which conversely guarantees in the *PF* geometry a lower thermal resistance.

By comparing the two cases in terms of melt fraction evolutions (Fig. 8.5), convection flow patterns appear during the PCM melting process in the conventional geometry rather than in the optimized one, thus depending on the shape of metal structure. Fig. 8.5 shows that the PCM phase change process around the

tree shaped heat sink is deeply influenced from the multiple ramifications, resulting in a complete melting even before 40 s.

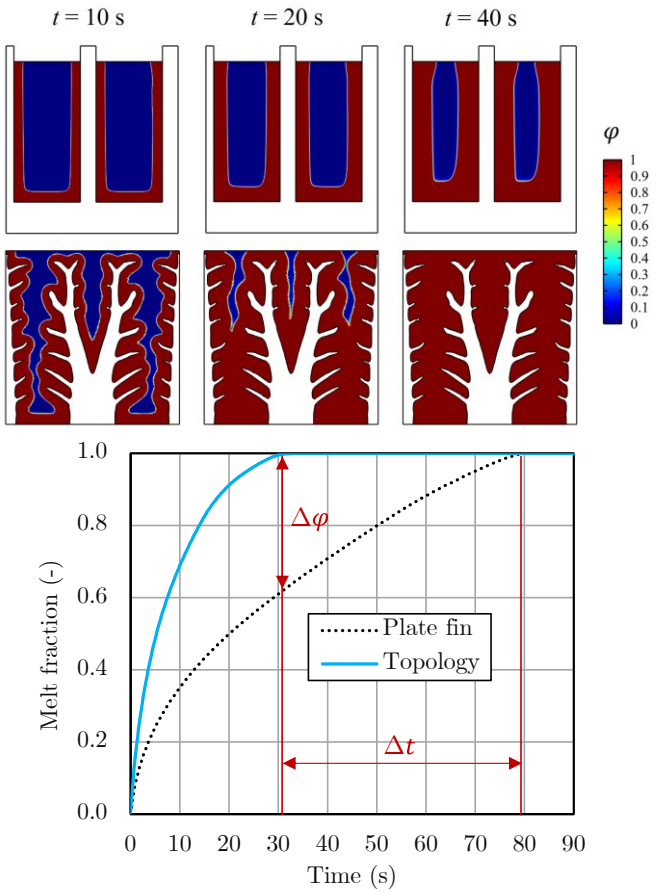

Fig. 8. 5. Comparison of heat sink melt fraction field at 3 time instants: t = 10 s, 20 s and 40 s; melt fraction evolution

Looking at Fig. 8.5, at $t = 31$ s – for which the PCM in the TO configuration is fully melted – the PCM inside the plate-fin heat sink has an average melt fraction value of 0.62. Therefore, adopting *TO* fins allows to reduce the time to melt about 50 s, as highlighted in Fig. 8.5.

Finally, Fig. 8.6 displays the comparison of heat fluxes resulting from the different geometries. Until the PCM fully melts in the *TO* heat sink *i.e.,* after 31 s, the heat flux is substantially higher than the plate-fin heat sink. At $t = 10$ s the

heat flux related to the plate-fin heat sink is about 2.42 W/cm^2, while for the topology one 4.7 W/cm^2. Therefore, at a fixed temperature, the *TO* configuration allows to dissipate up to 2 times the heat flux of a traditional one. This benefit lasts until the fully exploitation of the phase change, after which the difference between the heat fluxes tends to zero.

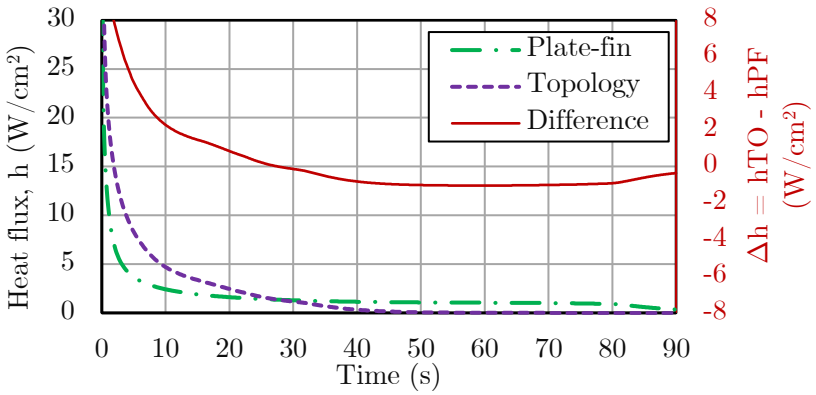

Fig. 8. 6. Comparison of plate-fin and topology heat sink heat fluxes

8.2. Comparison between TO design and traditional solutions

The baseline case study is taken from literature, as shown in Fig. 8.7 and described in [191], [192], where experimental and numerical investigations have been performed to optimize the embedding of the PCM, *i.e.*, paraffin waxes, in Aluminium foams [191] and periodic cellular structures (BCC, body-centred cubic) fabricated by additive manufacturing [192]. The whole experimental device is simulated and detailed are reported in the following. heatsink has a central zone where a phase change material (PCM) is placed. This central zone is surrounded by two Aluminium plates. The purpose of the heat sink is to dissipate the heat generated by an electric current passing through a nickel-chromium alloy conductor, which is inserted into a copper plate.

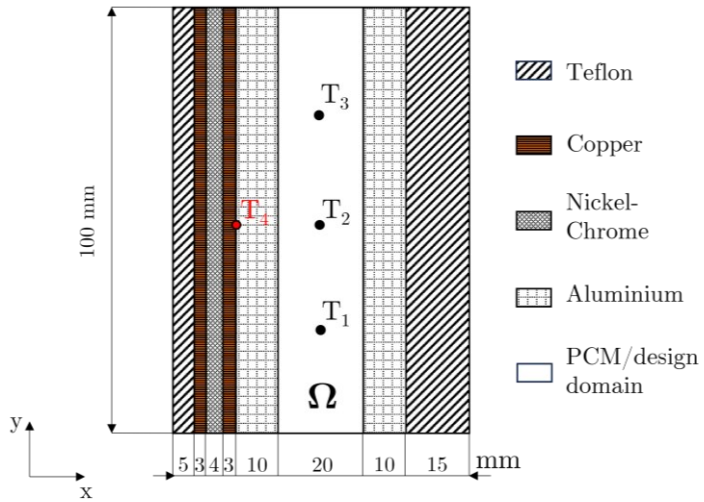

Fig. 8. 7. Sketch of the heat sink here investigated: materials, domains and numerical probes location.

The heat sink is structurally designed with two Teflon insulating layers placed on the side of the copper plate and the side of the Aluminium plate that is farthest from the copper plate. At the bottom and rear of the structure, there are two layers of bakelite, as insulating material. Both bakelite and Teflon layers ensure that the PCM absorbs the maximum amount of heat, avoiding losses to the surrounding

environment. The front of the structure is enclosed with glass, while the top remains open to allow unrestricted expansion of the PCM during equipment operation. Three different points, i.e., T_1, T_2, and T_3 – chosen in such a way as to be equidistant and at a height of 25, 50, and 75 mm respectively – are the access point for the three T-type thermocouples [192] aimed at monitoring the temperature distribution in the PCM as it varies in height. In this work those points are used to evaluate PCM temperature evolution in time. Furthermore, the heater temperature is evaluated on the highlighted location T_4, at mid-height on the aluminium copper interface. Thermophysical properties of the heat sink materials are listed in Tab. 8.1, while PCM thermophysical properties are presented in Tab. 8.2.

Table 8. 1. Geometry and thermophysical parameters

Domain	Length (mm)	Density (kg m^{-3})	Thermal conductivity (W m^{-1} K^{-1})	Specific heat capacity (J kg^{-1} K^{-1})
PCM/design domain	20	-	-	-
Teflon (left)	5	2200	0.3	1300
Teflon (right)	15	2200	0.3	1300
Nickel-Chrome	4	8900	60	440
Copper	3	8978	387.6	381
Aluminium	10	2719	175	871

Table 8. 2. PCM properties

Property	RT42	RT55	RT64HC
Melting temperature range (°C)	38 - 43	51 -57	63 – 65
Phase change interval (°C)	2.5	3.0	1.0
Heat storage capacity (kJ kg^{-1})	165	170	250
Specific heat capacity (J kg^{-1} K^{-1})	2000	2000	2000
Thermal conductivity (W m^{-1} K^{-1})	0.2	0.2	0.2
Density of solid (kg m^{-3})	880	880	880
Density of liquid (kg m^{-3})	760	770	780
Dynamic viscosity (Pa s)	0.02534	0.00455	0.00585

Transient heat conduction equation is used for all the solid parts of the device shown in Fig. 8.7. The PCM thermo-fluid dynamic model is developed under the following assumptions:

- PCM is isotropic but not homogeneous.

- Phase change during solidification/melting occurs within a temperature range (see Tab. 2).
- Volume reduction/expansion during phase change and air gaps resulting from it are omitted.
- PCM liquid phase is modelled using a laminar flow approach, treating it as a Newtonian fluid.
- Boussinesq approximation is used to account for buoyancy effects.

Depending on the temperatures, one can distinguish three regions within the PCM: a fully liquid region, a solid region, and a mushy zone where both phases coexist. Boundary conditions are listed in Tab. 8.3. To define the boundary conditions for horizontal and vertical faces, convective heat transfer coefficients are evaluated from heat transfer correlations:

Table 8. 3. Boundary conditions

Boundary	Thermal	Momentum
Bottom surface	Adiabatic	-
Lateral surfaces	Eq. (8.6)	-
Upper surface	Eq. (8.7)	-
PCM upper surface	Eq. (8.7)	Slip flow condition
PCM bottom and lateral surfaces	-	No Slip flow condition
PCM upper-left vertex	-	$p_0 = 1$ atm

$$h = \begin{cases} \dfrac{k}{H}\left[0.68 + \dfrac{0.67Ra_H^{\frac{1}{4}}}{\left[1+\left(\dfrac{0.492k}{\mu c_p}\right)^{\frac{9}{16}}\right]^{\frac{4}{9}}}\right] & for\ Ra_H \le 10^9 \\ \dfrac{k}{H}\left[0.825 + \dfrac{0.387Ra_H^{\frac{1}{6}}}{\left[1+\left(\dfrac{0.492k}{\mu c_p}\right)^{\frac{9}{16}}\right]^{\frac{8}{27}}}\right] & for\ Ra_H > 10^9 \end{cases} \tag{8.6}$$

$$h = \begin{cases} \dfrac{k}{L_c} 0.54 Ra_{L_c}^{\frac{1}{4}} \;\; if\ T_{surf} > T_\infty \ and\ 10^4 \leq Ra_{L_c} \leq 10^7 \\ \dfrac{k}{L_c} 0.54 Ra_{L_c}^{\frac{1}{4}} \;\; if\ T_{surf} > T_\infty \ and\ 10^7 \leq Ra_{L_c} \leq 10^{10} \\ \dfrac{k}{L_c} 0.54 Ra_{L_c}^{\frac{1}{4}} \;\; if\ T_{surf} \leq T_\infty \ and\ 10^5 \leq Ra_{L_c} \leq 10^7 \end{cases} \tag{8.7}$$

where the Rayleigh number is evaluated referring to the enclosure height. With reference to the model geometry shown in Fig. 8.7, the entire domain is initially assumed to be at an initial temperature $T_{in} = T_\infty$, whose value is based on experimental data [192], equal to 25 °C. The PCM RT42 is still solid at the beginning of the simulation; to help numerical convergence, it is here assumed that it presents a quasi-null initial velocity field, *i.e.,* 10^{-6} m/s. In terms of pressure, the starting condition assigned to the domain in which the PCM is encased is 1 atm. To efficiently replicate a three-dimensional problem in a two-dimensional form, it is necessary to account for heat losses that occur through the frontal glass surface, which are not negligible [192]. Consequently, a calibration step of the numerical model against the experimental data [192] is performed. Furthermore, a second aspect to be considered is the dynamic behavior of the heat source (conduction inside the Nickel-Chromium layer) because the external heat source is not exactly constant through time; this external source reaches a steady-state value of 2.5 MW/m^3. To model these effects, first heat losses through the glass are represented as energy losses per unit volume, proportional to the temperature difference between the environment and the average temperature of each analyzed layer (PCM, right or left aluminum layer). These contributions are weighted using a coefficient, K_{loss}, which is specific to each of the three layers mentioned. The formulation for the losses through the glass is given by Eq. (8.8) and differs depending on the domain referred to. Secondly, as for the dynamic behavior of the heat source, the heat loss is dependent on an exponential function, Eq. (8.9), characterized by a time constant τ, expressed in seconds, that is calibrated too.

$$Q_{loss} = K_{loss} \left(\frac{\int_\Omega T \, d\Omega}{\int_\Omega d\Omega} - T_\infty \right) \tag{8.8}$$

$$Q_{source,heater} = Q_{source} \left(1 - e^{-\frac{1}{\tau}} \right) \tag{8.9}$$

The tuning of this time constant and the three loss coefficients is crucial to achieve the closest possible agreement with the experimental data, *i.e.,* MAE < 2.5 °C. Resulting values are listed in the following:

Table 8. 4. Model calibration parameters

Parameter	Value
$K_{loss,Al,left}$	4500 (W m^{-3} K^{-1})
$K_{loss,Al,right}$	0 (W m^{-3} K^{-1})
$K_{loss,PCM}$	50 (W m^{-3} K^{-1})
τ	215 s

Based on parameters from calibration, a further mesh independence test is performed. Four grids are compared, and results are presented in Fig. 8.8.

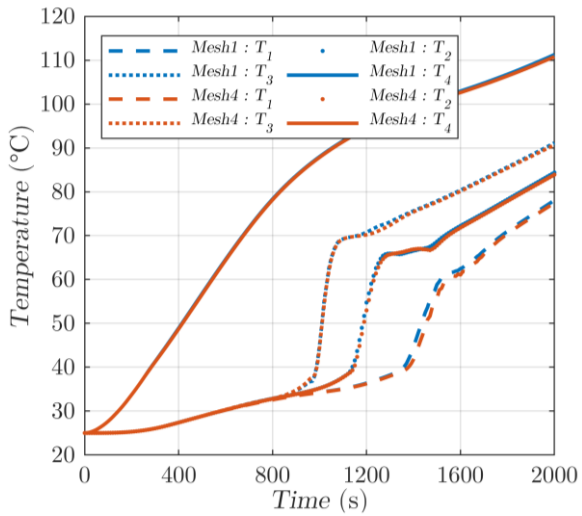

Fig. 8. 8. Mesh independence test: temperature evolution in time at T_1, T_2 ,T_3, and T_4 locations for Mesh1 and Mesh4.

In detail, the triangular element number in the PCM region for "Mesh1" is 2747, while is about 10300 for "Mesh4". Fig. 8.8 does not show results for the intermediate grids, *i.e.,* Mesh3 and Mesh4, as they are between the two extremes. The following simulations are run with Mesh4. The independence of the solution from the timestep is investigated by selecting Mesh4 as a reference, following a similar approach to the handling of the calculation grid density. Initially, an adaptive time step is employed by the solver, determined based on the gradients of the state

variables and with an absolute tolerance of 10^{-4}. Subsequently, simulations are conducted using fixed time steps of 0.75, 0.5, and 0.25 seconds. Resulting deviations are so negligible that the adaptive timestep can be considered the preferred solution due to its low computational costs. Finally, the evolution of the melt fraction, together with streamlines in the liquid region, is depicted in Fig. 8.9. One can see how the melt front is gradually moving from the hot source (left) to the right surface, revealing a non-negligible recirculation due to convective motions. In addition, towards the end of the transient the right wall is not perfectly adiabatic and therefore induces the PCM to melt near the wall, as demonstrated by the presence of streamlines.

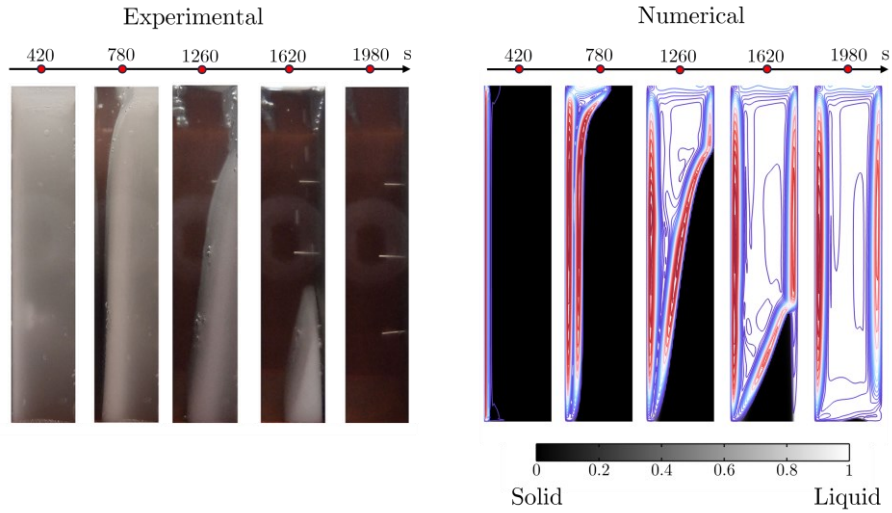

Fig. 8. 9. Evolution in time of PCM melt fraction, every 400 seconds. Black regions are solid, white ones liquid, as also shown by the streamlines: experimental VS numerical

The density-based topology optimization (TO) model currently consists of two distinct phases, distinguished based on the value of the pseudo-density, which serves as the decision variable for our optimization problem. However, considering the true nature of the Phase Change Material (PCM), the problem becomes more complex, encompassing three distinct phases. The challenge lies in accurately modeling the forces acting on these different phases, which include the solid PCM, liquid PCM, and structural solid. This complexity raises still open questions within the scientific community regarding the application of TO in PCM case studies. Apart from the challenges in accurately modeling the physics of the problem, there

is an additional issue of the high computational burden associated with PCM modeling, as previously discussed in the literature. This computational burden becomes even more significant when incorporating TO into the analysis. To address this, in our case study, the geometry of the heat sink is simplified to the only rectangular PCM/design domain (already evidenced in Fig. 8.7). To ensure consistency with the original model of the heat sink, the domain is defined as having the same initial temperature, *i.e.,* 25.0 °C. Regarding the assignment of the boundary conditions, since the assumption is to consider the PCM as a solid-phase material at the beginning, only boundary conditions related to the temperature field need to be assigned: all walls are considered adiabatic, while the temperature of the remaining wall, *i.e.,* left one, is set to a reference value, typically 0 °C. Additionally, in our case study, the domain is assumed to be uniformly heated by a heat source, set at 100 W, to maintain consistency with the original case study. This heat source represents the total external heat source/power dissipated (due to the Joule effect) by the Nickel-Chromium conductor. A fixed solid fraction constraint is set to bound the conductive material occurrence, equal to 13% of the total volume of the PCM region, to make a comparison with equal solid material of cases analysed in [192]. A final term, shown later in Eq. (8.10), is added with the aim of limiting the presence of intermediate pseudo-densities (not having physical correspondence). The M_{nd} evaluation, known as the coefficient of non-discreteness, is a method for determining if an optimized design converges to a discrete solution. For fully discrete design, $M_{nd} = 0$. In this work M_{nd} upper bound is set to 0.1. Based on these premises, introducing a design field, γ, and assuming that this pseudo-density can range from 0 to 1, the following optimization formulation can be written:

$$\begin{cases} \quad minimize \quad \dfrac{\int_\Omega T \, d\Omega}{\int_\Omega d\Omega} \\ s.t.: \begin{cases} \nabla \cdot -k \, \gamma \, \nabla T = Q \\ \dfrac{\int_\Omega \gamma \, d\Omega}{\int_\Omega d\Omega} \leq 0.13 \\ \dfrac{\int_\Omega 4\gamma \, 1-\gamma \, d\Omega}{\int_\Omega d\Omega} \leq M_{nd} \\ 0 \leq \gamma \, X_{\,i} \leq 1 \quad i = 1, \ldots, X \in \Omega \end{cases} \end{cases} \tag{8.10}$$

The design variable γ, presented here in canonical form, can also be represented by it downstream of the application of the filter and projection scheme. In parallel,

the thermal conductivity appearing in the previous formulation (Eq. 8.10), as denoted in the equation itself, is a function of the decision variable according to the interpolation scheme used. In this case, solid isotropic material with penalisation (SIMP) type of interpolation is chosen, such that a value of γ equal to zero identifies the material with lower conductivity (PCM assumed to be solid in this case), while a value equal to one identifies the material with higher conductivity (aluminium): the interpolation scheme used here is shown, for a generic variable ψ, in Eq. (8.11).

$$\psi\ \gamma\ = \psi_{min} + \ \psi_{max} - \psi_{min}\ \gamma^{p_{SIMP}} \tag{8.11}$$

In Eq. (8.11), the values of $\psi_{\min}$ and $\psi_{\max}$ are the values for the property that is being interpolated for the two different materials considered (aluminium, *i.e.,* our structural solid, and PCM, here considered in solid phase only). In the same equation, one can find two further terms: γ, the design variable of our optimisation problem, is such that it assumes the value of zero if the reference finite element in our simulation is to be solid PCM or the value of one if the reference finite element is to be aluminium. As the intermediate values of the decision variable are not physically sensible, penalty factors are used for the intermediate values of the decision variable, here given by the exponent p_{SIMP} and assumed to be 3. To mitigate the checkerboard, effect the Helmholtz filter is used during the simulations. This approach involves setting the filter radius to 2.5 times [193] the maximum mesh element size. By doing so, structures less prone to the checkerboard effect are obtained, as the value of the pseudo-density considers the surrounding elements in addition to the element being considered.

To address the issue that intermediate pseudo-densities between 0 and 1 do not correspond to either the structural solid or the fluid (in this case), a projection scheme based on the hyperbolic tangent function is employed. The threshold parameter η is set to 0.5 [193]. However, to achieve structures with fewer intermediate densities, the slope parameter β undergoes several continuation schemes, with values from 3 to 11.

Results with traditional enhancers, *i.e.,* rectangular fins, BCC 5 [192]and BCC 10 [192], are here compared with TO-based ones, whereas the TO optimized cases are obtained starting from different number of fins. All configurations share the same amount of conductive material, *i.e.,* 13% solid fraction. Specifically, to select the number and thickness of rectangular fins, a parametric analysis has been carried out, and results are presented in Fig. 8.10, before running the TO.

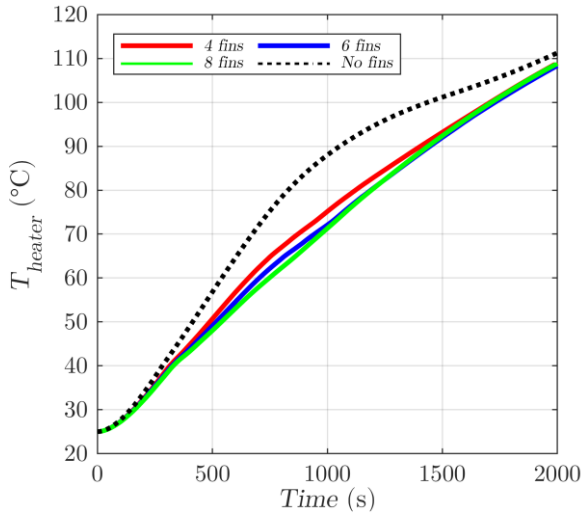

Fig. 8. 10. Heater temperature evolution in time, for configuration without fins, with 4, 6 and 8 rectangular fins

Of all the configurations analyzed, the one with 8 fins exhibits the best performance, *i.e.,* it reduces the heater temperature the most. In this case, fins have a length of 16 mm, a thickness of 2.03 mm, and a pitch of 10 mm. On the TO side, multiple configurations have been analyzed. They derive from different continuation scheme approaches (values iteratively assigned to β and p_{SIMP}), chosen to vary across iterations in a gentle or sharp way. In detail, more than 20 final designs can be obtained: they slightly differ in terms of objective value, while the difference in terms of fins configurations can be appreciated in Fig. 8.12. Subscripts numbered, say 1, 11, 4, and 13, in Fig. 8.12, refers to the design analyzed. It's worth noting that these values are computed at a time instant equal to $t = 840$ s for the sake of comparison.

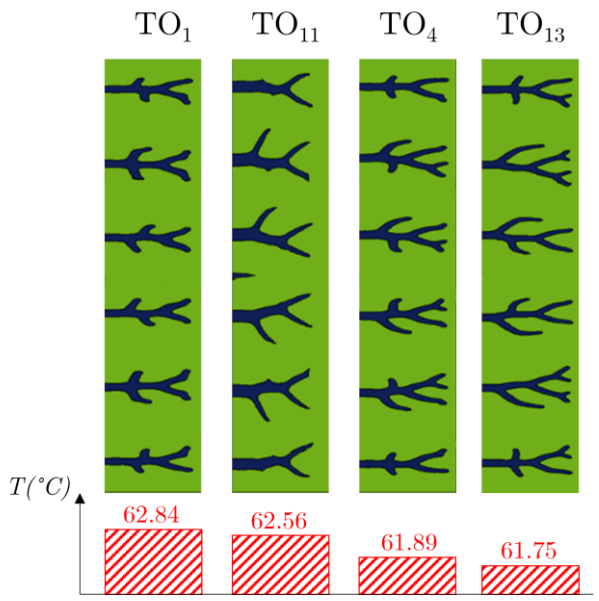

Fig. 8. 12. Rectangular fins heat sink (left) and TO-based heat sink (right).

Based on these results, the final configuration, *i.e.,* TO_{13}, together with resulting design from topology optimization, is presented in Fig. 8.13.

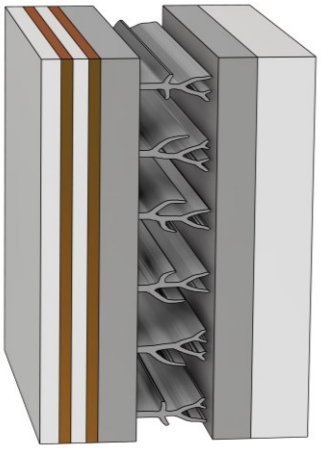

Fig. 8.13. TO-based heat sink integrated in the experimental device

Because of the 2D approximation, the 3D design can be derived by extruding the 2D plane by a length of 100 mm, that correspond to the one shown in the reference. From a quantitative point of view, the use of topology-optimized geometry within the PCM region allows a maximum temperature relative to the source plate of 61.75 °C to be reached at the end of the observed period. At the final instant of the thermal transient, considering the basic structure without any enhancer for the PCM, the temperature reached at the same point is 80.61 °C. At the same time instant, for the case of 8 fins as enhancers, the heater temperature reaches 64.01 °C. The "no-fins" configuration allows the temperature of 61.75 °C to be reached after only 563 s from the start of the transient (277 s earlier than with the TO-optimised structure), while considering 8 rectangular fins the advance with respect to the TO-derived structure is 55 s and approximately 30 s for the BCC structures, respectively. The data described above are shown in Fig. 8.14, and schematically listed in Tab. 8.5, for the sake of a better description.

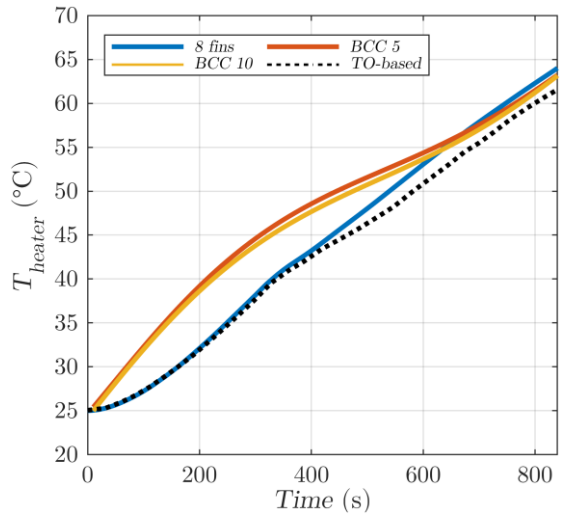

Fig. 8. 14. Heater temperature evolution in time, for configuration with 8 fins, BCC 5, BCC 10 and TO-based.

Table 8. 5. Evaluation of the time required to reach peak temperature in the different structures used as PCM enhancers

Structured used as PCM enhancer	Peak temperature (°C)	Time needed to reach the TO peak (after 840 s) temperature (s)
TO configuration	61.75	840.00
Finned structure	64.01	787.30
BCC5 structure	63.21	806.37
BCC10 structure	63.14	811.34
No-fins configuration	80.61	563.04

This case study addresses the design of a passive phase change material (PCM)-based heat sink (HS) via topology optimization (TO), which is proposed as alternative to solutions such as Body Centered Cubic (BCC) structures or rectangular fins, to enhance the efficiency of heat transfer. Since PCMs have low thermal conductivity, they require the use of structures, including those previously mentioned, as enhancers in the transfer of thermal energy, preventing the low conductivity from limiting the potential energy stored in the form of latent heat in the PCM. By comparing the average temperature of a plate – subjected to a thermal dissipation due to Joule effect – in the case of BCCs, rectangular fins or TO-derived structures, the following results can be resumed:

- the peak temperature (T_{peak}) reached by the source plate in the thermal transient considered (0 – 840 s), is 61.75 °C, approximately 20 °C lower than the peak temperature reached without the use of any enhancer, showing how the exploitation of structures with high thermal conductivity as enhancers can improve the management of temperature peaks;
- the peak temperature (T_{peak}) reached by the heater, with the achieved TO structure, is delayed by 30 s compared to the BCC structure and by 55 s compared to an optimal plate-finned one. In addition, T_{peak} is around 62 °C, 20 °C lower than the one without metallic enhancers.

Results show that topology optimization can be an effective tool to optimize the structures of heat sinks coupled with PCMs, by reducing and delaying the peak temperatures compared to other solutions, such as plate fins, metal foams and periodic cellular structures. Unlike the past, the achieved unconventional structures, which often follow typical shapes of nature (like trees) can be easily fabricated via additive manufacturing.

8.3. Influence of initial guess: coupling GA with TO for microchannel design

While TO has been widely used in structural design, its application in CFD problems is relatively new and presents intricate challenges, involving both purely numerical and conceptual aspects [194]. When coupling TO to CFD problems, the objective is to optimize shape and topology of the solid/fluid domain to achieve desired flow characteristics and fulfil thermal targets. In this frame, the choice of design variables, the selection of appropriate constraints and boundary conditions is a well-known challenge, as well as the complex physics of fluid flow, *e.g.,* turbulence, nonlinearity, and multiphase flow [65].
However, among these issues, one of the critical input parameters that can significantly impact the optimization process and the final design is the initial guess [195]. The initial guess is an initial estimate of the optimized design that serves as a starting point for the TO algorithm. The choice of the initial guess can affect the convergence rate, as well as the topology and performance of the optimized design. In this case the problem can be defined as initial guess dependent (IGD). This means that different initial designs result in diverse topologies, although having close objective values [196]. Since the initial guess can affect the convergence rate and the quality of the optimized design, a reasonable option should be a starting guess close to the optimal solution, with features of the expected design [194]. Thus, the initial guess should be chosen based on prior knowledge of the design problem, which is not always feasible, especially in the area of thermofluid-dynamics where designs tend to have aerodynamic or fluid-based shapes.
Thermofluid-dynamics topology optimization problems are quite non-convex and can easily converge to only locally optimal topologies depending on the starting guess or initial design [196], [197]. Thus, exploring different initial design options is mandatory to comprehensively explore the design domain and avoid trivial solutions. More specifically, regarding thermal management, microchannel heat sink optimization has proven to be IGD [195],[197]. An apriorist evaluation of various configurations with different fin placements can be time-consuming, which added to the computational cost of TO makes the process lengthy and tedious. To this end, the aim of this work is to apply a heuristic approach for integrating a genetic algorithm (GA) as an outer algorithm into the TO routine: GA generates multiple pin fins' configurations that are used as initial guesses by TO to find a final design

able to minimize the thermal resistance between the channel layer and the base plate layer, and the pressure drop. By doing this, starting guesses can be correlated with final objectives, defining new helpful insights on microchannel optimization.

The model is based on a pseudo-3D formulation [197]. A full 3D optimization is computationally expensive since topology optimization (TO) typically requires several hundred iterations before convergence to a final design. Accordingly, the pseudo 3D heat sink model approximates the original 3D one with two 2D thermally coupled problems, which are not independent themselves. Figure 1 shows a 3D sketch of the forced convection heat sink here considered. The base plate – the one concerned by the heat source – is thermally coupled to the channel layer thanks to an additional term. At the same time, this term is balanced on the channel layer side through a complementary one. Consequently, this approach – even being 2D – considers out-of-plane effects. The design domain, *i.e.,* channel layer, is also depicted in Fig. 8. 15. It consists of a rectangular domain, with an internal rectangular subdomain (Ω_d) where topology takes place. The outer ones (Ω_f) serve as inflow and outflow sections. Therefore, Ω_d represents the domain where the initial guess has to be set.

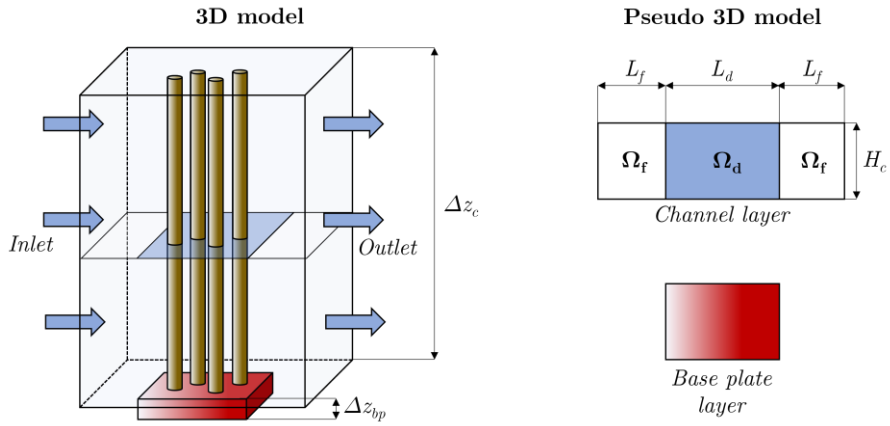

Fig. 8. 15. Sketch of 3D heat sink design and its reduction to a pseudo 3D model.

The starting design is chosen to be a microchannel heat sink with round pins. The arrangement and the number of round pins are not defined as constraints, whereas the initial volume constraint, *i.e.,* the ratio between the area of the solid material

and the total of Ω_d, is fixed to a value of 0.2. Note that this constraint is only set on the initial design and not on the final one. Therefore, the aim of this work is to investigate the effect of varying pins position and size as initial guess for the TO problem.

To define the model equations, a continuous design field, $\gamma(x)$ is defined in Ω_d. Its values range from 0 to 1, and the upper value represents the fluid, whereas the lower one represents heat sink fin material. The reason why $\gamma(x)$ takes one value over the other is specified later.

An incompressible, laminar, and steady-state flow is assumed throughout this case. The fluid and heat transfer problems in the thermofluid-dynamic design layer are modelled two-dimensionally, as described in the previous section. The 2D assumption is motivated by the fin height, significantly larger than the baseplate one. In addition, since the base plate's extension is much larger than its height, the original 3D thermal diffusion problem in the base plate is simplified to a 2D problem. Under these assumptions [197], the governing equations for the fluid are written as:

$$\nabla \cdot u = 0 \tag{8.12}$$

$$\rho_f \; u \cdot \nabla \; u = -\nabla p + \mu_f \nabla^2 u + F \tag{8.13}$$

$$F \; \gamma \; = -\alpha u I_\alpha \; \gamma \; = \frac{\mu_f}{Da L_c^2} u I_\alpha \; \gamma \tag{8.14}$$

where ϱ_f is the fluid density, u is the fluid velocity vector, p is the pressure field, μ_f is the dynamic viscosity of the fluid, and F is the Brinkman friction term, which is used in TO flow problems to penalize flow through solid areas within the design domain. is the maximum inverse permeability of the porous medium and $I_a(\gamma)$ a suitable function for the inverse permeability interpolation. Da is the Darcy number and L_c is a characteristic length which corresponds to the design domain width. It is worth noting that there is no Brinkman friction on the fluid outside of the design domain.

The 2D thermal convection-diffusion equations with/without a heat source are solved in the thermofluid design layer inside/outside the design domain:

$$\rho_f c_f u \nabla T_f - \nabla \cdot (k_f \nabla T_f) = 0 \quad in \; \Omega_f \tag{8.15}$$

$$\gamma \rho_f c_f u \nabla T_f - \nabla \cdot (k_f I_k \; \gamma \; \nabla T_f) = \frac{q_{inter} \; \gamma}{\Delta z_{channel}} \quad in \; \Omega_d \tag{8.16}$$

where T_f is the temperature field in the thermofluid design layer, c_f is the specific fluid heat capacity, k_f the thermal conductivity of the fluid, $I_k(\gamma)$ is a function that interpolates between thermal conductivities. $\Delta z_{channel}$ is the height of the air channel and fins, and $q_{inter}(\gamma)$ is the heat transferred from the solid base plate to the thermofluid design layer.
A 2D heat conduction problem is solved in the metal base plate:

$$\nabla \cdot k_s \nabla T_s = -\frac{Q_{source}}{V_{bp}} + \frac{q_{inter}\ \gamma}{\Delta z_{bp}} \quad in\ \Omega_d \tag{8.17}$$

where k_s is the thermal conductivity of the base plate, T_s is the temperature field in the base plate, Q_{source} is the prescribed heat production rate, V_{bp} is the base plate volume, and Δz_{bp} is the base plate height. The base plate is assumed to produce heat at a constant rate in this study. The conductive heat transfer from the base plate into the heat sink fins, as well as the convective heat transfer from the base plate to the fluid, must be represented flexibly in the out-of-plane heat transfer between base plate and thermo-fluid design layer, $q_{inter}(\gamma)$. This is accomplished by interpolating between a high conductive heat transfer into the fins and a lower convective heat transfer to the fluid using a heat transfer coefficient:

$$q_{inter}\ \gamma = h_f I_h(\gamma)(T_s - T_f) \tag{8.18}$$

where h_f is the convective heat transfer coefficient to the fluid, and $I_h(\gamma)$ is a function that interpolates between h_f and the heat transfer coefficient from the base plate into the heat sink fins, h_s. The conductive heat transfer resistance in the z-direction in the fins is represented by the parameter h_s, which is empirically determined. All walls are adiabatic, except for the inlet where the temperature T_{in} is fixed. The thermophysical properties of air that are used in this study are: c_{air} = 1006 J/(kg K), k_{air} = 0.024 W/(m K), μ_{air} = 1.94 $\cdot 10^{-5}$ Pa s, and ρ_{air} = 1.204 kg/m^3. Pressure drop between inlet and outlet, Δp, is computed as difference of pressure at the inlet and outlet and a normal laminar inflow is set at the inlet boundary Γ_{in}. A symmetry boundary condition for the fluid flow is applied on bottom and upper boundaries.
Density based TO is here applied [57]. This method supports regularization via Helmholtz filter. The filter size is defined as two times the mesh size, which is set

as 0.02 mm. Interpolation functions are used to represent intermediate values in the given design problem. An interpolation function is used in this work for the Brinkman friction term (Eq. 8.19):

$$I_\alpha\ \gamma\ = \frac{1-\gamma}{1+b_\alpha \gamma} \tag{8.19}$$

where b_a is a parameter that determines the interpolation's convexity. A rational approximation of material properties (RAMP)-style interpolation is used to interpolate the thermal conductivity within the design layer and the heat transfer between the heat sink base plate and the thermo-fluid design layer:

$$j\ \gamma\ = \frac{\gamma[C_j(1+b_j)-1]+1}{C_j(1+b_j\gamma)} \tag{8.20}$$

where b_j is the interpolation convexity parameter and C_j is defined in the respective case as k_f/k_s and h_f/h_s. The following optimization problem has been solved:

$$\begin{cases} minimize\ \ \Phi = w_{Rth}\Phi_{Rth} + w_{\Delta p} + \Phi_{\Delta p} \\ \quad with: \begin{cases} \Phi_{Rth} = \dfrac{(T_{bp,avg}\ \gamma\ - T_{in})}{Q_{source}} \\ \Phi_{\Delta p} = p|_{\Gamma_{in}} - p|_{\Gamma_{out}} \end{cases} \end{cases} \tag{8.21}$$

As described in Eq. (8.21), Φ is the composition of 2 terms, Φ_{Rth} and $\Phi_{\Delta p}$, which are weighted through the terms w_{Rth} and $w_{\Delta p}$. Minimizing both the objectives defines a multi-objective problem. To reduce the thermal resistance, the heat transfer area has to increase, while to minimize the pressure drop less flow resistance is required. In this work, the weighting factors have been considered equals. It is worth specifying that in order to consider pressure drop as part of the objective, only inlet velocity, *i.e.,* 0.1 m/s, has been specified as fluid boundary condition. Further, no volume constraint has been defined, apart from the one related to the initial guess.

A genetic algorithm (GA) is run as outer algorithm into the TO routine to investigate the initial design condition that simultaneously fulfils thermal and fluid dynamic objectives. The design variables used in this work are the minimum circle radius (r_{min}) and the minimum distance between the circles (s_{min}).

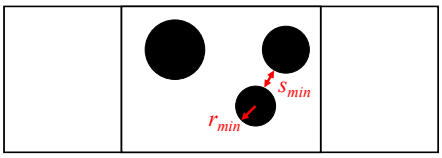

Fig. 8. 16. Parameters affecting the round pins size and displacement (r_{min}, s_{min}) used as design variables for the GA.

The parameter r_{min} can vary from 0.06 mm to 0.13 mm, each 0.005 mm, whereas s_{min} varies from 0.04 mm to 0.08 mm, each 0.01 mm. The reason for these ranges will be explained later. However, s_{min} is set to be higher than the maximum mesh size. By doing this, an excessive mesh refinement between two circles – which should compromise the TO convergence – is avoided. All settings for GA tuning are taken from [132].

The fitness function code generates a figure of randomly positioned circles within the rectangular domain. The code takes as input the dimensions of the rectangular domain, the minimum radius and distance between the circles, and a vector of target ratios between the total area of the circles and the area of the rectangle. For each target ratio, the code generates circles randomly until the total area of the circles reaches or exceeds the target ratio times the area of the rectangle. The code uses a while loop to generate circles one at a time. For each new circle, the code generates a random radius and position, and checks whether it intersects with any of the existing circles or exceeds the boundary limits of the rectangle. If the new circle is valid, it is added to the figure and the total area of the circles is updated. The loop continues until the total area of the circles reaches or exceeds the target ratio times the area of the rectangle, or the maximum number of iterations, *i.e.,* 100, is reached (see Fig. 8. 17).

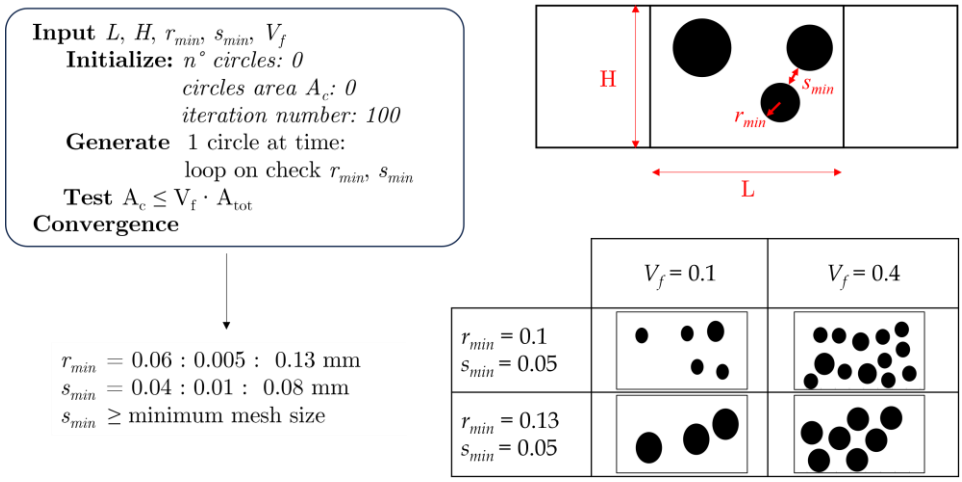

Fig. 8. 17. Schematic of the code to generate the initial guess

The code also sets up a figure window with a fixed size and saves the final image as a PNG file with a name that includes the target ratio. Note that the code assumes that the aspect ratio of the rectangular domain is 1.7:1 – equal to the design domain one – and that the circles are black with a solid fill. By doing this, the image can be imported in the COMSOL file and processed as initial guess (see Fig. 8. 18). The method of moving asymptotes (MMA) is used to perform TO.

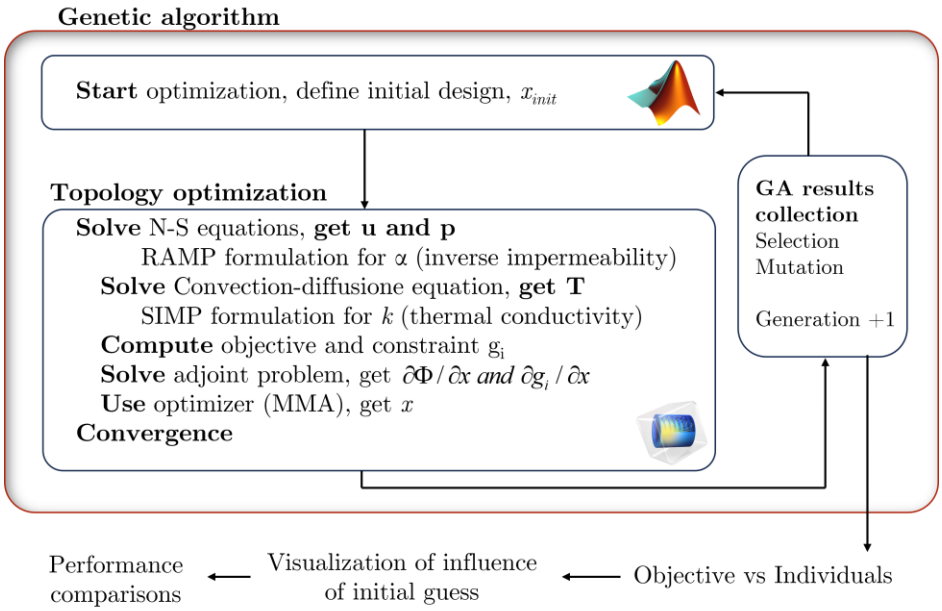

Fig. 8. 18. Coupling GA and TO

The successive step consists of the validation of the presented model under a Δp equal to 3 Pa and minimizing the thermal resistance R_{th}, and discussing results on the investigation of the initial guess by optimization using GA + TO. Each GA simulation lasts around 40 min, using a continuation scheme for the TO algorithm similar to the reference one [197]. The number of overall iterations has been reduced from 1160 (reference) to 400, without losing accuracy (as proved in the following).

Before running simulations about the optimization problem of equation (10), the TO reliability is tested replacing the optimization problem solved in [197]. Thus, the model validation is assessed comparing qualitatively (Fig. 8.19) the final design, velocity magnitude field, temperature field of channel layer and base plate, with the one used in the reference work, and quantitatively through the value of the thermal resistance, R_{th}. The one reported in the reference is 144.6 (K/W), while the one evaluated in this work is 144.9 (K/W).

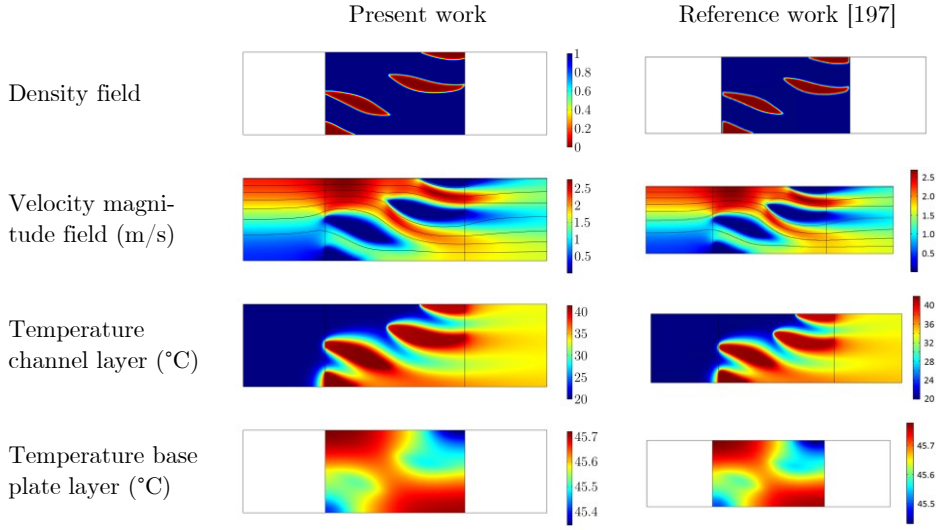

Fig. 8. 19. Model validation results: design domain; velocity field, design plate temperature; baseplate temperature field.

The main difference that can be spotted in the final design is the presence of material on the vertical boundaries, since in the present work there is no prescribed density condition on them. 170 Individuals computed through the GA + TO routine are depicted in Fig. 8.20.

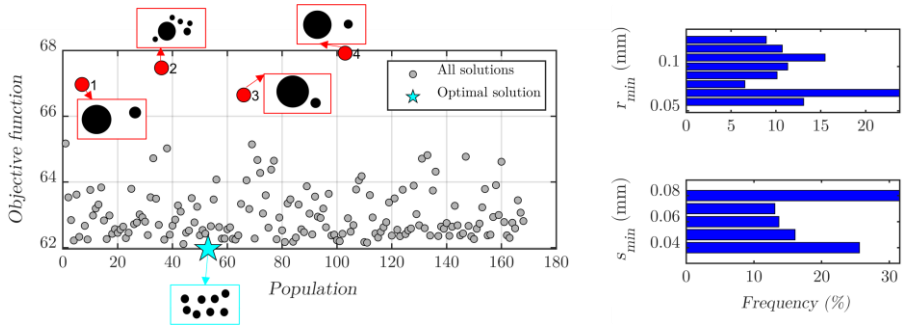

Fig. 8. 20. left: GA population's objective function history: detection of the optimal solution and four individuals with worst, and related initial designs. Right: Design variables distribution.

Among these, 5 relevant individuals have been highlighted: the optimal solution ($\Phi = 61.95$) and four worst solutions. In detail, in order to visualize a hypothetical

dependency between the value of the objective function and the initial design, the plot of the initial design is shown for each of these individuals. By doing so, it can immediately be seen that the presence of a pin with a larger radius leads to a reduction in performance, while the presence of several pins with a smaller radius result in an optimal solution. To confirm what is presented through the plot of the objective function, the values of the design variables are grouped according to population and the frequency with which they occurred (Fig. 8.20). It shows that the GA preferred smaller radii and longer distances. Nevertheless, with regards to r_{min}, a non-negligible number of individuals can be noted, *i.e.,* 26 designs with $r_{min} = 0.11$ mm, to which correspond to individuals with intermediate Φ. At this point, it is useful to check the advantage of adopting a proper initial design (Optimal solution), as opposed to one of those "worst" highlighted above (Case 4). The comparison (Fig. 8.21) is made in terms of initial guess, final design, channel layer temperature field and velocity magnitude field.

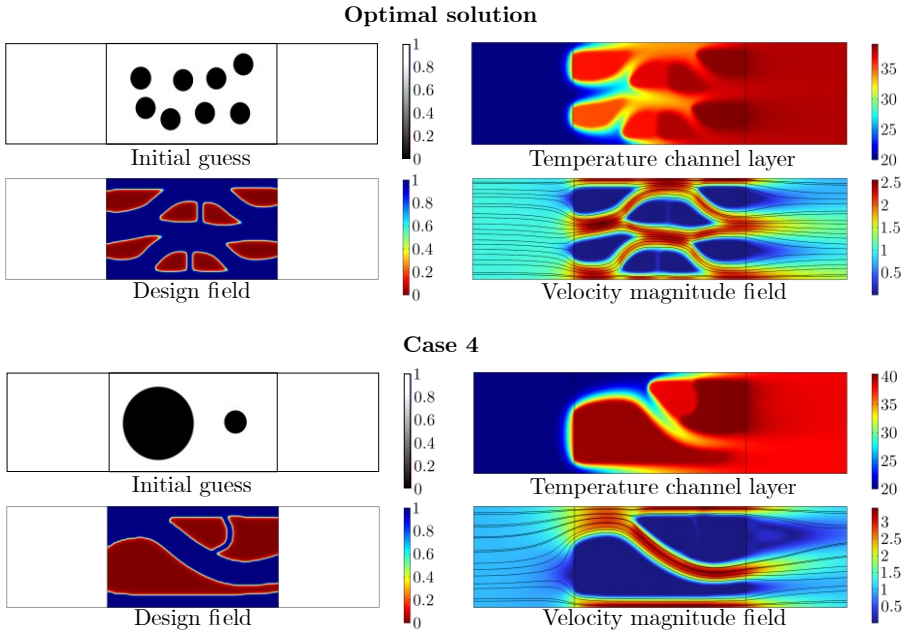

Fig. 8. 21. Optimal solution and "case 4": initial guess, final design, temperature channel layer and velocity modulus field.

Starting the optimization with more pins with lower radii allows to reach a better final solution. The increase in the heat transfer allows to reduce the thermal resistance (Tab. 8.6), and more aerodynamically shaped fins ensure a lower pressure drop than in Case 4, *i.e.,* 12.46 Pa against 15.66 Pa. However, pressure drop values are consistently higher than the one used in the validation step, *i.e.,* 3 Pa, which explains why the thermal resistance is significantly lower.

Table 8. 6. Model results comparison.

	Optimal solution	so-Case 4	Validation
R_{th} (K/W)	111.5	120.1	144.9
Δp (Pa)	12.46	15.66	3.00
$T_{max,c}$ (°C)	38.90	40.21	41.22
$T_{max.bp}$ (°C)	39.80	41.10	45.72

Moreover, as listed in table 1, the maximum temperature at both channel and base plate layers is lower, because of the reduced thermal resistance. It is worth noting that the resulting solid fraction – computed on the design domain Ω_{d} differs from the optimal solution (31%) to Case 4 (48%). This is an interesting outcome because even if the Case 4 design has more solid material available, its displacement does not imply improved thermal diffusion. Lastly, the difference between thermal resistance values is slight. This confirms the need for searching a proper initial guess before running the TO. Indeed, running TO without exploring the field of possible initial solutions would risk experiencing a local minimum, whose value is really close to the global one.

8.4. Multi-material TO for microchannel heat sink design with metal foams

Microchannel heat sinks (MCHSs) play a pivotal role in numerous fields, including electronics cooling, chemical processing, and biomedical applications. Conventional design approaches for MCHSs often rely on predefined geometries or empirical trial-and-error methods, limiting the exploration of the design space and leading to suboptimal performance. Density-based topology optimization (TO), on the other hand, leverages gradient-based procedure to systematically explore and optimize the material distribution within MCHSs. On these premises, this work aims to study the combined use of porous materials like metal foams and TO in a multi-material topology optimization (MMTO) to improve MCHS thermo-fluid dynamic performance. Starting from a baseline design, a 2D numerical model has been developed with a conjugate heat transfer formulation, *i.e.,* the governing equations of heat conduction inside solid material, and forced convection inside fluid/foam domains. For the multi-material topology optimization, the solid isotropic material with penalization (SIMP) model with two pseudo densities is used to handle the three phases problem. By strategically placing solid and foam materials, the aim is to balance the trade-off between low-pressure drop and high heat transfer rate. Overall, the optimized designs, *i.e.,* TO and MMTO-based, turn out to be nonintuitive and show significantly higher thermo-fluid dynamic performance when both compared to a baseline case, with a reduction in the required pumping power of 88% at constrained inlet velocity. The MMTO microchannel, compared to the one developed with topology optimization, improves the performance evaluation criteria (PEC) about 59-84% at different fixed pressure drop and inlet velocities. Moreover, the weight saving – with respect to the baseline case – is assessed to range from 80 to 83 %. This newly designed devices might be really helpful to improve the thermal performances of available microchannel heat sinks.

8.4.1. Introduction: State-of-the-art and research significance

The current scenario concerning the thermal management of any device is predominantly covered by heat pipes and microchannels, defined by different ranges of application and functionality. Specifically, microchannel heat sinks (MCHSs) are devices able to remove the excess of heat from one medium to another one in a highly reduced space. Nowadays they turn out to be capable of dissipating high heat fluxes, even higher than 100 W/cm^2 unlike the conventional channels which can dissipate up to 20 W/cm^2 [198]. This testifies to the enormous progress made since the first contribution by Tuckerman and Pease in 1981 [199], which were the first to develop a MCHS for electronic cooling, providing a thermal resistance of 0.09 K/W. They demonstrated that an increase in heat transfer coefficient could be achieved with a reduction in channel hydraulic diameter. Since their substantial finding, scholars have focused on the development and study of MCHSs while also providing an impetus for the development of higher computational capabilities due to the equally high cooling capacity and compactness provided by the MCHS, thanks to their miniaturization and high heat transfer surface. In order to differentiate between MCHSs and other devices, several classifications were proposed, and among them the most used is the one based on the hydraulic diameter (D_h), *i.e.,* the one by Kandlikar and Grande [200] and Mehendale *et al.* [201]. According to them, microchannels are characterised by 10 µm $< D_h <$ 200 µm, while minichannels by 200 µm $< D_h <$ 3 mm. The size is thus a crucial point, which enables to use such devices in many applications, especially where compactness and efficiency are required: cooling of electronic equipment [202], membrane fuel cells [203], laser diode arrays [204], combustors [205], although their greatest use is in the field of electronics thermal management, for which devices have to show both compactness and high efficiency [206]. To ensure such performance, it was therefore necessary to overcome the main limitations revealed by these components, as the trade-off in the design between heat fluxes and pressure drop. In particular, in [207] the authors analysed the thermo-mechanical performance by keeping the cross-sectional area of the microchannels constant and varying shapes aspect ratio and Reynolds number. They found a remarkable link between channel shapes and thermo-mechanical performance, specifically finding that an increase in the number of microchannels reduces the thermal resistance, but with an increase in pressure drops showing in each case a range of optimal conditions. Liu *et al.* [208] and Sahar *et al.* [209]

performed similar experiments showing that thermal resistance decreases at constant pressure and increases whit higher slant angles.

Beyond the scope of the microchannel, much effort has recently been put into the development of techniques that help to increase performance, changing or keeping the same design. Techniques to develop efficient systems are still ongoing, *e.g.*, two-layered design, for which the rise in temperature on the baseplate surface is substantially reduced if compared to that of the one-layered [210]. On the contrary, while keeping the solid material distribution unchanged – among several possibilities – a method to enhance the heat transfer is using porous media. Many heat sink types based on metal foams – a cellular material since one could distinguish more or less regular cells within the porous medium - have been proposed through the years, switching from the flow type, *i.e.,* natural or forced convection, direction, *e.g.,* parallel, impinging, and varying PPIs (pores per inches) [211], [212], [213]. As regard air and forced convection, this research showed that the Nusselt number increases together with the Reynolds number and both porosity and PPI. Non-finned and finned aluminum foam heat sinks with flow orthogonal to fins height have been deeply investigated in [214]. They concluded that finned foam heat sinks strongly improve heat transfer capability, with convective heat transfer enlargement when thermal boundary layers between adjacent fins merges. Several experimental studies on thermal performance of different metal foam heat sinks have been presented and compared with conventional solid heat sinks [215], [216]. Aluminum metal foams having 93% porosity with pore density of 4 and 8 PPI have been investigated under forced convection, and results show that heat sink with thermal spray coating outperforms a thermally glued sample with up to 9.8% higher temperature drop under the same operating test conditions. Likewise, the local heat transfer characteristics of a circular air jet impingement on an aluminum metal foamed flat plate have been investigated using a thin metal foil technique, enhancing the overall heat transfer performance [217]. With reference to natural convection, experimental studies in slender metal foams with length 254 mm and width 25.4 mm were carried out in [218]. A fixed porosity of 0.93 and two pore densities, *i.e.,* 10 and 20 PPI, were varied, founding that the 10 PPI foam performed up to 25% better in heat transfer compared with the same dimensioned 20 PPI foam. A graphical recap of the applications vs heat fluxes over the years is illustrated in Fig. 8. 22, where is clearly displayed the actual frontier in terms of heat flux for metal foam heat sinks.

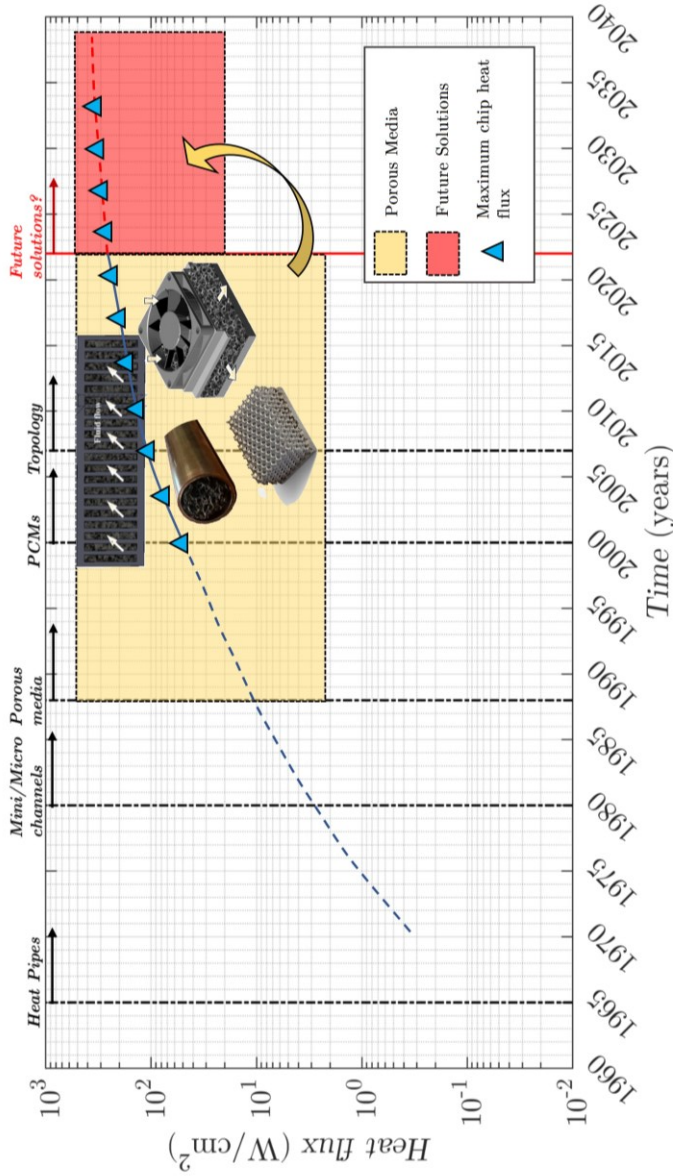

Fig. 8. 22. Heat fluxes obtained via porous media heat sinks through the years

The current relevance of this topic is proved by several studies, which have examined in depth: the combined effects of the gradients of gradient porous media on thermal and hydraulic performance [219]. It has been proved that thanks to additive manufacturing techniques it is now possible to "customize" the foams and maximize the heat transfer [220], [221]. Moreover, optimization techniques play a fundamental role to obtain high-performance solutions within a reasonable timeframe [222] and finally help to remove obstacles to large-scale deployment. To this end, topology optimization [57] is setting up as one of the most promising optimization techniques in this field of research. This optimization method has its roots in structural design optimization but has gained relevant importance in the field of thermal management in recent years [223]. Specifically, the amount of contributions about forced convection conjugate heat transfer consistently grows through the years [65]. The main difference is about the approaches, *i.e.,* 2D, 3D or pseudo-3D models, which differ in terms of accuracy, computational efforts, and final design. The effectiveness of 3D approaches have been proved when applied to two-fluid heat exchangers [64], to turbulent flows [224], and to microchannels [225]. All these works share final designs able to double the performance of baseline ones, under the same pressure drop. The enhancement gradually becomes less significant if increasingly stringent assumptions are introduced, *i.e.,* using pseudo-3D approaches lead [197], [226] or 2D ones [227], [228].

As far as TO on MCHS, in [60] the authors performed topology optimization obtaining better performance as thermal resistance for a fixed pressure drop and vice versa. TO on an air MCHS leads to a 54.9% saving in pumping power at the same average temperature of the MCHS [226]. Furthermore, if performing various topological optimizations on a web spider MCHS, one can obtain an achievement in temperature reduction of 57% compared to the base case using a multi-objective function which minimizes temperature differences and total power dissipation [229]. One of the key points of topology optimization by means of the density-based method lies in the use of a gradient-based approach. The aim is to obtain a final design with only two phases: solid, fluid. However, as discussed before, many real-world engineering applications require the use of multiple materials with different properties and behaviours, such as composites or heterogeneous structures. To address these challenges, multi-material topology optimization (MMTO) has emerged as an advanced approach that enables the simultaneous optimization of multiple materials within a design. The effort of integrating porous media in topology-optimized design is testified by several works. Among these, the optimization of the distribution of the wick, *i.e.,* a porous medium, used to transport condensate to the evaporator due to capillary effects, in a heat pipe [230]. Further, a multiscale

approach to address the thermofluid challenge in the design of metal printed lattice structures has been proposed in [231]. They determined effective values for permeability, form drag, and conductivity of a representative orthogonal truss microstructure. These parameters were then employed in a macroscopic material distribution technique, which incorporated the Brinkman–Forchheimer equation and a convection–diffusion equation. The most used formulation is the one by Sigmund and Torquato, in 1996, who proposed a three-phase MMTO for a structural case study introducing the SIMP technique for two solid materials, highlighting the main advantages of using this technique [59]. As regards MMTO with metal foams, in [232] the authors performed the optimization of a fluid-flow problem considering both solid and porous materials, in order to obtain the best configuration that minimizes the pressure drop by fixing the volume fraction of solid and porous medium. They also presented a way to define the inverse permeabilities of solid and porous materials. Furthermore, results collected by Li and Kim [233], provide a comparison of several MMTO and single material TO cases. The weight saving of up to 16.3% compared to the base case is surprising and the results achieved – although they refer to structural cases – are very promising for further application of these techniques to thermo-fluid dynamic cases.

On these premises, among the main knowledge gaps evidenced, *i.e.,* material property characterization and thermo-fluid dynamic modeling, the present work aims to focus on the latter. One of the key challenges in MMTO is accurately characterizing properties of different materials, *e.g.,* thermal resistance, specific heat, which strongly influence the performance and thermal behaviour of the heat sink. Obtaining exact material property data for various materials at the microscale can be challenging. To this end, interpolations schemes and permeability factors have been applied to define the metal foam to be used for MMTO simulations. The aim is to introduce metal foams in microchannel heat sink (MCHS) design that derives from MMTO runs, and whose distribution of the three phases, *i.e.,* fluid, metal foam – to be considered as a solid/fluid porous medium in local thermal equilibrium - and solid, allows the trade-off between pressure drop and heat flux to be exploited, resulting in lighter components that can be applied in more sectors. Since the problem involves fluid flow and heat transfer phenomena at small scales, accurate modeling of these phenomena is vital for evaluating the performance of optimized designs. To pursuit this target, a reliable and efficient numerical model is proposed – able to capture the intricacies of these phenomena – and its accuracy is verified against the local thermal equilibrium (LTE) model. According to a traditional approach, the porous material is placed heuristically where it is expected to provide the highest benefit. Thus, the material is added to the pre-existing geometry considering the trade-off between heat transfer gain and

fluid-dynamic penalization. In this work, the position and shape of the metal foam is defined by the algorithm itself, which enhances its potential for heat transfer. In this way, through the presence of the metal foam, the range of solutions that topology optimization can investigate can be further extended, for instance by placing the foam where the thermal resistance is largest. Therefore, results obtained by the MMTO of MCHS are expected to show huge improvements, introducing additional degrees of freedom during optimization, which can yield further performance improvements.

8.4.2. Materials and methods

This work aims to investigate the effects of using multi-material topology optimization to identify a design made by three phases, simultaneously, *i.e.,* solid, fluid and metal foam, whereas the metal foam is considered as a phase due to the local thermal equilibrium assumption, but it is made up by a solid bulk material and fluid that passes through the pores. This approach can offer valuable insights into the design and performance of complex structures, differing from traditional topology optimization techniques that consider only two phases (*e.g.,* solid and void/fluid). By extending the approach to three phases, it is possible to generate more complex and versatile designs that take advantage of the additional displacement of metal foams, providing lower pressure drops but worse attitude to dissipate heat compared to pure solid, and higher pressure drops but better heat transfer performance compared to pure fluid.

8.4.3. Physical model

The investigated microchannel heat sink is depicted in Fig. 8.23. It involves a conductive metal base plate in which there is a heat source – that could represent an electronic component – and an upper layer that, unlike the lower plate, is considered as domain for topology optimization.

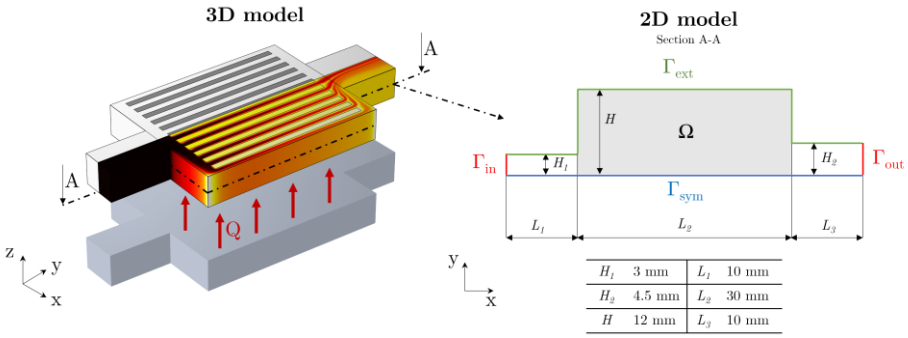

Fig. 8.23. Schematic of MCHS: 3D sketch and 2D design domain that is the cross-section on the x - y plane of the design layer of channels

Fluid enters the design layer from the inlet boundary (Γ_{in}), on the left side, and is subsequently expelled through the outlet located on the other side of the heat sink (Γ_{out}). All geometric features are presented in Fig. 8.23. The number of longitudinal fins is chosen so that the fluid area is equal to the maximum volume fraction, V_{max}, obtainable from the topology-optimized design. Based on the design of traditional MCHSs, the design consists of 11 longitudinal solid fins 0.5 mm thick and 26 mm long, positioned 2 mm from the entrance of the design domain. Because of the high computational cost due to the high number of iterations and fine mesh required, a simplified 2D model is analysed and only one half of the design domain is considered, due to the design symmetry, to perform topology optimization based on computational fluid dynamics (CFD) simulations [228].

8.4.4. Governing equations and topology optimization

The problem here analysed is about the conjugate heat transfer between the fluid, *i.e.,* water, and the solid, *i.e.,* copper, whose thermophysical properties are listed in Tab. 8.7.

Table 8. 7. MCHS materials thermophysical properties at 20 °C

Material	Density (kg m^{-3})	Specific heat (J kg^{-1} K^{-1}))	Thermal conductivity (W m^{-1} K^{-1}))	Dynamic viscosity (Pa s)
Solid (copper)	8978	381	387.6	
Fluid (water)	998.2	4186	0.065	$1004 \cdot 10^{-6}$

To define the model equations, a continuous design field, $\gamma(x)$, is defined in Ω. Its values range from 0 to 1, where 1 represents the fluid, whereas 0 represents the solid material. An incompressible, laminar, and steady-state flow is assumed in all analysed cases.

Ideally, the conjugate heat transfer problem would be simulated using a binary distribution if one knows the material distribution a-priori. However, to use the gradient-based optimization algorithm, the following equations, *i.e.*, continuity, momentum, and energy, can be written in the design domain:

$$\nabla \cdot u = 0 \tag{8.22}$$

$$\rho_f \; u \cdot \nabla \; u = -\nabla p + \mu_f \nabla^2 u + F(\gamma) \tag{8.23}$$

$$\rho_f c_f u \nabla T_f = \nabla \cdot (k_f \nabla T_f) + Q_s \tag{8.24}$$

with ϱ_f the fluid density, u the fluid velocity vector, p the pressure field, μ_f the dynamic viscosity of the fluid (water), and Q_S the heat source uniformly defined in the domain, which simulates the presence of a source as a CPU. For the porous medium, a local thermal equilibrium is used, and this assumption will be described later in a separate section together with the code verification. To handle fluid permeability and solid impermeability, a fictious body force, $F(\gamma)$, is added to the right-hand side of the momentum equation for the topology optimized case. This Brinkman friction term follows the Darcy's law and is defined according to Eq. (8.25) to penalize the fluid flow within the solid domain:

$$F \; \gamma \; = -\alpha \; \gamma \; u \tag{8.25}$$

Where $a(\gamma)$ denotes the inverse permeability of the porous medium, which can be expressed through the Rational Approximation of Material Properties (RAMP) interpolation model, as in Eq. (8. 26), according to [228]:

$$\alpha\ \gamma\ = \alpha_s \frac{q_\alpha\ 1-\gamma}{q_\alpha + \gamma} \tag{8.26}$$

Where q_a is a penalization parameter used to adjust the slope of $a(\gamma)$; this penalization parameter also suppresses the generation of design variables intermediate values that cause meaningless designs. The magnitude of $a(\gamma)$ over the permeable fluid domain needs to be sufficiently small to be close to 0; conversely over the impermeable solid domain it needs to be large enough to approach infinity [64]. Therefore, a value of $a(\gamma) = 0$ is chosen for the fluid; conversely the definition of a_s makes use of the Darcy number (Da) to consider the intermediate cases – whereas Da is ideally zero for a solid medium, as shown in Eq. (8.27) [64].

$$\alpha_s = \frac{\mu_f}{DaL_c^2} \tag{8.27}$$

where μ_f is the fluid dynamic viscosity at the inlet, L_c is the characteristic length equal to the inlet width, and Da is set to 10^{-4}. The other properties, *i.e.,* thermal conductivity, density, and heat capacity, are interpolated with the same scheme [223], as shown in Eqs. (8.28-8.29), respectively:

$$k\ \gamma\ = k_f + (k_s - k_f)\frac{q_k\ 1-\gamma}{q_k + \gamma} \tag{8.28}$$

$$\rho\ \gamma\ = \rho_f + (\rho_s - \rho_f)\frac{q_\rho\ 1-\gamma}{q_\rho + \gamma} \tag{8.29}$$

$$c\ \gamma\ = c_f + (c_s - c_f)\frac{q_c\ 1-\gamma}{q_c + \gamma} \tag{8.30}$$

Where the subscripts f and s represent fluid and solid phases properties, respectively. Parameters q_k, q_ϱ and q_c are the penalization parameters for thermal conductivity, density, and specific heat capacity, respectively. These penalization parameters are chosen based on previous studies [223]. Their choose, in fact, is not arbitrary. If the value of q is excessively high, the impact of the penalty becomes less apparent, leading to the occurrence of blurred boundaries or computational divergence. Conversely, when q is excessively low, the penalty effect is adequate, but it tends to result in numerical divergence and checkerboard problems [234]. Hence, the values of q_k, q_ϱ and q_c are chosen as 0.02, 0.02, and 100 respectively, as suggested by the reference work [228].

8.4.5. Multi-material topology optimization

By itself, topology optimization by density method involves the design domain – discretized into a finite number of elements – to be a porous medium. This assumption is mandatory in order to provide intermediate materials and exploit the gradient-based optimization logic. To contemplate a third material – porous by its definition - into the optimization algorithm, a second pseudo density, γ_2, is introduced, and material properties are interpolated through a Solid Isotropic Material with Penalization (SIMP) scheme according to a reference work [232]. The second pseudo density is required to build an explicit nonlinear relationship between the effective materials' properties and the ones introduced within the optimized design [228]. The aim is to suppress intermediate values so that the material distribution gets the value in the limits. When $\gamma_1 = 0$, then according to γ_2 the design presents metal foam and solid. To handle fluid permeability, solid impermeability, and metal foams partially permeable, the fictious body force F already introduced in Eq. (8.23) is here modified according to Eq. (8.31) to penalize the fluid flow within the solid domain with pressure losses:

$$F\ \gamma\ = -\alpha\ \gamma_1, \gamma_2\ u \tag{8.31}$$

With the addition of a third phase, *i.e.*, the porous material, the inverse permeability, say a, of the topology optimization iterations depends even on the second pseudo density, γ_2. To correctly consider the porosity of these materials and determine the pressure drop due to fluid crossing, a first attempt should be made by defining the permeability of solid, fluid and porous medium, according to [232], where a definition is proposed through Darcy number, dynamic viscosity, and characteristic length. In [232], the authors suggest a "solid and porous viscosity" of 10^5 Pa s and 10^{-2} Pa s, respectively, whilst for the fluid the viscosity is 10^{-3} Pa s. However, when applying this method to the case here analysed, by using a $Da = 10^{-3}$, several computational errors occur due to the too high values for the inverse permeabilities. In this regard, a maximum value of 10^6 (Pa s m^{-2}) for the inverse permeability is suggested [228]. To overcome these two issues, the inverse permeability of the metal foam (a_{por}) is set based on the definition of permeability (K) – measured in m^2 – whilst for the solid material according to Eq. (8.25) through the Darcy number, as function of fluid viscosity and Da [14]. Finally, a_f – that is the fluid inverse permeability – is set to 0.

$$\alpha_{por} = \mu_f / K \tag{8.32}$$

K is the permeability of the metal foam and μ_f is the fluid dynamic viscosity. In this way, the definitions of a for solid and fluid follow those widely used in literature, while the porous medium inverse permeability is defined depending on the own properties of the materials, *i.e.*, μ_f and K, which can be assessed empirically or through semi-empirical correlations. The remaining thermophysical properties are evaluated as follows: the metal foam thermal conductivity is evaluated following a semi empirical correlation provided by Iasiello *et al.* [235], see Eq. (8.33), where it is defined as a function of its porosity and of the thermal conductivity of the constituent material. This equation for the effective thermal conductivity is valid if the solid phase conductivity is much higher than that of the fluid phase [235] that is what happens here. Specific heat and density are defined by weighted averages through porosity according to Eqs. (8.34) and (8.35), respectively.

$$k_{por} = 0.313 k_f (1-\varepsilon) \tag{8.33}$$
$$c_{por} = c_f \varepsilon + c_s (1-\varepsilon) \tag{8.34}$$
$$\rho_{por} = \rho_s / \varepsilon \tag{8.35}$$

where k_{por} is the equivalent thermal conductivity of the porous medium, c_{por} the specific heat, ε the porosity of the metal foam, ϱ_{por} and ϱ_s the density of metal foam and solid material, respectively. By doing this, the MMTO applied to MCHSs allows to expand the degrees of freedom of optimization and preserve a general definition for a_{por}, ensuring that the model can be used with every metal foam knowing its own microstructure. As far as the interpolation model, in order to perform MMTO, the SIMP scheme is used [232] instead of the previous formulation that is based on the RAMP one, *i.e.,* Eqs. (8.26-8.28). Thus, related functions used to interpolate density, thermal conductivity, specific heat, and inverse permeability, are listed in Eq. (8.36).

$$\begin{gathered} J\ \gamma_1, \gamma_2\ = A + B \\ with\ \ J = [\alpha, k, \rho, c] \\ \begin{cases} A = \ 1 - \gamma_1^3\ \{\ \gamma_2^3\ \cdot J_s + [1 -\ \gamma_2^3\ ] \cdot J_{por} \\ B = \ \gamma_1^3\ \cdot J_f \end{cases} \end{gathered} \tag{8.36}$$

Where the variable J represents all the listed properties. Looking at this equation, when the first pseudo-density γ_1 is equal to 1, the term A becomes 0, and only the B term with fluid properties remains; if this pseudo-density is 0 then B becomes 0, and the second pseudo-density, through its value, determines which phase will be introduced. On the other hand, when the second pseudo-density equals 0, according to Eq. (8.36), all interpolated properties will assume those of porous material, while properties of solid if equals 1. To further focus on the physical sense of these equations, plots of two of them, *i.e.,* inverse permeability and specific heat, are depicted in Fig. 8.24. The first pseudo-density, represented on the x-axis, determines whether or not there is solid material within the optimized design. When it equals 1, all plotted properties show a value equal to those of water. When it differs from 1, the second pseudo-density, represented on the y-axis, decides which type of non-fluid material should fill the domain.

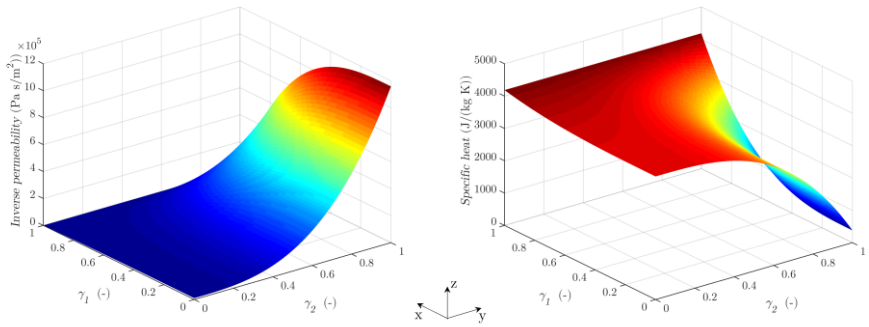

Fig. 8. 24. Example plots of how two of the interpolated properties - according to Eq. (15) – appear: inverse permeability (left), and specific heat (right)

Concerning geometry and related parameters, the mesh is generated by fixing a maximum element size – whose choice is justified in the following – to avoid checker boarder designs, and to reduce grey areas; therefore, for these aims, both Helmholtz filtering and projection scheme are applied [57].

The filter radius is fixed to $\sqrt{3}/2$ the mesh element size [68] whilst, for the projection, a slope value of 4 and a projection threshold of 0.5 are used to avoid computational problems linked to higher values of the first parameter. Concerning heat transfer, a fluid inlet temperature of 20 °C, a uniform heat source of $5 \cdot 10^7$ W/m^3 [228], and adiabatic walls are set as boundary conditions, while concerning the flow conditions, uniform inlet velocity – which is varied to investigate its

influence on final designs – and constant pressure at the outlet surface, are imposed. Therefore, based on the value of the heat source and considering a microchannel height of 9 mm, the resulting heat flux to be dissipated is 45 W/cm^2. Thus, the device here analysed clearly stands inside the region highlighted in Fig. 1, which represents the actual frontier in terms of heat flux for metal foam heat sinks. No heat transfer is allowed between the MCHS and the environment, and no-slip conditions are assigned over the walls, except for a symmetry condition applied along the lower wall of the computational domain. All the specified boundary conditions are resumed in Tab. 8.8.

Table 8. 8. Boundary conditions

Location	Flow condition	Thermal condition
Γ_{in}	$u = u_{in}$	$T = T_{in}$
Γ_{out}	$p = p_0 = 0$	$\partial T/\partial n = 0$
Γ_{sym}	$\begin{cases} \boldsymbol{u} \cdot \boldsymbol{n} = 0 \\ \boldsymbol{\tau}_{jk} = 0 \end{cases}$	$\partial T/\partial n = 0$
Γ_{ext}	Verticals: $u = 0$ Horizontals: $u = 0$	Verticals: $\partial T/\partial n = 0$ Horizontals: $\partial T/\partial n = 0$

Thermophysical properties are considered constant over the working temperature ranges, while gravitational and radiation effects are considered negligible. Finally, the metal foam is assumed to be homogeneous, isotropic, and completely saturated with the fluid with a non-Darcian flow. Based on these assumptions, the optimization problem is summarized in Eq. (8.37).

$$\begin{cases} \quad minimize \quad \dfrac{\int_\Omega T \, d\Omega}{\int_\Omega d\Omega} \\ s.t.: \begin{cases} p_{in} - p_{out} = \Delta p \\ \dfrac{\int_\Omega \gamma \, d\Omega}{\int_\Omega d\Omega} \leq V_{max} \end{cases} \end{cases} \tag{8.37}$$

According to this, MMTO is guided toward a T_{avg} minimization with two constraints; a first one limiting pressure drop between inlet and outlet, Δp, and a second one related to the volume fraction (V_{max}), set to 0.6, which is the maximum portion of the design surface that can be occupied by the fluid. This constraint helps to avoid trivial solutions, *i.e.,* fully fluid domain.

8.4.6. Numerical implementation

All the topology optimization runs are performed via COMSOL Multiphysics, where the gradient-based topology optimization is carried out via the method of moving asymptotes (MMA). The MMA, as a gradient-based numerical optimization algorithm, requires the design variable set to be updated by objective and constraints gradients (adjoint problem). This requires an iterative procedure, and the design is progressively refined until a certain criterion chosen for convergence is reached. In this work, convergence is achieved when either the difference between the two last solutions of the objective function is less than 10^{-6} or the number of simulations reaches 250. This results in an average simulation time of about 19 hours for each case investigated. All the simulations have been run through a workstation equipped with an Intel® Core ™ i7-8700K 3.70 GHz processor and 32 GB and 2133 MHz RAM. Topology optimization can suffer from mesh-dependency problem, with the influence of mesh resolution altering the final design [236]. Thus, mesh sensitivity represents a fundamental step in both model definition and reliable final solutions achievement. Simulations are performed with a quadrilateral structured mesh, for seven different maximum mesh element sizes, with an inlet velocity of 0.02 m/s and a Δp of 0.5 Pa. For all the runs, a maximum size of the mesh element is set, *i.e.,* mesh size, which is varied from 0.12 mm to 0.25 mm. Results – in terms of average temperature (objective function) vs number of iterations – are summarised in Fig. 8.25.

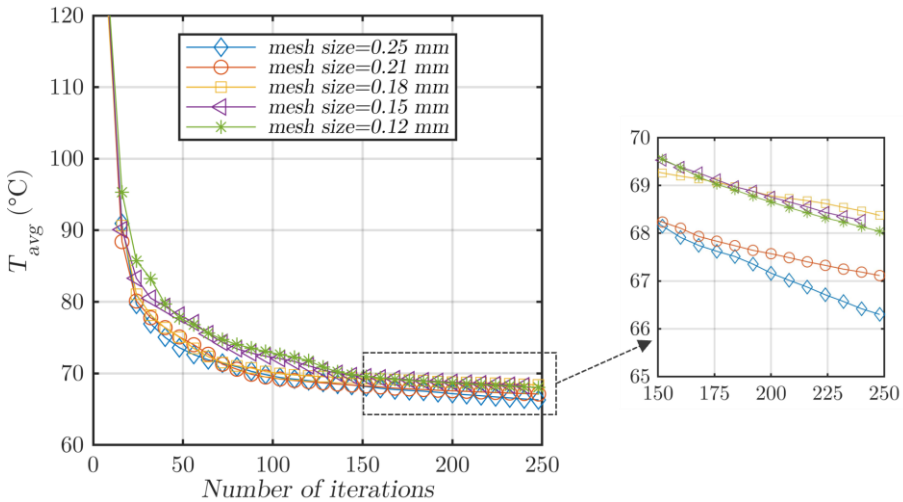

Fig. 8. 25. Plots of the objective function path for different mesh sizes

The paths followed by the objective function show a sharp decrease in the first 30 iterations. Conversely, from 100 iterations onward, the values are in between 66 °C and 75 °C. Taking a closer look at the last 100 iterations, the paths of the topology optimization processes can be seen in detail. The objective function decreases at most of two 2.5 °C with a decrease of about 0.02 °C/iteration. Final solutions, *i.e.,* average temperature of the heat sink surface, for mesh sizes between 0.12 mm and 0.18 mm, are all enclosed in a 1 °C range, while for mesh sizes higher than 0.18 mm the discrepancy increases. From a first look it seems that it may be convenient to adopt a mesh with a lower resolution. However, the final design is strongly compromised in terms of surface quality at the interface between materials. To this end, further remarks can be drawn looking at the shape of optimized designs. In this regard, Fig. 8.26 reveals the final solutions for the topology optimization runs performed with 0.25 mm, 0.18 mm, and 0.12 mm of mesh element size.

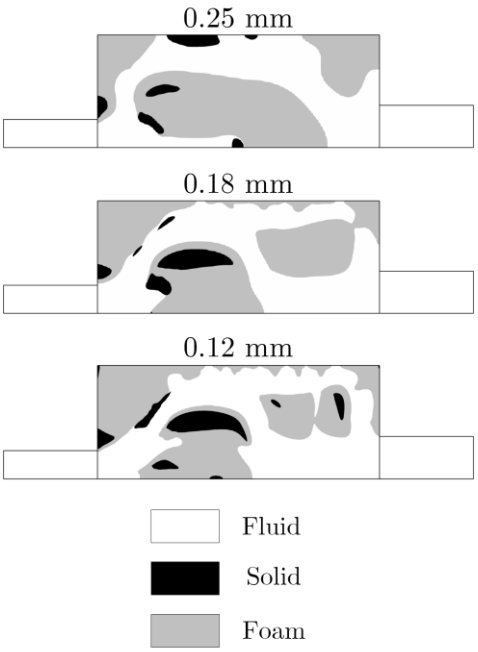

Fig. 8. 26. Final solutions for four mesh element sizes: 0.12 mm, 0.18 mm, and 0.25 mm

The figure shows how much the design is sensitive to the mesh size. In the transition from the mesh size design of 0.25 mm to that of 0.12 mm, the increase in quality of the characteristic surfaces of the MCHS is evident. For instance, in

moving from 0.25 to 0.18 mm, a solid fin appears in the central part of the domain, which remains almost unchanged in the latest design (0.12 mm). Similarly, in the 0.25 mm mesh design one can note the presence of porous material region in the right-hand part, which in other cases splits into two elements, with smaller solid fins inside as well. In general, it can also be seen that in the cases with smaller mesh sizes, the path followed by the fluid tends to assume a preferential direction compared to the 0.25 mm case. A further remark concerns the number of the solid fins varying the mesh size. In the first case, *i.e.,* 0.25 mm, those features are of homogeneous size, showing how the filter – which depends on mesh size – does not allow for finer details. By reducing the mesh size, the difference in features size is more marked. Because of the limit on the volume fraction, once a solid fin of considerable size appears, the remaining part of the domain is lacking other solid features. Only a further reduction of the mesh size allows a more uniform distribution, which also results in an improvement of the objective function – albeit very small. An additional, non-negligible, aspect concerns the subsequent verification of the design obtained. In the case of 0.25 mm mesh, this comparison leads to considerable discrepancies in terms of pressure drop. All these evidence result in the selection of 0.12 mm as mesh size value for carrying out the subsequent analysis.

8.4.7. Metal foam model: LTE

To assess the quality of the results obtained through topology optimization with metal foams, and to evaluate their reliability, MMTO results are compared and tested with a model that includes just a porous media coupled with microchannels. This also because at the present stage no studies are available for this particular hybrid solution. Once the optimized design is reached, the final topology-optimized geometry is exported, and used as starting point for the comparisons step. Numerous researches and analyses on heat transfer in porous media are based on local thermal equilibrium (LTE) or local thermal non-equilibrium (LTNE) assumptions, where the first of which assumes that the local temperatures of fluid phase and solid phase are the same with references to a representative elementary volume [237]. With this assumption, only one energy equation is needed the model. The difference in results deriving from LTNE and LTE models for water cooled heat sink is scarce, especially at high flow rates [238]. The assumption of LTE is commonly justified for modeling microchannel heat sinks with metal foams due to the following factors. The porous structure of metal foams, consisting of interconnected voids and metallic struts, facilitates the homogeneous distribution of heat

throughout the foam. This promotes local thermal equilibrium by facilitating the heat transfer from hotter to cooler regions. Furthermore, microchannel heat sinks are designed with small channel dimensions, resulting in small characteristic length scale that minimizes temperature gradients, and enhances the likelihood of local thermal equilibrium because the boundary layers rapidly cover all the fluid domain. Also, under forced convection, the flow helps uniformity within the foam, continuously replenishing the heat transfer medium and minimizing temperature variations, thereby promoting thermal equilibrium. According to the findings of Ghorbani *et al.* [239], when both the Reynolds number (Re) and the Darcy number (Da) grow, the assumption of local thermal equilibrium (LTE) might be no longer valid. In this work, Re does not exceed 150, and the maximum Da value considered is 10^{-3}. To this end, the range in which the LTE assumption holds true can be determined by both Biot number (Bi) and effective thermal conductivity ratio, according to the map presented by Lee *et al.* [240]. As a result, in the current study, the LTE assumption – considering a value of the thermal conductivity ratio, $k_r \geq 25$ and a Bi ≥ 1.5 – suffers from maximum inaccuracy from the LTNE model of about 3% on Nusselt number. Thermophysical properties of metal foam used for the LTE model for the topology optimization are here described. Correlation for linking cell size (d_c) and pores per inches (PPI) is here used to set PPI as an independent variable [241], based on previous definitions (Eqs. (8.33)-(8.35)). As for permeability and Forchheimer coefficient, those proposed by Calmidi *et al.* [242] are used, shown in Eqs. (8.39) and (8.40), respectively.

$$d_c = 10^{-3}[-0.921 \cdot \ln PPI + 5.3564] \tag{8.38}$$

$$K = 0.00073 \cdot 1 - \varepsilon \left(\frac{d_f}{d_c}\right)^{-1.11} (d_c^2) \tag{8.39}$$

$$C_f = 0.00212 \cdot 1 - \varepsilon \left(\frac{d_f}{d_c}\right)^{-1.63} \tag{8.40}$$

Where K is the permeability, C_f the Forchheimer coefficient, and ε the porosity of the metal foam. The model assumes local thermal equilibrium (LTE) to use the equivalent thermal conductivity, k_{por}, already presented for the MMTO case in Eq. (8.33) while, $(\varrho c)_e$ is calculated as a weighted average of water and copper properties according to Eqs. (8.34-8.35). C_f is evaluated based on Eq. (8.40). Therefore, governing equations are written as continuity equation, *i.e.,* Eq. (8.41), momentum equation – Eq. (8.42) – which are written as the Brinkman-Darcy-Forchheimer form to account for the existence of a porous medium, and energy equation outside and within the porous medium, *i.e.,* Eq. (8.43) and Eq. (8.44), respectively. Volume-average symbols are dropped for simplicity.

$$\nabla \cdot u = 0 \tag{8.41}$$

$$\frac{\rho_f}{\varepsilon^2}\, u \cdot \nabla u \;= -\nabla p + \frac{\mu_f}{\varepsilon}\, \nabla^2 u - \frac{\mu_f}{K} u - \frac{C_f \rho_f}{\sqrt{K}} |u| u \tag{8.42}$$

$$\rho_f c_f u \nabla T_f = \nabla \cdot (k_f \nabla T_f) \tag{8.43}$$

$$\rho_e c_e u \nabla T = \nabla \cdot (k_{por} \nabla T) \tag{8.44}$$

Where μ_f, c_f, ϱ_f, u, are fluid viscosity, specific heat, density, and velocity, respectively. K and ε the permeability and porosity of the metal foam. This set of equations solves the temperature, velocity, and pressure field when the microchannel is equipped with metal foams. Thus, once the material distribution has been obtained from the optimization process, the next step is to carry out simulations using this LTE model and to analyse, if any, discrepancies with the MMTO result.

8.4.8. Results

Multi-material topology optimization aims to increase the number of degrees of freedom to enable a better optimized design and to develop geometries with higher performances, even compared to simple topology-optimized design with two materials, since it looks for avoiding local optimum. To this end, an initial TO investigation is performed with a single solid material and compared with results from a baseline case to underline advantages from pure topology. Comparisons with available literature data will also be done to witness the reliability of the present approach. Various TO runs are performed to explore different designs depending on the boundary conditions. Then, once it has been proved that TO outperforms the baseline case, the multi-material topology optimized (MMTO) designs are presented and compared with previous cases. Finally, a parametric analysis on the effects of varying operating conditions and parameters affecting foam permeability is proposed.

8.4.9. Baseline and TO-base designs

To verify the benefits obtainable from the application of multi-material topology optimization, a baseline MCHS with the same geometric characteristics – say the available design domain – and under the same boundary conditions as the previous

one shown, is introduced and also studied through 2D simulations. The baseline geometric features of the empty designs are the same of the TO one. First of all, in order to assess the step forward achieved applying topology optimization to the MCHS, the baseline case is assessed, and results are shown in Fig. 8. 27 in terms of temperature and velocity magnitude fields. The same figure also shows results obtained from the TO case performed under the same boundary conditions used in the reference [228], *i.e.,* 0.02 m/s and 1 Pa of inlet velocity and maximum pressure drop, respectively. At first glance, the optimized design shows the presence of a series of "alveoli" – as already shown in [228] – consisting of solid material and, between which, the fluid (water) flows giving rise to a series of microchannels of various sizes. Those fluid paths cover almost the entire surface and ensure excellent performance in terms of average temperature and uniformity over the surface.

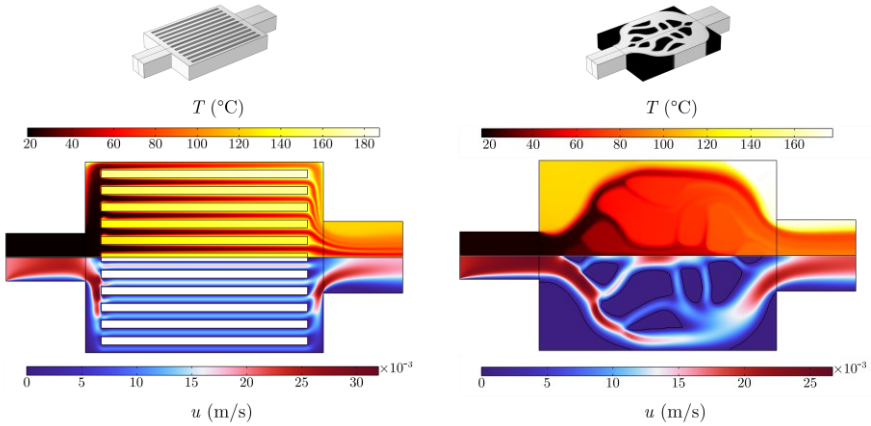

Fig. 8. 27. Plots of temperature and velocity magnitude fields about the baseline and TO-based MCHS

By looking at the temperature fields, the TO one is more uniform, and solid structures are designed to avoid recirculation zones, showing overall lower temperatures than in the baseline case. Precisely, the baseline shows a pressure drop of 3.18 Pa, with T_{max} and T_{avg} of 187.2 °C and 106.0 °C, respectively. These values are up to 20 °C higher than the ones achieved by applying TO with one third of the pressure drop imposed as constraint, *i.e.,* 1 Pa vs 3.18 Pa. In addition to the plots, a focus on the final solutions for maximum and average temperatures, as well as velocities, is shown in Tab. 8.9 to compare the final results obtained with those provided in the reference. The data provided by the reference work and those collected in the present work show a good overlap between the two simulations, providing a maximum relative percentage error of 3.38% in the average velocity magnitude, whereas maximum and average temperature differ of 2.0 °C and 0.85

°C, respectively. Remarkably, all results are obtained by constraining pressure drop up to 1 Pa. It should be noted how, according to the results provided in Tab. 8.9, topology optimization is able to improve both thermal and fluid-dynamics designs, leading to lower pressure drop and temperatures under the same mass flow rate. From this initial evidence, it is clear that the application of this technique to MCHSs is able to lead to concrete results that are also able to justify the cost of model development due to significant benefit as concerns both heat transfer and pumping power. This baseline case will be further compared with the performance of an MCHS developed, with the same boundary conditions, through MMTO.

Table 8. 9. MCHS TO-base verification

	T_{max} (°C)	T_{avg} (°C)	u_{max} (m/s)	u_{avg} (m/s)
Baseline design	187.2	106.0	0.0320	0.0096
Present work	176.9	79.85	0.0260	0.0061
Reference work [228]	174.9	80.70	0.0258	0.0059
Deviations: present vs reference work	+ 2.00	- 0.85	+ 0.0002	+0.0002

8.4.10. Parametric Analysis on TO design

Additional simulations are here carried out to show the differences in the final design and in the thermo-fluid dynamic results for different values of velocity and pressure drops. Furthermore, this will help to compare overall performance of the MCHS – by using the same boundary conditions – but developed using MMTO and metal foams. For this purpose, an inlet velocity of 0.02 m/s and 0.05 m/s is chosen, whereas different constrained maximum pressure drop equal to 0.5, 2, and 3 Pa, are assumed, respectively. Looking at Fig. 8.28, where temperature and velocity magnitude are plot for 0.02 m/s and 0.5 Pa (left) and 0.02 m/s and 2 Pa (right), first evidence comes by final designs of the optimized geometries: these become more and more full of “alveoli” as the pressure drop allowed increases.

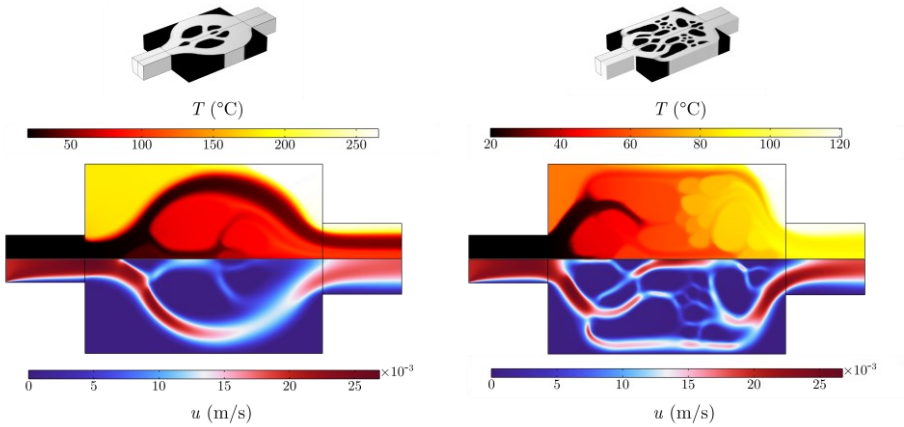

Fig. 8. 28 Plots of material distribution, temperature, and velocity magnitude fields for: left) 0.02 m/s and 0.5 Pa; right) 0.02 m/s and 2 Pa

As the pressure drop increases the number of the "alveoli" becomes higher and, at the same time, their size becomes smaller and smaller, making the microchannel narrower and more numerous. The distribution of fins is closely related to pressure drop constraints and resulting thermal performance. Since a relatively large number of fins provides a larger convective heat transfer area, heat dissipation efficiency increases as the number of fins increases, even though a larger number of fins results in higher pressure drops. That's why an increase in the maximum pressure drop allowed leads to higher number of fins and lower T_{max} and T_{avg} as it can be seen in Tab. 8.10.

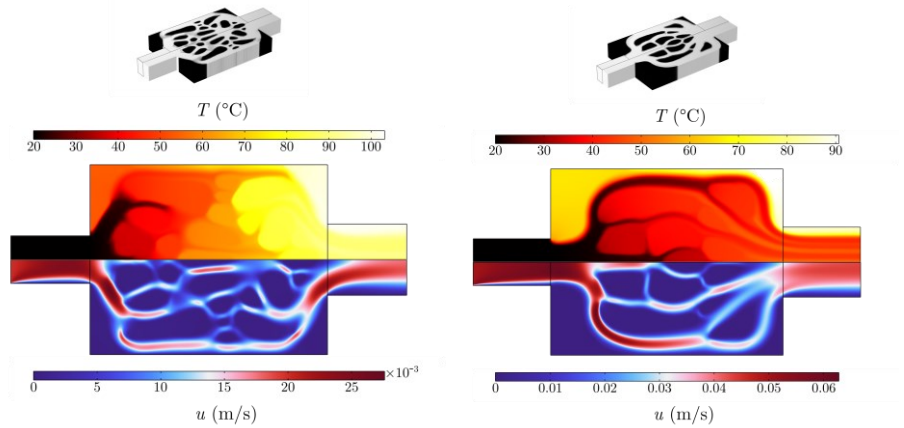

Figure 8. 29. Plots of material distribution, temperature, and velocity magnitude fields for: left) 0.02 m/s and 3 Pa; right) 0.05 m/s and 3 Pa

A further comparison may be done over the two case studies analysed with a 3 Pa pressure drop, say a first with 0.02 m/s as the inlet velocity, and a second one with an inlet velocity of 0.05 m/s (see Fig. 8.29 where this comparison is shown in terms of velocity and temperature fields). The latter achieved the best results in terms of lower thermal resistance – as witness by the generally lower temperatures achieved – due to the higher inlet velocity leading to higher convective heat transfer coefficients, even though it should be pointed out that the number of fins is lower, because of the higher inlet velocity that leads to higher pressure drops [14]. Finally, the relationship between average and inlet velocities should be emphasized because these are inherently linked to both pressure drop and thermal performances. In the case of an inlet velocity of 0.02 m/s the maximum velocity inside is up to 30% higher than the inlet velocity, and for an inlet velocity of 0.05 m/s the maximum is about 20% higher. In addition, the average velocity is about 30% of the inlet velocity and increases slowly with pressure drops due to the increase in the number of microchannels. A further parameter that is linked to the thermal resistance and gives information about the thermal performances of the device is the convective heat transfer coefficient, h_{MCHS} – evaluated as in Eq. (8.41) – which shows an increase for the TO design of almost 70% over the base case with the same boundary conditions and pressure drop (see Table 8.10).

$$h_{MCHS} = \frac{Q_s}{T_{avg} - T_{in}} \tag{8.41}$$

The fact that the heat transfer coefficient is much higher for the TO confirms that this approach is able to generate designs that can reproduce the same thermodynamic results with lower power consumption – or better thermodynamic results at equal power consumption - when references is done to both baseline case and TO one for 0.02 m/s and 3 Pa. For instance, for this case, at almost equal pressure drop, the heat transfer coefficient for the TO case becomes about 66% higher.

Table 8. 10. Comparisons between case studies for 0.5, 1, 2, 3 Pa and 0.02 and 0.05 m/s

	T_{max} (°C)	T_{avg} (°C)	u_{max} (m s^{-1})	u_{avg}	h_{MCHS}

				(m s^{-1})	(kW m^{-2} K^{-1})
TO: 0.5 Pa - 0.02 m/s	265.60	113.99	0.02683	0.0057	5.32
TO: 1 Pa - 0.02 m/s	176.86	79.85	0.02601	0.0061	8.33
TO: 2 Pa - 0.02 m/s	120.47	64.36	0.02674	0.0062	11.27
TO: 3 Pa - 0.02 m/s	103.19	61.20	0.02759	0.0060	12.14
TO: 3 Pa - 0.05 m/s	90.665	44.377	0.06280	0.0149	20.512
Baseline: 3.18 Pa - 0.02 m/s	187.17	106.00	0.03200	0.0096	7.28

Multi-material topology optimization of the above mentioned MCHS has been firstly performed in this work for an inlet velocity of 0.02 m/s, maximum constrained pressure drop across the MCHS of 0.5 Pa, and a maximum fluid volume fraction of 0.6. Figs. 8.20-8.31 show the distribution of materials within the optimized design, and the velocity/ temperature fields of the achieved optimal MCHS, respectively.

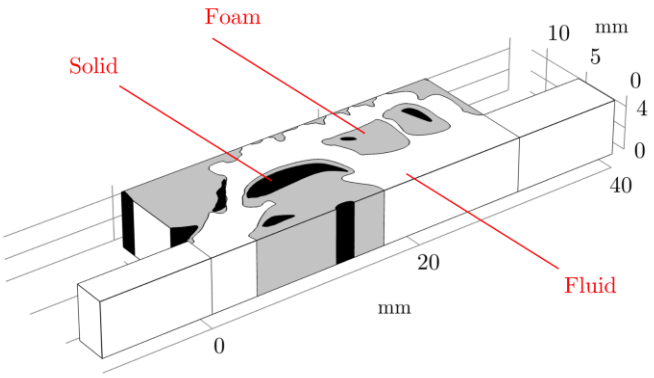

Figure 8. 30. MMTO optimal design of the MCHS: distribution of materials

The distribution of materials – *i.e.*, solid, metal foam and fluid (water) – has been achieved from the distribution of the two densities, γ_1 and γ_2. The solid is represented in black, the metal foam in grey, and the fluid in white. The solid has the highest thermal conductivity, so that the algorithm locates this material where there is a large thermal power to be dissipated. This is why this is placed near the fluid inlet, where the fluid has the lowest temperature within the optimized design;

therefore, the highest conduction is required in that area to dissipate heat flux. In addition, the larger fin also has the purpose of channelling the fluid properly, preventing it from entering the foam excessively, causing high local pressure drop. In contrast, the other solid fins are introduced in the area occupied by the porous material and near the channels.

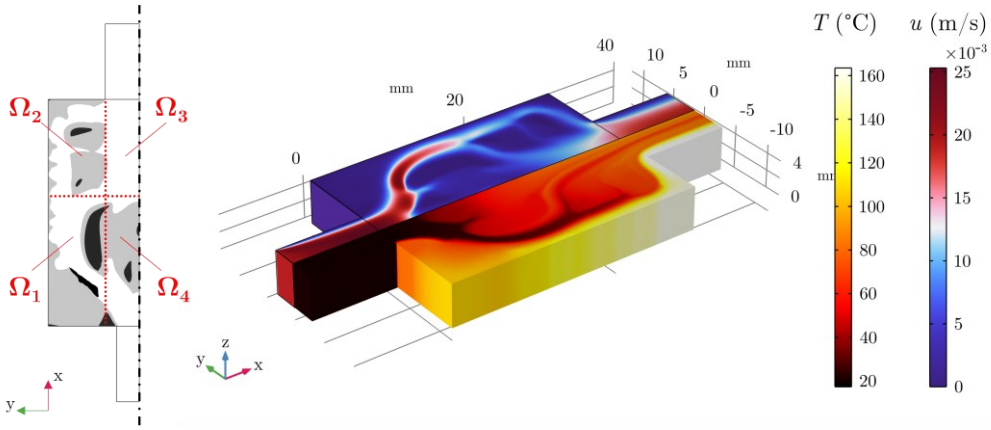

Fig. 8. 31. MMTO optimal design of the MCHS: left) characteristic areas; right) temperature and velocity magnitude fields

Since the porous material provides a large heat transfer surface area to volume ratio, a large amount of heat is dissipated in the areas occupied by the porous material; on the other hand, a solid is required to reduce the thermal resistance, to enable high heat flow to be transferred between the solid base plate and the fluid flowing through the pores. The temperature field shows a great uniformity of temperature in the design domain, except for the final design area before the outlet, where some hotspots arise at the boundaries. This is also the reason why the topology-optimized design includes a solid fin in the upper right area, Ω_1, trying to dissipate as much thermal power as possible. Looking at the velocity field, it can be seen that the upper area at the inlet, *i.e.,* corresponding to Ω_1, has little fluid flowing through it, as well as the upper right area, *i.e.,* Ω_2, whilst most of the fluid flows through the main microchannel between the two porous areas distributed at the inlet of the heat sink. In this region, velocities reach the highest values. In the metal foam domain, velocity magnitude is in between 1 and $5 \cdot 10^{-3}$ m/s, testifying how the porous material enabled, through reverse permeability modelling, its crossing by the coolant at very low velocities. At the same time, in the regions occupied by the solid, the velocity field approaches zero values. This testifies the correct

modeling of the media through inverse permeability. In general, it can be concluded that the initial modeling of the materials involved in the optimization can be considered correct because, mainly, the values of the velocity magnitude range agree with the types of materials and the penetrability of the porous medium, accounting for the fact that three materials are here considered.

Overall, the solution achieved through MMTO, and shown in Figs 8.30-8.31, has a fairly similar basic structure compared to the one developed with the base topology optimization and for the same boundary conditions already shown in Fig. 6. There remains mainly the attitude to create a structure similar to "alveoli," but with the addition of the solid material inside them to allow the MCHS to exchange a higher heat flux, as mentioned earlier, and to obtain more uniform temperature distributions. The number of alveoli for the analysed section is still four as for the optimized TO design, although their boundaries are not as clear as for the base case due to the absence of a microchannel between the two solid fins at the bottom centre of the design. Tab. 5 collects results in terms of h_{MCHS}, average and maximum temperature and velocity, for the baseline case, and also for pressure drop constraints of 1 and 2 Pa. The MMTO optimized design shows lower values for all the parameters analysed, showing that the advantage obtained by using both metal foams and MMTO is enormous, with a huge gain in terms of mean and maximum temperature and h_{MCHS}, as shown in Tab. 8.11. The average temperature is about 45 °C lower and the maximum temperature about 100 °C lower than the case developed with TO for 0.02 m/s and 0.5 Pa pressure drop. To obtain the same result in terms of average temperature, the case study for a 2 Pa pressure drop should be considered; on the other hand, this case allows to much lower maximum temperature. This behaviour can be explained by the fact that the fluid can flow easily through the metal foams, unlike the base case in which the ability to achieve lower average temperatures, through the formation of more and more microchannels, was limited by the pressure drop constraint. In this case, the MMTO takes advantage of both the formation of a few microchannels through which the fluid can flow without incurring in excessive pressure losses, and the low-velocity flow in the porous layer, where advantages in terms of increased heat transfer surface area are exploited. MMTO design reaches the same T_{avg} of the 2 Pa TO optimized one, and the other way around the T_{max}, where the higher pressure drops available make the optimized design with TO full of microchannels across the design, reaches also a better maximum temperature. A last but impressive improvement is available looking at the h_{MCHS}, say almost 100% higher than the basic case developed with the simple TO and the same pressure drop and fluid velocity inlet.

Table 8. 11. Comparisons among performance of optimized designs developed with TO and MMTO for an inlet velocity of 0.02 m/s

	T_{max} (°C)	T_{avg} (°C)	u_{max} (m s^{-1})	u_{avg} (m s^{-1})	h_{MCHS} (kW m^{-2} K^{-1})
Baseline: 3.18 Pa	187.2	106.0	0.03200	0.0096	7.28
TO: 0.5 Pa	265.6	114.0	0.02683	0.0057	5.32
TO: 1 Pa	176.9	79.85	0.02601	0.0061	8.33
TO: 2 Pa	122.6	64.36	0.02823	0.0062	11.27
MMTO: 0.5 Pa	163.5	68.68	0.02490	0.0059	10.27

8.4.11. MMTO model verification

To evaluate the quality of the results obtained through MMTO with metal foams and to assess their reliability, results are compared against the ones obtained with the LTE-based model, with the latter performed on the geometry derived from MMTO. The case studies analysed consider an inlet velocity of 0.02 m/s with a constrained Δp of 0.5 Pa, and two different Darcy numbers, say 10^{-3} and 10^{-4}. The geometry used is obtained applying the COMSOL filter function, particularly considering the area with the first and second pseudo-densities greater than 0.8, so as to reconstruct the areas occupied by the fluid ($\gamma_1 > 0.8$) and those occupied by the solid ($\gamma_2 > 0.8$) and porous media ($\gamma_2 < 0.8$) with a good accuracy. Results from the two simulations are shown in terms of velocity and temperature fields in Fig. 8.32 and 8.33, for Da equal to 10^{-3} and 10^{-4}, respectively. Firstly, two phenomena need to be emphasized: the material properties in the LTE porous model developed here are uniform, and there are no intermediate materials between solid, porous, and fluid phases, differently from the case to be validated.

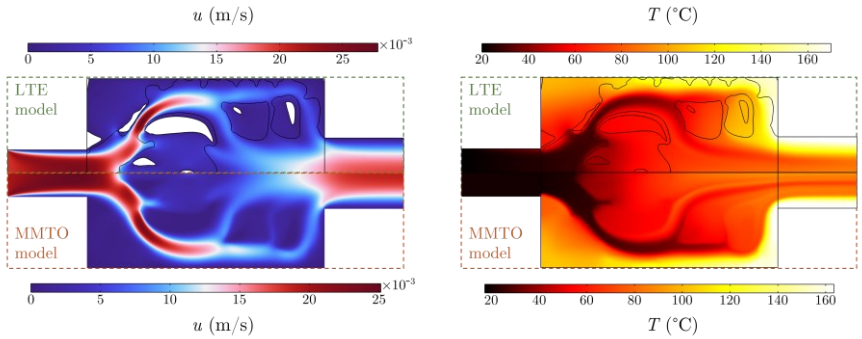

Figure 8. 32. Comparison for temperature and velocity magnitude fields between LTE model (upper) and MMTO (lower) for Da = 10^{-3}

The second phenomenon concerns the geometry, which, in Fig. 8.32, being obtained through the contour of the two pseudo-densities, exhibit slightly different characteristics from those shown in Fig. 8.31. The main consequence of the geometry change is on the fluid dynamics that affects temperature field and pressure drop. This effect, together with the one introduced earlier, is undoubtedly the main cause of the slight mismatch between these results and those obtained from the MMTO simulations. However, the value of T_{avg} is very close to the ones achieved through the MMTO, with errors up to 3%. Results concerning the maximum temperature differ a little more with errors up to 8%, but as mentioned above, a complete overlap of the results is also particularly difficult due to slight geometric differences.

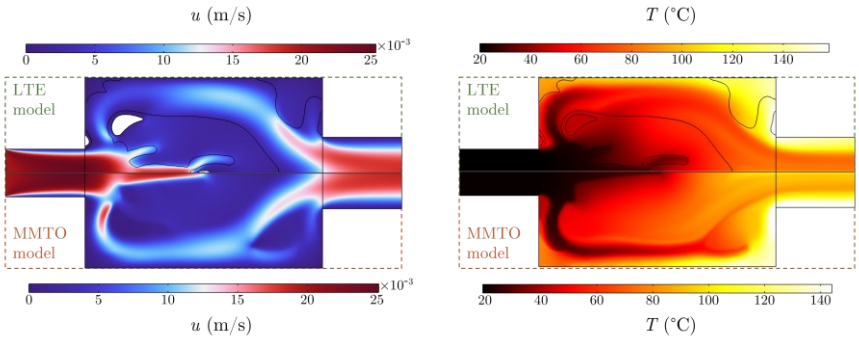

Fig. 8. 33. Comparison for temperature and velocity magnitude fields between LTE model (upper) and MMTO (lower) for Da = 10^{-4}

Comparing the temperature and velocity fields of the two simulations, a high degree of correspondence is evident; the areas where maximum velocities and temperatures are recorded coincide and, at the same time, very similar values in their distributions can be assessed by looking at the fields in comparison. Finally, a parameter to be compared is the pressure drop across inlet and outlet, constrained but obtained since we are assuming the inlet flow rate as a boundary condition here.In order to ensure that the geometries exported and used for the designs and the impermeability model used in the MMTO can be considered valid, it is necessary that the pressure drop realized in the design under the same boundary conditions are similar. As can be seen in Tab. 8.12 the value reached for the two porous models show an almost perfect overlap with a maximum percentage error of 0.7 %.

Table 8. 12. T_{max}, T_{avg}, and Δp, for LTE model MMTO at different Darcy numbers

	$Da = 10^{-3}$		$Da = 10^{-4}$	
	LTE	MMTO	LTE	MMTO
T_{max} (°C)	167.7	163.5	154.1	144.0
T_{avg} (°C)	70.40	68.68	63.83	65.51
Δp (Pa)	0.486	0.500	0.499	0.500

8.4.12. Parametric Analysis

Once the verification of the MMTO has been provided, the interests is pointed on the investigation of different designs that can be achieved by varying significant parameters that affect the problem. To this end, this section shows how the final design changes depending on several factors, *i.e.,* operating conditions and Darcy number value, which affects the fluid penetration in solid and metal foam regions.

To assess the behaviour of the optimized design, a variation in pressure drop across inlet and outlet and fluid inlet velocity is performed. The following MMTO runs have been performed, keeping other boundary conditions unchanged:

- with an inlet velocity of 0.02 m/s: pressure drop of 1 Pa and 3 Pa;
- with an inlet velocity of 0.05 m/s: pressure drop of 3 Pa and 5 Pa.

Firstly, it should be outlined which are the two most important consequences of increasing velocity and pressure drops. As the velocity increases, the Reynolds number increases, which leads to a higher convective heat transfer coefficient and, at the same time, an increase in pressure drop. Such increase allows more mass flow inside the metal foam, increasing the thermal performances. Based on the latter two phenomena, the material distributions for the inlet velocity of 0.02 m/s and 3 Pa show almost exclusive deployment of porous material, with a not well-defined shape, near the inlet section; only by increasing the allowable pressure drop to 5 Pa and using a fluid inlet velocity of 0.1 m/s, two main central fins appear, with the optimized design that still show large "grey areas". Similar remarks can be stated for the 0.05 m/s and 5 Pa case. Conversely, solutions for 0.02 m/s, 0.05 m/s look more interesting. These are evaluated considering 1 Pa and 3 Pa of pressure drop, respectively. The one obtained for a pressure drop of 1 Pa, shown in Fig. 8.34, consists mainly of a larger fin in the centre of the design and four others.

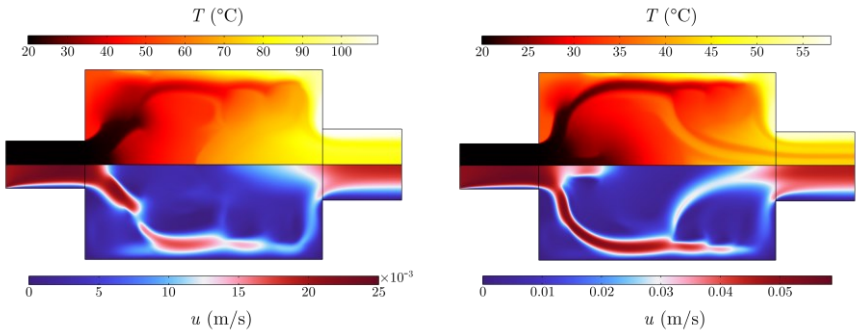

Fig. 8. 34. Temperature and velocity magnitude field: left) 0.02 m/s and 1 Pa; right) 0.05 m/s and 3 Pa

Solid fins are mainly arranged near the inlet, where most of the heat transfer needs to be transferred. A further one is arranged in the upper right corner, where usually – according to the simulations carried out in this work – the microchannel shows areas with highest temperatures. In general, the optimized design is still similar to the one depicted in Fig. 8.32, and the higher allowable pressure drop leads to a higher mass flow rate through the porous material, increasing the thermal performance, according to the velocity plot in Fig. 8.34. The average temperature achieved for this case study is 13 °C lower than that achieved in the base case, *i.e.,* 0.5 Pa and 0.02 m/s, confirming the trend previously shown in Tab. 8.12 where, by going from 0.5 Pa to 1 Pa the largest gain is on the maximum temperature. As for the design optimized for 0.05 m/s, an interesting result is here achieved due to the lower velocity and the fairly higher pressure drop allowed. A wide main channel appears, the distribution of solid fins follows the other designs optimized for 0.02 m/s and 0.5, 1 Pa, where the largest number of fins is arranged on the left side of the design domain. Observing the velocity field, the flow streamlines show how the fluid does not flow within the solid domain, and what the fluid distribution is, highlighting the link between the less dense areas of fluid and the higher temperature above the MCHS, which can be confirmed for all the simulations performed in this work. Indeed, using metal foams is something helpful to avoid these dense areas, that makes temperature higher everywhere. A final observation should be made about the optimized design, which despite the projection and Helmholtz filtering does not appear clear enough, with some "grey areas". This problem leads to the need to perform post-processing optimization of the design and extrapolate a final design through the filtering function with which this problem can be almost completely limited.

Table 8. 13. Temperature, h_{MCHS}, and velocity comparison among the optimized design with MMTO

	T_{max} (°C)	T_{avg} (°C)	u_{max} (m s^{-1})	u_{avg} (m s^{-1})	h_{MCHS} (kW m^{-2} K^{-1})
Baseline: 0.02 m/s - 3.18 Pa	187.17	106.00	0.03200	0.0096	7.28
TO: 0.02 m/s - 0.5 Pa	176.86	79.85	0.02601	0.0061	8.33
MMTO: 0.02 m/s - 0.5 Pa	163.49	68.68	0.02490	0.0059	5.14
MMTO: 0.02 m/s – 1 Pa	109.25	55.71	0.02380	0.0060	13.20
MMTO: 0.05 m/s - 3 Pa	58.07	33.28	0.05712	0.0015	37.66

Further analysis is carried out to evaluate the behaviour of the optimized design by varying the Darcy number (Da) used to define the impermeability of the solid phase. In the previous section, the Darcy value that ensured a better fit with the results of the LTE model comes out to be $Da = 10^{-3}$. According to Eq. (6), impermeability is inversely proportional to Da, which means that by decreasing this parameter the impermeability of the solid domain becomes more pronounced. For this reason, two more simulations were carried out for the case studies with an input velocity of 0.02 m/s, 0.5 Pa and 1 Pa pressure drop, respectively, also to verify any further changes in the results obtained in terms of both design and thermodynamic performance. The simulations were run with a different Da, set to 10^{-4}, leading to an inverse permeability of an order of magnitude greater than that used in previous sections. Fields about the simulations performed are shown in Fig. 8.35, while h_{MCHS}, maximum and average temperatures, and velocities reached, are listed in Tab. 8. The differences on heat transfer results are in most cases not far apart; on the other hand, the same cannot be reported for optimized designs and the associated temperature and fluid velocity distribution fields. Fig. 8.35 shows the plots about temperature and velocity magnitude fields for the presented cases.

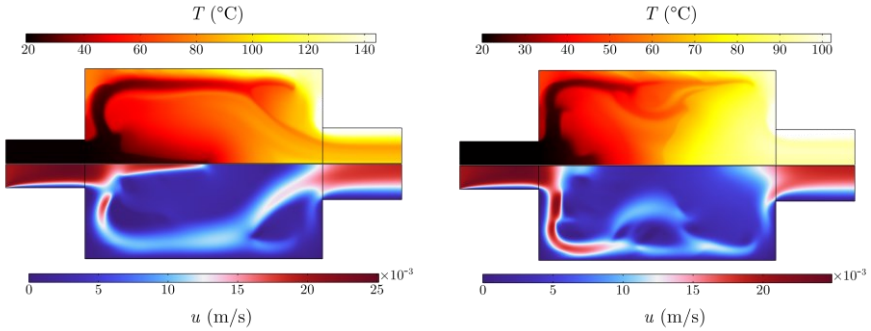

Fig. 8. 35. Temperature and velocity magnitude field with a Da = 10⁻⁴: left) 0.02 m/s and 0.5 Pa; right) 0.02 m/s and 1 Pa

The first impact is related to the smaller number of solid fins present in the optimized designs. Just three solid fins are realized in the optimized design in both cases. In the case with the pressure drop of 0.5 Pa, mainly only one large channel is realized, and through that, the fluid is carried to the upper right, where the highest temperatures are reached; this explains the much lower temperature recorded compared to the same case analysed in the previous section. The cooling of the lower zone is ensured by the presence of the porous material that ensures the flow of the cooler inside. About the case study with 1 Pa of pressure drop, the optimized design is still much different than the one showed for a higher *Da*. The optimized design shows mainly three "alveoli" with three little solid fins, and none in the right side of the design domain. Thermal performance for this run are not particularly improved when compared with the case study with 0.5 Pa of pressure drop, with a difference of 80 °C between inlet and outlet, that is the same achieved for the $Da = 10^{-3}$ case but with half the pressure drop allowed. A first look must be given to Tab. 8.14 to compare the current results with the ones already presented in Tab. 7 where simulations are referred to a one size order lower *Da*. Mainly the differences between results that share same boundary conditions but different Darcy values for T_{avg} are around 4.0 °C, whilst the differences on the T_{max} reached for 0.5 Pa is far higher, about 19 °C higher for the case developed for the higher *Da*.

Table 8. 14. MMTO results for $Da = 10^{-4}$

MMTO	*Da*	T_{max} (°C)	T_{avg} (°C)	u_{max} (m s^{-1})	u_{avg} (m s^{-1})	h_{MCHS} (kW m^{-2} K^{-1})
0.02 m/s - 0.5 Pa	10^{-4}	144.04	65.51	0.02439	0.0059	10.89
0.02 m/s - 1 Pa		102.09	58.53	0.02313	0.0061	12.98

0.02 m/s - 0.5 Pa	10^{-3}	163.49	68.68	0.02490	0.0059	5.14
0.02 m/s - 1 Pa		109.25	55.71	0.02380	0.0060	13.20

8.4.13. Discussion

Finally, it is possible to compare the performance obtained for baseline, TO and MMTO (for $Da = 10^{-3}$) designs, not only by observing parameters such as maximum and average temperatures but, also the h_{MCHS}, the pumping power (P_p) and the PEC, *i.e.,* performance evaluation criteria [243] (see Eq. (27)), sometimes also labelled as Figure Of Merit (FOM), in order to get an overview of the thermo-mechanical efficiency between the optimized and the baseline design.

$$PEC = \frac{(h_{avg,new} / h_{avg,baseline})}{(P_{p,new} / P_{p,baseline})^{1/3}} \tag{27}$$

Results are shown in Tab. 8.15, which collects the above data showing as the first significant finding that TO and MMTO increase the performance evaluation criteria (PEC) from 2 to 4 times, respectively, if compared with the baseline case. Overall, PEC increases as pressure drop and inlet velocity increase, except for the TO case with 3 Pa and 0.02 m/s of inlet velocity, due to the larger increase in pumping power with respect to h_{MCHS}. Moreover, the positive impact of MMTO is evident from the larger h_{MCHS} obtained by MMTO-optimized designs compared to those with basic TO, due to the presence of the metal foams that yield larger heat transfer efficiency benefits at the same pressure drop, thus improving the thermo-mechanical efficiency.

Table 8. 15. Comparison between TO, MMTO and baseline designs

Cases	Δp (Pa)	u_{in} (m s^{-1})	T_{max} (°C)	T_{avg} (°C)	h_{MCHS} (kWm^{-2} K^{-1})	P_p (W · 10^{-4})	PEC (-)
Baseline	3.18	0.02	187.17	106	7.28	7.6	1.00
TO	0.5	0.02	265.6	113.99	5.32	1.2	1.35
TO	1	0.02	176.86	79.85	8.33	2.4	1.68
TO	2	0.02	120.47	64.36	11.27	4.8	1.81
TO	3	0.02	103.19	61.2	12.14	7.2	1.70
TO	3	0.05	90.665	44.38	20.51	18	2.12

MMTO	0.5	0.02	163.49	68.68	10.27	1.2	2.61
MMTO	1	0.02	109.25	55.71	13.2	2.4	2.67
MMTO	3	0.05	58.07	33.28	37.66	18	3.89

Another relevant aspect here, especially with references to applications like aerospace engineering, is about the weight of the proposed device. Metal foams are lightweight materials made of a metallic matrix with numerous interconnected pores. These pores significantly reduce the overall weight of the material compared to solid metals. By incorporating metal foams into microchannel heat sinks, the overall weight can be significantly reduced. This weight reduction is especially advantageous in applications where weight is a critical factor, *e.g.,* aerospace, automotive, and portable electronics. In order to quantify the benefits derived from the MMTO, a final comparison on the percentage weight saving is here proposed. The evaluation is carried out referring to the weight of the solid portion in the design domain, without considering the weight of the baseplate and inlet/outlet channels. All cases are compared with the baseline, as reported in Fig. 8.36. In detail, the baseline case – with a 40% of solid material with respect to the entire domain volume – has a weight of 23.27 g. TO designs, having no porous material, and with a solid fraction equal to the baseline case – except for small variations due to convergence – deviate by a maximum of 2%. Conversely, as metal foams are introduced, a huge improvement in terms of weight saving can be observed. The MMTO solutions weigh from 4.05 to 4.88 g, thus lead to a weight reduction of 80 to 83 %.

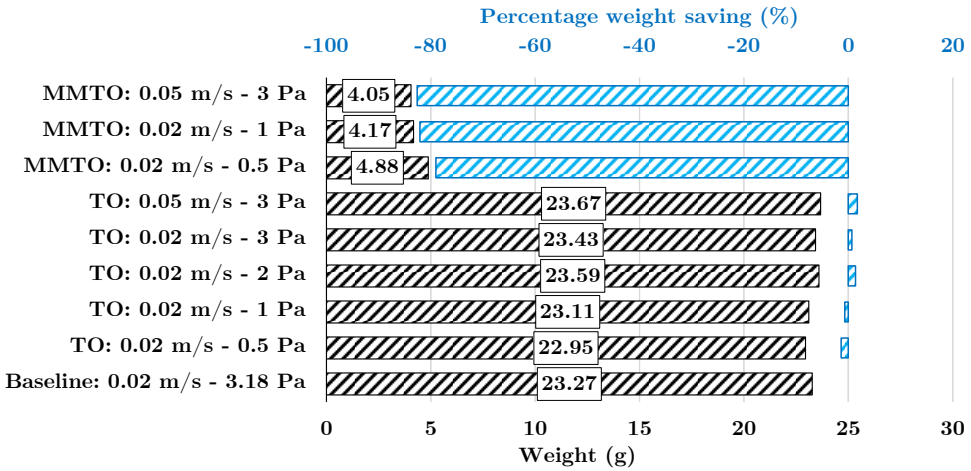

Fig. 8. 36. Evaluation of the weight of the solid portion in the design domain for baseline, TO and MMTO configurations: percentage weight savings (comparisons are done at equal solid fraction).

8.4.14. Manufacturability

Once the validity of the MMTO model has been evidenced and the achievable performance improvements have been evaluated, a final but essential issue needs to be clarified. The manufacture of topology-optimized designs including metal foams presents a challenge and – at the same time – crucial issue, which plays a fundamental role to take advantage of the performance improvements achievable with the application of this technique. Conventionally, TO-optimized devices can be realized through additive manufacturing (AM), *e.g.,* "force edging" technique, which enables to overcome limitations linked to traditional manufacturing processes. In detail, small air gaps that occur between the material layers – responsible for thermal contact resistances – can be substantially reduced with 3D printing techniques. As regards metal foams, this issue becomes even more relevant: if foams are manufactured separately – using traditional techniques – and then placed where TO final design predicts, contact thermal resistances between them and microchannel surfaces could cause a significant reduction in performance. For this reason, realizing metal foams also through AM ensures a closer correspondence between numerical performance and the one that could be obtained empirically. A sketch of the achievable microchannel design is reported in Fig. 8. 37.

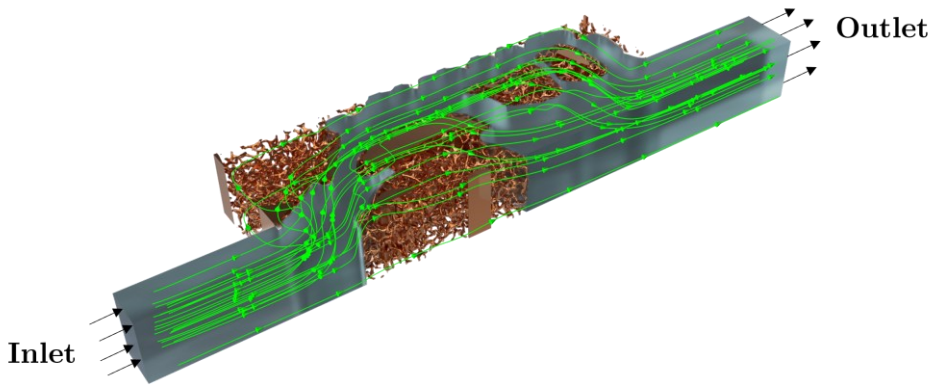

Fig. 8. 37. MMTO design of the MCHS combining topology optimization and metal foams

Recently, considerable efforts have been made to investigate new additive manufacturing techniques and methodologies for their production. Through the use of additive manufacturing techniques starting from tomography, three different lattice morphologies (rotated cube, Weaire-Phelan, and tetrakaidecahedron) were investigated to evaluate pressure drop and heat transfer coefficient (HTC) [221]. Du *et al.* [244] provided a solution for fabricating structures in porous ceramic material, but also usable for metal foams. It is based on the use of the "replica method," "X-ray computed tomography" and "3D printing". Firstly, the porous medium is scanned with an X-ray inspection system, then the 3D model is reconstructed with the commercial software "Mimics". In this way, the internal structure of the metal foam can be evaluated and replicated in a CAD file, its geometric characteristics can be also used to define the properties of the metal foam to perform simulations. Finally, the optimized design with metal foams can be precisely fabricated through the 3D printing technique based on the digital 3D model and local laser melting.

8.4.15. Final remarks

Microchannel heat sinks are widely used in a variety of industries, including large-electronic products like air conditioners and refrigerators, as well as small-electronic products like power devices and computer CPUs. The need of reducing size and weight of this device has raised concern about performance degradation, leading to the consequent need of the enhancement of thermal power dissipation density. The topology optimization (TO) method is a promising technique for proposing a novel and non-intuitive geometry that is not constrained by the baseline design. In this work, the formulation of a model capable of performing multi-material topology optimization of a MCHS is performed by introducing porous materials and in particular metal foams. To pursuit this target, a MCHS with metal foams has been validated to evaluate the numerical model and correlations validity used in MMTO runs. Results obtained by the MMTO for MCHS show huge improvements, confirming how the introduction of additional degrees of freedom, during optimization, yields further performance improvements. The main outcomes are here listed:

- To correctly consider the porosity of these materials and determine the pressure drop due to fluid crossing, the inverse permeability of the metal foam (a_{por}) is set based on the definition of permeability (K). MMTO supports SIMP interpolations for evaluating thermophysical properties of metal foam.

- Mesh independence analysis shows the high dependence of MMTO to minimum mesh size. Among the several grids investigated, the one with a minimum element size of 0.12 mm has been selected.
- TO runs have been validated against a reference work with satisfactory overlapping. By itself, TO provides a reduction of approximately 26 °C in terms of average temperature (T_{avg}), and 10 °C in terms of maximum temperature (T_{max}). Moreover, in the case of an inlet velocity of 0.02 m/s the maximum velocity inside the domain is up to 30% higher than the inlet velocity, and for an inlet velocity of 0.05 m/s the maximum is about 20% higher.
- When using the MMTO framework – embedding metal foams – the average temperature is about 45 °C lower and the maximum temperature about 100 °C lower than the case developed with TO for 0.02 m/s and 0.5 Pa pressure drop. To obtain the same result in terms of average temperature, it must be considered the case study for 2 Pa of pressure drop, which, however, leads to a much lower maximum temperature.
- The model verification of MMTO runs is performed against LTE model: the deviation in main performance, *i.e.,* T_{avg}, T_{max}, u_{avg}, and u_{max}, is limited when considering a Darcy number equal to 10^{-3}, while it becomes more important as the Darcy decreases.
- In general, the optimized designs based on TO and MMTO prove to significantly improve thermo-fluid dynamic performance compared to a baseline scenario. This improvement includes an 88% reduction in required pumping power while maintaining a fixed inlet velocity. Comparing the MMTO microchannel to the one designed through topology optimization, the PEC is enhanced by 59-84% across various pressure drop and inlet velocity conditions. Furthermore, the weight savings compared to the baseline case are estimated to be in the range of 80 to 83%.
- A final result regards the feasibility of the developed MCHS fabrication with metal foams. Such feasibility is provided by X-ray computed tomography and 3D printing techniques, already studied, and tested, which ensures the productivity of this MCHS and provides the possibility of empirical testing for evaluation and comparison of performance against the numerical model.

While simulation and modeling play a crucial role in optimizing microchannel heat sinks, experimental validation is essential to ensure the accuracy and reliability of the finally optimized designs. Comprehensive experimental studies on the

manufactured heat sinks can help bridge the gap between simulations and real-world performance to test such designed devices in real conditions. Future work is still needed, particularly to improve several important aspects of the TO, such as perform time-dependent studies to analyze the behavior of the optimized domain in time. Finally, a multi-objective TO should help to include a further indicator to control the trade-off between metal foam weight and solid thermal diffusivity.

Part IV: Conclusions

This thesis offers a comprehensive exploration of the critical role that numerical optimization methods play in the domain of heat transfer. Heat transfer is a fundamental aspect of thermal engineering and science, impacting the design and operation of numerous systems in our modern world. As heat transfer problems continue to grow in complexity, numerical tools have become indispensable for addressing the intricate challenges they pose. However, it is essential to recognize that heat transfer is not a one-size-fits-all domain; it encompasses a diverse spectrum of scenarios, each governed by distinct heat transfer mechanisms.

In this context, the choice of optimization method is crucial, and it must be tailored to the specific characteristics and constraints of each heat transfer problem. This thesis emphasizes the distinction between large-scale and small-scale systems, highlighting the preference for genetic algorithms (GAs) in large-scale systems and gradient-based methods, particularly topology optimization-based procedures, in small-scale systems. The decision to employ GAs in large-scale systems is pragmatic, as it sidesteps the computational burden associated with detailed computational fluid dynamics (CFD) simulations or complex numerical formulations. GAs excel in enhancing heat transfer efficiency, making them a suitable choice for large-scale heat transfer applications.

For instance, a proof of how effective GA for complex systems can be, is given by the optimization of a dual-pressure Heat Recovery Steam Generator (HRSG). Thanks to a global Sensitivity Analysis (SA) to select key design variables impacting cost minimization and power maximization, six design variables are chosen for optimization, and a multi-objective Genetic Algorithm (GA) is used to obtain the Pareto front. The results highlight the importance of reducing the gas-to-water mass flow rate ratio for increasing power output. The optimal design features a high-pressure economizer with a final volume of 60.7 m^3 and an HRSG volume of approximately 360 m^3. By limiting vertical development, the HRSG section length is increased, resulting in significant cost savings of around 20%. The study's objective was to combine heat exchanger modeling with a robust optimization methodology, offering potential for future developments.

However. the application of gradient-free algorithm is not only confined to large scale systems. When dealing with systems like latent heat thermal energy storage (LHTES), they can help to reach optimal solutions within quitting the CFD approach. As shown, with reference to the application of such technology to cold thermal storage, it was evident that the design of the storage system alone falls short in fully realizing the potential of Phase Change Materials (PCMs). The limited thermal diffusivity of PCM led to an ineffective discharge phase. To tackle this challenge, a comprehensive approach has been introduced, employing a multi-objective optimization methodology. Genetic algorithms (GAs) have played a crucial role in this framework, facilitating the efficient and precise determination of solutions. The system's performance is substantially enhanced through the integration of a finite element numerical model with MATLAB. By adjusting the chiller's operating conditions, optimal results are achieved, including specifying water flow rates and temperature reductions. Additionally, the optimization process reveals that up to 40% of the PCM's potential can be effectively utilized. Subsequent optimization stages further improve the system by decreasing the shell diameter and adopting specific tube configurations, ultimately exploiting 72% of the PCM's potential. This proposed methodology not only offers economic benefits through PCM amount optimization and a reduced system size but also delivers environmental benefits. It achieves this by saving primary energy demand through multi-objective optimization.

Furthermore, with reference to latent heat recovery and ventilation units that incorporate PCMs, the interactions between the PCM and the surrounding air become complex. These interactions involve heat transfer, phase changes, and fluid flow, which can be challenging to be modelled accurately. CFD allows for a detailed representation of these interactions, but it also increases model complexity. A GA can help optimize such complex models effectively.

On the other hand, small-scale systems demand precision and detail. In such cases, gradient-based techniques become feasible because of the limited degrees of freedom. Therefore, advanced design techniques, especially topology optimization, take the forefront. Topology optimization allows for intricate control over design parameters, enabling the optimization of fluid pathways and heat transfer surfaces with precision. This approach ensures that every aspect of the system is fine-tuned to achieve maximum heat transfer efficiency.

The thesis also highlights the design flexibility that gradient-based techniques, particularly topology optimization, offer. Researchers can explore innovative configurations and geometric patterns, optimizing not only for energy efficiency but also for innovative form factors and structural considerations. This level of design

flexibility is invaluable, particularly in small-scale systems where every element must be meticulously tuned for optimal performance. For instance, the use of topology optimization, including multi-material topology optimization with metal foams, demonstrates significant improvements in thermal performance and energy efficiency.

The role of Multi-Material Topology Optimization (MMTO) in the context of microchannel heat sinks (MCHS) is pivotal. MCHS are widely employed in various industries, from large electronic products to smaller ones such as power devices and computer CPUs. The demand for smaller and lighter MCHS has raised concerns about performance degradation, necessitating the enhancement of thermal power dissipation density. MMTO has been used to develop a model capable of performing multi-material topology optimization for MCHS by introducing porous materials, particularly metal foams. To achieve this goal, the model is validated using a MCHS with metal foams, assessing the numerical model and correlation validity for MMTO runs. The results obtained through MMTO demonstrate significant performance improvements, underlining the advantages of introducing additional degrees of freedom during optimization.

The study's key findings and outcomes encompass several significant aspects. Firstly, the research emphasizes the accurate consideration of metal foam porosity and the determination of pressure drop due to fluid flow. This is accomplished by setting the inverse permeability of the metal foam based on permeability (K), with the added support of SIMP interpolations in MMTO for evaluating thermophysical properties of metal foam. Furthermore, the research unveils the influence of minimum mesh size on MMTO through a thorough mesh independence analysis, ultimately leading to the selection of a specific grid configuration.

In addition, the study validates topology optimization (TO) runs against a reference work. These validations underscore the tangible benefits of TO in terms of temperature reductions and improved fluid velocity profiles. When the MMTO framework is employed in conjunction with metal foams, it yields substantial temperature reductions and enhances fluid dynamics. This translates into a noteworthy overall improvement in both performance and energy efficiency.

References

[1] A. Quarteroni, *Numerical Models for Differential Problems*. Milano: Springer Milan, 2014. doi: 10.1007/978-88-470-5522-3.

[2] M. N. Özişik, *Finite Difference Methods in Heat Transfer*. CRC Press, 2017. doi: 10.1201/9781315168784.

[3] J. N. Reddy, N. K. Anand, and P. Roy, *Finite Element and Finite Volume Methods for Heat Transfer and Fluid Dynamics*. Cambridge University Press, 2022. doi: 10.1017/9781009275453.

[4] L. M. Jiji, *Heat Conduction*. Berlin, Heidelberg: Springer Berlin Heidelberg, 2009. doi: 10.1007/978-3-642-01267-9.

[5] S. Ostrach, "Natural Convection in Enclosures," *J. Heat Transfer*, vol. 110, no. 4b, pp. 1175–1190, Nov. 1988, doi: 10.1115/1.3250619.

[6] P. Le Quéré, "Accurate solutions to the square thermally driven cavity at high Rayleigh number," *Comput. Fluids*, vol. 20, no. 1, pp. 29–41, Jan. 1991, doi: 10.1016/0045-7930(91)90025-D.

[7] O. Turan, R. J. Poole, and N. Chakraborty, "Influences of boundary conditions on laminar natural convection in rectangular enclosures with differentially heated side walls," *Int. J. Heat Fluid Flow*, vol. 33, no. 1, pp. 131–146, Feb. 2012, doi: 10.1016/j.ijheatfluidflow.2011.10.009.

[8] Y. K. Wu and M. Lacroix, "Melting of a PCM inside a vertical cylindrical capsule," *Int. J. Numer. Methods Fluids*, vol. 20, no. 6, pp. 559–572, Mar. 1995, doi: 10.1002/fld.1650200610.

[9] Y. Cao and A. Faghri, "Performance characteristics of a thermal energy storage module: a transient PCM/forced convection conjugate analysis," *Int. J. Heat Mass Transf.*, vol. 34, no. 1, pp. 93–101, 1991, doi: 10.1016/0017-9310(91)90177-G.

[10] D. González-Peña, I. Alonso-deMiguel, M. Díez-Mediavilla, and C. Alonso-Tristán, "Experimental analysis of a novel PV/T panel with PCM and heat pipes," *Sustain.*, vol. 12, no. 5, 2020, doi: 10.3390/su12051710.

[11] S. Moench and R. Dittrich, "Influence of Natural Convection and Volume Change on Numerical Simulation of Phase Change Materials for Latent Heat Storage," *Energies*, vol. 15, no. 8, p. 2746, Apr. 2022, doi: 10.3390/en15082746.

[12] M. K. Soni, N. Tamar, and S. Bhattacharyya, "Numerical simulation and parametric analysis of latent heat thermal energy storage system," *J. Therm. Anal. Calorim.*, vol. 141, no. 6, pp. 2511–2526, Sep. 2020, doi: 10.1007/s10973-020-10175-2.

[13] A. Fragnito, N. Bianco, M. Iasiello, G. M. Mauro, and L. Mongibello, "Experimental and numerical analysis of a phase change material-based shell-and-tube heat exchanger for cold thermal energy storage," *J. Energy Storage*, vol. 56, no. PA, p. 105975, 2022, doi: 10.1016/j.est.2022.105975.

[14] L. . Cabeza and H. Mehling, *Heat and cold storage with PCM. An up to date introduction into basics and applications - Publisher:Springer; ISBN:978-3-540-68557-9.* 2008. [Online]. Available: http://www.springer.com/us/book/9783540685562

[15] L. Que *et al.*, "Numerical simulation and experimental research progress of phase change hysteresis: A review," *Energy Build.*, vol. 253, p. 111402, 2021, doi: 10.1016/j.enbuild.2021.111402.

[16] I. Shamseddine, F. Pennec, P. Biwole, and F. Fardoun, "Supercooling of phase change materials:

A review," *Renew. Sustain. Energy Rev.*, vol. 158, no. January, p. 112172, 2022, doi: 10.1016/j.rser.2022.112172.

[17] K. Biswas, Y. Shukla, A. Desjarlais, and R. Rawal, "Thermal characterization of full-scale PCM products and numerical simulations, including hysteresis, to evaluate energy impacts in an envelope application," *Appl. Therm. Eng.*, vol. 138, pp. 501–512, Jun. 2018, doi: 10.1016/j.applthermaleng.2018.04.090.

[18] Y. Hu, R. Guo, P. K. Heiselberg, and H. Johra, "Modeling PCM Phase Change Temperature and Hysteresis in Ventilation Cooling and Heating Applications," *Energies*, vol. 13, no. 23, p. 6455, Dec. 2020, doi: 10.3390/en13236455.

[19] F. Kuznik and J. Virgone, "Experimental investigation of wallboard containing phase change material: Data for validation of numerical modeling," *Energy Build.*, vol. 41, no. 5, pp. 561–570, May 2009, doi: 10.1016/j.enbuild.2008.11.022.

[20] T. Barz and A. Sommer, "Modeling hysteresis in the phase transition of industrial-grade solid/liquid PCM for thermal energy storages," *Int. J. Heat Mass Transf.*, vol. 127, pp. 701–713, Dec. 2018, doi: 10.1016/j.ijheatmasstransfer.2018.08.032.

[21] E. Günther, L. Huang, H. Mehling, and C. Dötsch, "Subcooling in PCM emulsions - Part 2: Interpretation in terms of nucleation theory," *Thermochim. Acta*, vol. 522, no. 1–2, pp. 199–204, 2011, doi: 10.1016/j.tca.2011.04.027.

[22] R. A. Taylor, N. Tsafnat, and A. Washer, "Experimental characterisation of sub-cooling in hydrated salt phase change materials," *Appl. Therm. Eng.*, vol. 93, pp. 935–938, 2016, doi: 10.1016/j.applthermaleng.2015.10.032.

[23] M. Azad, D. Groulx, and A. Donaldson, "Natural convection onset during melting of phase change materials: Part I – Effects of the geometry, Stefan number, and degree of subcooling," *Int. J. Therm. Sci.*, vol. 170, no. July, p. 107180, 2021, doi: 10.1016/j.ijthermalsci.2021.107180.

[24] M. P. Vikram, V. Kumaresan, S. Christopher, and R. Velraj, "Experimental studies on solidification and subcooling characteristics of water-based phase change material (PCM) in a spherical encapsulation for cool thermal energy storage applications," *Int. J. Refrig.*, vol. 100, pp. 454–462, 2019, doi: 10.1016/j.ijrefrig.2018.11.025.

[25] M. Faucheux, G. Muller, M. Havet, and A. LeBail, "Influence of surface roughness on the supercooling degree: Case of selected water/ethanol solutions frozen on aluminium surfaces," *Int. J. Refrig.*, vol. 29, no. 7, pp. 1218–1224, 2006, doi: 10.1016/j.ijrefrig.2006.01.002.

[26] A. Ribezzo, G. Falciani, L. Bergamasco, M. Fasano, and E. Chiavazzo, "An overview on the use of additives and preparation procedure in phase change materials for thermal energy storage with a focus on long term applications," *J. Energy Storage*, vol. 53, no. April, p. 105140, 2022, doi: 10.1016/j.est.2022.105140.

[27] M. Thonon, G. Fraisse, L. Zalewski, and M. Pailha, "Analytical modelling of PCM supercooling including recalescence for complete and partial heating/cooling cycles," *Appl. Therm. Eng.*, vol. 190, no. October 2020, p. 116751, 2021, doi: 10.1016/j.applthermaleng.2021.116751.

[28] J. Bony and S. Citherlet, "Numerical model and experimental validation of heat storage with phase change materials," *Energy Build.*, vol. 39, no. 10, pp. 1065–1072, 2007, doi: 10.1016/j.enbuild.2006.10.017.

[29] E. Günther, H. Mehling, and S. Hiebler, "Modeling of subcooling and solidification of phase change materials," *Model. Simul. Mater. Sci. Eng.*, vol. 15, no. 8, pp. 879–892, 2007, doi: 10.1088/0965-0393/15/8/005.

[30] A. Y. Uzan, Y. Kozak, Y. Korin, I. Harary, H. Mehling, and G. Ziskind, "A novel multi-dimensional model for solidification process with supercooling," *Int. J. Heat Mass Transf.*, vol. 106, pp. 91–102, 2017, doi: 10.1016/j.ijheatmasstransfer.2016.10.046.

[31] X. Jin *et al.*, "A new heat transfer model of phase change material based on energy asymmetry," *Appl. Energy*, vol. 212, no. 2, pp. 1409–1416, 2018, doi: 10.1016/j.apenergy.2017.12.103.

[32] T. Davin, B. Lefez, and A. Guillet, "Supercooling of phase change: A new modeling formulation using apparent specific heat capacity," *Int. J. Therm. Sci.*, vol. 147, no. September 2019, p. 106121, 2020, doi: 10.1016/j.ijthermalsci.2019.106121.

[33] X. Jin, H. Hu, X. Shi, and X. Zhang, "Energy asymmetry in melting and solidifying processes of PCM," *Energy Convers. Manag.*, vol. 106, pp. 608–614, 2015, doi: 10.1016/j.enconman.2015.10.001.

[34] A. Bejan, *Convection Heat Transfer*. Wiley, 2013. doi: 10.1002/9781118671627.

[35] Y. Dutil, D. R. Rousse, N. Ben Salah, S. Lassue, and L. Zalewski, "A review on phase-change materials: Mathematical modeling and simulations," *Renew. Sustain. Energy Rev.*, vol. 15, no. 1, pp. 112–130, Jan. 2011, doi: 10.1016/j.rser.2010.06.011.

[36] C. Bellecci and M. Conti, "Phase change thermal storage: transient behaviour analysis of a solar receiver/storage module using the enthalpy method," *Int. J. Heat Mass Transf.*, vol. 36, no. 8, pp. 2157–2163, Jan. 1993, doi: 10.1016/S0017-9310(05)80146-2.

[37] A. D. Brent, V. R. Voller, and K. J. Reid, "Enthalpy-porosity technique for modeling convection-diffusion phase change: Application to the melting of a pure metal," *Numer. Heat Transf.*, vol. 13, no. 3, 1988, doi: 10.1080/10407788808913615.

[38] R. T. Tenchev, J. A. Mackenzie, T. J. Scanlon, and M. T. Stickland, "Finite element moving mesh analysis of phase change problems with natural convection," *Int. J. Heat Fluid Flow*, vol. 26, no. 4 SPEC. ISS., pp. 597–612, 2005, doi: 10.1016/j.ijheatfluidflow.2005.03.003.

[39] M. Faden, A. König-Haagen, S. Höhlein, and D. Brüggemann, "An implicit algorithm for melting and settling of phase change material inside macrocapsules," *Int. J. Heat Mass Transf.*, vol. 117, pp. 757–767, Feb. 2018, doi: 10.1016/j.ijheatmasstransfer.2017.10.033.

[40] N. Hannoun, V. Alexiades, and T. Z. Mai, "A reference solution for phase change with convection," *Int. J. Numer. Methods Fluids*, vol. 48, no. 11, pp. 1283–1308, 2005, doi: 10.1002/fld.979.

[41] M. Iasiello, M. Mameli, S. Filippeschi, and N. Bianco, "Metal foam/PCM melting evolution analysis: Orientation and morphology effects," *Appl. Therm. Eng.*, vol. 187, no. September 2020, p. 116572, 2021, doi: 10.1016/j.applthermaleng.2021.116572.

[42] M. Caliano, N. Bianco, G. Graditi, and L. Mongibello, "Analysis of a phase change material-based unit and of an aluminum foam/phase change material composite-based unit for cold thermal energy storage by numerical simulation," *Appl. Energy*, vol. 256, no. February, p. 113921, 2019, doi: 10.1016/j.apenergy.2019.113921.

[43] F. Samara, D. Groulx, and P. H. Biwole, "Natural Convection Driven Melting of Phase Change Material: Comparison of Two Methods," *COMSOL Conf.*, pp. 1–8, 2012.

[44] A. C. Kheirabadi and D. Groulx, "THE EFFECT OF THE MUSHY-ZONE CONSTANT ON SIMULATED PHASE CHANGE HEAT TRANSFER," 2015. doi: 10.1615/ichmt.2015.intsympadvcomputheattransf.460.

[45] B. Kamkari and D. Groulx, "Experimental investigation of melting behaviour of phase change material in finned rectangular enclosures under different inclination angles," *Exp. Therm. Fluid Sci.*, vol. 97, pp. 94–108, Oct. 2018, doi: 10.1016/j.expthermflusci.2018.04.007.

[46] A. C. Kheirabadi and D. Groulx, "THE EFFECT OF THE MUSHY-ZONE CONSTANT ON SIMULATED PHASE CHANGE HEAT TRANSFER," in *Proceeding of Proceedings of CHT-15. 6th International Symposium on ADVANCES IN COMPUTATIONAL HEAT TRANSFER , May 25-29, 2015, Rutgers University, New Brunswick, NJ, USA*, 2015, p. 22. doi: 10.1615/ICHMT.2015.IntSympAdvComputHeatTransf.460.

[47] M. Zeneli, A. Nikolopoulos, S. Karellas, and N. Nikolopoulos, "Numerical methods for solid-liquid phase-change problems," in *Ultra-High Temperature Thermal Energy Storage, Transfer*

and Conversion, Elsevier, 2021, pp. 165–199. doi: 10.1016/B978-0-12-819955-8.00007-7.

[48] J. R. R. A. Martins and A. Ning, *Engineering Design Optimization*. Cambridge University Press, 2021. doi: 10.1017/9781108980647.

[49] F. J. Solis and R. J.-B. Wets, "Minimization by Random Search Techniques," *Math. Oper. Res.*, vol. 6, no. 1, pp. 19–30, Feb. 1981, doi: 10.1287/moor.6.1.19.

[50] F. Gao and L. Han, "Implementing the Nelder-Mead simplex algorithm with adaptive parameters," *Comput. Optim. Appl.*, vol. 51, no. 1, pp. 259–277, Jan. 2012, doi: 10.1007/s10589-010-9329-3.

[51] P. J. M. van Laarhoven and E. H. L. Aarts, "Simulated annealing," in *Simulated Annealing: Theory and Applications*, Dordrecht: Springer Netherlands, 1987, pp. 7–15. doi: 10.1007/978-94-015-7744-1_2.

[52] M. Srinivas and L. M. Patnaik, "Genetic algorithms: a survey," *Computer (Long. Beach. Calif).*, vol. 27, no. 6, pp. 17–26, Jun. 1994, doi: 10.1109/2.294849.

[53] Y. Zhang, S. Wang, and G. Ji, "A Comprehensive Survey on Particle Swarm Optimization Algorithm and Its Applications," *Math. Probl. Eng.*, vol. 2015, pp. 1–38, 2015, doi: 10.1155/2015/931256.

[54] M. Pelikan, "Hierarchical Bayesian Optimization Algorithm," 2005, pp. 105–129. doi: 10.1007/978-3-540-32373-0_6.

[55] O. Sigmund, "On the usefulness of non-gradient approaches in topology optimization," *Struct. Multidiscip. Optim.*, vol. 43, no. 5, pp. 589–596, May 2011, doi: 10.1007/s00158-011-0638-7.

[56] W. W. Hager and H. Zhang, "A New Conjugate Gradient Method with Guaranteed Descent and an Efficient Line Search," *SIAM J. Optim.*, vol. 16, no. 1, pp. 170–192, Jan. 2005, doi: 10.1137/030601880.

[57] M. P. Bendsøe and O. Sigmund, *Topology Optimization*. Berlin, Heidelberg: Springer Berlin Heidelberg, 2004. doi: 10.1007/978-3-662-05086-6.

[58] M. P. Bendsøe and N. Kikuchi, "Generating optimal topologies in structural design using a homogenization method," *Comput. Methods Appl. Mech. Eng.*, vol. 71, no. 2, pp. 197–224, Nov. 1988, doi: 10.1016/0045-7825(88)90086-2.

[59] O. Sigmund and S. Torquato, "Design of smart composite materials using topology optimization," *Smart Mater. Struct.*, vol. 8, no. 3, pp. 365–379, Jun. 1999, doi: 10.1088/0964-1726/8/3/308.

[60] S. Ozguc, L. Pan, and J. A. Weibel, "Topology optimization of microchannel heat sinks using a homogenization approach," *Int. J. Heat Mass Transf.*, vol. 169, p. 120896, 2021, doi: 10.1016/j.ijheatmasstransfer.2020.120896.

[61] M. P. Bendsøe and O. Sigmund, "Material interpolation schemes in topology optimization," *Arch. Appl. Mech. (Ingenieur Arch.*, vol. 69, no. 9–10, pp. 635–654, Nov. 1999, doi: 10.1007/s004190050248.

[62] T. Dbouk, "A review about the engineering design of optimal heat transfer systems using topology optimization," *Appl. Therm. Eng.*, vol. 112, pp. 841–854, Feb. 2017, doi: 10.1016/j.applthermaleng.2016.10.134.

[63] O. Sigmund and J. Petersson, "Numerical instabilities in topology optimization: A survey on procedures dealing with checkerboards, mesh-dependencies and local minima," *Struct. Optim.*, vol. 16, no. 1, pp. 68–75, 1998, doi: 10.1007/BF01214002.

[64] L. C. Høghøj, D. R. Nørhave, J. Alexandersen, O. Sigmund, and C. S. Andreasen, "Topology optimization of two fluid heat exchangers," *Int. J. Heat Mass Transf.*, vol. 163, p. 120543, 2020, doi: 10.1016/j.ijheatmasstransfer.2020.120543.

[65] J. Alexandersen and C. S. Andreasen, "A review of topology optimisation for fluid-based

problems," *Fluids*, vol. 5, no. 1, pp. 1–32, 2020, doi: 10.3390/fluids5010029.

[66] J. Alexandersen, N. Aage, C. S. Andreasen, and O. Sigmund, "Topology optimisation for natural convection problems," *Int. J. Numer. Methods Fluids*, vol. 76, no. 10, pp. 699–721, Dec. 2014, doi: 10.1002/fld.3954.

[67] F. Wang, B. S. Lazarov, and O. Sigmund, "On projection methods, convergence and robust formulations in topology optimization," *Struct. Multidiscip. Optim.*, vol. 43, no. 6, pp. 767–784, 2011, doi: 10.1007/s00158-010-0602-y.

[68] X. Qian and O. Sigmund, "Topological design of electromechanical actuators with robustness toward over- and under-etching," *Comput. Methods Appl. Mech. Eng.*, vol. 253, pp. 237–251, 2013, doi: 10.1016/j.cma.2012.08.020.

[69] M. Zhou, B. S. Lazarov, F. Wang, and O. Sigmund, "Minimum length scale in topology optimization by geometric constraints," *Comput. Methods Appl. Mech. Eng.*, vol. 293, pp. 266–282, 2015, doi: 10.1016/j.cma.2015.05.003.

[70] X. Qian, "Undercut and overhang angle control in topology optimization: A density gradient based integral approach," *Int. J. Numer. Methods Eng.*, vol. 111, no. 3, pp. 247–272, 2017, doi: 10.1002/nme.5461.

[71] Y. Luo, O. Sigmund, Q. Li, and S. Liu, "Additive manufacturing oriented topology optimization of structures with self-supported enclosed voids," *Comput. Methods Appl. Mech. Eng.*, vol. 372, 2020, doi: 10.1016/j.cma.2020.113385.

[72] "COMSOL Multiphysics® v. 5.6. www.comsol.com. COMSOL AB, Stockholm, Sweden."

[73] D. Asprone, F. Auricchio, C. Menna, and V. Mercuri, "3D printing of reinforced concrete elements: Technology and design approach," *Constr. Build. Mater.*, vol. 165, pp. 218–231, 2018, doi: 10.1016/j.conbuildmat.2018.01.018.

[74] A. Franco, M. Shaker, D. Kalubi, and S. Hostettler, "A review of sustainable energy access and technologies for healthcare facilities in the Global South," *Sustain. Energy Technol. Assessments*, vol. 22, pp. 92–105, Aug. 2017, doi: 10.1016/j.seta.2017.02.022.

[75] K. M. Powell *et al.*, "Thermal energy storage to minimize cost and improve efficiency of a polygeneration district energy system in a real-time electricity market," *Energy*, vol. 113, pp. 52–63, Oct. 2016, doi: 10.1016/j.energy.2016.07.009.

[76] A. Ganjehkaviri, M. N. Mohd Jaafar, P. Ahmadi, and H. Barzegaravval, "Modelling and optimization of combined cycle power plant based on exergoeconomic and environmental analyses," *Appl. Therm. Eng.*, vol. 67, no. 1–2, pp. 566–578, Jun. 2014, doi: 10.1016/j.applthermaleng.2014.03.018.

[77] Z. Aminov, N. Nakagoshi, T. D. Xuan, O. Higashi, and K. Alikulov, "Evaluation of the energy efficiency of combined cycle gas turbine. Case study of Tashkent thermal power plant, Uzbekistan," *Appl. Therm. Eng.*, vol. 103, pp. 501–509, Jun. 2016, doi: 10.1016/j.applthermaleng.2016.03.158.

[78] "MATLAB version 9.10.0.1613233 (R2021a)." The Mathworks, Inc., Natick, Massachusetts. [Online]. Available: https://it.mathworks.com/

[79] V. Ganapathy, *Industrial Boilers and Heat Recovery Steam Generators: Design, Applications, and Calculations*. CRC Press, 2002. [Online]. Available: https://books.google.it/books?id=K8Ucuj-Mx-oC

[80] F. P. I. D. P. D. A. S. L. Theodore L. Bergman, *Fundamentals of Heat and Mass Transfer*. 2011.

[81] H. Martin, "The generalized Lévêque equation and its practical use for the prediction of heat and mass transfer rates from pressure drop," *Chem. Eng. Sci.*, vol. 57, no. 16, pp. 3217–3223, Aug. 2002, doi: 10.1016/S0009-2509(02)00194-X.

[82] A. G. McDonald and H. L. Magande, *Fundamentals of Heat Exchanger Design*. 2012. doi: 10.1002/9781118403198.ch4.

[83] R. K. Shah and D. P. Sekulic, *Fundamentals of Heat Exchanger Design*. Wiley, 2003. [Online]. Available: https://books.google.it/books?id=beSXNAZblWQC

[84] K. Deb, *Multi-Objective Optimization using Evolutionary Algorithms*. Wiley, 2001. [Online]. Available: https://books.google.it/books?id=OSTn4GSy2uQC

[85] M. Mehrgoo and M. Amidpour, "Constructal design and optimization of a dual pressure heat recovery steam generator," *Energy*, vol. 124, pp. 87–99, Apr. 2017, doi: 10.1016/j.energy.2017.02.046.

[86] J. C. Helton, J. D. Johnson, C. J. Sallaberry, and C. B. Storlie, "Survey of sampling-based methods for uncertainty and sensitivity analysis," *Reliab. Eng. Syst. Saf.*, vol. 91, no. 10–11, pp. 1175–1209, Oct. 2006, doi: 10.1016/j.ress.2005.11.017.

[87] R. Jin, W. Chen, and T. W. Simpson, "Comparative studies of metamodelling techniques under multiple modelling criteria," *Struct. Multidiscip. Optim.*, vol. 23, no. 1, pp. 1–13, Dec. 2001, doi: 10.1007/s00158-001-0160-4.

[88] T. Deng, Y. Ran, Y. Yin, and P. Liu, "Multi-objective optimization design of thermal management system for lithium-ion battery pack based on Non-dominated Sorting Genetic Algorithm II," *Appl. Therm. Eng.*, vol. 164, p. 114394, Jan. 2020, doi: 10.1016/j.applthermaleng.2019.114394.

[89] A. Saltelli *et al.*, *Global Sensitivity Analysis: The Primer*. Wiley, 2008. [Online]. Available: https://books.google.it/books?id=wAssmt2vumgC

[90] C. Casarosa, "Thermoeconomic optimization of heat recovery steam generators operating parameters for combined plants," *Energy*, vol. 29, no. 3, pp. 389–414, Mar. 2004, doi: 10.1016/S0360-5442(02)00078-6.

[91] I. Dinçer, M. A. Rosen, and P. Ahmadi, *Optimization of Energy Systems*. Wiley, 2017. [Online]. Available: https://books.google.it/books?id=UD_CDgAAQBAJ

[92] I. Dinçer, M. A. Rosen, and P. Ahmadi, *Optimization of Energy Systems*. Wiley, 2017.

[93] F. Samanipour and J. Jelovica, "Adaptive repair method for constraint handling in multi-objective genetic algorithm based on relationship between constraints and variables," *Appl. Soft Comput.*, vol. 90, p. 106143, May 2020, doi: 10.1016/j.asoc.2020.106143.

[94] M. D. Durán, M. Valdés, A. Rovira, and E. Rincón, "A methodology for the geometric design of heat recovery steam generators applying genetic algorithms," *Appl. Therm. Eng.*, vol. 52, no. 1, pp. 77–83, Apr. 2013, doi: 10.1016/j.applthermaleng.2012.10.041.

[95] R. Long, B. Li, Z. Liu, and W. Liu, "Reverse electrodialysis: Modelling and performance analysis based on multi-objective optimization," *Energy*, vol. 151, pp. 1–10, May 2018, doi: 10.1016/j.energy.2018.03.003.

[96] K. M. Powell, W. J. Cole, U. F. Ekarika, and T. F. Edgar, "Optimal chiller loading in a district cooling system with thermal energy storage," *Energy*, vol. 50, no. 1, pp. 445–453, 2013, doi: 10.1016/j.energy.2012.10.058.

[97] S. Mazzoni, J. Y. Sze, B. Nastasi, S. Ooi, U. Desideri, and A. Romagnoli, "A techno-economic assessment on the adoption of latent heat thermal energy storage systems for district cooling optimal dispatch & operations," *Appl. Energy*, vol. 289, no. March, p. 116646, 2021, doi: 10.1016/j.apenergy.2021.116646.

[98] D. Rodríguez, G. Bejarano, M. Vargas, J. M. Lemos, and M. G. Ortega, "Modelling and cooling power control of a TES-backed-up vapour-compression refrigeration system," *Appl. Therm. Eng.*, vol. 164, no. October 2019, p. 114415, 2020, doi: 10.1016/j.applthermaleng.2019.114415.

[99] Y. H. Yau and B. Rismanchi, "A review on cool thermal storage technologies and operating strategies," *Renew. Sustain. Energy Rev.*, vol. 16, no. 1, pp. 787–797, 2012, doi: 10.1016/j.rser.2011.09.004.

[100] A. Mammoli and M. Robinson, "Numerical analysis of heat transfer processes in a low-cost, high-performance ice storage device for residential applications," *Appl. Therm. Eng.*, vol. 128, pp. 453–463, 2018, doi: 10.1016/j.applthermaleng.2017.09.043.

[101] Harald Mehling; Luisa F. Cabeza, *Heat and cold storage with PCM*, vol. 11, no. 3. 2000.

[102] "Handbook of air conditioning and refrigeration," *Choice Rev. Online*, vol. 32, no. 02, 1994, doi: 10.5860/choice.32-0959.

[103] O. S. Elsanusi and E. C. Nsofor, "Melting of multiple PCMs with different arrangements inside a heat exchanger for energy storage," *Appl. Therm. Eng.*, vol. 185, Feb. 2021, doi: 10.1016/j.applthermaleng.2020.116046.

[104] P. Wang, X. Wang, Y. Huang, C. Li, Z. Peng, and Y. Ding, "Thermal energy charging behaviour of a heat exchange device with a zigzag plate configuration containing multi-phase-change-materials (m-PCMs)," *Appl. Energy*, vol. 142, pp. 328–336, Mar. 2015, doi: 10.1016/j.apenergy.2014.12.050.

[105] L. Mongibello, N. Bianco, M. Caliano, and G. Graditi, "Influence of heat dumping on the operation of residential micro-CHP systems," *Appl. Energy*, vol. 160, pp. 206–220, 2015, doi: 10.1016/j.apenergy.2015.09.045.

[106] DPR, *Decree DPR 412/93*. 1993.

[107] M. Fabbri and V. R. Voller, "The phase-field method in the sharp-interface limit: A comparison between model potentials," *J. Comput. Phys.*, vol. 130, no. 2, pp. 256–265, 1997, doi: 10.1006/jcph.1996.5585.

[108] V. V. R. & P. C., "A Fixed grid numerical modelling methodology for convection diffusion mushy region phase change problems," *Int. Jounal Heat Mass Transf.*, vol. 30, no. 8, pp. 1709–1719, 1978.

[109] E. M. Sparrow, S. V. Patankar, and S. Ramadhyani, "Analysis of melting in the presence of natural convection in the melt region," *J. Heat Transfer*, vol. 99, no. 4, pp. 520–526, 1977, doi: 10.1115/1.3450736.

[110] ISO, "ISO 11357-1:2016 Plastics — Differential scanning calorimetry - General Principles," *Int. Stand.*, vol. 2016, pp. 1–33, 2016.

[111] T. Cebeci, "LAMINAR-FREE-CONVECTIVE-HEAT TRANSFER FROM THE OUTER SURFACE OF A VERTICAL SLENDER CIRCULAR CYLINDER.," 1974. doi: 10.1615/ihtc5.2830.

[112] COMSOL Multiphysics, "Comsol Multiphysics Reference Manual: Version 5," *Manual*, 2014.

[113] C. T. Kelley, *Solving Nonlinear Equations with Newton's Method*. 2003. doi: 10.1137/1.9780898718898.

[114] I. B. Celik, U. Ghia, P. J. Roache, C. J. Freitas, H. Coleman, and P. E. Raad, "Procedure for estimation and reporting of uncertainty due to discretization in CFD applications," *J. Fluids Eng. Trans. ASME*, vol. 130, no. 7, 2008, doi: 10.1115/1.2960953.

[115] A. H. Mosaffa, F. Talati, H. Basirat Tabrizi, and M. A. Rosen, "Analytical modeling of PCM solidification in a shell and tube finned thermal storage for air conditioning systems," *Energy Build.*, vol. 49, pp. 356–361, Jun. 2012, doi: 10.1016/j.enbuild.2012.02.053.

[116] W.-W. Wang, K. Zhang, L.-B. Wang, and Y.-L. He, "Numerical study of the heat charging and discharging characteristics of a shell-and-tube phase change heat storage unit," *Appl. Therm. Eng.*, vol. 58, no. 1–2, pp. 542–553, Sep. 2013, doi: 10.1016/j.applthermaleng.2013.04.063.

[117] D. Zhao and G. Tan, "Numerical analysis of a shell-and-tube latent heat storage unit with fins for air-conditioning application," *Appl. Energy*, vol. 138, pp. 381–392, Jan. 2015, doi: 10.1016/j.apenergy.2014.10.051.

[118] M. J. Hosseini, M. Rahimi, and R. Bahrampoury, "Experimental and computational evolution of a shell and tube heat exchanger as a PCM thermal storage system," *Int. Commun. Heat*

Mass Transf., vol. 50, pp. 128–136, Jan. 2014, doi: 10.1016/j.icheatmasstransfer.2013.11.008.

[119] M. A. Dekhil, J. V. Simo Tala, O. Bulliard-Sauret, and D. Bougeard, "Numerical analysis of the performance enhancement of a latent heat storage shell and tube unit using finned tubes during melting and solidification," *Appl. Therm. Eng.*, vol. 192, p. 116866, Jun. 2021, doi: 10.1016/j.applthermaleng.2021.116866.

[120] N. A. M. Amin, M. Belusko, F. Bruno, and M. Liu, "Optimising PCM thermal storage systems for maximum energy storage effectiveness," *Sol. Energy*, vol. 86, no. 9, pp. 2263–2272, Sep. 2012, doi: 10.1016/j.solener.2012.04.020.

[121] W.-W. Wang, L.-B. Wang, and Y.-L. He, "The energy efficiency ratio of heat storage in one shell-and-one tube phase change thermal energy storage unit," *Appl. Energy*, vol. 138, pp. 169–182, Jan. 2015, doi: 10.1016/j.apenergy.2014.10.064.

[122] J. Gasia, N. H. S. Tay, M. Belusko, L. F. Cabeza, and F. Bruno, "Experimental investigation of the effect of dynamic melting in a cylindrical shell-and-tube heat exchanger using water as PCM," *Appl. Energy*, vol. 185, pp. 136–145, Jan. 2017, doi: 10.1016/j.apenergy.2016.10.042.

[123] M. Esapour, A. Hamzehnezhad, A. A. Rabienataj Darzi, and M. Jourabian, "Melting and solidification of PCM embedded in porous metal foam in horizontal multi-tube heat storage system," *Energy Convers. Manag.*, vol. 171, no. January, pp. 398–410, 2018, doi: 10.1016/j.enconman.2018.05.086.

[124] M. Esapour, M. J. Hosseini, A. A. Ranjbar, Y. Pahamli, and R. Bahrampoury, "Phase change in multi-tube heat exchangers," *Renew. Energy*, vol. 85, pp. 1017–1025, 2016, doi: 10.1016/j.renene.2015.07.063.

[125] A. H. N. Al-Mudhafar, A. F. Nowakowski, and F. C. G. A. Nicolleau, "Enhancing the thermal performance of PCM in a shell and tube latent heat energy storage system by utilizing innovative fins," *Energy Reports*, vol. 7, pp. 120–126, May 2021, doi: 10.1016/j.egyr.2021.02.034.

[126] R. Anish, V. Mariappan, S. Suresh, M. M. Joybari, and A. M. Abdulateef, "Experimental investigation on the energy storage/discharge performance of xylitol in a compact spiral coil heat exchanger," *Int. J. Therm. Sci.*, vol. 159, no. September 2020, p. 106633, 2021, doi: 10.1016/j.ijthermalsci.2020.106633.

[127] A. Pizzolato, A. Sharma, K. Maute, A. Sciacovelli, and V. Verda, "Design of effective fins for fast PCM melting and solidification in shell-and-tube latent heat thermal energy storage through topology optimization," *Appl. Energy*, vol. 208, pp. 210–227, Dec. 2017, doi: 10.1016/j.apenergy.2017.10.050.

[128] A. Pizzolato, A. Sharma, R. Ge, K. Maute, V. Verda, and A. Sciacovelli, "Maximization of performance in multi-tube latent heat storage – Optimization of fins topology, effect of materials selection and flow arrangements," *Energy*, vol. 203, p. 114797, Jul. 2020, doi: 10.1016/j.energy.2019.02.155.

[129] H. Liang, J. Niu, and Y. Gan, "Performance optimization for shell-and-tube PCM thermal energy storage," *J. Energy Storage*, vol. 30, p. 101421, Aug. 2020, doi: 10.1016/j.est.2020.101421.

[130] H. Shamsi, M. Boroushaki, and H. Geraei, "Performance evaluation and optimization of encapsulated cascade PCM thermal storage," *J. Energy Storage*, vol. 11, pp. 64–75, 2017, doi: 10.1016/j.est.2017.02.003.

[131] S. Sridharan, R. Srikanth, and C. Balaji, "Multi objective geometric optimization of phase change material based cylindrical heat sinks with internal stem and radial fins," *Therm. Sci. Eng. Prog.*, vol. 5, pp. 238–251, Mar. 2018, doi: 10.1016/j.tsep.2017.10.003.

[132] N. Bianco, A. Fragnito, M. Iasiello, and G. Maria Mauro, "A comprehensive approach for the

multi-objective optimization of Heat Recovery Steam Generators to maximize cost-effectiveness and output power," *Sustain. Energy Technol. Assessments*, vol. 45, p. 101162, Jun. 2021, doi: 10.1016/j.seta.2021.101162.

[133] N. Bianco, S. Busiello, M. Iasiello, and G. M. Mauro, "Finned heat sinks with phase change materials and metal foams: Pareto optimization to address cost and operation time," *Appl. Therm. Eng.*, vol. 197, p. 117436, Oct. 2021, doi: 10.1016/j.applthermaleng.2021.117436.

[134] A. Abdelkader, A. Rabeh, D. Mohamed Ali, and J. Mohamed, "Multi-objective genetic algorithm based sizing optimization of a stand-alone wind/PV power supply system with enhanced battery/supercapacitor hybrid energy storage," *Energy*, vol. 163, pp. 351–363, Nov. 2018, doi: 10.1016/j.energy.2018.08.135.

[135] F. Ascione, R. F. De Masi, M. Mastellone, and G. P. Vanoli, "Building rating systems: A novel review about capabilities, current limits and open issues," *Sustain. Cities Soc.*, vol. 76, no. September 2021, p. 103498, 2022, doi: 10.1016/j.scs.2021.103498.

[136] L. Li, W. Sun, W. Hu, and Y. Sun, "Impact of natural and social environmental factors on building energy consumption: Based on bibliometrics," *J. Build. Eng.*, vol. 37, no. June 2020, 2021, doi: 10.1016/j.jobe.2020.102136.

[137] E. Zender–świercz, "A review of heat recovery in ventilation," *Energies*, vol. 14, no. 6, 2021, doi: 10.3390/en14061759.

[138] X. Fan and X. Li, "Performance comparison analysis for different single-zone natural ventilation building indoor temperature prediction method combined thermal mass," *Energy*, vol. 255, p. 124518, 2022, doi: 10.1016/j.energy.2022.124518.

[139] H. Y. Bai, P. Liu, M. Justo Alonso, and H. M. Mathisen, "A review of heat recovery technologies and their frost control for residential building ventilation in cold climate regions," *Renew. Sustain. Energy Rev.*, vol. 162, no. December 2021, p. 112417, 2022, doi: 10.1016/j.rser.2022.112417.

[140] A. Mardiana-Idayu and S. B. Riffat, "Review on heat recovery technologies for building applications," *Renew. Sustain. Energy Rev.*, vol. 16, no. 2, pp. 1241–1255, 2012, doi: 10.1016/j.rser.2011.09.026.

[141] X. Bai and Z. Tang, "A numerical study of rock bed seasonal thermal storage used for mine ventilation," *Sustain. Energy Technol. Assessments*, vol. 50, no. November 2021, p. 101867, 2022, doi: 10.1016/j.seta.2021.101867.

[142] A. I. Khdair and G. A. Rumman, "Adopting PCM and natural ventilation in buildings to reduce energy demand in HVAC -Examining various PCM along with various natural ventilation scenarios," *J. Build. Eng.*, vol. 57, no. May, p. 104770, 2022, doi: 10.1016/j.jobe.2022.104770.

[143] K. Faraj, M. Khaled, J. Faraj, F. Hachem, and C. Castelain, "Phase change material thermal energy storage systems for cooling applications in buildings: A review," *Renew. Sustain. Energy Rev.*, vol. 119, no. November 2019, p. 109579, 2020, doi: 10.1016/j.rser.2019.109579.

[144] N. Morovat, A. K. Athienitis, J. A. Candanedo, and V. Dermardiros, "Simulation and performance analysis of an active PCM-heat exchanger intended for building operation optimization," *Energy Build.*, vol. 199, pp. 47–61, 2019, doi: 10.1016/j.enbuild.2019.06.022.

[145] M. Labat, J. Virgone, D. David, and F. Kuznik, "Experimental assessment of a PCM to air heat exchanger storage system for building ventilation application," *Appl. Therm. Eng.*, vol. 66, no. 1–2, pp. 375–382, 2014, doi: 10.1016/j.applthermaleng.2014.02.025.

[146] M. Dardir, K. Panchabikesan, F. Haghighat, M. El Mankibi, and Y. Yuan, "Opportunities and challenges of PCM-to-air heat exchangers (PAHXs) for building free cooling applications—A comprehensive review," *J. Energy Storage*, vol. 22, no. January, pp. 157–175, 2019, doi: 10.1016/j.est.2019.02.011.

[147] C. Suresh, T. Kumar Hotta, and S. K. Saha, "Phase change material incorporation techniques

in building envelopes for enhancing the building thermal Comfort-A review," *Energy Build.*, vol. 268, p. 112225, 2022, doi: 10.1016/j.enbuild.2022.112225.

[148] F. Ascione, N. Bianco, C. De Stasio, G. M. Mauro, and G. P. Vanoli, "Simulation-based model predictive control by the multi-objective optimization of building energy performance and thermal comfort," *Energy Build.*, vol. 111, pp. 131–144, 2016, doi: 10.1016/j.enbuild.2015.11.033.

[149] H. Manz, H. Huber, A. Schälin, A. Weber, M. Ferrazzini, and M. Studer, "Performance of single room ventilation units with recuperative or regenerative heat recovery," *Energy Build.*, vol. 31, no. 1, pp. 37–47, 2000, doi: 10.1016/S0378-7788(98)00077-2.

[150] J. Liu, W. Li, J. Liu, and B. Wang, "Efficiency of energy recovery ventilator with various weathers and its energy saving performance in a residential apartment," *Energy Build.*, vol. 42, no. 1, pp. 43–49, 2010, doi: 10.1016/j.enbuild.2009.07.009.

[151] J. K. Calautit, D. O'Connor, P. W. Tien, S. Wei, C. A. J. Pantua, and B. Hughes, "Development of a natural ventilation windcatcher with passive heat recovery wheel for mild-cold climates: CFD and experimental analysis," *Renew. Energy*, vol. 160, pp. 465–482, 2020, doi: 10.1016/j.renene.2020.05.177.

[152] W. Yaïci, M. Ghorab, and E. Entchev, "Numerical analysis of heat and energy recovery ventilators performance based on CFD for detailed design," *Appl. Therm. Eng.*, vol. 51, no. 1–2, pp. 770–780, 2013, doi: 10.1016/j.applthermaleng.2012.10.003.

[153] M. Jourabian, A. A. Rabienataj Darzi, O. A. Akbari, and D. Toghraie, "The enthalpy-based lattice Boltzmann method (LBM) for simulation of NePCM melting in inclined elliptical annulus," *Phys. A Stat. Mech. its Appl.*, vol. 548, p. 123887, 2020, doi: 10.1016/j.physa.2019.123887.

[154] M. Bayat, M. R. Faridzadeh, and D. Toghraie, "Investigation of finned heat sink performance with nano enhanced phase change material (NePCM)," *Therm. Sci. Eng. Prog.*, vol. 5, no. October 2017, pp. 50–59, 2018, doi: 10.1016/j.tsep.2017.10.021.

[155] M. El Mankibi, N. Stathopoulos, N. Rezaï, and A. Zoubir, "Optimization of an Air-PCM heat exchanger and elaboration of peak power reduction strategies," *Energy Build.*, vol. 106, pp. 74–86, 2015, doi: 10.1016/j.enbuild.2015.05.023.

[156] S. R. Yan *et al.*, "Energy efficiency optimization of the waste heat recovery system with embedded phase change materials in greenhouses: A thermo-economic-environmental study," *J. Energy Storage*, vol. 30, no. April, p. 101445, 2020, doi: 10.1016/j.est.2020.101445.

[157] T. Pekdogan, A. Tokuç, M. A. Ezan, and T. Başaran, "Experimental investigation on heat transfer and air flow behavior of latent heat storage unit in a facade integrated ventilation system," *J. Energy Storage*, vol. 44, no. July, pp. 1–11, 2021, doi: 10.1016/j.est.2021.103367.

[158] S. S. Mostafavi Tehrani, G. Diarce, and R. A. Taylor, "The error of neglecting natural convection in high temperature vertical shell-and-tube latent heat thermal energy storage systems," *Sol. Energy*, vol. 174, pp. 489–501, Nov. 2018, doi: 10.1016/j.solener.2018.09.048.

[159] R. K. Shah and D. P. Sekuli, *Selection of Heat Exchangers and Their Components*. 2007. doi: 10.1002/9780470172605.ch10.

[160] L. F. Cabeza, G. Zsembinszki, and M. Martín, "Evaluation of volume change in phase change materials during their phase transition," *J. Energy Storage*, vol. 28, no. September 2019, p. 101206, 2020, doi: 10.1016/j.est.2020.101206.

[161] M. Fesanghary, E. Damangir, and I. Soleimani, "Design optimization of shell and tube heat exchangers using global sensitivity analysis and harmony search algorithm," *Appl. Therm. Eng.*, vol. 29, no. 5–6, pp. 1026–1031, Apr. 2009, doi: 10.1016/j.applthermaleng.2008.05.018.

[162] "https://www.alfa.com/it/catalog/A18050/."

[163] N. Bianco, A. Fragnito, M. Iasiello, G. M. Mauro, and L. Mongibello, "Multi-objective optimization of a phase change material-based shell-and-tube heat exchanger for cold thermal energy storage: experiments and numerical modeling," *Appl. Therm. Eng.*, vol. 215, p. 119047, Oct. 2022, doi: 10.1016/j.applthermaleng.2022.119047.

[164] P. Promoppatum, S. C. Yao, T. Hultz, and D. Agee, "Experimental and numerical investigation of the cross-flow PCM heat exchanger for the energy saving of building HVAC," *Energy Build.*, vol. 138, pp. 468–478, 2017, doi: 10.1016/j.enbuild.2016.12.043.

[165] *European Standard EN 13141-8:2014.*

[166] "Eurostat: Electricity price statistics." https://ec.europa.eu/eurostat/statistics-explained/index.php?title=Electricity_price_statistics

[167] L. F. Cabeza, D. Urge-Vorsatz, M. A. McNeil, C. Barreneche, and S. Serrano, "Investigating greenhouse challenge from growing trends of electricity consumption through home appliances in buildings," *Renew. Sustain. Energy Rev.*, vol. 36, pp. 188–193, 2014, doi: 10.1016/j.rser.2014.04.053.

[168] P. Liu, M. Justo Alonso, and H. M. Mathisen, "Global sensitivity analysis and optimal design of heat recovery ventilation for zero emission buildings," *Appl. Energy*, vol. 329, no. June 2022, p. 120237, 2023, doi: 10.1016/j.apenergy.2022.120237.

[169] G. De Schutter, K. Lesage, V. Mechtcherine, V. N. Nerella, G. Habert, and I. Agusti-Juan, "Vision of 3D printing with concrete — Technical, economic and environmental potentials," *Cem. Concr. Res.*, vol. 112, pp. 25–36, Oct. 2018, doi: 10.1016/j.cemconres.2018.06.001.

[170] B. Furet, P. Poullain, and S. Garnier, "3D printing for construction based on a complex wall of polymer-foam and concrete," *Addit. Manuf.*, vol. 28, pp. 58–64, Aug. 2019, doi: 10.1016/j.addma.2019.04.002.

[171] M. Kaszynka *et al.*, "Thermal-Humidity Parameters of 3D Printed Wall," *IOP Conf. Ser. Mater. Sci. Eng.*, vol. 471, p. 082018, Feb. 2019, doi: 10.1088/1757-899X/471/8/082018.

[172] B. Baz, G. Aouad, J. Kleib, D. Bulteel, and S. Remond, "Durability assessment and microstructural analysis of 3D printed concrete exposed to sulfuric acid environments," *Constr. Build. Mater.*, vol. 290, p. 123220, Jul. 2021, doi: 10.1016/j.conbuildmat.2021.123220.

[173] H. Marais, H. Christen, S. Cho, W. De Villiers, and G. Van Zijl, "Computational assessment of thermal performance of 3D printed concrete wall structures with cavities," *J. Build. Eng.*, vol. 41, no. December 2020, 2021, doi: 10.1016/j.jobe.2021.102431.

[174] S. Pessoa, A. S. Guimarães, S. S. Lucas, and N. Simões, "3D printing in the construction industry - A systematic review of the thermal performance in buildings," *Renew. Sustain. Energy Rev.*, vol. 141, p. 110794, May 2021, doi: 10.1016/j.rser.2021.110794.

[175] R. K. MacGregor and A. F. Emery, "Free Convection Through Vertical Plane Layers—Moderate and High Prandtl Number Fluids," *J. Heat Transfer*, vol. 91, no. 3, pp. 391–401, Aug. 1969, doi: 10.1115/1.3580194.

[176] A. Rubel and F. Landis, "LAMINAR NATURAL CONVECTION IN A RECTANGULAR ENCLOSURE WITH MODERATELY LARGE TEMPERATURE DIFFERENCES," in *Proceeding of International Heat Transfer Conference 4*, 1970, pp. 1–11. doi: 10.1615/IHTC4.3530.

[177] *UNI EN ISO 13788:2013 "Hygrothermal performance of building components and building elements - Internal surface temperature to avoid critical surface humidity and interstitial condensation - Calculation methods."*

[178] "ISO 6946:1996 (1996) Building components and building elements—thermal resistance and thermal transmittance—calculation method."

[179] D. Saury, N. Rouger, F. Djanna, and F. Penot, "Natural convection in an air-filled cavity: Experimental results at large Rayleigh numbers," *Int. Commun. Heat Mass Transf.*, vol. 38, no. 6, pp. 679–687, Jul. 2011, doi: 10.1016/j.icheatmasstransfer.2011.03.019.

[180] G. Barakos, E. Mitsoulis, and D. Assimacopoulos, "Natural convection flow in a square cavity revisited: Laminar and turbulent models with wall functions," *Int. J. Numer. Methods Fluids*, vol. 18, no. 7, pp. 695–719, Apr. 1994, doi: 10.1002/fld.1650180705.

[181] "UNI EN 15026:2008 'Hygrothermal performance of building components and building elements - Assessment of moisture transfer by numerical simulation.'"

[182] G. Henrique dos Santos, M. A. Fogiatto, and N. Mendes, "Numerical analysis of thermal transmittance of hollow concrete blocks," *J. Build. Phys.*, vol. 41, no. 1, pp. 7–24, Jul. 2017, doi: 10.1177/1744259117698522.

[183] Z. He, Y. Yan, and Z. Zhang, "Thermal management and temperature uniformity enhancement of electronic devices by micro heat sinks: A review," *Energy*, vol. 216, p. 119223, Feb. 2021, doi: 10.1016/j.energy.2020.119223.

[184] W. Hua, L. Zhang, and X. Zhang, "Research on passive cooling of electronic chips based on PCM: A review," *J. Mol. Liq.*, vol. 340, p. 117183, Oct. 2021, doi: 10.1016/j.molliq.2021.117183.

[185] S. K. Sahoo, M. K. Das, and P. Rath, "Application of TCE-PCM based heat sinks for cooling of electronic components: A review," *Renew. Sustain. Energy Rev.*, vol. 59, pp. 550–582, Jun. 2016, doi: 10.1016/j.rser.2015.12.238.

[186] S. Yan, F. Wang, J. Hong, and O. Sigmund, "Topology optimization of microchannel heat sinks using a two-layer model," *Int. J. Heat Mass Transf.*, vol. 143, p. 118462, Nov. 2019, doi: 10.1016/j.ijheatmasstransfer.2019.118462.

[187] A.-C. Iradukunda, A. Vargas, D. Huitink, and D. Lohan, "Transient thermal performance using phase change material integrated topology optimized heat sinks," *Appl. Therm. Eng.*, vol. 179, p. 115723, Oct. 2020, doi: 10.1016/j.applthermaleng.2020.115723.

[188] X.-Q. Wang, C. Yap, and A. S. Mujumdar, "A parametric study of phase change material (PCM)-based heat sinks," *Int. J. Therm. Sci.*, vol. 47, no. 8, pp. 1055–1068, Aug. 2008, doi: 10.1016/j.ijthermalsci.2007.07.016.

[189] E. M. Dede, S. N. Joshi, and F. Zhou, "Topology Optimization, Additive Layer Manufacturing, and Experimental Testing of an Air-Cooled Heat Sink," *J. Mech. Des.*, vol. 137, no. 11, Nov. 2015, doi: 10.1115/1.4030989.

[190] F. Lange *et al.*, "Numerical optimization of active heat sinks considering restrictions of selective laser melting Topology Optimization considering the restrictions of Additive Manufacturing View project ShipLight View project Numerical optimization of active heat sinks co," no. November, 2018, [Online]. Available: https://www.researchgate.net/publication/328738213

[191] A. Diani and M. Campanale, "Transient melting of paraffin waxes embedded in aluminum foams: Experimental results and modeling," *Int. J. Therm. Sci.*, vol. 144, no. August 2018, pp. 119–128, 2019, doi: 10.1016/j.ijthermalsci.2019.06.004.

[192] A. Diani, C. Nonino, and L. Rossetto, "Melting of phase change materials inside periodic cellular structures fabricated by additive manufacturing: Experimental results and numerical simulations," *Appl. Therm. Eng.*, vol. 215, no. June, p. 118969, 2022, doi: 10.1016/j.applthermaleng.2022.118969.

[193] X. hui Han, H. ling Liu, G. Xie, L. Sang, and J. Zhou, "Topology optimization for spider web heat sinks for electronic cooling," *Appl. Therm. Eng.*, vol. 195, no. May, p. 117154, 2021, doi: 10.1016/j.applthermaleng.2021.117154.

[194] O. Sigmund and K. Maute, "Topology optimization approaches: A comparative review," *Struct. Multidiscip. Optim.*, vol. 48, no. 6, pp. 1031–1055, 2013, doi: 10.1007/s00158-013-0978-6.

[195] H. Li, X. Ding, F. Meng, D. Jing, and M. Xiong, "Optimal design and thermal modelling for liquid-cooled heat sink based on multi-objective topology optimization: An experimental and numerical study," *Int. J. Heat Mass Transf.*, vol. 144, p. 118638, 2019, doi:

10.1016/j.ijheatmasstransfer.2019.118638.

[196] X. Zhao, M. Zhou, O. Sigmund, and C. S. Andreasen, "A 'poor man's approach' to topology optimization of cooling channels based on a Darcy flow model," *Int. J. Heat Mass Transf.*, vol. 116, pp. 1108–1123, 2018, doi: 10.1016/j.ijheatmasstransfer.2017.09.090.

[197] J. H. K. Haertel, K. Engelbrecht, B. S. Lazarov, and O. Sigmund, "Topology optimization of a pseudo 3D thermofluid heat sink model," *Int. J. Heat Mass Transf.*, vol. 121, pp. 1073–1088, 2018, doi: 10.1016/j.ijheatmasstransfer.2018.01.078.

[198] T. Dixit and I. Ghosh, "Review of micro- and mini-channel heat sinks and heat exchangers for single phase fluids," *Renew. Sustain. Energy Rev.*, vol. 41, pp. 1298–1311, 2015, doi: 10.1016/j.rser.2014.09.024.

[199] D. B. Tuckerman and R. F. W. Pease, "High-Performance Heat Sinking for VLSI," *IEEE Electron Device Lett.*, vol. EDL-2, no. 5, pp. 126–129, 1981, doi: 10.1109/EDL.1981.25367.

[200] S. G. Kandlikar and W. J. Grande, "Evolution of microchannel flow passages-thermohydraulic performance and fabrication technology," *Heat Transf. Eng.*, vol. 24, no. 1, pp. 3–17, 2003, doi: 10.1080/01457630304040.

[201] S. S. Mehendafe, A. M. Jacobi, and R. K. Shah, "Fluid flow and heat transfer at micro- and meso-scales with application to heat exchanger design," *Appl. Mech. Rev.*, vol. 53, no. 7, pp. 175–193, 2000, doi: 10.1115/1.3097347.

[202] G. Lu, J. Yang, X. Zhai, and X. Wang, "Hotspot thermal management in microchannel heat sinks with vortex generators," *Int. J. Therm. Sci.*, vol. 161, no. July 2020, p. 106727, 2021, doi: 10.1016/j.ijthermalsci.2020.106727.

[203] Y. Yang *et al.*, "Highly efficient and stable fuel-catalyzed dendritic microchannels for dilute ethanol fueled solid oxide fuel cells," *Appl. Energy*, vol. 307, no. November 2021, p. 118222, 2022, doi: 10.1016/j.apenergy.2021.118222.

[204] M. Datta and H. W. Choi, "Microheat exchanger for cooling high power laser diodes," *Appl. Therm. Eng.*, vol. 90, pp. 266–273, 2015, doi: 10.1016/j.applthermaleng.2015.07.012.

[205] D. Deng, Y. Xie, L. Chen, G. Pi, and Y. Huang, "Experimental investigation on thermal and combustion performance of a combustor with microchannel cooling," *Energy*, vol. 181, pp. 954–963, 2019, doi: 10.1016/j.energy.2019.06.034.

[206] K. N. Ramesh, T. K. Sharma, and G. A. P. Rao, *Latest Advancements in Heat Transfer Enhancement in the Micro-channel Heat Sinks: A Review*, vol. 28, no. 4. Springer Netherlands, 2021. doi: 10.1007/s11831-020-09495-1.

[207] H. Wang, Z. Chen, and J. Gao, "Influence of geometric parameters on flow and heat transfer performance of micro-channel heat sinks," *Appl. Therm. Eng.*, vol. 107, pp. 870–879, 2016, doi: 10.1016/j.applthermaleng.2016.07.039.

[208] H. ling Liu, D. hao Qi, X. dong Shao, and W. dong Wang, "An experimental and numerical investigation of heat transfer enhancement in annular microchannel heat sinks," *Int. J. Therm. Sci.*, vol. 142, no. December 2018, pp. 106–120, 2019, doi: 10.1016/j.ijthermalsci.2019.04.006.

[209] A. M. Sahar, J. Wissink, M. M. Mahmoud, T. G. Karayiannis, and M. S. Ashrul Ishak, "Effect of hydraulic diameter and aspect ratio on single phase flow and heat transfer in a rectangular microchannel," *Appl. Therm. Eng.*, vol. 115, pp. 793–814, 2017, doi: 10.1016/j.applthermaleng.2017.01.018.

[210] K. Vafai and L. Zhu, "Analysis of two-layered micro-channel heat sink concept in electronic cooling," *Int. J. Heat Mass Transf.*, vol. 42, no. 12, pp. 2287–2297, Jun. 1999, doi: 10.1016/S0017-9310(98)00017-9.

[211] W. H. Shih, W. C. Chiu, and W. H. Hsieh, "Height effect on heat-transfer characteristics of aluminum-foam heat sinks," *J. Heat Transfer*, vol. 128, no. 6, pp. 530–537, 2006, doi: 10.1115/1.2188461.

[212] J. Wang, H. Kong, Y. Xu, and J. Wu, "Experimental investigation of heat transfer and flow

characteristics in finned copper foam heat sinks subjected to jet impingement cooling," *Appl. Energy*, vol. 241, no. March, pp. 433–443, 2019, doi: 10.1016/j.apenergy.2019.03.040.

[213] W. H. Shih, F. C. Chou, and W. H. Hsieh, "Experimental investigation of the heat transfer characteristics of aluminum-foam heat sinks with restricted flow outlet," *J. Heat Transfer*, vol. 129, no. 11, pp. 1554–1563, 2007, doi: 10.1115/1.2759972.

[214] C. DeGroot, T., A. Straatman, G., L. Betchen, and J., "Modeling Forced Convection in Finned Metal Foam Heat Sinks," *J. Electron. Packag.*, vol. 131, no. 2, Jun. 2009, doi: 10.1115/1.3103934.

[215] S. P. Aly, A. F. M. Arif, K. S. Al-Athel, J. Mostaghimi, and S. M. Zubair, "Performance of open pore metal foam heat sinks fabricated with thermally sprayed interface," *Appl. Therm. Eng.*, vol. 105, pp. 411–424, 2016, doi: 10.1016/j.applthermaleng.2016.03.012.

[216] M. A. Alfellag, H. E. Ahmed, M. G. Jehad, and M. Hameed, "Assessment of heat transfer and pressure drop of metal foam-pin-fin heat sink," *Int. J. Therm. Sci.*, vol. 170, no. February, p. 107109, 2021, doi: 10.1016/j.ijthermalsci.2021.107109.

[217] K. Yogi, M. M. Godase, M. Shetty, S. Krishnan, and S. V. Prabhu, "Experimental investigation on the local heat transfer with a circular jet impinging on a metal foamed flat plate," *Int. J. Heat Mass Transf.*, vol. 162, p. 120405, 2020, doi: 10.1016/j.ijheatmasstransfer.2020.120405.

[218] S. De Schampheleire *et al.*, "Experimental study of buoyancy-driven flow in open-cell aluminium foam heat sinks," *Appl. Therm. Eng.*, vol. 59, no. 1–2, pp. 30–40, 2013, doi: 10.1016/j.applthermaleng.2013.05.010.

[219] C. Shi, M. Wang, J. Yang, W. Liu, and Z. Liu, "Performance analysis and multi-objective optimization for tubes partially filled with gradient porous media," *Appl. Therm. Eng.*, vol. 188, no. November 2020, p. 116530, 2021, doi: 10.1016/j.applthermaleng.2020.116530.

[220] S. Pusterla, M. Barbato, A. Ortona, and C. D'Angelo, "Numerical study of cell morphology effects on convective heat transfer in reticulated ceramics," *Int. J. Heat Mass Transf.*, vol. 55, no. 25–26, pp. 7902–7910, 2012, doi: 10.1016/j.ijheatmasstransfer.2012.08.013.

[221] E. Rezaei, M. Barbato, S. Gianella, A. Ortona, and S. Haussener, "Pressure Drop and Convective Heat Transfer in Different SiSiC Structures Fabricated by Indirect Additive Manufacturing," *J. Heat Transfer*, vol. 142, no. 3, Mar. 2020, doi: 10.1115/1.4045732.

[222] N. Bianco, M. Iasiello, G. M. Mauro, and L. Pagano, "Multi-objective optimization of finned metal foam heat sinks: Tradeoff between heat transfer and pressure drop," *Appl. Therm. Eng.*, vol. 182, no. July 2020, p. 116058, 2021, doi: 10.1016/j.applthermaleng.2020.116058.

[223] V. Subramaniam, T. Dbouk, and J. L. Harion, "Topology optimization of conjugate heat transfer systems: A competition between heat transfer enhancement and pressure drop reduction," *Int. J. Heat Fluid Flow*, vol. 75, no. December 2018, pp. 165–184, 2019, doi: 10.1016/j.ijheatfluidflow.2019.01.002.

[224] C. B. Dilgen, S. B. Dilgen, D. R. Fuhrman, O. Sigmund, and B. S. Lazarov, "Topology optimization of turbulent flows," *Comput. Methods Appl. Mech. Eng.*, vol. 331, pp. 363–393, 2018, doi: 10.1016/j.cma.2017.11.029.

[225] B. Rogié and C. S. Andreasen, "Design complexity tradeoffs in topology optimization of forced convection laminar flow heat sinks," *Struct. Multidiscip. Optim.*, vol. 66, no. 1, pp. 1–22, 2023, doi: 10.1007/s00158-022-03449-w.

[226] S. Zeng, B. Kanargi, and P. S. Lee, "Experimental and numerical investigation of a mini channel forced air heat sink designed by topology optimization," *Int. J. Heat Mass Transf.*, vol. 121, pp. 663–679, 2018, doi: 10.1016/j.ijheatmasstransfer.2018.01.039.

[227] A. A. Koga, E. C. C. Lopes, H. F. Villa Nova, C. R. D. Lima, and E. C. N. Silva, "Development of heat sink device by using topology optimization," *Int. J. Heat Mass Transf.*, vol. 64, pp.

759–772, 2013, doi: 10.1016/j.ijheatmasstransfer.2013.05.007.

[228] J. Zhou, M. Lu, Q. Zhao, D. Hu, H. Qin, and X. Chen, "Thermal design of microchannel heat sinks using a contour extraction based on topology optimization (CEBTO) method," *Int. J. Heat Mass Transf.*, vol. 189, p. 122703, 2022, doi: 10.1016/j.ijheatmasstransfer.2022.122703.

[229] X. hui Han, H. ling Liu, G. Xie, L. Sang, and J. Zhou, "Topology optimization for spider web heat sinks for electronic cooling," *Appl. Therm. Eng.*, vol. 195, no. February, p. 117154, 2021, doi: 10.1016/j.applthermaleng.2021.117154.

[230] S. A. Lurie, L. N. Rabinskiy, and Y. O. Solyaev, "Topology optimization of the wick geometry in a flat plate heat pipe," *Int. J. Heat Mass Transf.*, vol. 128, pp. 239–247, 2019, doi: 10.1016/j.ijheatmasstransfer.2018.08.125.

[231] A. Takezawa, X. Zhang, T. Tanaka, and M. Kitamura, "Topology optimisation of a porous unit cell in a fluid flow considering Forchheimer drag," *Int. J. Comut. Fluid Dyn.*, vol. 34, no. 1, pp. 50–60, 2020, doi: 10.1080/10618562.2019.1705968.

[232] C. Shen, L. Hou, E. Zhang, and J. Lin, "Topology optimization of three-phase interpolation models in Darcy-stokes flow," *Struct. Multidiscip. Optim.*, vol. 57, no. 4, pp. 1663–1677, Apr. 2018, doi: 10.1007/s00158-017-1836-8.

[233] D. Li and I. Y. Kim, "Multi-material topology optimization for practical lightweight design," *Struct. Multidiscip. Optim.*, vol. 58, no. 3, pp. 1081–1094, Sep. 2018, doi: 10.1007/s00158-018-1953-z.

[234] J. Alexandersen, O. Sigmund, and N. Aage, "Large scale three-dimensional topology optimisation of heat sinks cooled by natural convection," *Int. J. Heat Mass Transf.*, vol. 100, pp. 876–891, 2016, doi: 10.1016/j.ijheatmasstransfer.2016.05.013.

[235] M. Iasiello, N. Bianco, W. K. S. Chiu, and V. Naso, "Thermal conduction in open-cell metal foams: Anisotropy and Representative Volume Element," *Int. J. Therm. Sci.*, vol. 137, pp. 399–409, Mar. 2019, doi: 10.1016/j.ijthermalsci.2018.12.002.

[236] A. Chandrasekhar and K. Suresh, "Multi-Material Topology Optimization Using Neural Networks," *Comput. Des.*, vol. 136, p. 103017, Jul. 2021, doi: 10.1016/j.cad.2021.103017.

[237] H. J. Xu, L. Gong, C. Y. Zhao, Y. H. Yang, and Z. G. Xu, "Analytical considerations of local thermal non-equilibrium conditions for thermal transport in metal foams," *Int. J. Therm. Sci.*, vol. 95, pp. 73–87, Sep. 2015, doi: 10.1016/j.ijthermalsci.2015.04.007.

[238] Y. Li, L. Gong, B. Ding, M. Xu, and Y. Joshi, "Thermal management of power electronics with liquid cooled metal foam heat sink," *Int. J. Therm. Sci.*, vol. 163, p. 106796, May 2021, doi: 10.1016/j.ijthermalsci.2020.106796.

[239] M. Ghorbani, M. R. Salimpour, and K. Vafai, "Microchannel thermal performance optimization utilizing porous layer configurations," *Int. J. Heat Mass Transf.*, vol. 133, pp. 62–72, Apr. 2019, doi: 10.1016/j.ijheatmasstransfer.2018.12.063.

[240] D.-Y. Lee and K. Vafai, "Analytical characterization and conceptual assessment of solid and fluid temperature differentials in porous media," *Int. J. Heat Mass Transf.*, vol. 42, no. 3, pp. 423–435, Feb. 1999, doi: 10.1016/S0017-9310(98)00185-9.

[241] A. Andreozzi, N. Bianco, M. Iasiello, and V. Naso, "Natural convection in a vertical channel with open-cell foams," *J. Phys. Conf. Ser.*, vol. 1599, no. 1, p. 012013, Aug. 2020, doi: 10.1088/1742-6596/1599/1/012013.

[242] V. V. Calmidi and R. L. Mahajan, "Forced Convection in High Porosity Metal Foams," *J. Heat Transfer*, vol. 122, no. 3, pp. 557–565, Aug. 2000, doi: 10.1115/1.1287793.

[243] Z.-J. Zheng, M.-J. Li, and Y.-L. He, "Optimization of porous insert configurations for heat transfer enhancement in tubes based on genetic algorithm and CFD," *Int. J. Heat Mass Transf.*, vol. 87, pp. 376–379, Aug. 2015, doi: 10.1016/j.ijheatmasstransfer.2015.04.016.

[244] S. Du, T. Xia, Y.-L. He, Z.-Y. Li, D. Li, and X.-Q. Xie, "Experiment and optimization study on the radial graded porous volumetric solar receiver matching non-uniform solar flux

distribution," *Appl. Energy*, vol. 275, p. 115343, Oct. 2020, doi: 10.1016/j.apenergy.2020.115343.

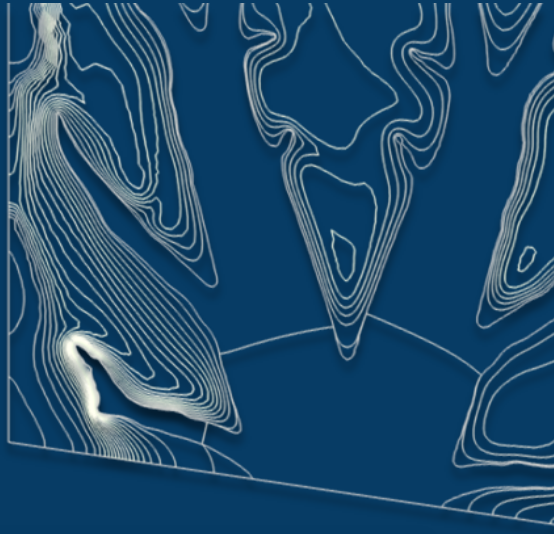

Summary

This thesis offers a comprehensive exploration of the critical role that numerical optimization methods play in the domain of heat transfer. Heat transfer is a fundamental aspect of thermal engineering and science, impacting the design and operation of numerous systems in our modern world. As heat transfer problems continue to grow in complexity, numerical tools have become indispensable for addressing the intricate challenges they pose. However, it is essential to recognize that heat transfer is not a one-size-fits-all domain; it encompasses a diverse spectrum of scenarios, each governed by distinct heat transfer mechanisms. In this context, the choice of optimization method is crucial, and it must be tailored to the specific characteristics and constraints of each heat transfer problem. This thesis emphasizes the distinction between large-scale and small-scale systems, highlighting the preference for genetic algorithms (GAs) in large-scale systems and gradient-based methods, particularly topology optimization-based procedures, in small-scale systems. The thesis also highlights the design flexibility that gradient-based techniques, particularly topology optimization, offer. Researchers can explore innovative configurations and geometric patterns, optimizing not only for energy efficiency but also for innovative form factors and structural considerations. This level of design flexibility is invaluable, particularly in small-scale systems where every element must be meticulously tuned for optimal performance. For instance, the use of topology optimization, including multi-material topology optimization with metal foams, demonstrates significant improvements in thermal performance and energy efficiency.